7.8 - 1 0 0. 6 9

CR 151612

MICROWAVE REMOTE SENSING AND ITS APPLICATION TO SOIL MOISTURE DETECTION

By

Richard Wayne Newton

January 1977

TEXAS A&M UNIVERSITY
REMOTE SENSING CENTER
COLLEGE STATION, TEXAS

MICROWAVE REMOTE SENSING AND ITS APPLICATION

# TO SOIL MOISTURE DETECTION

By

Richard Wayne Newton

January 1977

Supported by

National Aeronautics and Space Administration

NAS9-13904

ABSTRACT

Microwave Remote Sensing and Its Application to Soil
Moisture Detection

-

Theoretical and experimental studies of the thermal
microwave emission from moist soil were performed. The
theoretical study was undertaken to provide a physical
understanding of the emission from soil and its relation-
ship to soil moisture. It is shown that the soil permit-
tivity is dependent on the soil water matric potential
independent of soil texture. Relationships describing the
effects of the soil permittivity profile, surface roughness
and vegetation cover on the microwave emission from soil
are developed. Emission from the soil volume is described
using a radiative transfer approach, the effect of surface
roughness is modeled using the Kirchhoff approximation and
vegetation cover is modeled as a dielectric slab.

Two experimental measurement programs were performed
in order to verify the theoretical predictions and demon-
strate the feasibility of estimating soil moisture remotely

using passive microwave sensors. Antenna temperature ·
measurements of bare and vegetated, smooth and rough soil
surfaces were obtained at 1.4 GHz and 10.6 GHz. These data
demonstrate that a uniform surface roughness decreases the
antenna temperature sensitivity to soil moisture at both
1.4 GHz and 10.6 GHz, but that the 10.6 GHz wavelength is
sensitive to much smaller scales of surface roughness than
is the 1.4 GHz wavelength. The effects of a periodic row
structure are also demonstrated. It is also shown that
uniform vegetation up to 125 cm tall has a minimal effect
on the response of 1.4 GHz emission to soil moisture.
However, such vegetation effectively masks the soil mois-
ture response at 10.6 GHz.

A technique of estimating the average soil moisture
within a surface layer is demonstrated. It is shown that
at 1.4 GHz the depth of this surface layer ranges from a
few centimeters up to approximately 20 centimeters depend-
ing on the soil moisture conditions. At 10.6 GHz this
surface layer is never more than 2 centimeters thick.
This technique is shown to be effective for a range of
uniform surface roughness conditions. However, the soil
moisture estimation accuracy decreases with surface rough-
ness. At 1.4 GHz the approximate soil moisture estimation
accuracy is shown to be +3% to -6% for a smooth surface,
+4% and -5% for a medium rough surface, and +5.5% and -6%

for a rough surface. At 10.6 GHz it was estimated that
the surface soil moisture could be measured to within ±10%
for "smooth" and medium rough surfaces, and to within ±6%
for a rough surface.

Since soil moisture can be measured to different
depths by using different wavelengths, the surface soil
moisture profile can be estimated using a multifrequency
system. It is expected that a frequency between 1.4 GHz
and 10.6 GHz will yield better estimates of surface soil
moisture than 10.6 GHz due to a smaller sensitivity to
surface roughness. In addition, the soil moisture estima-
tion technique will apply equally well to soil water matric
potential independent of soil texture. This indicates that
the feasibility of remotely estimating available water to
plants in the near surface, or degree of soil saturation
(two parameters that are of interest to agriculturalists
and hydrologists) is realizable.

TABLE OF CONTENTS

LIST OF TABLES

LIST OF FIGURES

Figure   Page

CHAPTER I

INTRODUCTION

Problem Statement

During the past few years a considerable effort has
been devoted to the development of techniques for obtaining
information about the sub-visible surface of a scene. Remote
sensors operating in the microwave frequency spectrum pro-
duce data that contain subsurface information. The micro-
wave energy that is measured by the sensor interacts to a
certain extent with the subsurface medium. As a result,
investigations into subsurface phenomenon have been
approached in most cases by utilizing sensors operating in
the microwave spectrum. Both passive and active microwave
sensors have been utilized in these studies. The research
reported in this document deals primarily with passive
microwave sensors.

The application of microwave sensors that has stirred
the majority of interest in the last few years is the
remote measurement of soil moisture. This application
is felt to be viable since it has been demonstrated by

laboratory measurements that the microwave permittivity of soil is highly dependent on soil moisture. This result indicates the existence of an interaction mechanism between electromagnetic energy and soil moisture. Such a mechanism is required in order for a scene to have a microwave response that is dependent on soil moisture. However, other factors such as inhomogeneities in the soil, the geometry of the surface boundary, and vegetation above the soil interact with the electromagnetic energy and also affect the microwave response of the soil.

This study is an experimental investigation into the interaction of electromagnetic energy in the microwave frequency spectrum with soil to determine the ability, quantitatively, to estimate soil moisture from remote measurements made with microwave sensors. This investigation results in a technique for extracting soil moisture information from data acquired with microwave sensors. The technique is analyzed to demonstrate its limitations and predicted accuracy.

Approach

In order to determine the ability to estimate soil moisture remotely, it is necessary to understand the

physical phenomena that are responsible for the interaction
mechanisms that produce the microwave response of a scene,
and to understand the inherent limitations of using this
response to estimate soil moisture. The inherent limita-
tions in the ability to estimate soil moisture are a result
of the effects of physical scene parameters on the micro-
wave response of the scene. These parameters are soil type,
soil inhomogeneities, surface roughness, soil moisture and
temperature variation with depth, and vegetation cover.

The investigation of the interaction of electromagnetic
energy with the scene is made less complicated experimentally
by considering the subsurface, surface, and vegetation
separately. It is also advantageous to study each of these
scene components separately in order to obtain a physical
interpretation of the effect of each on the microwave
measurements.

The general approach to this research was to generate
physical models that describe the individual effects of each
component on the emitted microwave energy of the scene.
Combinations of these physical models were then utilized
to assess the ability to estimate soil moisture and to
determine the optimum techniques of doing so. In addition,
ground-based field experiments were performed with passive
microwave sensors to measure the effects of each scene
component independently under controlled conditions.

Results of these experimental measurements were compared
to predictions made with the models.

Scope of the Report

This report establishes a technique of measuring soil
moisture with microwave sensors. Chapter II provides
background information on soils, the interaction of water
with soils, and the uptake of soil water by plants as
well as a reasonably detailed discussion on the effects of
soil water on the microwave permittivity of soil. Chapter
III completes the background material by providing a review
of published thermal microwave measurements of soil-
vegetation scenes, as well as modeling techniques that have
been used to describe these data. In the review of Chapter
III the advantages and disadvantages of these modeling
techniques and the limitations of the previously published
microwave measurements are discussed.

Chapter IV contains the development of the models used
as the basis of this research. These models are evaluated
in detail to demonstrate the effects of scene parameters
on the microwave response of the soil. Chapter V is a
description of measurement programs designed to acquire
experimental data appropriate for validating the models
described in Chapter IV. In Chapter VI the effects of the
sensor system on the true microwave response of a scene

are described. These effects must be considered when
comparing model predictions to actual measurements.

In Chapter VII the passive microwave measurements
described in Chapter V are analyzed to determine a proce-
dure for estimating soil moisture. Of special importance
is the effect of the soil moisture distribution with depth.
An analysis is provided to demonstrate to which part of the
soil moisture profile a microwave measurement is responsive.
In this analysis a parameter is obtained that is related
to the average available soil water within an effective
skin depth. This parameter describes the response of the
microwave measurement to soil moisture. It is used in the
remainder of the analysis and is the parameter that is
estimated from microwave measurements.

Chapter VIII contains a summary of the results of
this report and recommendations for future studies.

CHAPTER II

SOIL MOISTURE

The emission or scattering of microwave energy from
a soil surface is governed to a large extent by the per-
mittivity of the soil. Soil permittivity is dependent on
the moisture content of the soil. As a result, the micro-
wave emission of soil varies with soil moisture. The
interaction between soil and soil water is explained as
background for an analysis of the mechanism that causes the
permittivity of soil to vary with soil moisture. In
addition, since soil moisture measurements are utilized in
some applications to determine the availability of soil
water to vegetation, it is also instructive to discuss
the soil-water-plant interrelationship. In order to address
all of these topics in a logical manner, Chapter II is
divided into three main sections. The first topic is soil
and soil-water interaction, the second is soil-water-plant
interrelationships, and the third is soil permittivity.
The first two sections are tutorial in nature and draw
largely from Baver, Gardner, and Gardner [1], Kezdi [2]
and Spangler [3].

Soil-Water Interaction

Soil Composition

Soil is defined as the unconsolidated mineral matter

on the earth's surface that serves as a medium for plant growth [3]. The solid phase of soil consists of organic matter and the product of weathering of parent rocks and the minerals that they contain. Soil is categorized by describing the physical properties that determine the utility of a soil. This is true in either agriculture or civil engineering. A major property used in categorizing soils is the size of the particles making up a soil. The individual or primary soil particles are referred to as textural separates.

Textural separates - The different textural separates in soils are classified into various sized groups. Soil particles are not generally spherical in nature; however, their size distribution is classified on the basis of equivalent diameters. The larger textural separates can be isolated by means of mechanical sieving. In this case the equivalent diameter refers to the diameter of a sphere that will pass through a given size opening. The finest mesh readily available (No. 200 B.S. sieve) has an aperture of approximately 0.08 mm. Textural separates smaller than this must be isolated using sedimentation techniques [2]. In the sedimentation technique, the soil is suspended in water and the velocity with which the particles fall is measured to determine their equivalent diameters. In this case, the equivalent diameter refers to the diameter of a

sphere that has the same density and settling velocity as the soil particles.

Several systems have evolved for classifying textural separates. Figure II-1 contains a comparison of some of these classifications. Both the United States Department of Agriculture (USDA) and the International Society of Soil Science classifications are used by agriculturists. Although these classifications are dissimilar in their definitions of sand and silt size ranges, they both use 0.002 mm (2 μ) as the upper size limit of clays. Clay is the key textural separate in these two classifications. The physical and chemical properties of soil are affected to a much greater degree by the clay content of the soil than by the sand and silt content of the soil.

Atterburg [4], who suggested the International classification, established the 2 μ upper limit of clay size based on bacteriological and physical properties. Bacteria cannot move in pores between grains smaller than this size. Also, clay particles finer than 2 μ do not settle from suspensions but remain in a state of Brownian movement for a period of at least 24 hours [1]. Further justification for this definition of clay was provided by mineralogical studies which showed that relatively few unweathered primary minerals existed in fractions smaller than 2 μ [2].

All soils contain a continuum of soil particle sizes however, the distribution of soil particle sizes varies

DA-CE USBR	Fines (silt or clay)							Fine sand	Coarse sand	
FAA	Clay			Silt			Fine sand		Coarse sand	
AASHO ASTM	Colloids 1)	Clay		Silt				Fine sand	Coarse sand	
USDA	Clay		Silt				Very fine sand	Fine sand	Medium sand	Coarse sand	Very coarse sand
ISSS	Clay		Silt		Fine sand				Coarse sand	

0.001 0.002 0.005 0.01 0.02 0.05 0.10 0.20 0.50 1.0 2.0

Particle Size (mm)

```
DA-CE = Department of Army, Corps of Engineers
 USBR = U.S. Bureau of Reclamation
  FAA = Federal Aviation Authority
AASHO = American Association of State Highway Officials
 ASTM = American Society of Testing and Materials
 USDA = U.S. Department of Agriculture
 ISSS = International Society of Soil Science
Note (1) = Reported with clay
```

Figure II-1. Classification of soil separates ≤2.0 mm on the basis of particle size (after Baver, Gardner, and Gardner [1]).

from soil to soil. The most accurate method of character-
izing a soil is by its particle size distribution. An
example of such a distribution is given in Figure II-2.
The particle size distribution is generally integrated
(averaged) over some specified particle size intervals, such
as those given in Figure II-1. These averages are then
ratioed with the integral of the entire particle size
distribution, thereby providing the percentage content of
each size interval chosen for averaging.

The composition of a soil according to such percentages
can be visualized with the aid of a triangular diagram such
as shown in Figure II-3. This triangular diagram illustrates
soil categories based on the USDA textural separate classi-
fication shown in Figure II-1. A point corresponding to
clay loam (35% clay, 30% silt, and 35% sand) is marked on
the triangle as an example. The USDA soil classification
diagramed in Figure II-1 and the resulting triangle of
Figure II-3 will be used throughout the remainder of this
document.

As pointed out earlier, it is the clay fraction of
the soil that is most important in determining the physical
and chemical characteristics of soils. This is a result
of the fact that these properties are highly associated
with the surface activity of the individual soil particles.
Clay particles have a layered platelike structure that

Gravel   Sand   Mo

100

Percentage Finer by Weight

3%

8%

Retained on
Seive = 48%

12%

25%

50

23%

8%

Passing the
Sieve = 52%

9%

8%

4%

0

9.42   4.74   2.74   1.24   0.58   0.29   0.21   0.15   0.1   0.08

Particle Size (mm)
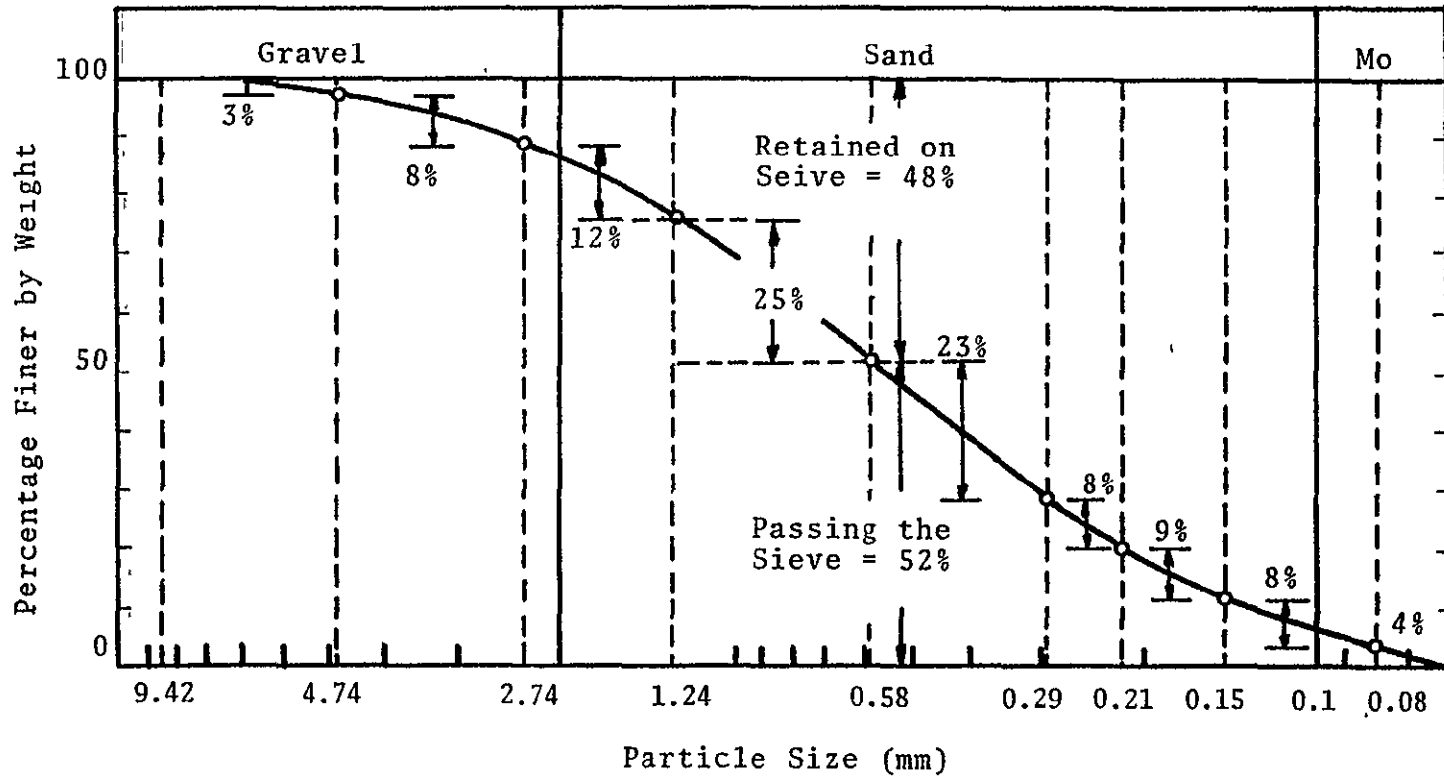
Figure II-2.   Construction of grain-size distribution curve (after Kezdi [2]).
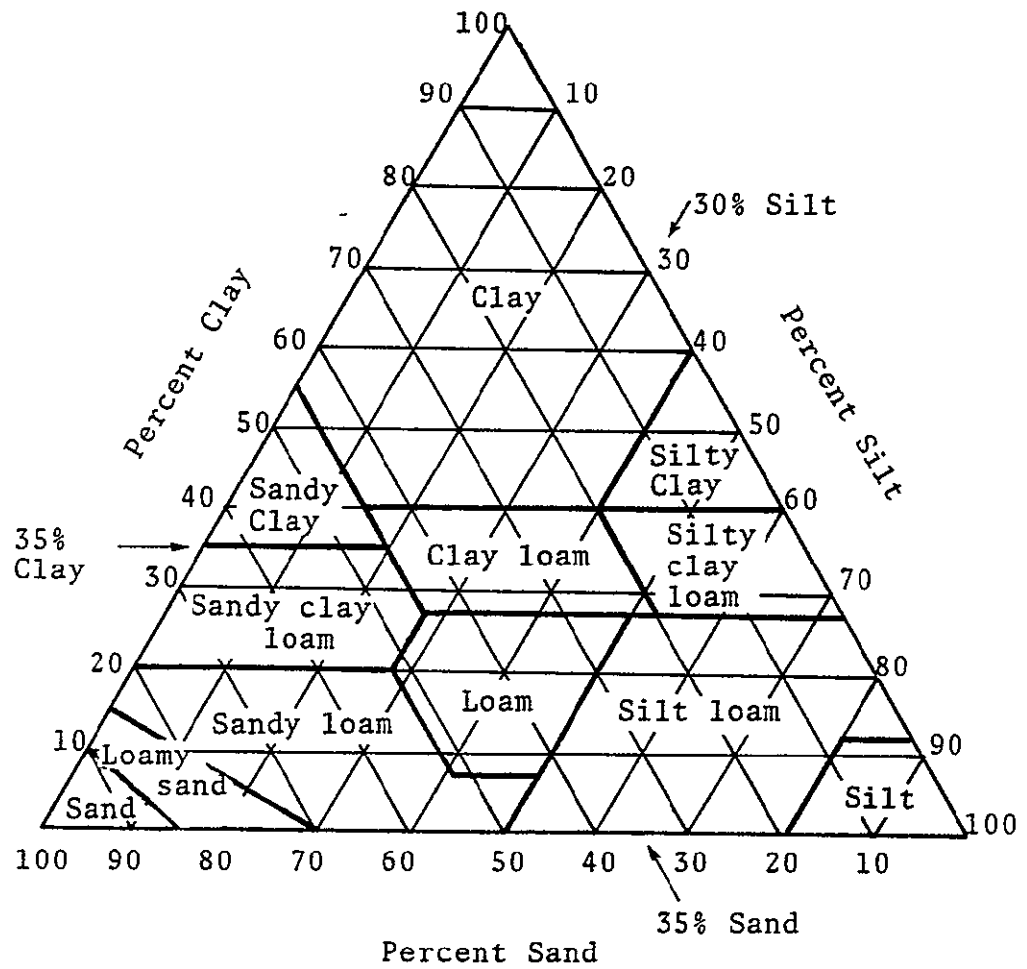
Figure II-3. USDA soil textural classification triangle.

results in very large surface areas per unit weight, much larger than the other textural separates. In addition, clay particles are not electrically neutral, but have negative charges associated with their surfaces. The large surface areas in conjunction with the surface charges allow clay particles to interact with other polar molecules and ions to a greater extent than the other textural separates. Since this interaction takes place on the surface of the clay particles it is termed "surface activity". A more detailed discussion on clay structure is provided in the next two sections.

The surface of clay particles - The extent of surface of a clay is generally expressed in terms of specific surface, square centimeters of surface per gram or per cubic centimeter of dispersed phase where the individual clay particles are separated. The specific surface of a particle is dependent on its size as well as its shape. This can be demonstrated by comparing the specific surfaces of different textural separates utilizing their equivalent diameters and assuming that they are spherical. Table II-1 demonstrates that a very small amount of material ($\pi/6$ cm^3) may have a very large surface area for very small individual particles. Note that a given volume of a 2 μ clay has 50 times the surface area of an equal volume of very fine sand. Collodial clay (100 mμ) has 20 times the surface area of 2 μ clay and 1000 times the surface area of very fine sand.

TABLE II-1

The Relation of Surface to Particle Size (after Baver, Gardner and Gardner [1])

Diameter of sphere	Textural name	Volume per particle $(\pi/6)\ D^3$	Number of particles in $\frac{\pi}{6}$ cc	Total surface πD^2 x number of particles
1 cm	Gravel	$(\pi/6)\ (1)^3$	1	3.14 cm^2 (0.49 in.^{2})
0.1 cm (1 mm)	Coarse sand	$(\pi/6)\ (0.1)^3$	1×10^3	31.42 cm^2 (4.87 in.^{2})
0.05 cm (500 μ)	Medium sand	$(\pi/6)\ (0.05)^3$	8×10^3	62.83 cm^2 (9.74 in.^{2})
0.01 cm (100 μ)	Very fine sand	$(\pi/6)\ (0.01)^3$	1×10^6	314.16 cm^2 (48.67 in.^{2})
0.005 cm (50 μ)	Coarse silt	$(\pi/6)\ (0.005)^3$	8×10^6	628.32 cm^2 (97.34 in.^{2})
0.002 cm (20 μ)	Silt	$(\pi/6)\ (0.002)^3$	125×10^6	1,570.8 cm^2 (1.69 ft^2)
0.0005 cm (5 μ)	Fine silt	$(\pi/6)\ (0.0005)^3$	8×10^9	6,283.2 cm^2 (6.76 ft^2)
0.0002 cm (2 μ)	Clay	$(\pi/6)\ (0.0002)^3$	125×10^9	15,708 cm^2 (16.9 ft^2)
0.0001 cm (1 μ)	Clay	$(\pi/6)\ (0.0001)^3$	1×10^{12}	31,416 cm^2 (33.8 ft^2)

TABLE II-1 (Continued)

Diameter of sphere	Textural name	Volume per particle $(\pi/6)\ D^3$	Number of particles in $\frac{\pi}{6}$ cc	Total surface πD^2 x number of particles	
0.00005 cm (500 mμ)	Clay	$(\pi/6)\ (0.00005)^3$	8×10^{12}	62,832	cm^2 (67.6 ft^2)
0.00002 cm (200 mμ)	Colloidal Clay	$(\pi/6)\ (0.00002)^3$	125×10^{12}	157,080	cm^2 (169 ft^2)
0.00001 cm (100 mμ)	Colloidal Clay	$(\pi/6)\ (0.00001)^3$	1×10^{15}	314,160	cm^2 (338 ft^2)
0.000005 cm (50 mμ)	Colloidal Clay	$(\pi/6)\ (0.000005)^3$	8×10^{15}	628,320	cm^2 (676 ft^2)

In the above examples the shape of the particles was
assumed to be spherical. In reality, as will be described
in the next section, clay particles have a platelike
structure. Spheres have the smallest surface area per
unit volume of all geometrical shapes. Platelike structures
or disks have the largest. This is demonstrated in
Table II-2 in which a 2 μ spherical particle was used as
the reference surface. It is seen that the surface area
increases dramatically with particle shape. This indicates
that if the shape of the particles had been taken into
account in Table II-1, there would be an even more dramatic
increase in specific surface as the particle size decreased.
This results from the fact that clay particles tend to be
plate-shaped particles with a thickness that is smaller than
the lateral demension.

Chemical and mineralogical makeup of clay - It was
mentioned above that clay is the surface active fraction
of soil, and it was demonstrated that clay has the largest
specific surface area of all the textural separates. As
a result, clay has a high degree of physical and chemical
activity and is the primary factor in determining the
physical properties of the soil. Sand and silt separates
contain many primary minerals that have considerable im-
portance from the standpoint of soil development; however,
influence on the physical properties of a soil is small.

TABLE II-2

Surface Area in Relation to Shape of Particle

(after Baver, Gardner, and Gardner [1])

Shape	Radius (cm)	Volume (cm^3)	Surface (cm^2)	Increase in surface (percent)
Sphere	1×10^{-4}	4.2×10^{-12}	1.26×10^{-7}	
Disk				
h = 1×10^{-4} cm	1.155×10^{-4}	4.2×10^{-12}	1.56×10^{-7}	23.8
h = 5×10^{-5} cm	1.67×10^{-4}	4.2×10^{-12}	1.84×10^{-7}	45.8
h = 2×10^{-5} cm	2.58×10^{-4}	4.2×10^{-12}	4.51×10^{-7}	257.8
h = 1×10^{-5} cm	3.65×10^{-4}	4.2×10^{-12}	8.59×10^{-7}	538.9

The clay mineral structure that causes clay to be highly surface active is discussed in the following paragraphs.

X-ray and petrographic techniques came into use in mineralogical studies of clays in the late 1920's and throughout the 1930's [1]. Through the use of these techniques it was demonstrated that clays are primarily crystalline minerals with the major constituent being silicon, aluminum, ferrous and ferric iron, magnesium, and oxygen atoms, plus hydroxyl groups. There are two basic structural units that are responsible for the various clay structures. One is a silicon tetrahedron (Figure II-4) in which a silicon atom holds oxygen atoms in such a way that they form corners of a tetrahedron. The other structural unit is the aluminum octahedron. In this unit six hydroxyl groups (OH) or oxygen atoms are arranged such that each forms a corner of an octahedron with an aluminum atom in the center holding them together. The details of how these basic structural units interact to form a clay mineral is provided in Baver, Gardner, and Gardner [1]. The general mechanism of the structural combination of these two basic structural units is important to understanding the interaction of clay with water.

In an idealized structure the silicon tetrahedrans link together forming a sheet known as the silica or tetrahedra sheet. In a similar fashion the aluminum octrahedrons link together forming an alumina or octahedral

Basic Silicon Tetrahedron
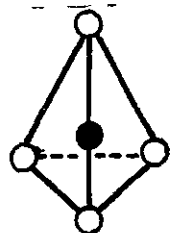
Represented by

⟸ ⟹
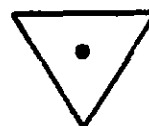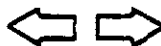
○ - Oxygen

● - Silicon

Basic Aluminum Octahedron
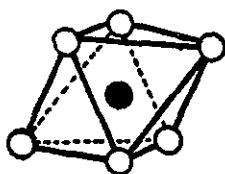
Represented by

⟸ ⟹
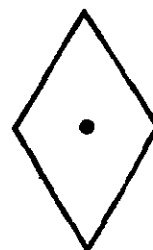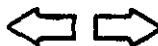
○ - Oxygen or OH

● - Aluminum, magnesium or iron

Figure II-4. The basic tetrahedron and octahedron struc-
tures and their graphical representations.

sheet. The base of the silica sheet is formed by oxygen atoms and the top and bottom of the alumina sheet are hydroxyl surfaces. These two sheets link together to form a clay mineral that has a platelike structure.

There are two clay mineral structures that can be formed by combining the silica and alumina sheets. A 1:1 lattice structure is formed by an alumina sheet and a silica sheet. A 2:1 lattice structure is formed by a alumina sheet sandwiched between two silica sheets. Schematic representations of these mineral structures are given in Figure II-5, as well as a representation of the linking of the structural units to form a clay.

As noted in Figure II-5, the idealized clay structures are electrostatically neutral and have clear-cut surfaces. This does not generally occur in nature. There can be substitutions in the crystal lattice (isomorphous substitutions) that cause the clay crystal to become negatively charged as well as causing the crystal structure to become expanded out of shape. For example, a trivalent aluminum atom can substitute for the tetravelent silicon atom in the silicon tetrahedron sheet. Similarly, the divalent magnesium and ferrous iron atoms and trivalent ferric iron can substitute for the aluminum atom in the alumina octahedron sheet. Both of these isomorphous substitutions increase the negative charge of the structure.

1:1 Mineral

Basic Mineral Structure

Basic Unit

<u>Charge</u>

-6 O		-12
-4 Si	+16	
-4O+20H		-14
-4 AL	+12	
-6 OH		- 6
	+28	-28
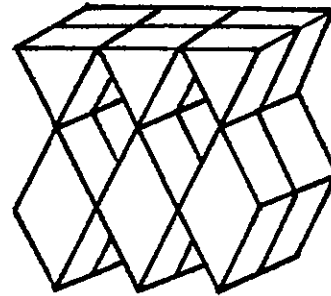
2:1 Mineral

Basic Mineral Structure

Basic Unit

<u>Charge</u>

-6 O		-12
-4 Si	+16	
-4O+20H		-10
-4 AL	+12	
-4O+20H		-10
-4 Si	+16	
-6 O		-12
	+44	-44
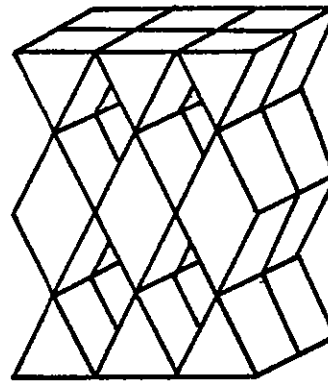
Figure II-5. Diagramatic sketches of clay mineral
structures showing the sheeting effect.

This negative charge is generally balanced by an extra cation absorbed to the surface of the clay mineral. Cations that balance negative charges originating from substitutions within the crystal structure are called exchangeable cations. They can be displaced from the planar surfaces of the clay minerals by other cations or water molecules.

Isomorphous substitution of atoms with larger radii than the original atom causes strains in the crystal lattice and results in a nonidealized clay mineral structure. In addition, other physical departures from the ideal structure occur as a result of silica tetrahedra being inverted instead of having the apex pointed at the octahedra sheet. These nonidealized situations cause the planar surfaces of the clay mineral to be rough instead of smooth. Moreover, the edges of the crystal may be beveled and frayed resulting in broken bonds on these edges. These broken bonds also create negative charges that can be balanced by exchangeable cations. The total number of exchangeable cations is referred to as "cation exchange capacity".

The degree to which each of the above mechanisms (isomorphous substitutions and edge effects) contribute to the cation exchange capacity of a clay mineral depends on the type of clay structure under consideration. There are basically three major groups of clay minerals:

1) Kaoline (1:1 lattice)

2) Hydrous mica; major subgroup is illite (2:1 lattice)

3) Montmorillonite (2:1 expanding lattice).

There is little isomorphous substitution in the Kaolin group. The silica and alumina are held together through hydrogen bonding and are held together so tightly that cations or water molecules cannot permeate the interlayer positions between the kaolinite clay mineral layers. As a result, its collodial properties are determined by the external clay surfaces only, and the surface area per unit weight is small. Since there is little isomorphous substitution, broken bonds on the edges of the clay mineral are primarily responsible for ionic reactions. This, coupled with the small surface area per unit weight, causes the cation exchange capacity to be very low, on the order of 10 milli-equivalents (me) per 100 grams of clay.

Illite, which is a major subgroup of the hydrous mica group, does have isomorphous substitution with the major substitutions occurring in the silica sheets. Non-exchangeable potassium ions balance these charges and hold the structural unit layers very tightly (Figure II-6). Since the unit layers are held tightly together the cation exchange capacity resides on the external surfaces or on the frayed edges of the crystal. The cation exchange capacity is on the order of 20 to 40 me per 100 grams of clay. For the most part, the nonexchangeable potassium ions

The distance A
increases with in-
creasing numbers of
exchangeable cations
in the interlayer
position .

A

Interlayer
Position
(potassium bond
for illite)
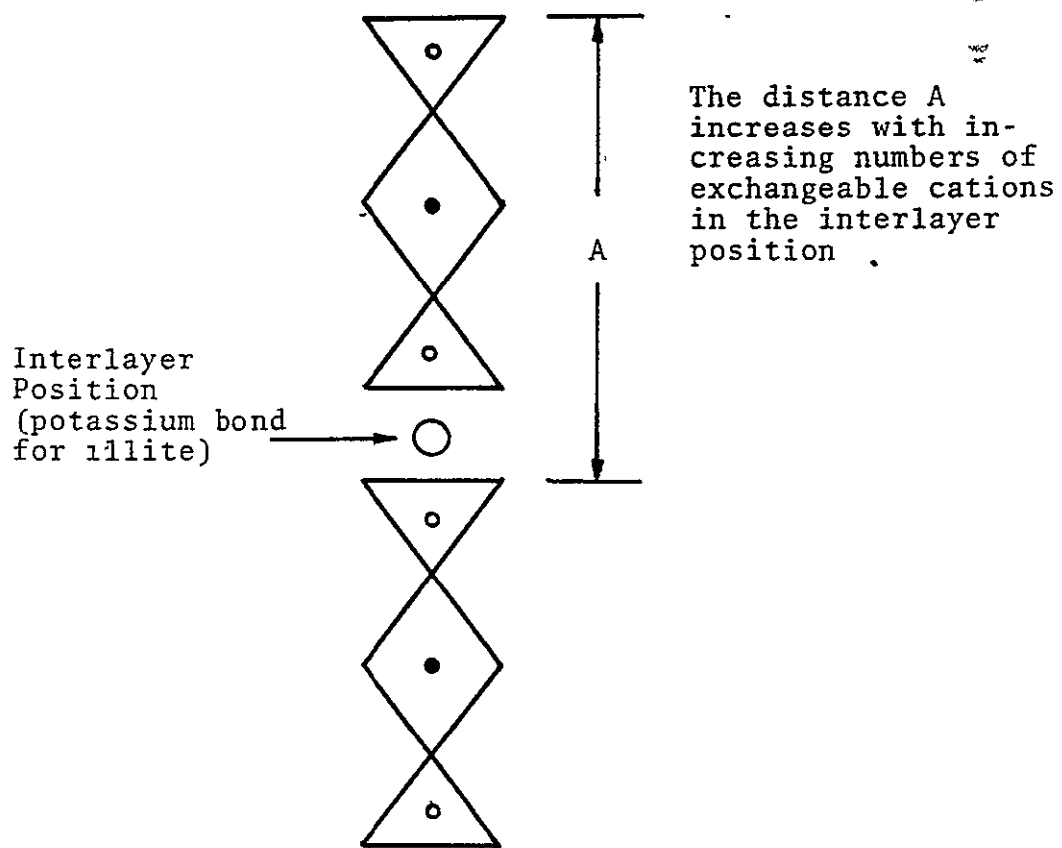
Figure II-6. Graphical representation of the layering
of basic mineral sheets that forms
interlayer positions for cations.

balances the charge imbalance resulting from the isomorphous
substitution and as a result the cation exchange capacity
does not reflect the degree of isomorophous substitution.

The montmorillinite group has a 2:1 unit layer structure
with isomorphous substitution occurring in both the silica
and alumina sheets. The crystal lattice structure can
expand and contract depending on the amount of exchangeable
cations present between the structural unit layers. Figure
II-6 diagrams the expanding lattice structure. Montmo-
rillonite has the highest cation exchange capacity of the
three major clay groups. It varies between 80 and 150 me
per 100 grams of clay.

The basic crystal lattice makeup of three groups
of clays has been discussed as part of the background
information for describing the interaction of water with
soil. The discussion dealt solely with idealized clay
minerals. It should be kept in mind that clay minerals
do occur in which the unit layers are not uniformly stacked.
These interstratified or mixed-layer clays can have dif-
ferent surface properties which affect the ionic exchange
capacity of the clay mineral. However, the major points of
the discussion were that clay is the dominating textural
separate in determining soil-water interaction phenomena,
and that the type of clay mineral structure is also of
importance in soil-water interaction.

Soil Water

From a structural standpoint there are four kinds of
soil water: pore water, solvate water, adsorbed water,
and structural water [2]. Pore water exhibits the same
physical and chemical characteristics as bulk water and
is capable of moving within the soil under hydrodynamic
forces unless restricted by capillary action or entrapped
by air bubbles. Solvate water is subject to polar, electro-
static, and ionic binding forces and forms a hydration
shell around the soil grains, persumably not more than 200
molecules thick. Solvate water has a greater density and
viscosity than bulk water, however, it can still move
under hydrodynamic forces. Adsorbed water is a very thin
layer of water of from 1 to 10 molecules (depending on
the clay mineral) in thickness attracted to the external sur-
face of clay minerals or held as interlayer water by minerals
with expanding lattice structure. Adsorbed water cannot
be moved by normal hydrodynamic forces. Structural water
is actually hydroxyl groups that constitute part of the
crystal lattice. Since this water is part of the soil
structure, it is in reality not water and is not driven
off unless the crystal lattice is destroyed.

Adsorbed and solvate water result from the fact that
the crystal surfaces of clays are polar. As a result, they
can attract polar molecules and ions from the environment

around them. Since water molecules are dipolar, they are
attracted to the clay particles and to cations that are
held by the clay lattice. A portion of the water molecules
can enter between the layers of a crystal (interlayer
water) such as montmorillonite, the most predominant type
of clay. It is this interlayer water that causes clay
to swell when wetted. The water molecules immediately
around the polar surfaces are arranged in a highly oriented
pattern and the electrostatic attractive forces are ex-
tremely great. Proceeding outward from the surface,
successive layers of water molecules are linked together
due to their polar nature to form a chainlike configuration,
but their degree of orientation diminishes farther away
from the crystal surface. The degree of orientation
diminishes with distance from the crystal surface since
the electrostatic attractive forces diminish with distance.

This entire complex is termed the adsorption complex,
however, only the layer of water a few molecules thick that
is tightly bound to the clay lattice is termed adsorbed
water. The more loosely bound water molecules are termed
solvate water. The type of cations adsorbed on a clay
mineral greatly influences the thickness of the adsorbed
and solvate layer of water the clay is capable of holding.

All solvate water can be driven off of a soil when
it is heated in an oven at moderate temperature. However,
adsorbed water cannot be completely driven off at moderate

oven temperatures since it is very tightly bound to the
clay crystal lattice. Soil samples are normally dried to
a constant weight at an oven temperature in the range of
105°C to 110°C [5]. However, this is an arbitrarily chosen
temperature range [6]. Figure II-7 demonstrates the effect
of oven temperature on the moisture of three types of
clay minerals. Zero percent moisture in Figure II-7
corresponds to complete dehydration at which point all of
the adsorbed water has been removed. Since there are no
distinguishing features of these hydration curves at 105°C,
it is obvious that 105°C is arbitrary and that the amount
of adsorbed water left in the soil is a function of clay
type.

Soil-Water-Plant Interrelationships

The interaction of water with soil was described
earlier in terms of the interaction of water with the clay
particles. In this section techniques of describing the
amount of water held in soil will be discussed; the energy
state of the water held in the soil will be described in
terms of potentials; and finally, the ability of crops to
utilize the water in the soil is described in terms of
these potential gradients. This discussion is designed
to provide insight as to the parameters that are of im-
portance in remotely measuring soil moisture for agricultural
purposes.
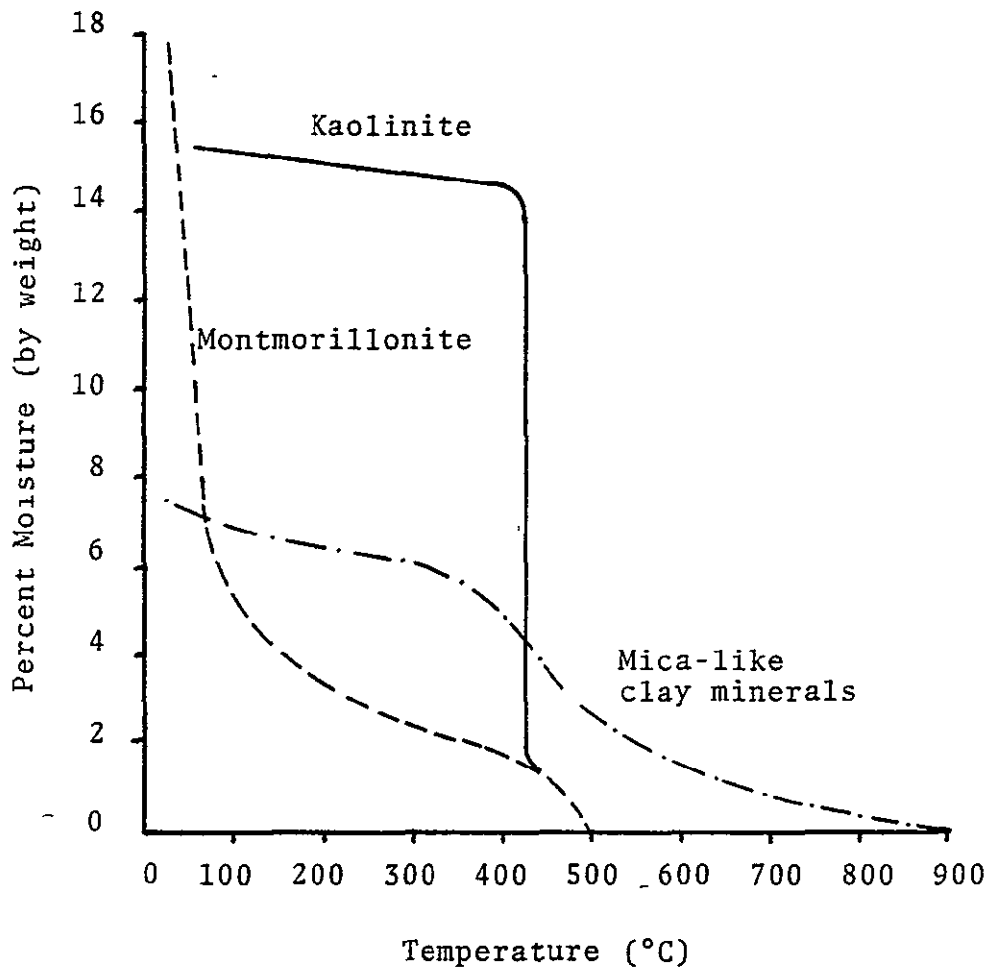
Figure II-7. Typical dehydration curves of different
clay minerals (after Kezdi [2]).

Soil Water Descriptions

There are two methods of describing the amount of water in a soil. One is to measure the water content on a per unit mass basis (gravimetric water content) and the other is to measure it on a per unit volume basis (volumetric water content). The importance of the basis used to measure soil moisture will become apparent in the section on soil permittivity.

Any specified volume of soil can be subdivided into three subvolumes as shown in Figure II-8.

$$V_T = V_a + V_w + V_s \tag{II-1}$$

where

V_T = total volume of soil

V_a = volume of air

V_w = volume of water

V_s = volume of mineral and organic matter.

Obviously, the same equation holds true for the masses of each of the subgroups. The gravimetric water content, Θ_m, is defined by:

$$\Theta_m = \frac{M_w}{M_s} \tag{II-2}$$

where

M_w = mass of water in the total volume

M_s = mass of mineral matter in the total volume

Generally, the soil moisture on a per unit mass basis is

Depth   Volume   Mass

Air

V_a M_a

D

d   Water

V_w M_w

Mineral
and
Organic
V_s Matter M_s
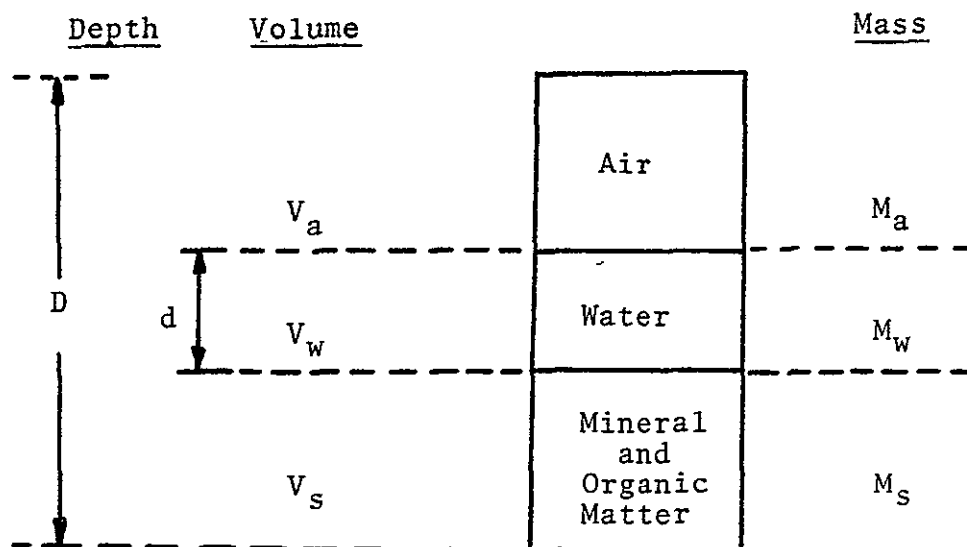
$$V_{Total} = V_a + V_w + V_s$$

Figure II-8.   Components of the soil-water complex.

converted to percentage by multiplying Θ_m by 100. The mass of water in a soil sample is generally determined by drying the soil sample in an oven. In order for soil moisture measurements to be consistent between soil samples, all of the soil samples should be dried at the same oven temperatures. In conventional ovens 105°C is generally used to dry soil. At this temperature, the absorbed water is not driven off.

When using microwave ovens to dry soil samples, consistency of drying is generally dependent on the experience of the operator. The load voltage standing wave ratio and the temperature of the sample have been shown to be good indicators of exposure time to obtain properly dried samples [7]. In most situations these parameters are not easily measurable. Care must be exercised when using microwave ovens since errors as high as 20% moisture by mass can occur as a result of inconsistency in drying different clay types [8]. However, the ability to utilize microwave ovens for drying soil samples adequately has been demonstrated by Miller et al. [9].

Water content by volume Θ_v, is defined by

$$\Theta_v = \frac{V_w}{V_T} \qquad (\text{II-3})$$

Θ_m and Θ_v can therefore be related by the bulk density, ρ_B,

of the soil which is defined as the mass of the soil divided by the total volume.

$$\rho_B = \frac{M_s}{V_a + V_w + V_s} = \frac{M_s}{V_T} \qquad (II-4)$$

Since

$$\theta_m = \frac{M_w}{M_s} = \frac{\rho_w V_w}{\rho_B V_T} \qquad (II-5)$$

then

$$\theta_m = \frac{\rho_w}{\rho_B} \theta_v \qquad (II-6)$$

The bulk density of water is unity by definition. As a result, the water content by volume is simply the water content by weight multiplied by the bulk density

$$\theta_v = \rho_B \theta_m \qquad (II-7)$$

The soil moisture by volume is not only a useful parameter from the standpoint of permittivity of soil, but it can also be used to calculate the equivalent depth of water in some specified soil column from which the sample was acquired. The equivalent depth of the water specified by "d" in Figure II-8 could be a useful parameter in the determination of irrigation needs. The equivalent depth is calculated by multiplying the volumetric soil moisture

by D, the depth of the volume from which the soil sample
was acquired, i.e.

$$d = D \rho_B \theta_m \qquad \text{(II-8)}$$

The Energy State of Soil-Water

Most processes involving water in soil and plant
systems can be described in terms of the potential energy
of the water in the soil. Potential energy is measured
by the force required to move a body directly against a
force field. It is the product of the force times the
distance. The potential energy associated with an increment
of water can be assessed by the forces acting upon it.
Potential energy differences from point to point in
isothermal systems determine the direction of flow of
water through a soil.

There are several forces that act upon water in soil;
for example, the pull of the earth's gravitational field,
the attractive forces of the soil surfaces, and weight of
unsupported soil acting upon water below that soil. Also,
ions that are dissolved in the water attract water molecules
and resist their being pulled away.

Each of these forces, plus others not mentioned, give
rise to a potential energy. However, some of these sep-
arate potentials are combined into a single potential for

convenience. The total water potential is the sum of matric, gravity, pressure, osmotic, and overburden potentials. When water is at rest in the soil its total potential must be zero.

Matric potential is a measure of the attraction of solid soil surfaces for water as well as the attraction of water molecules for each other. It is this potential that gives rise to the unbalanced forces across air-water interfaces that cause the phenomenon of surface tension. The matric potential is historically referred to as capillary potential since it is analogous over a significant part of its range to the situation that exists where water rises in small capillary tubes. However, in a disperse system such as soil, it extends beyond simple capillary phenomena. As the water content of the soil decreases, a point is reached where the water content of the pore spaces between soil particles (which is affected by capillary action) becomes negligible compared to the water held directly on the particle surfaces. Matric potential is defined with respect to some reference water table. Matric potential of water above the reference water table is negative while the matric potential increases to zero at the reference water table and remains zero below the reference water table.

Gravity potential is that potential that arises due to the pull of gravity. Work must be done on water to

raise it to a point above the reference water table where
the gravity potential is positive. Below the reference
water table, work is done by the water and the gravity
potential is negative. For water at equilibrium below
the reference water table, the gravity and matric potentials
are equal and opposite in sign.

Osmotic potential results from the hydration of ions
in the soil solution. The polar nature of water causes
water molecules to be attracted to ions in the soil solu-
tion. These attractive forces tend to orient water around
ions and the osmotic potential refers to the work required
to pull water away from these ions. Clay particles sus-
pended in a solution will cause the same phenomenon because
of the attraction of clay for water. However, since the
clay particle is a solid and is not an ion, this is
considered to be a matric effect.

Osmotic potentials are important in dealing with
plants. Assuming a plant root can be modeled as a semi-
permeable membrane across which water molecules can pass,
but salt ions cannot, then osmotic potential can develop
across this membrane if there are dissolved ions in the soil
water. (Actually, plant membranes selectively pass ions.)
The attraction of ions in the soil water to water molecules
in the plant root require the plant to develop a larger
root potential in order to acquire water from the soil.

Pressure potential is due either to the weight of water at a point under consideration or to gas pressure that is different from that which exists at the reference position. Changes in atmospheric pressure can produce a pressure potential, however, the pressure potential produced in this fashion is generally negligible in comparison to the pressure potential resulting from water weight. The pressure potential at a point beneath the water table is equal and opposite to the gravity potential that is measured from the free water surface. Overburden weight of unsupported soil produces a potential similar to pressure potential except that it is a result of the weight of the soil that is free to move. This potential is termed overburden potential.

Soil-Water-Plant Relations

All of the potentials briefly described in the paragraphs above are related to the flow of water through soil. However, the controlling potentials in soil-water-plant relations are the matric potential and the osmotic potential. These potentials describe the energy that is required by the plant to draw water from the soil. Gravity potential also affects the uptake of water by plants since work is required to move water from the root zone to the plant. However, this potential is small in comparison to the matric and osmotic potentials the plant must overcome.

It is quite significant that soil-water potential is a major factor in the ability of a plant to take water from the soil. Its importance lies in the fact that soil of different textures can hold different percentages of soil moisture by weight at the same matric potential. The significance of this to the remote sensing of soil water using microwave sensors will become apparent in the discussion of soil-water-permittivity relationships. It will be demonstrated that the microwave permittivity of soil is dependent not only upon soil moisture by volume (total number of water molecules), but also on the matric potential at which that water is held. This suggests that it may be possible to make a direct measurement of the water available to a plant.

The ability of different soil types to hold different amounts of water at the same matric potential is graphically demonstrated by Figure II-9. Figure II-9 is a plot of gravimetric water content (soil moisture by weight) as a function of matric potential (this assumes pure water so that the osmotic potential is zero). Notice that the matric potential is given in bars of pressure. This arises from the fact that the potential energy of soil water is generally expressed in terms of per unit quantity of water on a volume basis. The units are force-length divided by volume, which is the equivalent unit of pressure.
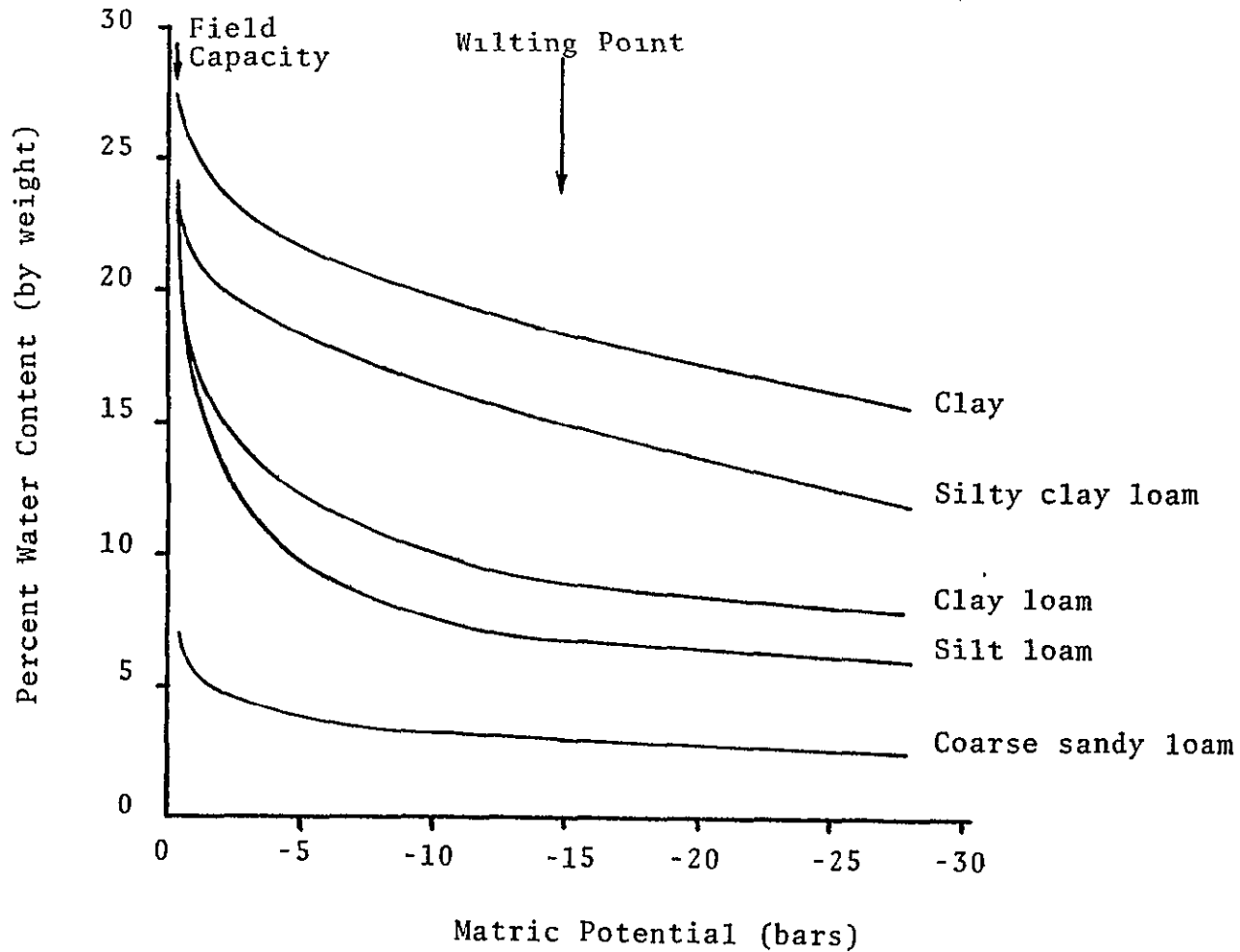
Figure II-9. Matric potential of soil fractions as a function of texture and water content (after Taylor and Ashcroff [10]).

A matric potential of zero bars corresponds to a saturated soil water condition. At this point all of the soil pores are filled with water. The matric potential at which water is held to the soil particles as the soil dries is a function of the specific surface of the soil and the cation exchange capacity. As a result, soils with larger clay contents hold more water than soils with lesser clay contents at the same matric potential. The very steep section of the curves of Figure II-9 correspond to water draining from the large soil pores where there is little effect due to matric potential. As the pores empty, a higher percentage of the remaining water is in contact with the soil surfaces where it is held by higher matric potential forces.

Soil water that is available to the plant can be defined in terms of the field capacity and wilting point of the soil. Field capacity has been defined as the water content of a soil profile, usually in the rooting zone, after the rate of drainage from an initially saturated profile has become negligibly small.

No single criterion exists for determining what is considered to be negligible drainage. As a result, the definition of field capacity is somewhat arbitrary. Generally, -1/3 bar of matric potential is arbitrarily taken to be field capacity [11]. However, soils of different

percentages of textural separates, compaction, stratifica-
tion, etc., have considerably different drainage character-
istics. This means that different fields or even different
locations within the same field could be at different
matric potentials but could have equivalent "negligible"
drainage. This effect could result in very large errors
of water retention estimates when field capacity is
arbitrarily associated with a particular matric potential
such as -1/3 bar. The wilting point of a plant is defined
as that water content below which the plant cannot recover
from the wilting symptoms. This has been shown to occur
at approximately -15 bars [12], however, it is somewhat
dependent on plant type and the speed at which the plant
was wilted.

The water that is available to a plant is roughly that
water content at the field capacity minus the water content
at the wilting point. Figure II-10 is a plot of the avail-
able water as a function of percentage clay content. This
data was obtained from Figure II-9. Figure II-10 demon-
strates that from an available water standpoint, loams are
the optimum soil for vegetation. It should be noted that
moisture is only one ingredient for good vegetation growth.
Soil temperature and soil aeration in the root zone are
also critical items that cannot be overlooked in agricultural
situations.
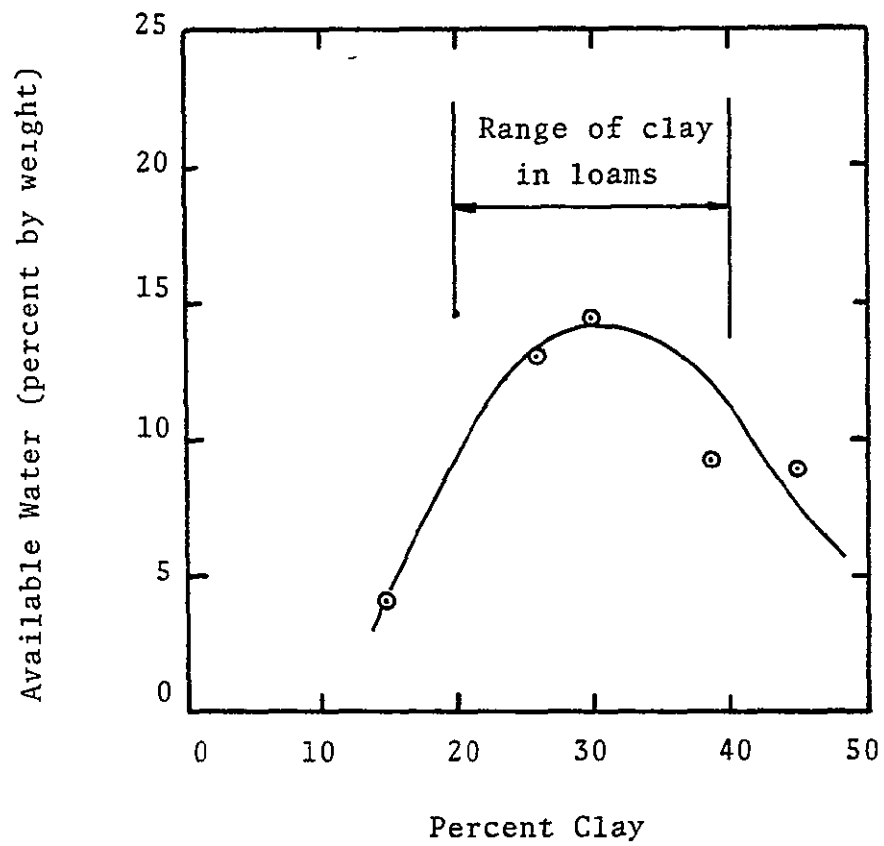
Figure II-10. The availability of water to plants as a function of percentage clay content.

Soil Permittivity

Quantitative measurements of soil permittivity are of vital importance to the interpretation and basic understanding of the interactions of electromagnetic energy with natural and agricultural terrain. Values of permittivity are a basic input to models describing emission and scattering phenomena at microwave frequencies. As a result, an understanding of the permittivity of soil must be developed before quantitative methods of interpreting microwave measurements can be realized. Microwave measurements are analyzed to determine the effect of changes in the permittivity of the soil. The relationship between soil moisture and soil permittivity provides the soil moisture information available from measurements of the microwave response of soil. Permittivity measurements made at L-band (1.4 GHz) at Texas A&M University [13] will be used to demonstrate the effect of permittivity on moisture content. Following this discussion is a summary of the effects of soil temperature, frequency, and adsorbed cations.

In the following discussion, permittivity is a complex quantity. In the open literature the real part of the permittivity is often referred to as dielectric constant while the imaginary part is related to conductivity. Relative permittivity is the ratio of the real and imaginary part of the permittivity to the dielectric constant of

free space. As a result, relative permittivity is a dimensionless quantity.

Soil Moisture Dependence

Measurement results - The measurements of soil permittivity at L-band reported by Newton and McClellan [13] were made as a function of soil texture at a constant environmental temperature of about 25°C. Figures II-11 through II-16 contain plots of these measurements as a function of gravimetric moisture content. Table II-3 identifies the soil samples that were used by texture and indicates their respective salt contents. The permittivity of these soils appears to be dependent on soil texture when plotted as a function of percent moisture by weight.

All of the soils described in Figures II-11 through II-16, except the sand sample, have a relatively high clay content (greater than 31%) and as a result have two pronounced regions in the real part, ε_r', of the relative permittivity plots. The permittivity of the sand sample has two pronounced regions also, but the region near 0% moisture is smaller than for the samples with higher clay content. Each of the soils measured have the same value of ε_r' at 0% moisture. In addition, the slope of ε_r' is the same for all of the soils, approximately 0.144 per percent moisture, from 0% moisture to a "transition" region where
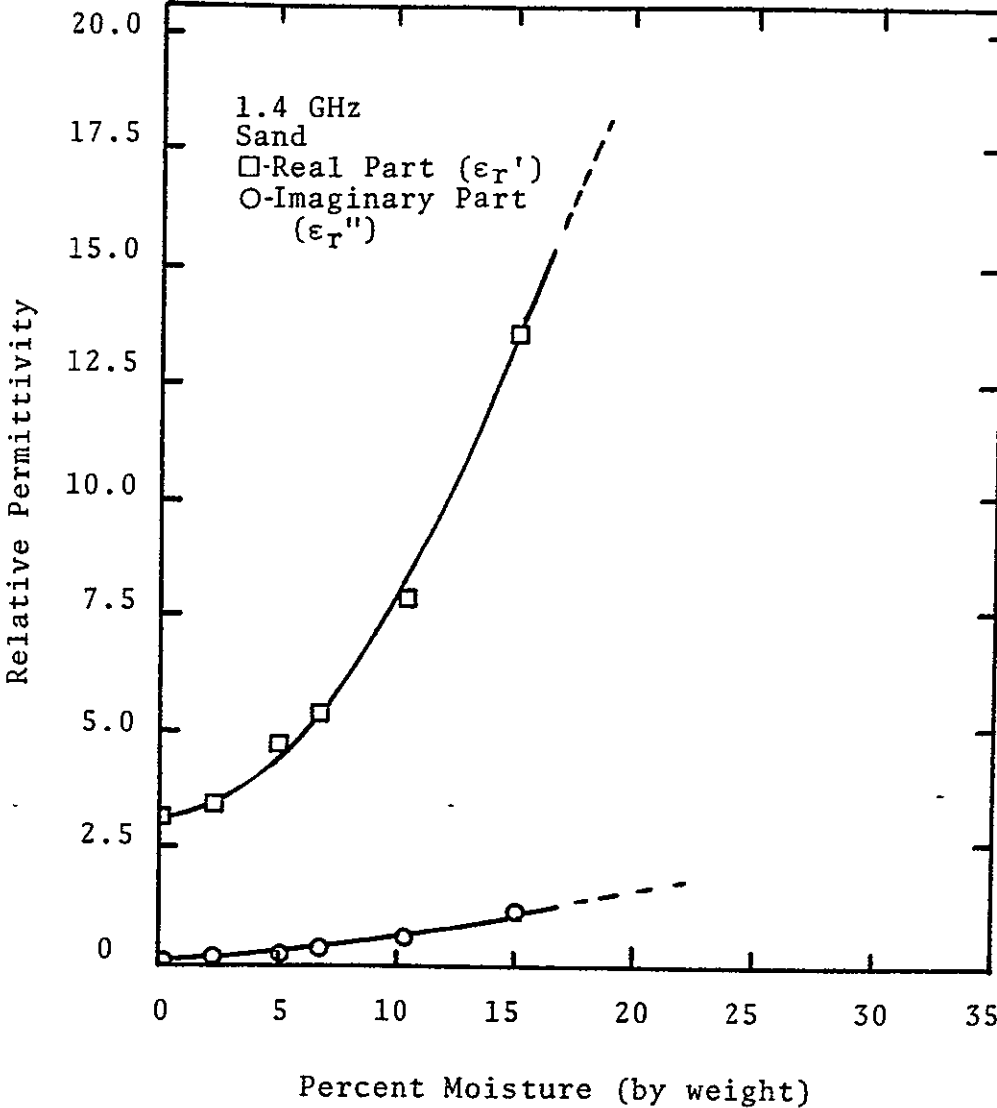
Figure II-11. Relative permittivity of sand as a
function of moisture by weight.
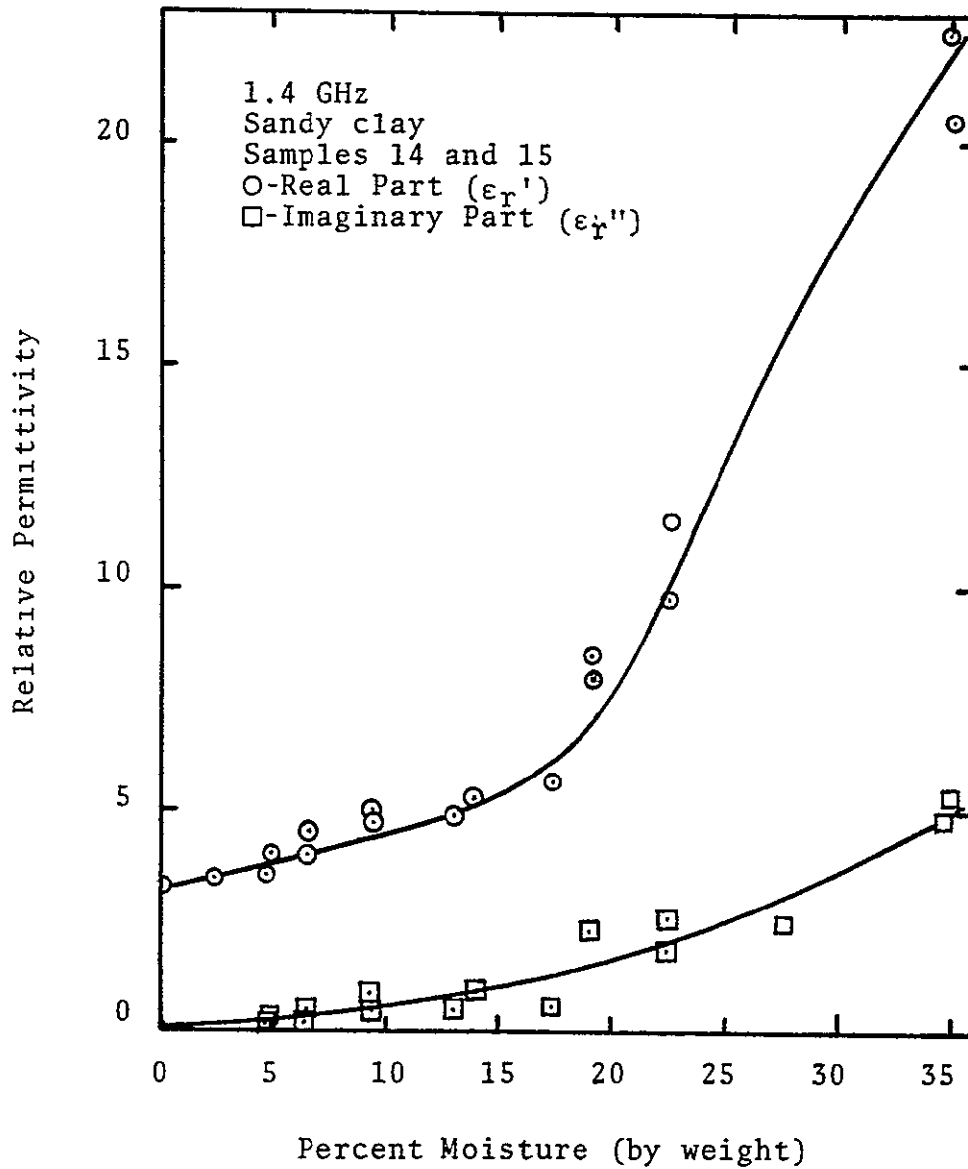
Figure II-12. Relative permittivity of sandy clay as a function of moisture by weight.
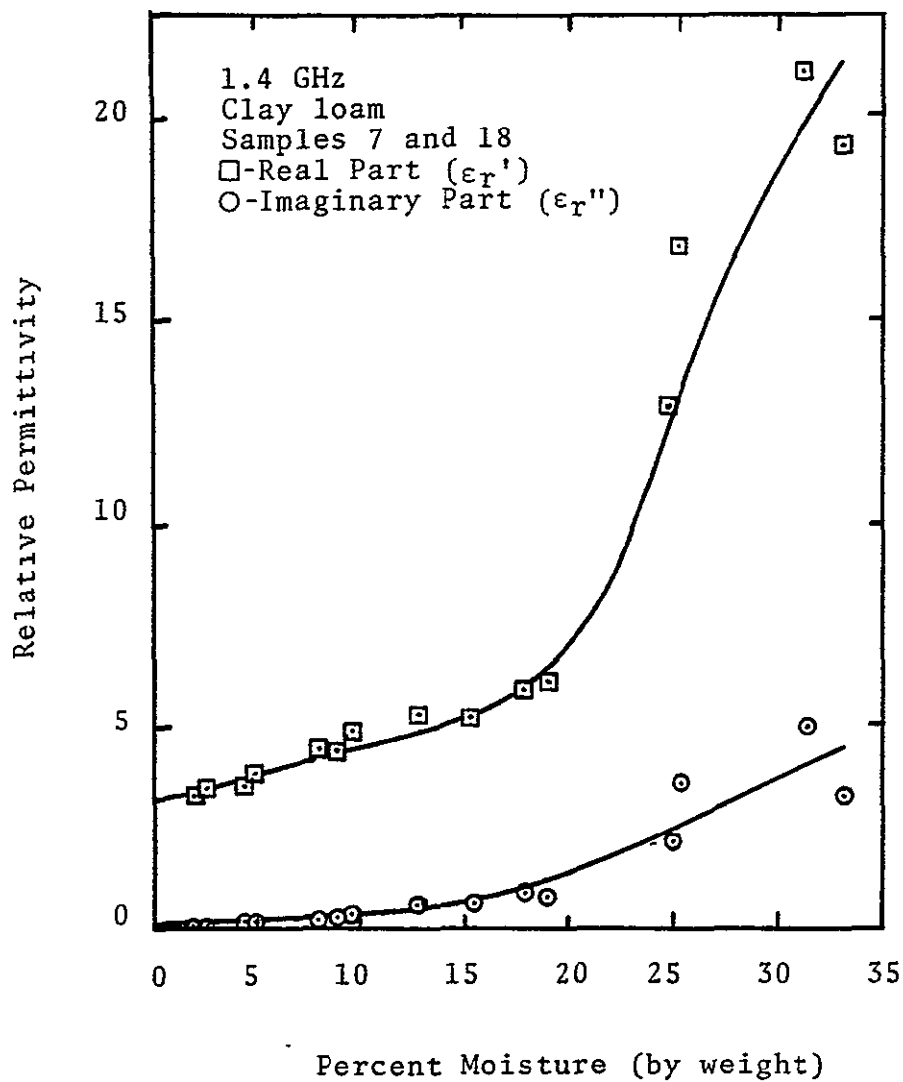
Figure II-13.   Relative permittivity of clay loam
samples 7 and 18 as a function of
moisture by weight.
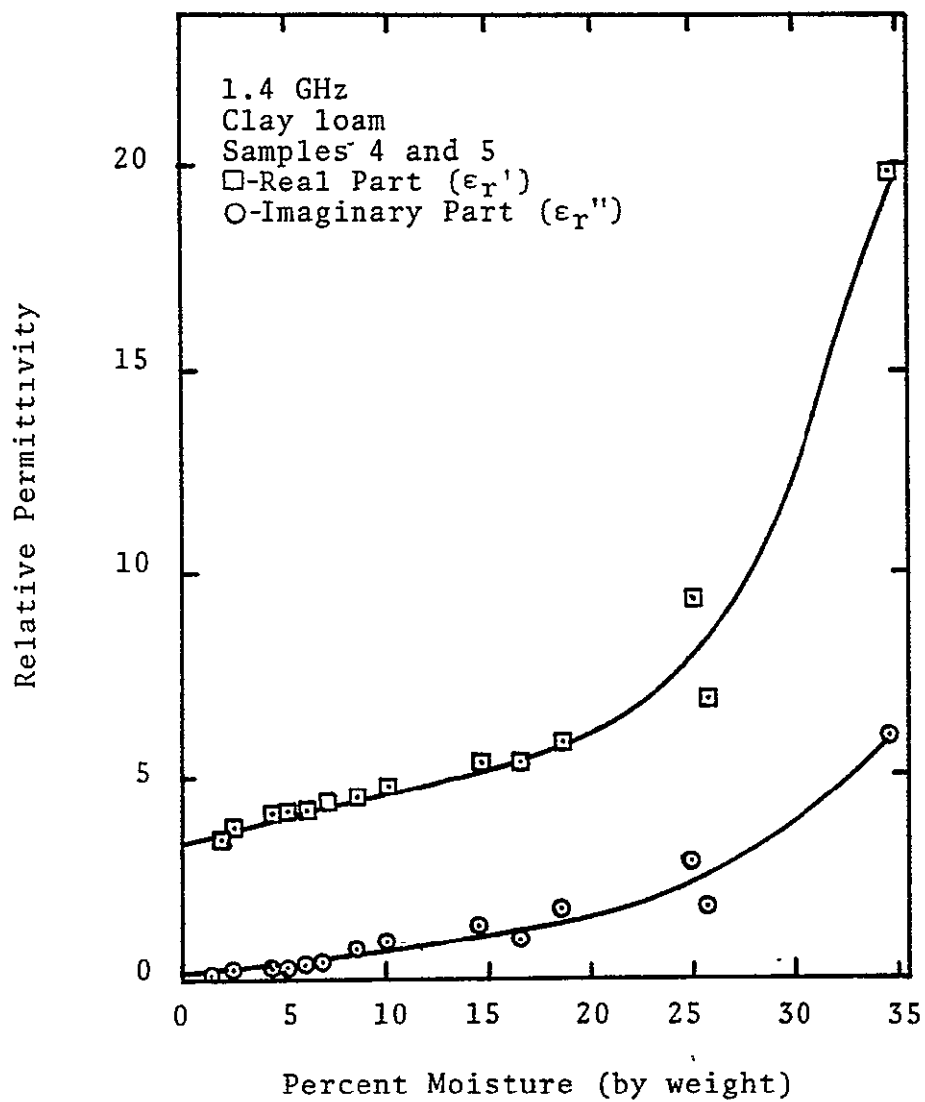
Figure II-14. Relative permittivity of clay loam
samples 4 and 5 as a function of
moisture by weight.
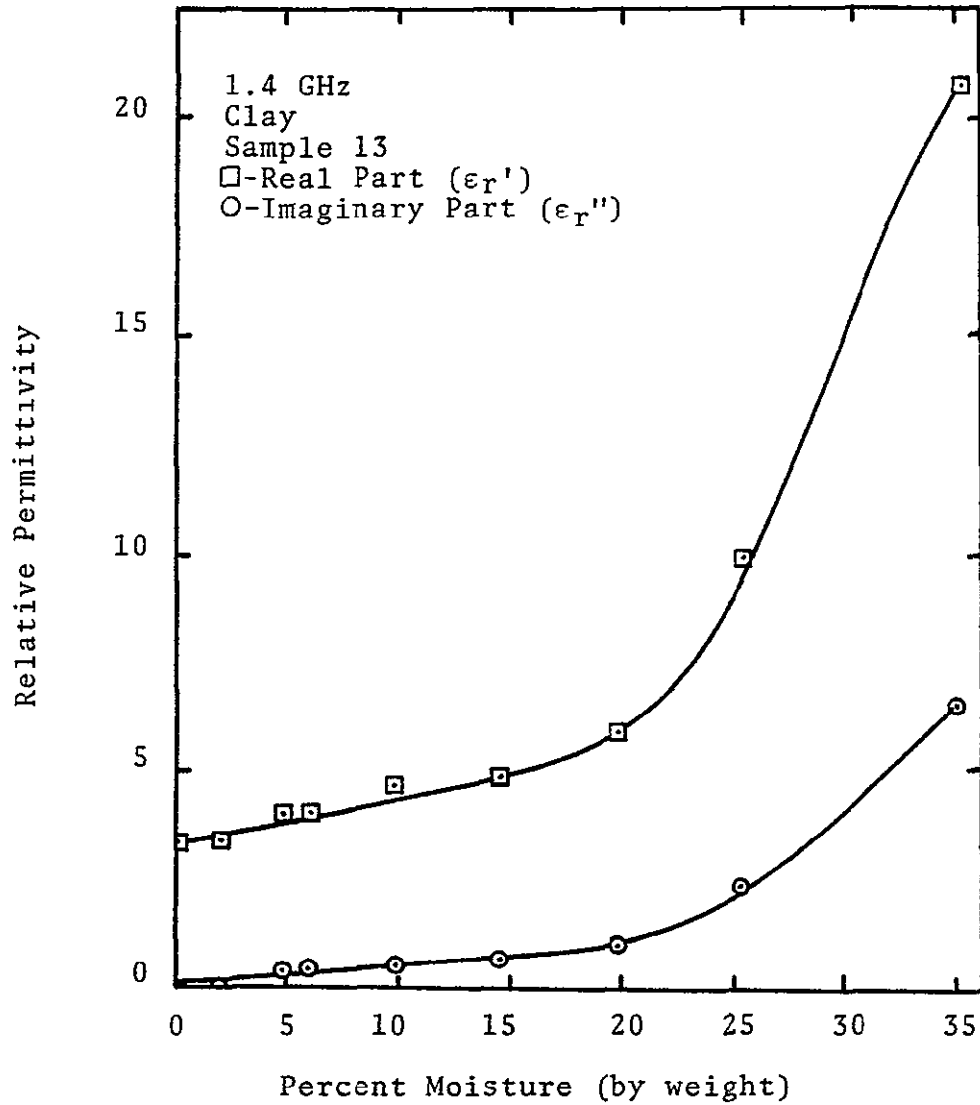
Figure II-15.   Relative permittivity of clay as
a function of moisture by weight.
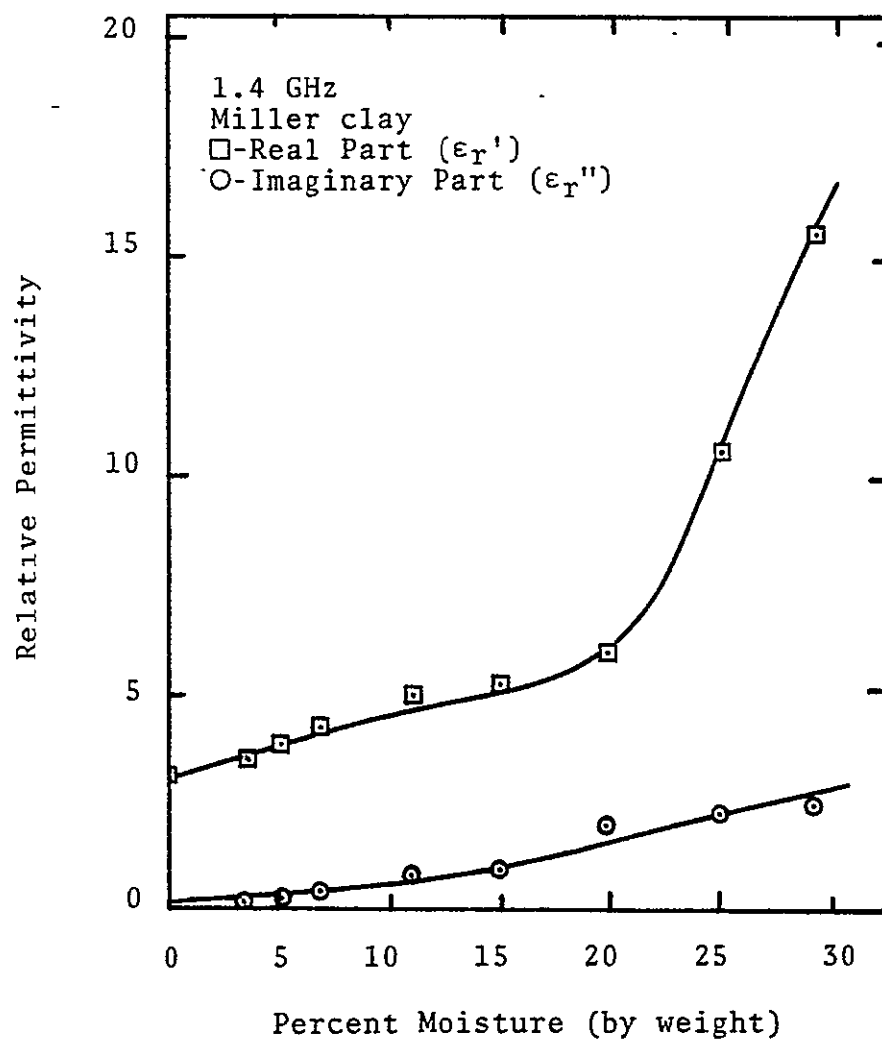
Figure II-16. Relative permittivity of miller clay
as a function of moisture by weight.

Table II-3

Results of Physical and Chemical Analysis of the Soil

Samples Used in the Permittivity Analysis

Sample	Clay	Silt	Sand	Texture*	Salt (ppm)	pH	Reaction Description
1	32.0	10.0	58.0	SCL	1523.2	6.6	Neutral
2	26.0	8.0	66.0	SCL	512.0	6.9	Neutral
3	27.2	18.8	54.0	SCL	550.4	7.0	Neutral
4	35.2	28.0	36.8	CL	371.2	7.2	Neutral
5	33.2	24.0	42.8	CL	166.4	7.4	Mildly Alkaline
6	33.2	16.0	50.8	SCL	204.8	7.5	Mildly Alkaline
7	39.0	22.0	39.0	CL	268.8	7.5	Mildly Alkaline
8	26.0	4.0	70.0	SCL	243.2	7.0	Neutral
9	32.0	14.0	54.0	SCL	268.8	7.3	Neutral
10	25.2	10.0	64.8	SCL	332.8	7.3	Neutral
11	26.0	12.0	62.0	SCL	449.2	6.7	Neutral
12	26.0	4.0	70.0	SCL	170.2	7.1	Neutral
13	43.6	12.0	44.4	C	320.0	7.3	Neutral
14	37.6	8.0	54.4	SC	170.2	7.5	Mildly Alkaline
15	41.6	10.0	49.4	SC	640.0	7.4	Mildly Alkaline
16	27.6	8.0	64.4	SCL	358.4	7.5	Mildly Alkaline
17	25.6	8.0	66.4	SCL	268.8	7.8	Mildly Alkaline
18	31.0	36.0	33.0	CL	256.0	7.6	Mildly Alkaline
Miller Clay	62	35	3	C			
Sand	7	7	86	S			

*S-sandy; C-clay; L-loam; based on the USDA textural classification

the slope quickly changes to approximately 1.02 per percent moisture.

The transition region is simply that moisture region within which the permittivity curve has a sharp slope change. The transition moisture is a function of soil texture. Notice that for sand, (Figure II-11) the transition moisture is low, approximately 3%. For heavy clay (Figures II-15 and II-16) it occurs at approximately 20%, while the soils with slightly less clay have a transition moisture that is generally a little less than 20%. The imaginary part of the permittivity, ε_r'', also changes slope at the transition moisture. This is clearly evident on all plots except Figures II-11 and II-16 which are sand and Miller clay, respectively.

Permittivity of soil has been reported by a number of authors in an effort to explain its dependence on moisture, temperature, and texture. Cihlar and Ulaby [14] provide a comprehensive review of these measurements. Experimental evidence indicates that "dry" soils exhibit practically the same dielectric properties (at a particular frequency) independent of their texture and that it is the water that is added to the soil (as distinguished from structural water) that produces the polarizing characteristics of soils. Wiebe [15] and Lundien [16] have explained the slow increase in the real part of the permittivity for moistures less than the transition moisture to be due to water in the

adsorption complex. Adsorbed water is tightly bound to
the clay particles and therefore cannot change positions
under the influence of an electric field unless it moves
in conjunction with the soil particle to which it is at-
tached. The theory is advanced that the adsorbed water does
not contribute to the dielectric properties of the soil
independent of the soil particles. This theory fits the
data in Figures II-11 through II-16, since ε_r' is constant
for all of the soils at 0% moisture (where there is no
solvate water). In addition, it is further theorized that
it is the solvate water that produces the dielectric res-
ponse of soil for moistures below the transition moisture,
and the combination of solvate and pore water that produces
the dielectric response above the transition moisture.

This theory seems plausible since all of the solvate
water has been driven off when a soil is oven dried. As
water is added to the soil, the water becomes loosely
attracted by the clay particles in the form of solvate
water until the capacity of the particular soil type has
been reached, at which time any additional water becomes
pore water. This is further supported by the fact that
solvate water is somewhat mobile, but is attracted by
electrostatic forces that can cause the relaxation pro-
perties of the solvate water molecules to be different
from that of bulk water. In addition, pore water can be

considered to be bulk water since it is essentially un-
modified by electrostatic forces.

The above theory indicates that the permittivity of
soil is only dependent on the soil texture by the fact
that the soil texture determines the amount of water that
can be held as solvate water. The transition moisture
should then correlate with field capacity since the amount
of solvate water a soil can hold and the field capacity of
a soil are both dependent on soil texture. Figure II-17
is a plot of field capacity as a function of transition
moisture. Field capacity was calculated based on a re-
gression equation generated for the soils of the Phoenix,
Arizona area by T. Schmugge of the NASA Goddard Space
Flight Center. The correlation between field capacity and
transition moisture is obvious. Wilting point defined
for a particular crop type can also be correlated in this
manner.

Since it is the number of dipole moments (water mole-
cules) that produce the dielectric properties of soil,
then the permittivity of soil should be examined as a
function of volumetric soil moisture (grams H_2O/cm^3). The
percent moisture by weight does not indicate the number
of water molecules present. The same percentages of
moisture by weight do not necessarily correspond to equal
amounts of water for different soil types since the bulk

Field capacity = 25.1 - 2.207 (% sand) + 0.221 (% clay)

△-Miller clay   □-Clay loam (7, 18)
○-Clay (13)   ▲-Clay loam (4, 5)
●-Sandy clay (14, 15) ⊙-Sand
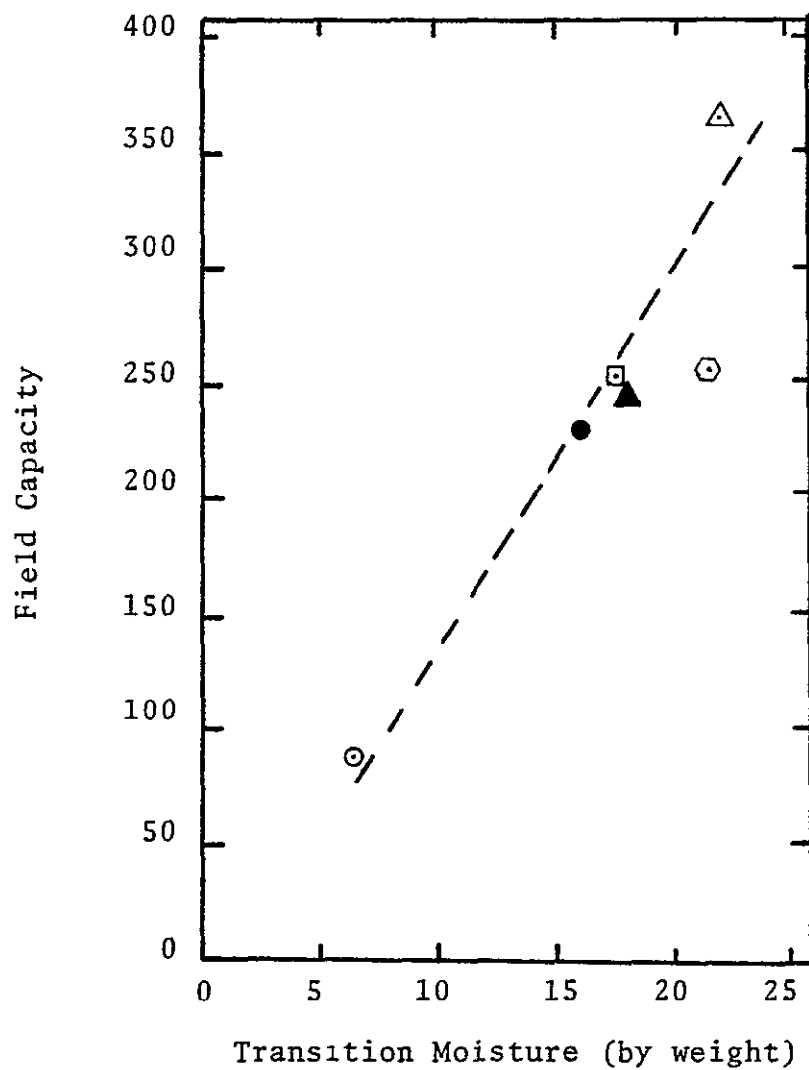
Figure II-17. Field capacity as a function of
transition moisture.

density of each could be different. This indicates that
the permittivities in Figures II-11 through II-16 should
be plotted as a function of volumetric water content thereby
removing the effects of bulk density. The moistures
corresponding to each permittivity measurements were
converted to a volumetric basis using the bulk density of
the soil corresponding to each individual measurement.
Figures II-18 through II-23 demonstrate the behavior of
permittivity as a function of volumetric water content
(grams H_2O/cm^3). These plots do not show as sharp
a break at the transition moistures as do Figures II-11
through II-16. Neglecting the sand sample, it can be seen
that the permittivities for moistures less than the transi-
tion region are independent of soil type, as expected, and
only dependent on the amount of solvate water. The sand
sample actually fits this criterion also since its per-
mittivity at zero moisture is equal to the others, but its
transition region starts almost immediately since coarse
sand holds practically no solvate water.

In addition, based on the theory set forth, it is
expected that the permittivity above the transition region
will be independent of soil type and only dependent on the
amount of pore water present in the soil. This can be
seen to hold true by plotting permittivity as a function
of volumetric moisture minus volumetric transition moisture
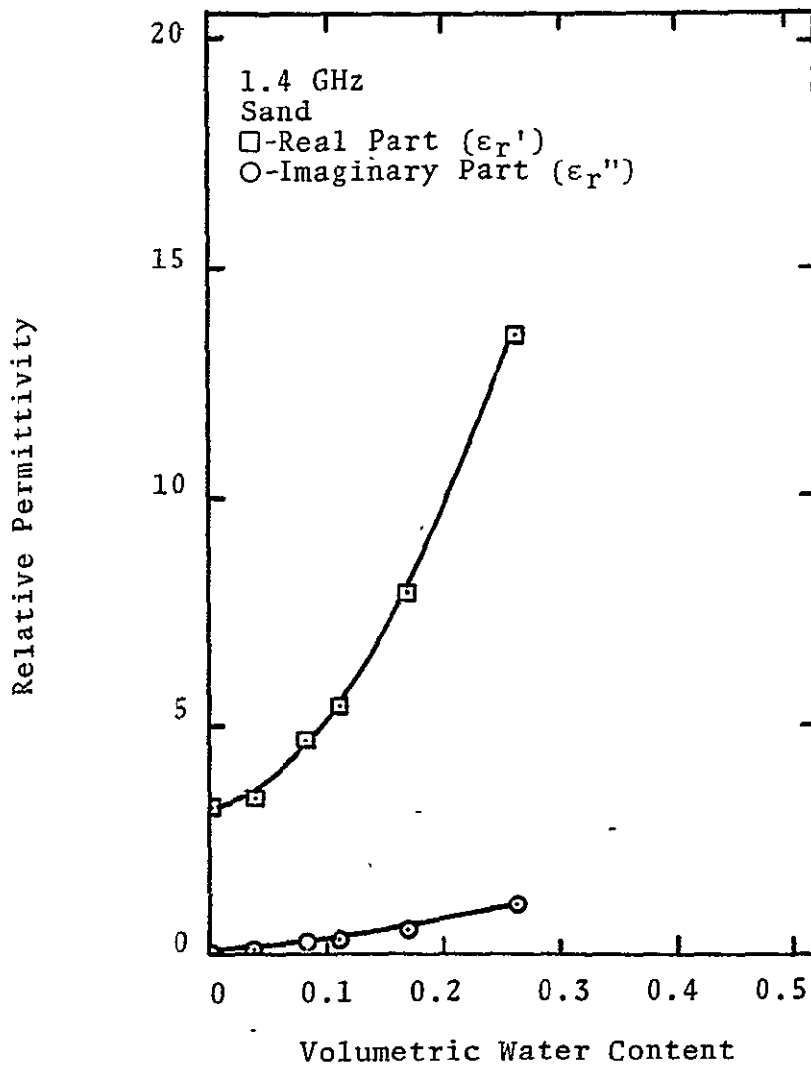
Figure II-18. Relative permittivity of sand as a
function of volumetric water content.
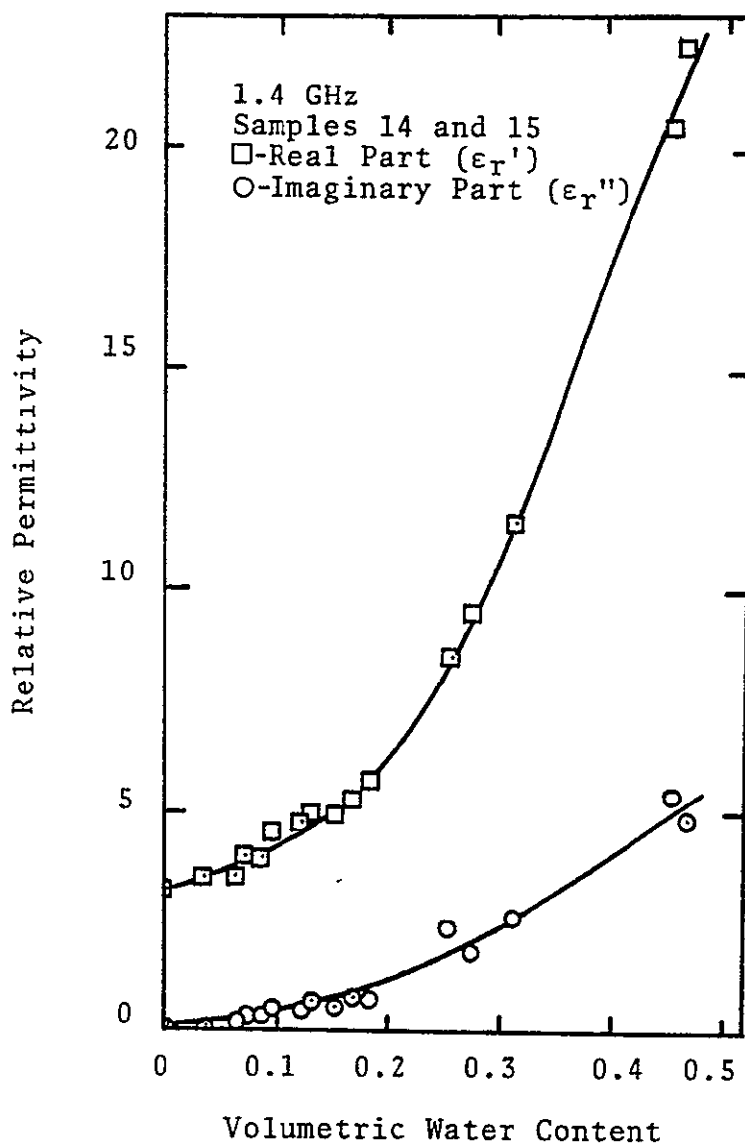
Figure II-19. Relative permittivity of samples 14 and 15 as a function of volumetric water content.
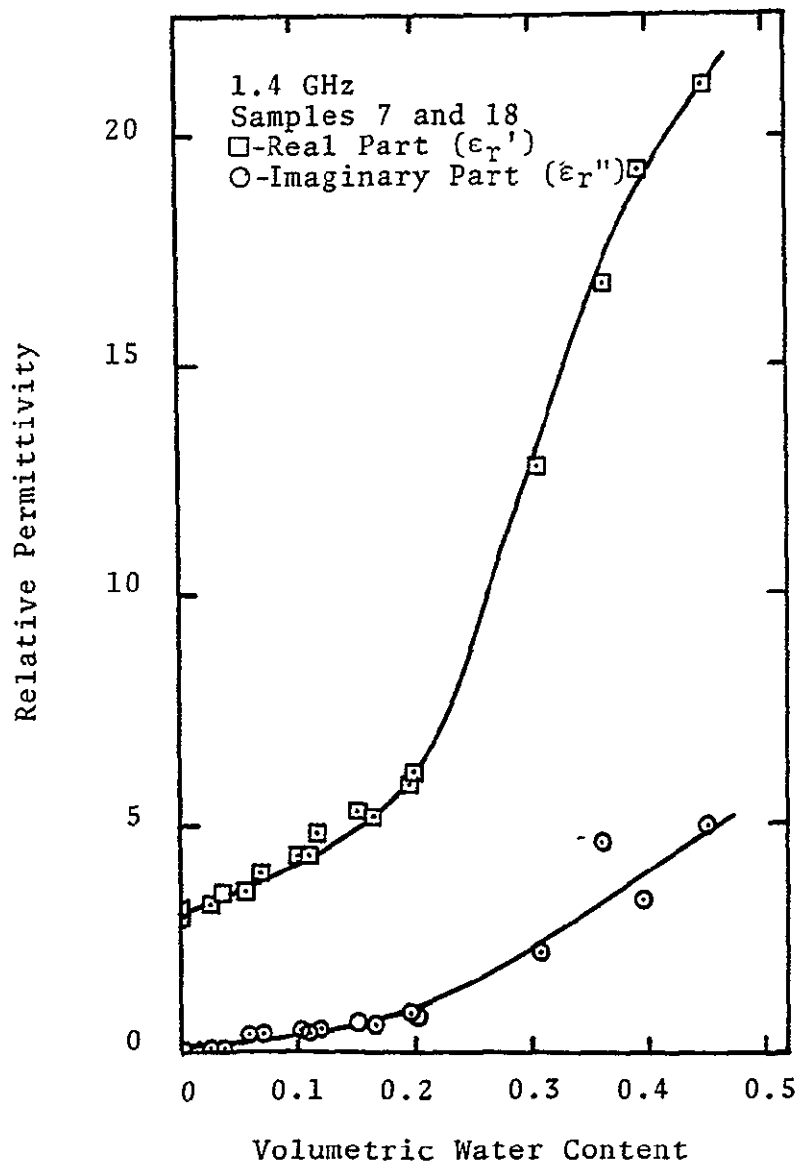
Figure II-20. Relative permittivity of samples 7 and 18 as a function of volumetric water content.
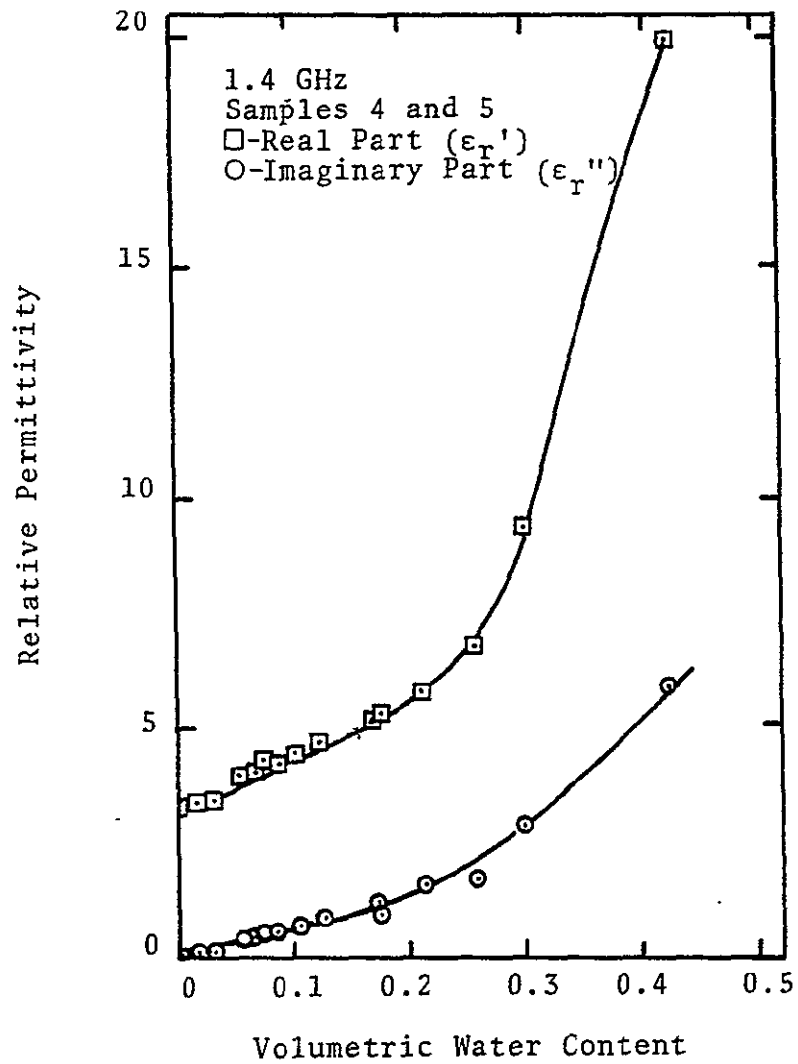
Figure II-21. Relative permittivity of samples 4 and 5 as a function of volumetric water content.
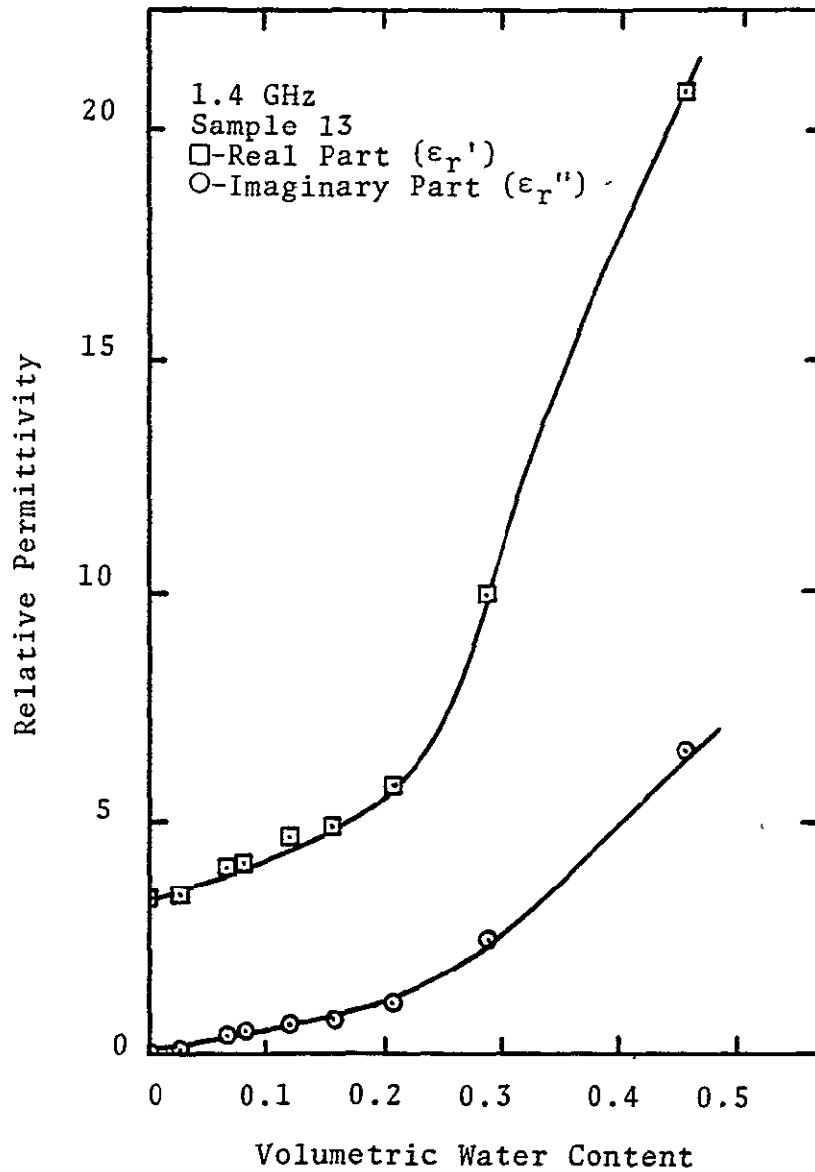
Figure II-22.   Relative permittivity of sample 13 as
                a function of volumetric water content.
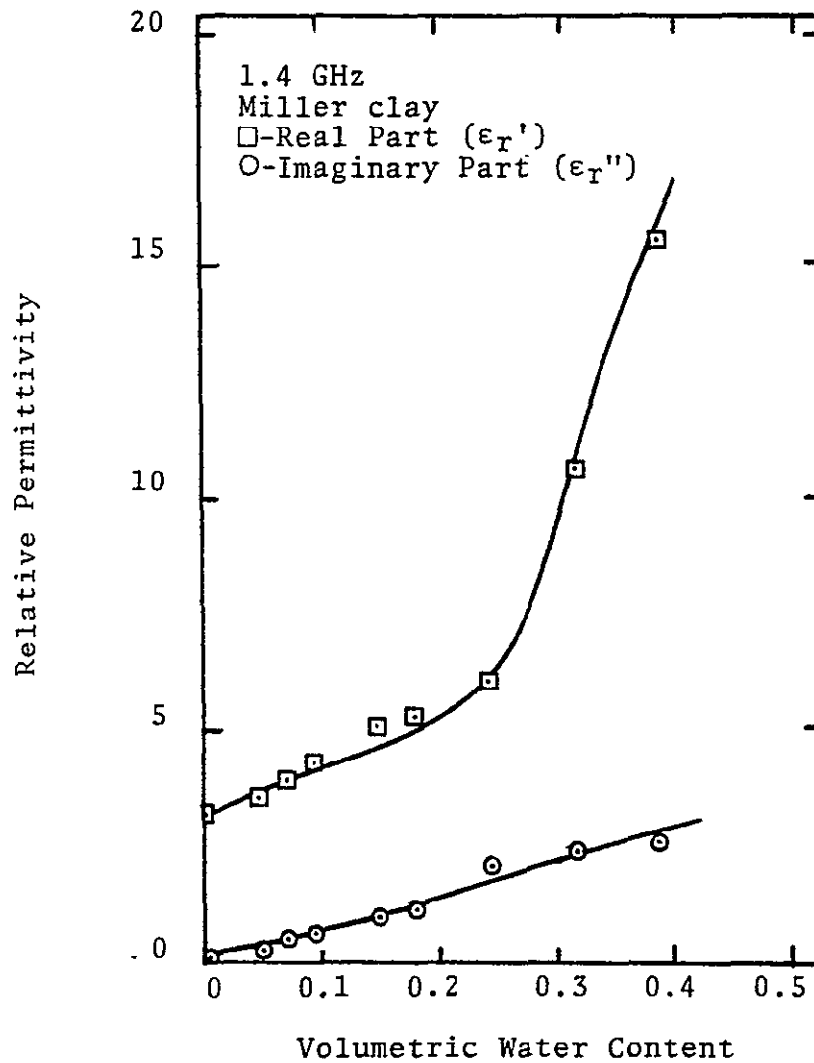
Figure II-23. Relative permittivity of Miller clay as a function of volumetric water content.

which is proportional to the amount of pore water. Volumetric transition moisture is defined by the intersection of two straight lines, one drawn through the points before the transition region and one drawn through the points after the transition region. Table II-4 is a tabulation of the transition moisture defined in this manner and Figure II-24 is a plot of the permittivities above the transition regions.

The analysis described above supports the hypothesis that the basic dependence of permittivity on soil water can be described in terms of the matric potential at which the soil water is held. The permittivity of soil is dependent not only upon the total number of dipole moments (water molecules), but it is also dependent upon the energy state at which they are held to the soil particles. This energy state is defined by the matric potential of the soil. This phenomena could be directly demonstrated by mapping the permittivity measurements as a function of volumetric water content (Figures II-18 through II-23) into the soil's matric potential as a function of volumetric water content. The resulting plot of permittivity versus matric potential should be independent of soil texture. However, reliable measurements of matric potential as a function of volumetric water content are not available for all of the soils for which permittivity measurements were

Table II-4

Tabulation of Volumetric Transition Moistures

Graphically Obtained from Figures

II-18 through II-23

Soil Samples	Volumetric Transition Moisture
Sand	0.106
14 & 15	0.20
7 & 18	0.21
4 & 5	0.24
13	0.22
Miller Clay	0.245
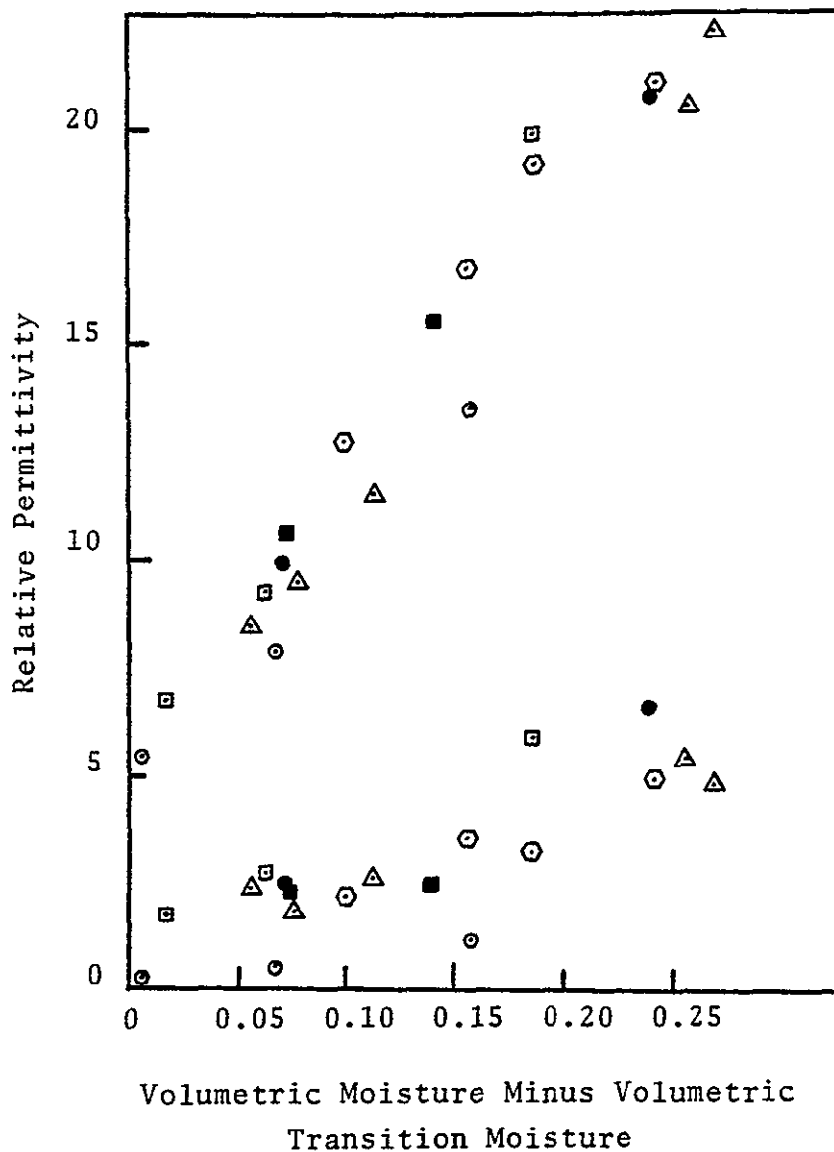
Figure II-24. Permittivity of all soils referenced to the transition moisture.

made. As a result a direct demonstration of the hypothesis is not possible.

Matric potential measurements of Avondale clay loam were obtained from T. Schmugge of the NASA Goddard Space Flight Center. These measurements were made by the U.S. Water Conservation Laboratory in Phoenix, Arizona. Similar measurements for other Phoenix soil textures are reported by Isdo et al. [17]. The soil used by Isdo et al. was obtained from the same general area as samples 1 through 18 listed in Table II-3. Of the soil samples listed in Table II-3, the characteristics of sample 7 and 18 most closely resemble those of Avondale clay loam.

Assuming the matric potential of Avondale clay loam is adequate to discribe the matric potential of samples 7 and 18, the hypothesis that permittivity is dependent on the soil matric potential independent of soil texture can be indirectly demonstrated. This will be done by using the matric potential measurements of Avondale clay loam as a reference for calculating matric potential curves for Miller clay and sand using their permittivity measurements. The resulting matric potential versus water content curves can then be compared to the independently reported measurements of matric potential for typical soil textures shown in Figure II-9.

Columns one and two of Table II-5 contain a tabulation of matric potential versus volumetric soil moisture for

Table II-5

Matric Potential Versus Soil Moisture for Samples 7 and 18,

Miller Clay and Sand

Matric Potential (bars) Avondale Clay Loam	Soil Moisture (cm^3/cm^3)	Permittivity Samples 7 and 18	Soil Moisture Miller Clay	Soil Moisture Sand
75.0	0.10	4.35	0.125	0.075
16.5	0.14	5.00	0.175	0.09
9.0	0.158	5.31	0.188	0.10
5.0	0.175	5.63	0.200	0.11
2.3	0.20	6.25	0.22	0.125
1.15	0.22	7.10	0.265	0.155
0.165	0.285	10.00	0.315	0.20
0.08	0.315	12.50	0.34	0.25

Avondale clay loam. Column three contains the permittivity

of samples 7 and 18 for the moisture contents in column

two. The moisture contents of Miller clay and the sand

sample that correspond to the permittivities of column

three are listed in columns four and five. Figure II-25

contains the resulting plots of matric potential versus

volumetric soil moisture for the three soil textures of

Table II-5. The general characteristics of these plots com-

pare very favorably with the typical plots of Figure II-9.

Note that the moisture contents of Figure II-25 are based on

volume while the moisture contents of Figure II-9 are based

on weight. Although the data of Figure II-25 are only

approximate, it does support the hypothesis that soil per-

mittivity is dependent on the matric potential at which

water molecules are held to the soil.

The apparent result that soil permittivity is in fact

independent of soil texture when it is plotted as a function

of matric potential is of vital importance to the under-

standing of the soil moisture information that is available

from microwave measurements. As explained in the last

section, it is the matric potential of the soil water that

is important in determining the ability of a plant to uptake

water, or for that matter in determining the state of

saturation of a soil (which is important in soil run-off

prediction). This leads to the conclusion that a microwave

sensor should yield information directly related to the
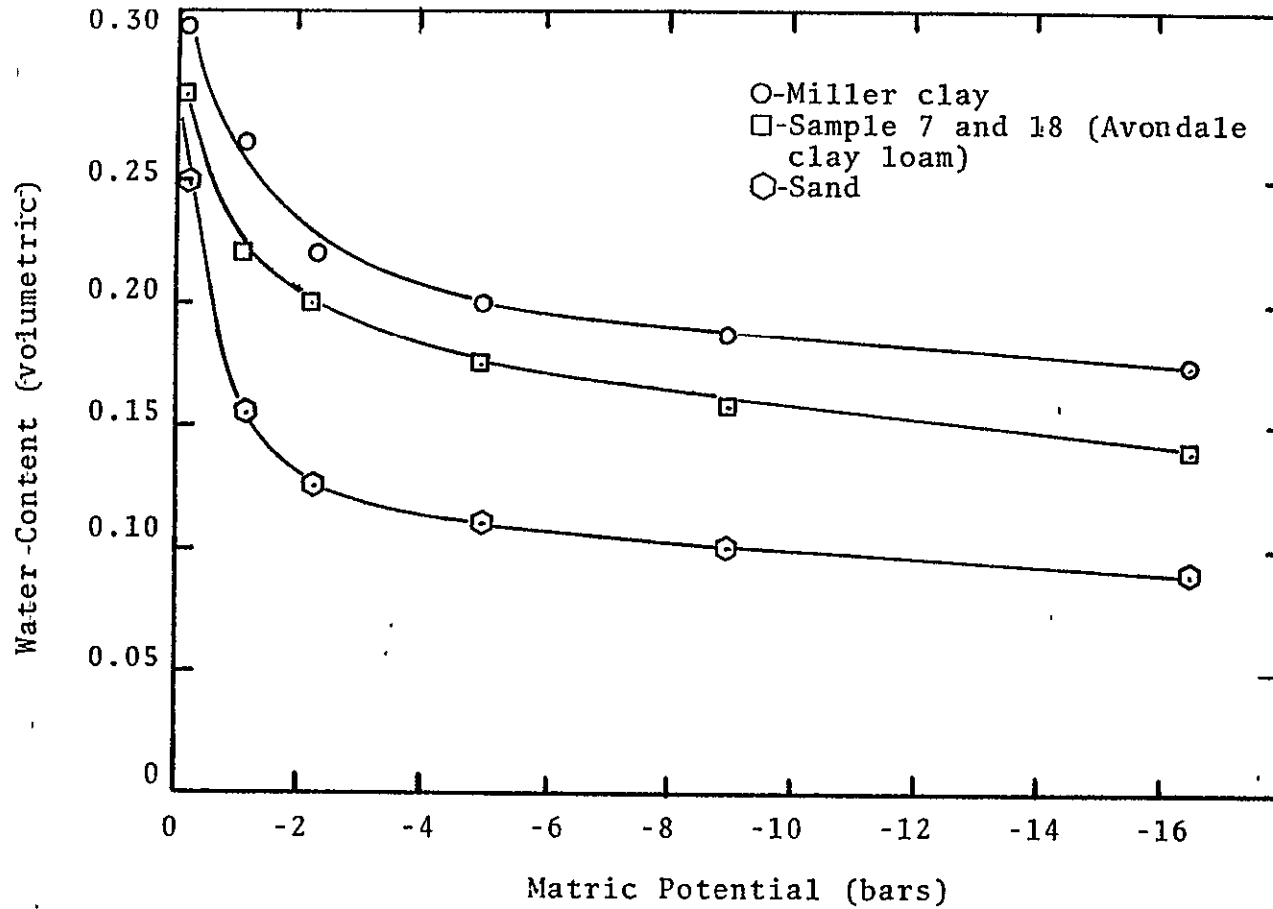
Figure II-25. Matric potential of Miller clay, samples 7 and 18, and sand assuming equivalence of permittivity versus soil moisture for all soil textures.

availability of soil water to vegetation. Further, this information is independent of soil type.

Comparison to other L-band measurements - Hoekstra and Delany [18] measured the permittivity of soil over a wide range of microwave frequencies. Their data show a dielectric relaxation where the real part of the permittivity decreases with frequency and the imaginary part goes through a maximum. This dielectric relaxation is attributed to water in the soil, but its characteristics are different from the dielectric relaxation of bulk water. Hoekstra and Delany have shown that the frequency of maximum dielectric loss (maximum ε_r'') of the relaxation of water in soils is displaced to a lower frequency than that of bulk water. Also, the relaxation occurs over a narrower frequency band than in bulk water.

Experimental results [19]-[21] have shown that the dielectric properties of bulk water and other materials with permanent dipole moments can be predicted using equations of the Debye form. Hoekstra and Delany [18] modeled the real part of the soil permittivity assuming two closely spaced relaxations. They describe each with a modification of the Debye equation by Cole and Cole [22]:

$$\varepsilon' = \varepsilon_{1s} + \frac{\varepsilon_{1s}' - \varepsilon_{1\infty}'}{(1+j\omega\tau_1)^{1-\alpha_1}}$$

$$+ \varepsilon_{2s}' + \frac{\varepsilon_{2s}' - \varepsilon_{2\infty}'}{(1+j\omega\tau_2)^{1-\alpha_2}}$$

(II-9)

where the subscripts 1 and 2 refer to the two separate
dispersions. The subscripts ∞ and s refer to the values
ϵ' at frequencies where $\omega\tau \gg 1$ and $\omega\tau \ll 1$, respectively; τ is
the relaxation time, α is a parameter indicating the dis-
tribution of relaxation times and ω is radian frequency.
The characteristic frequency of the dominant dispersion
was shown experimentally to range between 1.5 GHz and 4 GHz,
while the characteristic frequency of the second dispersion
corresponds roughly to that of bulk water.

Hoekstra and Delany [18] found that, within their
experimental error, the same relaxation parameters could
be used in their model to describe the dielectric relaxation
of the four types of soils that they measured at a constant
10% moisture by weight. These soils ranged from fine sand
to clay. Since the amounts of adsorbed water differs be-
tween sand and clay, Hoekstra and Delany concluded that
adsorption effects were not directly responsible for dielec-
tric relaxation of water in soils. This conclusion does
not necessarily agree with results of Newton and McClellan
[13]. It was shown earlier that permittivity of soil at
moistures below the transition moisture is dependent only on
the volumetric soil moisture and not on soil texture. The
dependence on soil texture is only evident for moistures
above the transition moisture and is a result of the fact
that the transition moisture is dependent on soil texture.
Figures II-18 through II-23 and Figure II-24 demonstrate

that the real part of the measurements reported by Newton and McClellan vary with soil texture only as a result of the fact that the transition moisture varies with soil texture. As noted by Cihlar and Ulaby [14], based on the review of many permittivity measurements, the difference between soils of various textures does appear smaller when the permittivities are plotted as a function of water content by volume. This is true simply because the plots are normalized to equal amounts of water.

Since the permittivity of soil is not only dependent upon volumetric water content, but also upon the matric potential of that water, it is possible for the measurements of Hoekstra and Delany [18] not to show evidence of a texture dependence when plotted as a function of volumetric water content if the water was held at approximately the same matric potential for all of the soils. Since no information is given by Hoekstra and Delany concerning the matric potential of the soil water, there is no way to check this possibility. However, if this were true it would support the hypothesis that the fine sand used as a sample could support at least 15% moisture in adsorbed and solvate water. This would mean that their measurements were made before the transition moisture. If this was the case, the permittivities they had to work with would be independent of soil type. It should also be noted that it takes a large texture difference to

produce a small change in volumetric transition moisture.
This leads to the fact that the permittivity of most
agricultural soils from the same general area will be in-
dependent of soil type when viewed as a function of volumet-
ric moisture content. As a result, soil type should be a
minor effect when analyzing microwave data for soil moisture,
at least at L-band.

Although the data reported by Hoekstra and Delany
[18] have not demonstrated the effects of soil texture as
did the data reported by Newton and McClellan [13], other
authors have measured effects of texture, although not
all at L-band. Lundien [16], Gieger and Williams [23],
Hipp [24], Wiebe [25] and Babai [26] have seen textural
effects even though the data have not been of sufficient
quality to make conclusive statements as to the dependence
of permittivity on water in the adsorption complex.

Other Effects

Up to this point there has been no mention of the
permittivity dependence on frequency, soil temperature,
or adsorbed cations. Cihlar and Ulaby [14] provide a good
compilation of most of the current literature containing
microwave permittivity measurements. It was pointed out
that measurements of Gieger and Williams [23] at K_a-band
demonstrate a dependence on soil texture, as well as
others including Wiebe [25] and Babai [26] at X-band.

However, it appears that the effect of soil texture is not nearly as great at K_a-band and X-band as it is at L-band. In fact, for frequencies other than L-band, experimental error in the permittivity measurements and the textural classifications appear to be as great as the true textural effects. As a result, the composite of all X-band measurements that are compiled by Cihlar and Ulaby [14] in Figure 23 of that report (p. 30) will be utilized in this document for all X-band calculations of microwave emission or scattering coefficient, regardless of the soil type being modeled.

Soil permittivity does depend on soil temperature as a result of the water contained in the soil. This has been demonstrated by Lundien [16], Hoekstra and Delany [18], and Poe [27]. However, the dependence on soil temperature is not a significant effect for temperatures over the range of 15°C to 30°C. As a result, effects of soil temperature on soil permittivity will not be considered in this document.

The type of cation adsorbed by the soil particle changes the cation exchange capacity of the soil and as a result has a large effect on the amount of water of hydration that can be held by the soil. Obviously, this affects the soil permittivity-matric potential relationship. In addition, the ion content of the soil water affects the

imaginary part of the soil permittivity. As the soil
water ion content is increased, the conductivity of the
soil increases. This effect has not been completely
verified experimentally, however, calculations of
permittivities of water-salt-soil mixtures provide a
good approximation of the effect (Figure II-26) [28].
Good agricultural soil will not have salt contents large
enough to greatly affect soil permittivity, however,
mapping areas of saline soils is an important and dif-
ficult task for agricultural planners.
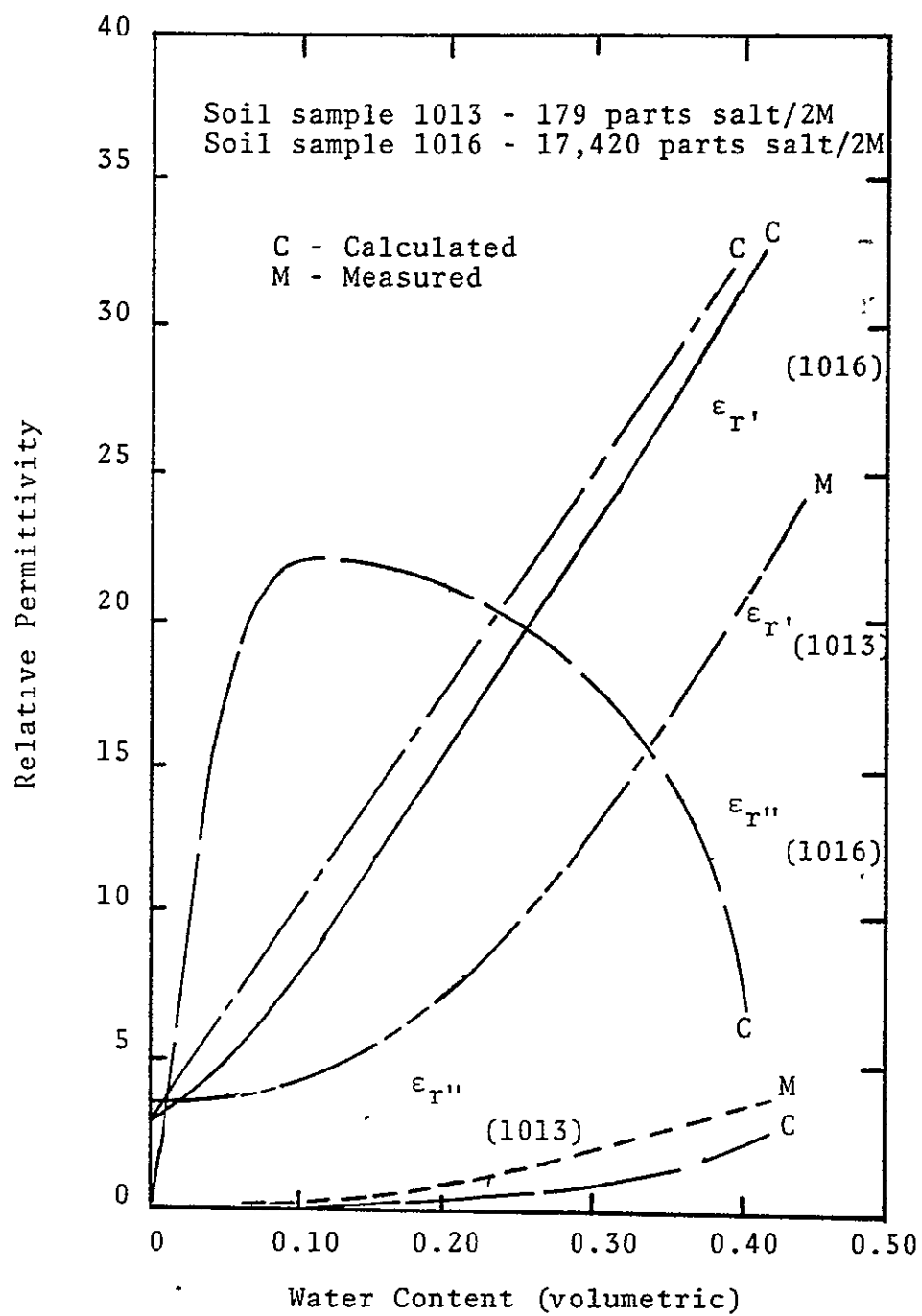
Figure II-26. Results of calculations of relative permittivity for soils of different salt contents (after Carver [28]).

CHAPTER III

MICROWAVE EMISSION

In Chapter II it was demonstrated that the electric permittivity of the soil is the driving function behind the dependence of soil emission on soil moisture. It is the purpose of this chapter to review techniques that have been used to model the emission of soil as a function of permittivity, or analogously, soil moisture. This discussion will include the techniques for describing the effects of surface roughness and vegetation cover since these parameters significantly modify the emission of the soil. In addition, previously reported measurements that demonstrate the soil moisture dependence, as well as the surface roughness effects and vegetation effects, will be discussed and their applicability to the study noted.

Before reviewing the techniques that have been used to model the microwave emission of a soil-vegetation complex, it is instructive to point out the various components that contribute to a measurement of the emission of such a scene. Although emission from the soil-vegetation complex is the primary source of energy, there are other contributing sources the importance of which depends on the measurement configuration. These sources include; the intervening atmosphere between the soil-vegetation complex and the antenna, atmospheric radiation reflected from the surface into

the antenna aperture, cosmic point sources such as the sun reflected from the surface into the aperture, and man-made radiation in the frequency band of measurement. Emission of the radiometer system backscattered from the surface into the receiving aperture also contributes to the measured antenna temperature. Figure III-1 graphically illustrates these various components of a passive microwave measurement.

The effects of sources other than the soil will be discussed in Chapter VI. The emission from the soil-vegetation complex is the component that is of primary importance to this work. It is only this component that contains information concerning the soil moisture distribution, and it is the only component that is discussed in this chapter.

Mathematical Description of Energy Transfer

Since the thermal microwave emission of a soil medium originates in the soil volume and propagates outwardly, it is reasonable to model the emission process within the volume separately from the modifying effects of the surface roughness and vegetation cover. These latter two effects can be modeled separately. In keeping with this line of reasoning, the literature review presented in this chapter is divided into descriptions of literature dealing with the subsurface, surface, and vegetation cover individually.
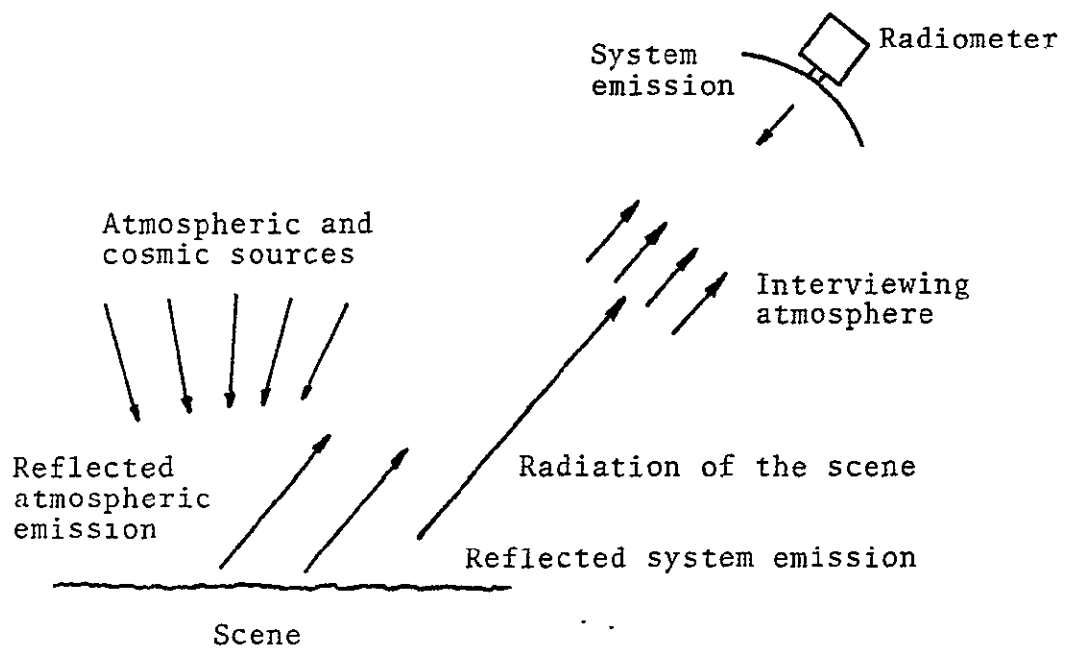
Figure III-1. Graphic illustration of the various
contributions to a radiometer measure-
ment.

Emission from the soil volume is discussed first.
Peake's [29] classical approach to modeling emission from
smooth and rough soil volumes is discussed and its in-
adequacies pointed out. Following that, the radiative
transfer approach to modeling emission from a smooth
surface soil volume is presented. Stogryn [30] and Tsang
et al. [31] provide general solutions, while Burke and
Paris [32] provide a more straightforward, but less
rigorous solution. A review of literature describing models
of surface roughness are provided next. This literature
is subdivided into the four general techniques of modeling
rough surface scatter. These techniques are geometrical
optics or ray tracing; the Kirchhoff solution (physical
optics); small perturbation theory; and the composite sur-
face theory. Subdivision of the discussion in this manner
organizes the techniques by their utility in handling
specific types of surface roughness. Following the review
of literature on surface roughness is a brief discussion
of the literature dealing with vegetation effects.

Soil Volume

Models of the emission from a soil volume have tradi-
tionally been derived for the case of a smooth surface.
This is convenient for the purposes of this discussion
since the smooth surface can be considered as a reference
surface for comparison of the various models of subsurface

emission. Ideally, the surface roughness models can be applied directly to the results of the subsurface emission models to determine the effect of surface roughness. In the following paragraphs two approaches to modeling emission from a non-scattering soil volume will be described. Then, literature dealing with the effects of scattering in the soil volume will be reviewed.

Peake's approach - In modeling the emission of a soil medium, one is concerned with the effects of spatial permittivity and temperature variations, as well as scatterers contained in the volume. The classical approach to modeling the thermal microwave emission was developed by Peake [29] in 1969. In Peake's approach the emissivity of the medium is defined as the ratio of energy emitted by a blackbody at the same temperature as the subject medium. Assuming that a semi-infinite soil medium is in thermodynamic equilibrium with blackbody (isotropic) radiation, Peake demonstrated that emissivity is equal to absorptivity using Kirchhoff's radiation law. For a semi-infinite medium, absorptivity is equal to one minus reflectivity. Reflectivity is the integral of the differential scattering coefficients of the surface. Peake's approach, therefore, relates the emissivity of a surface to its differential scattering coefficients.

Peake's formulation is, however, only rigorously valid for homogeneous soil with uniform moisture and temperature

profiles. This is due to Peake's necessary assumption that the soil medium be in thermodynamic equilibrium with isotropic radiation. The power intensity impinging on the underside of the soil surface due to the soil volume is only isotropic when both the soil moisture and soil temperature distributions are uniform with depth.

The Peake approach is the basis for describing the emissivity of a soil volume bounded by a plane surface in terms of the Fresnel reflection coefficient [33]. The Fresnel reflection coefficient can be used in conjunction with the Peake approach to describe a soil medium containing a uniform soil moisture and soil temperature distribution with depth. This technique can be used to approximate the emission from a nonuniform soil moisture distribution by replacing the Fresnel reflection coefficient with an effective Fresnel reflection coefficient calculated for the nonuniform profile. (This is only an approximation since a basic assumption of the Peake approach is isotropic radiation). Richerson [34] utilized an effective Fresnel reflection coefficient to describe emission from a soil medium composed of horizontally homogeneous layers. In that solution the direction of propagation was taken to be the direction that a ray would be refracted as it crosses the dielectric boundaries.

Another method for solving for the effective reflection coefficient of a plane stratified medium is given

by Casey [35]. Casey solves the equations of propagation

in the medium by putting them in the form of Hill's [36]

equations for which there are known series solutions.

Neither of the techniques presented by Richerson [34]

nor that due to Casey can take spatial temperature varia-

tions into account, since temperature does not enter into

the effective reflection coefficient calculations.

Radiative transfer - The Peake approach describes the

emission from a soil volume in terms of the emissivity of

the soil. Emissivity, as defined by Peake [29], is

computed based on the differential scattering coefficients

of the soil. This technique is not directly applicable

to the situation of nonconstant soil temperature pro-

files since the differential scattering coefficients are

not temperature dependent. The radiation flux of the

soil is emitted from a volume and is dependent on the

temperature distribution within that volume. Therefore,

models that describe the radiation flux emitted by a

soil volume must be dependent on the soil permittivity and

soil temperature profiles. Two techniques that meet these

requirements are described below; a rigorous solution by

Stogryn [30], and an approximate solution by Burke and

Paris [32].

Stogryn [30] solves for the specific intensity of

radiation from a semi-infinite soil volume with a planar

surface using Maxwell's equations. In his formulation
Stogryn makes no simplifying assumptions about the soil
temperature or soil permittivity variations. Stogryn
characterizes the soil medium by a randomly fluctuating
electric current. The random current is due to microscopic
fluctuations in the positions of charged particles within
the medium. These fluctuations result in a current density
whose average is zero, but whose mean square does not
vanish. Stogryn uses the fluctuation-dissipation theorem
[37], [38] to define the expected value of this current
density. Stogryn used Maxwell's equations to relate the
average value of this thermally induced current density
to the randomly fluctuating electric field in the soil
medium. The Fourier components of this field are related
to the intensity of emission. Since the Fourier components
of the electric field are related to intensity, Stogryn
obtained a formulation for the intensity of radiation
from a soil volume resulting from a thermally induced
current density.

The focal point of Stogryn's [30] formulation is
the relationship between the random current density and
the soil permittivity and soil temperature. As noted above,
this relationship is based on the fluctuation-dissipation
theorem [37], [38]. Although Stogryn's formulation is
general, the number of problems for which explicit solutions

can be obtained are very limited. The solution of Stogryn's formulation for actual soil permittivity and soil temperature profiles (even assuming two-dimensioned uniformity) requires a large amount of digital computer time.

A formulation for emission from a stratified medium with arbitrary moisture and temperature profiles is also provided by Tsang et al. [31]. Their approach is very similar to that of Stogryn [30]. However, numerical results are illustrated and compared with closed form analytical solutions and results obtained with the WKB method [39] for simple profiles.

An alternative to the general formulation by Stogryn [30] is provided by Burke and Paris [32] through an application of the radiation transfer equation to emission from soils. This formulation of the radiative transfer process was primarily an offshoot of the formulation by Paris [40] describing the transfer of microwave energy through the atmosphere. The radiative transfer equations derived by Burke and Paris were formulated for incoherent radiation and a plane homogeneously stratified soil medium containing a temperature variation with depth only. The results of this model were shown to compare favorably with airborne radiometric X-band data acquired by NASA over Phoenix, Arizona in 1974. The radiative transfer model is amenable to physical interpretation, is not

computationally difficult, and approaches the general
solution of Stogryn as the soil layers are allowed to become
infinitely thin. The Burke and Paris model will be des-
cribed in greater detail in Chapter IV.

Scattering in the soil volume - The formulations given
above assume that the soil permittivity varies smoothly
without discontinuities. Such discontinuities would
cause scattering within the soil volume. However, soil,
in its natural state, contains voids, rocks, plant roots,
etc., that cause permittivity discontinuities. The effect
of scattering within the soil volume has been addressed
by Stogryn [41], Wilhelmi et al. [42] and England [43],
among others.

Stogryn [41] treats the volume scattering due to
small random dielectric fluctuations in a medium bounded
by a plane surface. In this formulation, which is an
approximate first order perturbation method, Stogryn
allows the non-random part of the dielectric constant to
vary with depth. Stogryn provides calculations of back-
scatter cross section per unit area to demonstrate the ef-
fect of the volume scattering. The Peake approach would
have to be employed in applying this result to radiometric
applications. This immediately indicates that the theory
could only be used to predict the emission of a volume
containing uniform moisture and temperature profiles.

Wilhelmi et al. [42] described backscatter from rough
surfaces using the physical optics approach described in
the next section, but included effects of volume scatter
due to inhomogeneities in the subsurface. The thrust of
their work was to demonstrate volumetric depolarization
effects. The rationale of their theoretical technique
was that the electromagnetic field crossing the surface
and entering the volume experiences multiple scattering
and is returned back to the surface where it is transferred
across the boundary adding to the backscatter from the
surface. This addition of field power is possible since
the volume scattering mechanism destroys the coherence
of the internal and external fields. The efficiency of the
volume scatter mechanism was determined by experimentally
determined parameters. Although Wilhelmi et al. developed
this technique specifically for scatter of laser light,
it was described here as an example of another approach
to modeling volume scatter.

The approach used by England [43] was to apply a
modified version of scattering theory that has previously
been applied to atmospheric radiative transfer or to
neutron scattering. England's approach was based on a
radiative transfer approach similar to that of Burke and
Paris [32]. As a result, England's results are directly
applicable to the work reported in this document. In

his development, England assumed a linearily varying temperature profile with depth, homogeneous soil permittivity, and randomly distributed point scatters. England's results demonstrate that the reduction in the intensity of emission due to volume scattering may be tens of degrees, but that this "darkening" is dependent on the dominance of scattering over absorption. It is pointed out that scatterers have a greater effect the lower the real part of the soil permittivity. However, the real part of the permittivity of soil in the microwave frequency range increases significantly with soil moisture, while the imaginary part does not increase as greatly. This led England to conclude that... "The introduction of small amounts of liquid water (to a low loss soil) reduces or even effectively eliminates scatter-induced darkening. Therefore, scatterers tend to play an insignificant role in emission from moist soil or wet snow."

Surface Roughness

As described in the last section, the classical approach to analytical descriptions of emission from natural scenes was developed by Peake [29]. Stogryn [44] demonstrated the utility of this technique for describing the emissivity of scenes using a variety of surface scattering theories. Peake's approach inherently intertwines

the subsurface and surface effects into one formulation
since the scattering coefficients of the scene are func-
tions not only of surface profile, but also of subsurface
electrical properties. However, there have been no other
approaches to modeling the emission from rough surface[±]
except for a formulation by Johnson [45] which has not
been validated experimentally. As a result, the various
approaches that have been commonly used in the literature
to calculate scattering coefficients of rough surfaces
will be reviewed. These techniques are the geometrical
optics approach, the Kirchhoff solution, the small per-
turbation approach, and the composite surface theory.

Geometrical and pseudo-physical optics models - The
geometrical optics approach to modeling rough surfaces
applies when the frequency of the electromagnetic wave is
sufficiently high that the finiteness of the wavelength
may be neglected [46]. A geometrical optics model can be
viewed as a collection of infinitely large plane facets,
each of which generate a specular type reradiation pattern.
It is assumed that all facets which are not normal to the
direction of propagation can be ignored. Although this
is a very crude model, it is an effective one since all
viable theories of rough surface scatter reduce to this
model when the incident wavelength becomes very small
compared to the standard deviation and the autocorrelation

of the surface profile [47]. Examples of the geometrical
optics technique of modeling rough surfaces are given by
Kodis [48] and Barrick [49]. By comparing numerical com-
putations to geometrical optics theory, Fung et al. [50]
have shown the range of surface conditions for which the
geometrical optics theory is valid. The condition for
validity is

$$\lambda K < 0.31 \cos \theta$$

$$\sigma/_\lambda \geq 1.0$$

(III-1)

where σ is the rms surface height deviations, K is the
radius of curvature of the surface (for randomly rough
surfaces K is the average curvature), λ is the incident
wavelength and θ is the incident angle.

Several authors have presented extensions of the
basic geometrical optics approach that do not assume
specular reflection from infinite size facets. These models
can be considered pseudo-physical optics theories. Spetner
and Katz [51] and Waite [52] present models that assume a
collection of small facets with a uniform pattern and size
distribution. Both of these models assume that the radar
return is composed of the summation of the returns from a
collection of randomly located scatterers, although these
authors make different assumptions about the radar cross

cross section and reradiation pattern of individual facets.

Katzin [53] extended the pseudo geometrical optics models further by introducing two size ranges of facets to represent the surface. Katzin assumed a combination of facets large with respect to a wavelength and facets very small with respect to a wavelength. The reradiation pattern of the large facets is highly directive, but with a finite width about the specular return. The pattern of individual large facets was assumed to be proportional to the fourth power of the incident wavelength with a random reradiation pattern. Katzin further assumed that the facets were randomly located around a mean surface so that the backscattered energy from the two types of facets is additive. Katzin's model was extended by Khamsi et al. [54] to include a third facet size between the large and small facets assumed by Katzin. Khamsi et al. demonstrated that three size ranges provide better agreement between theory and measurements.

Kirchhoff solution - The Kirchhoff or physical optics approach to calculating fields scattered from rough surfaces is formulated according to Huygen's principal. The Helmhotz integral expresses the scattered fields in terms of the total field and its normal derivative or their equivalents on the surface [55]. The associated boundary conditions are not generally known and the Kirchhoff method

consists essentially in approximating these values such that the Helmhotz integral can be evaluated [56].

The field at each point on the surface is approximated by assuming that it is the sum of the incident wave and a wave reflected from a smooth plane tangent to the surface at the given point. The tangent plane approximation restricts the method to locally flat surfaces composed of irregularities with small curvatures and incident angles not near grazing. Brekkovskikh [57] has given the surface criterion for the Kirchhoff approach as:

$$4\pi r_c \cos\theta >> \lambda \tag{III-2}$$

where r_c is the radius of curvature, θ is the local incident angle, and λ is the wavelength. This criterion was based purely on geometrical considerations. Based on a comparison of numerical and theoretical computations, Fung et al. [50] gave the ranges of validity for physical optics theory as:

$$\lambda K \leq 2.92 \cos^3\theta \quad \text{for } \sigma/\lambda \leq 0.1$$
$$\lambda K \leq 0.31 \cos\theta \quad \text{for } \sigma/\lambda \geq 1.0 \tag{III-3}$$

where K is the radius of curvature of the surface, θ is the incident angle, σ is the rms surface height deviations, and λ is the wavelength. Although the conditions stated above describe the surface conditions for strict validity of the Kirchhoff approximation, Beckmann and Spizzichino [58] indicate that the technique works reasonably well for many surfaces that do not meet these conditions.

A number of authors have used the Kirchhoff approximation to solve for scatter from rough surfaces. Beckmann and Spizzichino [58] use the Kirchhoff approximation in conjunction with the Scalar Helmhotz integral to solve for scatter from a perfect conductor. Fung [59] formulated the vector solution of fields scattered from rough surfaces using the Stratton-Chu integral, but did not provide an explicit expression for the scattered fields. Stogryn [60] was able to obtain explicit expressions for scatter from normally distributed rough surfaces using the Kirchhoff approximation. Leader [61] generalized Fung's formulation to the case of bidirectional reflectance and was able to provide sample calculations.

Small perturbation - The small perturbation solution can be used to describe the scatter from surface irregularities that are small compared with the wavelength of the incident radiation. In addition, the slope of the surface should be much less than unity. The basic concept of the small perturbation technique is due to the work of Rice [62], who generalized the acoustic method of Rayleigh [63] to a vector wave and a random surface. Fung [55] provides a good summary of this approach.

Rice [62] described the surface by a two-dimensional Fourier series with coefficients that are random variables. The scattered and incident fields are described by an

infinite series. The coefficients of the series describing the fields are determined by using boundary conditions at the surface. Rice did not attempt to arrive at a solution that is directly applicable to a particular situation, his results were general in nature. Rice considered the situation of perfect conductivity, but found that the series solution diverged logarithmically. By allowing the surface to have a large but finite conductivity, Rice showed that the cause of the divergence could be eliminated. Valenzuela [64] applied Rice's theory to the case of scatter from slightly rough sea. For the case of finite conductivity, Valenzuela evaluated the boundary conditions to terms of the second order; one order beyond that evaluated by Rice for infinite conductivity.

The criterion of the surface roughness for validity of the small perturbation technique is so stringent that naturally occurring surfaces generally do not fit the criterion. Based on the Fung et al. [50] numerical-theoretical computational comparison, the range of surface conditions for validity of the small perturbation technique is:

$$\sigma/\lambda \leq 0.053 \qquad \text{(III-4)}$$

where σ is the rms height deviations and λ is the wavelength of the incident radiation. However, this technique is used

in conjunction with other theories to model more realistic surfaces. This technique is described below.

Composite surface theory - Beckmann [65] pointed out that many rough surfaces encountered in practical applications are superpositions of several scales of roughness. Beckmann attacked this problem by defining the surface as the sum of independent stationary random functions. He solved for the mean square amplitude of the scatter from each surface using the scalar Kirchhoff integral and summed the results to get the overall mean squared scattered amplitude. Using this technique Beckmann demonstrated that the dominant surface roughness component is not the one with the greatest surface roughness, but it is the one with the greatest rms slope. This result indicates the importance of small scale structure since small scale structure can have the greatest rms slope.

Although Beckmann's [65] solution was for composite rough surfaces, it is not what is currently termed the composite surface theory. The composite surface theory as used in the current literature jointly utilizes the Kirchhoff approximation and perturbation techniques to solve for the scatter from surfaces made up of large scale surface deviations upon which very small scale surface deviations are imposed. The criteria of validity of each roughness scale, in order for these techniques to be

applied, are as previously specified. Wright [66] first introduced this technique as a method of predicting scatter from sea surfaces where small scale waves ride on top of large scale swell.

Wright's [66] technique is known as an incoherent model since Wright calculated the scattered power resulting from the small scale surface deviations and simply averaged over the tilt angles resulting from the large scale surface deviations. This assumes that the total scattered power is the sum of two independent contributions, at least to the first order.

Chan and Fung [67] provide a technique for a coherent composite surface theory. Their technique is to solve for the fields at the surface due to the small scale undulations using perturbation techniques and then use this field in the Kirchhoff solution to solve for the scattered power from the composite surface.

An example of using the incoherent composite surface theory to calculate emissivity of the sea is given by Wu and Fung [68]. Wu and Fung simply utilize the Peake approach to convert differential scattering coefficients calculated using the composite surface theory to emissivity.

Vegetation

Models of scattering coefficients of vegetation -
There has been some concern with modeling the effects of

vegetation on the propagation of energy in the
MegaHertz frequency range as a result of communication
problems in forest environments [69] - [71]. However, there
are few published theoretical models of scatter or emission
from vegetation for the microwave frequency range.

Du [72] modeled the scattering from randomly distribut-
ed leaves. He assumed that the leaves were of uniform
thickness, arbitrary shape and planar, but much larger than
the wavelength of the incident radiation. The scatter
from each individual leaf was calculated based on the
reflection from an infinite plane of equivalent permittivity.
Comparison of calculations based on this model to measure-
ments of backscatter from soybeans at 10 GHz and 35 GHz
demonstrate that the general magnitude, angular dependence,
and polarization effects were fairly well predicted.

Another model of microwave scattering by vegetation
was formulated by Peake [73]. Peake modeled the scatter
from vegetation by assuming that the vegetation consisted
of long, thin, homogeneous dielectric cylinders arranged
in a random fashion, but with a higher probability of
vertical orientation. Peake's model required that the
diameter of the cylinders be much smaller than a wavelength
and that the spacing of the cylinders be large with respect
to a wavelength. At K_a-band, Peake found that this model
was adequate to account for the general intensity of radar

return from grass, and that a reasonable change in moisture content and blade density can account for the observed seasonal dependence. Measurements at X-band were not in as good agreement with the model since the grass was not deep enough to provide sufficient attenuation to satisfy the assumptions of the model.

More recently Waite and Cook [74] investigated the volume scatter from low level vegetation. As a result of their measurement program, they concluded that the behavior of grass could best be described not as a scattering volume, but as a homogeneous lossy dielectric. However, in order to get the best agreement between the measurements and model predictions, the measurements had to be corrected for roughness effects. Waite and Cook further noted that Peake's grass model was not entirely applicable to their data set since it assumes an infinite grass layer thickness.

Models of emission of vegetation - The literature cited thus far were concerned with developing models of vegetation applicable to active microwave measurements. Sibley [75] generated a simplistic vegetation model applicable to pas- sive microwave measurements to determine the effect of vegetation on the emission from the underlying soil. Sibley approached the problem from the standpoint of propagation through planar dielectric layers. Thermal

radiation originates in the soil and part is transmitted
across the surface of the soil into the vegetation canopy.
This radiation propagates through the vegetation and into
the atmosphere. The vegetation canopy is considered to be
a dielectric layer which is described by its permittivity.
Therefore, Sibley's problem reduced to describing the
permittivity of the vegetation layer and characterizing its
geometrical form mathematically such that effects of
propagation through the vegetation medium could be cal-
culated. Sibley considered two gemoetrical forms for
his model; a uniform vegetation cover and vegetation planted
in rows.

In describing the permittivity of the vegetation
canopy, Sibley postulated that the canopy was a mixture of
vegetation (primarily water) and air; therefore, its di-
electric properties could be described using the Weiner
model for a dielectric mixture as presented by Evans [76].
Peake and Oliver's [77] formulation of the permittivity of
vegetation was used in the dielectric mixture calculation.

Although Sibley [75] considered two geometrical forms
for his model, only the equations for a uniform vegetation
cover are given to demonstrate Sibley's technique. Sibley
assumed that the canopy not only attenuates the emission
from the soil, but also contributes to the total apparent
temperature through thermal emission. The contribution
of the canopy is derived from the general expression of the

apparent temperature of the dielectric layer of thickness
H. This requires the assumption that all points within the
canopy emit radiation equally. Assuming the temperature,
attenuation constant, and emittance are constant within
the canopy, the contribution of a uniform canopy is

$$T_{canopy} = t \left(\frac{\varepsilon}{2\alpha}\right)\left(1 - e^{-2\alpha H \sec \theta}\right) \qquad \text{(III-5)}$$

where t is the thermometric temperature of the canopy and
ε is the differential emission coefficient. Under the
assumption of thermal equilibrium, the differential emission
coefficient is equal to the absorption coefficient. However,
for a plant canopy this does not generally hold; therefore,
Sibley defined an energy transfer factor f.

$$T_{canopy} = t f \left(1 - e^{-2\alpha H \sec \theta}\right) \qquad \text{(III-6)}$$

where f < 1 represents a gain of energy by the canopy and
f > 1 represents a loss of energy by the canopy.

Another approach to modeling vegetation for the passive
case is given by Basharinov and Shutko [78]. Their char-
acterization of the vegetation is based primarily on the
quantity of water in the vegetation as given by

$$W = p G \ell S_o \rho \qquad \text{(III-7)}$$

where

p - density of filling of a unit volume

G - volumetric moisture content of the vegetation

1 - plant cover height

S_o - area of plant cover

ρ - specific gravity of water ,

Two cases of vegetation cover were considered; sparse plant cover and dense plant cover. The density of filling of a unit volume, p,-varies from 0.001 to 0.0001 for sparse cover and from 0.01 to 0.001 for dense cover.

The influence of sparse plant cover was estimated by Basharinov and Shutko [78] based on an estimate of the optical thickness, τ_p, of the plant cover using two extreme model approximations. The minimum influence of vegetation was modeled by assuming that the capillary moisture contained in the plant elements is a layer of fog. The optical depth of the fog was determined using the Rayleigh approximation without considering diffraction effects. The maximum influence of vegetation was modeled by assuming that the moisture content of the vegetation is a layer of precipitated water. The value of optical depth in this case was calculated on the basis of the attenuation of water for the given wavelength and the thickness of the assumed water layer.

Increments of radiometric brightness temperature resulting from the vegetation layer was calculated using:

$$\Delta T_p = t_o (1 - K_m)(1 - e^{-2\tau_p}) \qquad \text{(III-8)}$$

where

t_o - thermodynamic temperature of the soil and vegeta-
tion

K_m - radiating capacity of the soil

Note that the term defined as radiating capacity is simply
the square of the absolute value of the Fresnel reflection
coefficient, so that $1-K_m$ is the emissivity of the soil
(based on the Peake approach). Calculations by Basharinov
and Shutko [78] based on this equation, show that the two
extreme model approximations for sparse vegetation produce
results that differ by two orders of magnitude.

Basharinov and Shutko [78] modeled a dense cover of
vegetation as a smooth homogeneous dielectric slab over a
smooth soil surface. An effective radiating capacity of
the vegetation-soil complex was calculated based on a two-
layer Fresnel reflection coefficient model. An increment of
radiating capacity resulting from the vegetation cover was
calculated by taking the difference between the effective
radiating capacity of the vegetation-soil complex and the
radiating capacity of the soil:

$$\Delta K = K_{ef} - K_m \qquad \text{(III-9)}$$

where K_{ef} is the effective radiating capacity of the vegeta-
tion-soil complex. The increment of brightness temperature
due to the vegetation is then calculated simply by:

$$\Delta T = t_o \, \Delta K \qquad \text{(III-10)}$$

Qualitative comparisons between the models of
Basharinov and Shutko [78] and experimental data indicate
that the general trends observed in the data are predicted.
Their primary results are:

1) Sparse vegetation of ten decimeters high has very
   little influence on emission in the centimeter
   and decimeter wavelengths,

2) As thickness, height and moisture content of
   the vegetation increase, the emission of the
   vegetation increases first in the centimeter wave-
   lengths and then extends into the decimeter wave-
   lengths, and

3) Dense green vegetation one meter high effectively
   shields emission of the soil, even in decimeter
   wavelength range.

Microwave Measurements

Individual scientists have acquired measurements of
emission and scattering of natural scenes as a function of
soil moisture over the last several years. There was little
organization to the effort until 1974 when the NASA
Johnson Space Center initiated the Joint Soil Moisture
Experiment. Due to the lack of organization, measurements
reported in the literature prior to that time were generally
acquired to answer specific questions of concern to

individual scientists. Measurement programs were not de-
signed to systematically acquire data that could be used to
determine the effects of individual scene parameters on the
ability to estimate soil moisture with microwave sensors.
As a result, data that are adequate to address this study
do not currently exist in the literature. However, the
available measurements do demonstrate the effects of soil
moisture, surface roughness, and vegetation on the emission
and scattering of soil.

Active Microwave Measurements

Measurements made by researchers at the University of
Kansas with ground-based systems during the last two to
three years demonstrate the radar response to soil moisture.
These measurements are used to illustrate the response of
radar signals to soil moisture and vegetation in the dis-
cussion below.

Bare soil - The response of radar backscatter to the
moisture in soil is demonstrated in Figure III-2 [79]. The
data presented in Figure III-2 were acquired from a field
with a surface rms height deviation of 2.5 cm at an incident
wavelength of 6.4 cm. Figure III-2 indicates that the
response of the normalized radar cross section, σ°, to
the effective soil moisture in a skindepth is fairly linear,
but with increasing sensitivity to soil moisture for

Surface Height -2.5 cm RMS

Frequency -4.7 GHz
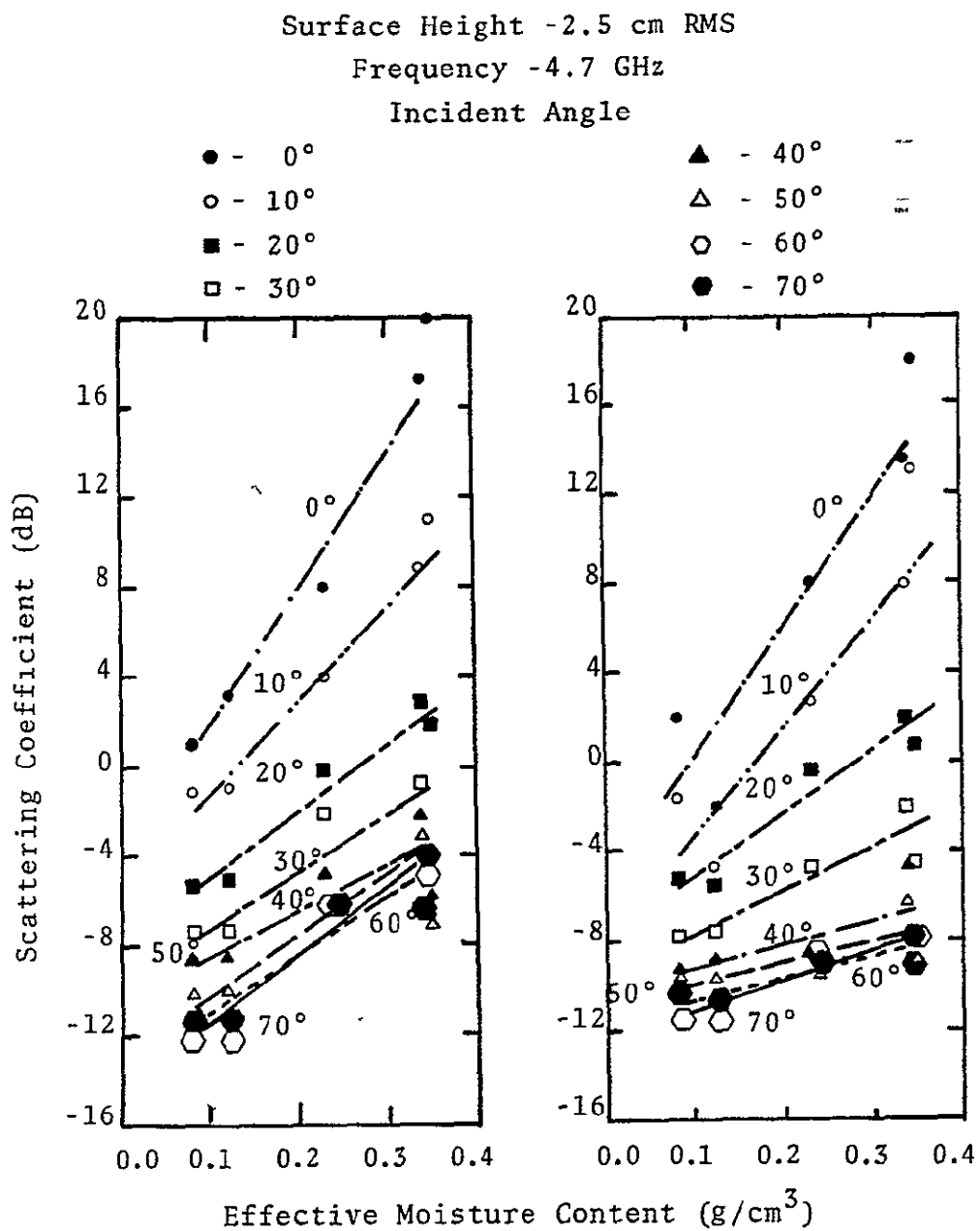
Incident Angle

Figure III-2. Scattering coefficient as a function of effective soil moisture content (after Ulaby et al. [79]).

decreasing incident angles. This variation of the sensi-
tivity of σ° to soil moisture with incident angle and
frequency is demonstrated in Figure III-3 [79]. From
Figure III-3 it is apparent that the sensitivity decreases
rapidly between nadir and the 20° incident angle and levels
off past 30° or 40°. In addition, the angular dependence
is more pronounced at 7.1 GHz as compared to 4.1 GHz. In
general, HH polarization exhibits better sensitivity than
VV polarization at the same frequency and incident angle.

Although σ° has a good response to soil moisture for
a single specific surface roughness, a scene with another
surface roughness may demonstrate a different response to
soil moisture for the same frequency and incident angle.
As surface roughness varies, the magnitude of σ° as well
as its sentitivity to soil moisture changes. Figures III-4
and III-5 demonstrate this effect for constant soil moisture
at 2.75 GHz and 7.25 GHz as a function of incident angle
[80]. Ulaby and Batlivala [80] performed an analysis to
determine the optimum radar parameters for soil moisture
detection and minimization of surface roughness effects of
bare soil. They concluded that the optimum radar parameters
are an incident angle range of 7° to 15°, a frequency of
about 4 GHz and either HH or VV polarization.

Vegetation - Ulaby [81] reports radar backscatter
measurements of corn, milo, soybeans and alfalfa. These
crops were planted using standard agricultural practices.
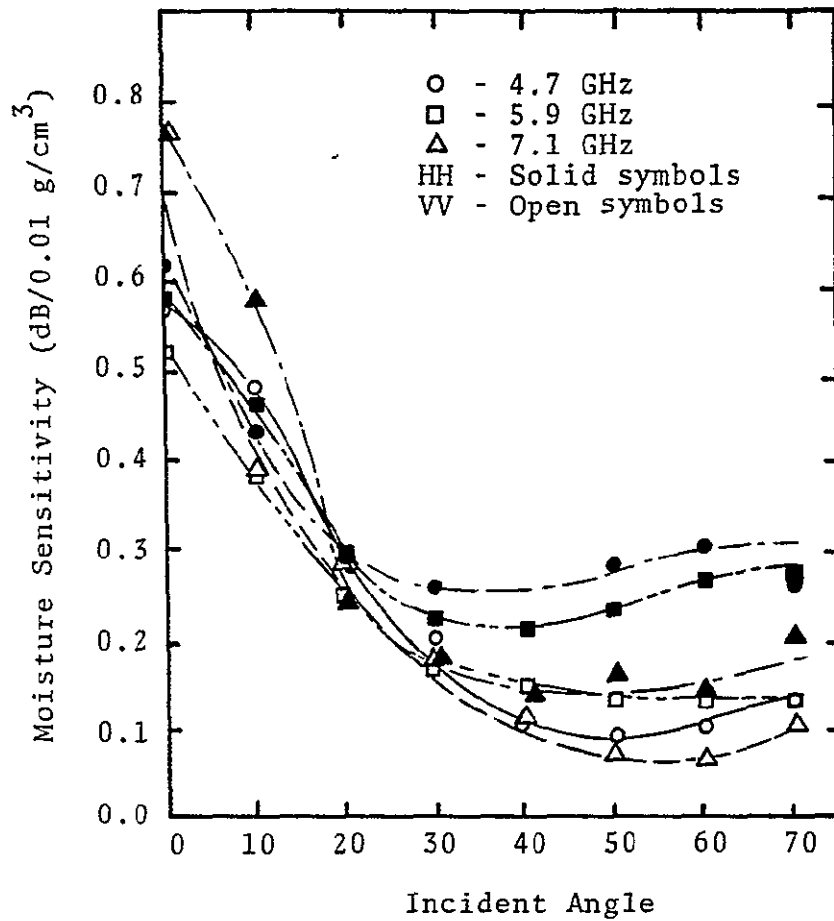
Figure III-3. Moisture sensitivity as a function of
              incident angle (after Ulaby et al. [79]).

Symbol	RMS Height (cm)	Soil Moisture (g/cm^3)
O --	0.88 ----	0.351
▽ --	2.6 ----	0.327
□ --	4.3 ----	0.306

Frequency - 2.75 GHz

Polarization - VV

Scattering Coefficient - σ° (dB)

Incident Angle
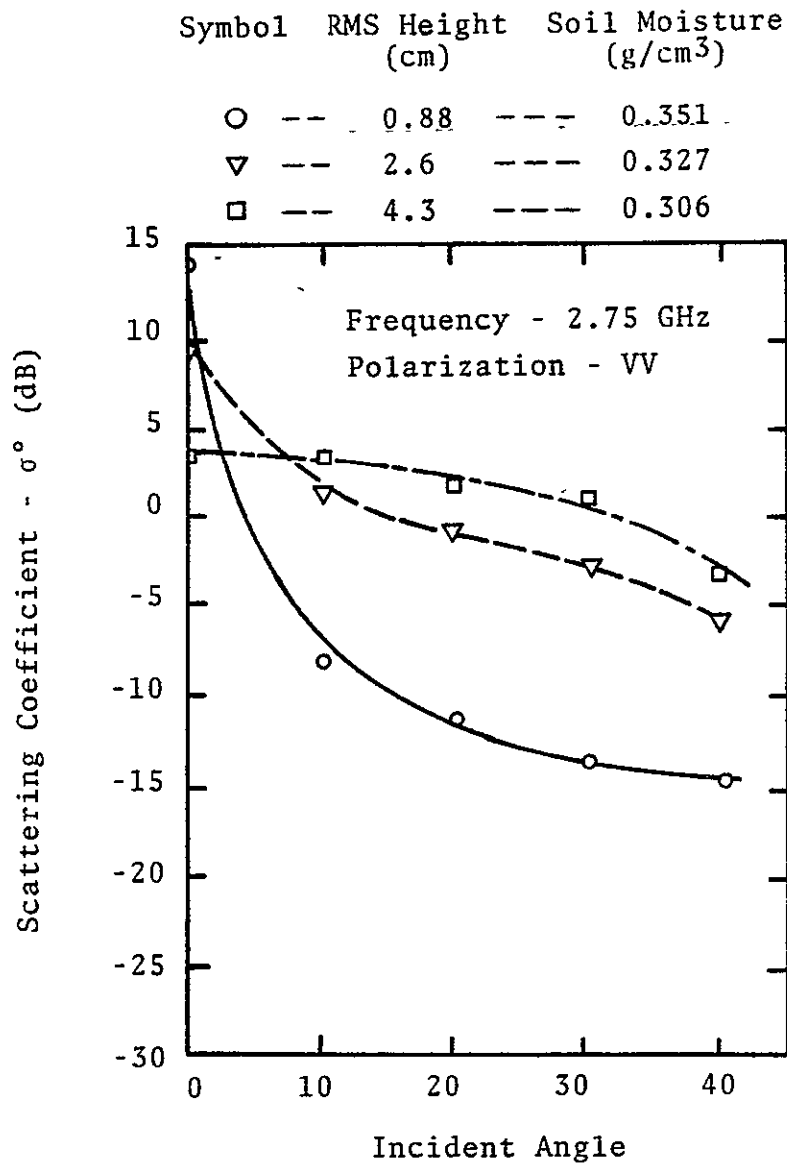
Figure III-4. Angular response for three bare fields with similar soil moisture but different surface roughness (after Ulaby and Batlivala [80]).

Symbol	RMS Height (cm)		Soil Moisture (g/cm³)
O	— —	0.88	— — — 0.335
▽	— —	2.6	— — — 0.344
□	— —	4.3	— — — 0.352

Frequency - 7.25 GHz

Polarization - VV

Scattering Coefficient - σ° (dB)

Incident Angle
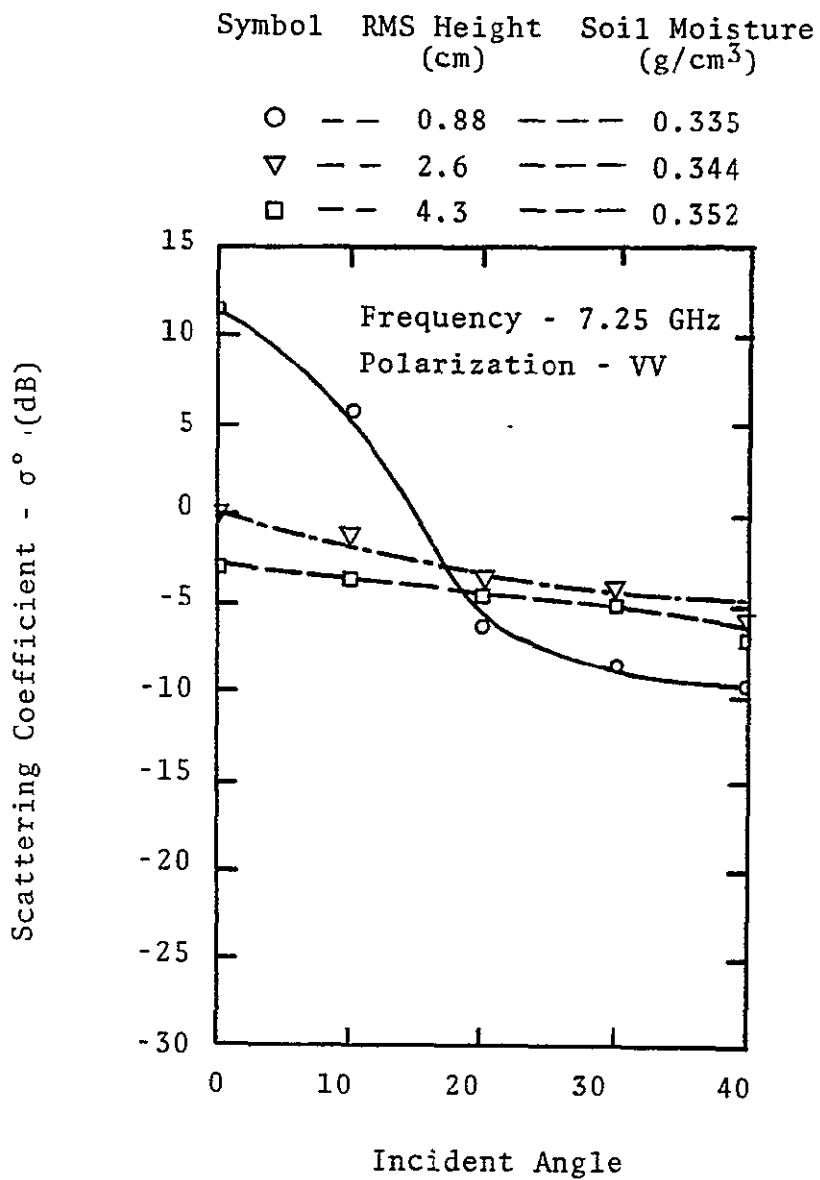
Figure III-5. Angular response for three bare fields with similar soil moisture but different surface roughness (after Ulaby and Batlivala [80]).

Data acquired at 5.9 GHz (Figure III-6) indicates that soil
moisture has a measurable effect on backscatter through
vegetation. The largest effect is at incident angles near
nadir. Ulaby points out that as the frequency is decreased,
the sensitivity to soil moisture increases slightly, and
as frequency is increased the sensitivity to soil moisture
decreases. Measurements of a uniform stand of very dense
sorghum indicate no response to soil moisture variations at
frequencies above 2.75 GHz [82]. However, the density at
which the measured sorghum field was planted was con-
siderably greater than would occur as a result of standard
agricultural practices.

Passive Airborne Microwave Measurements

Data reported by Jean [83] in 1971 at 1.42 GHz,
2.69 GHz, and 10.69 GHz over bare agricultural fields near
Weslaco, Texas demonstrate a definite dependence on the
soil moisture contained in the second and third centimeters
of soil. The data at 1.42 GHz demonstrated a linear
dependence on soil moisture, while the data at 2.69 GHz
and 10.69 GHz demonstrated a nonlinear dependence. This
nonlinear dependence is characterized by a small change
in measured antenna temperature per percent soil
moisture for moistures less than 20 percent soil moisture
by weight, and a large change in antenna temperature per
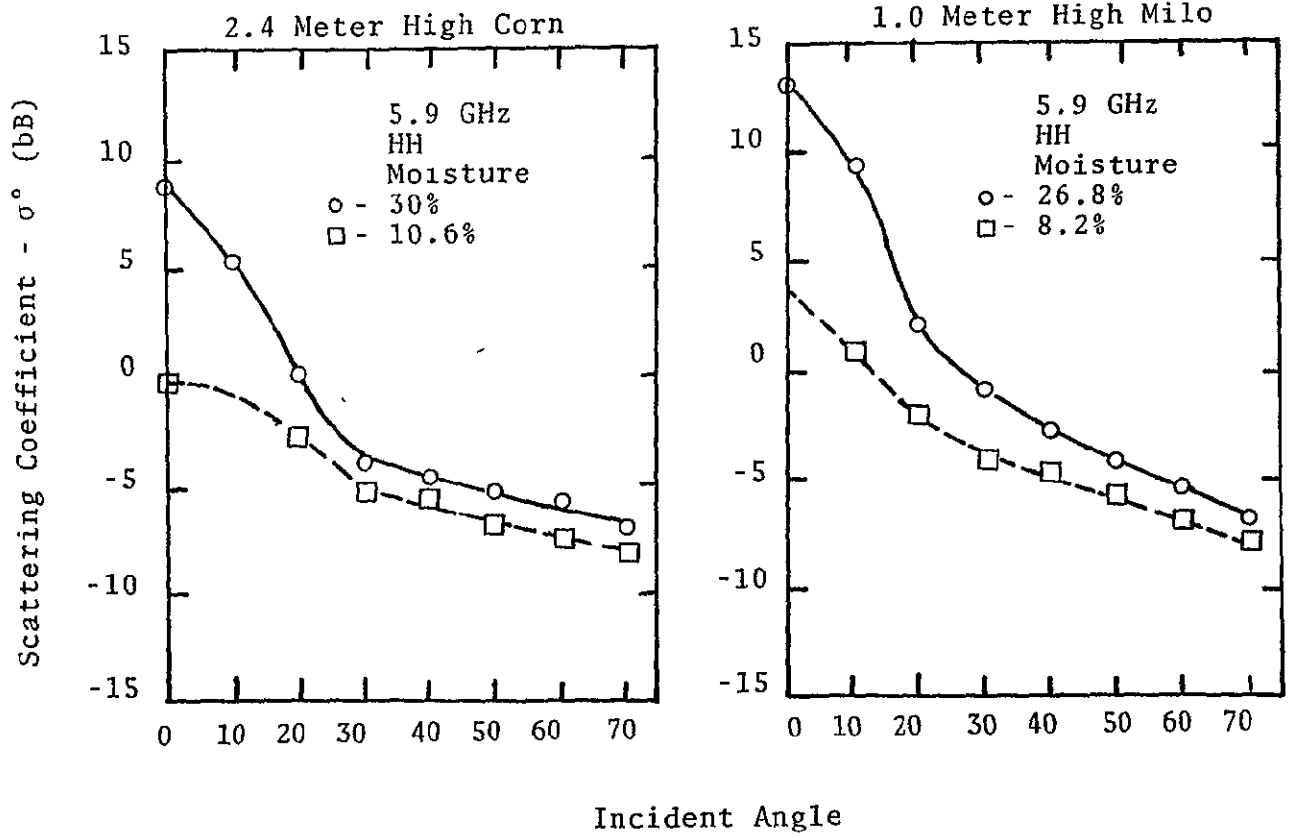
Figure III-6(a). Scattering coefficient measured at 5.9 GHz for low and high soil moisture conditions (after Ulaby [81]).
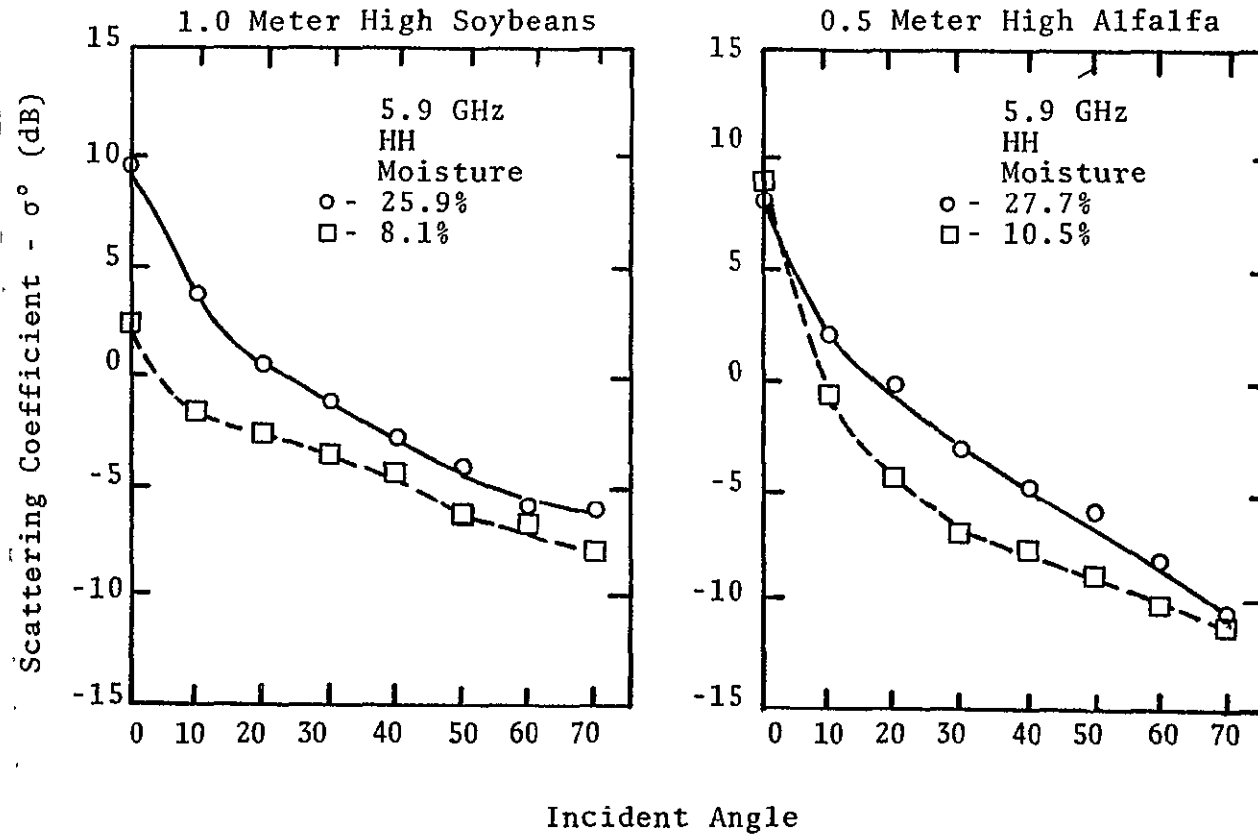
Figure III-6(b).   Scattering coefficient measured at 5.9 GHz for low and high soil moisture conditions (after Ulaby [81]).

percent soil moisture for moistures above 20 percent.
Although effects of soil texture, soil density, physical
temperature differences between fields and surface rough-
ness were not considered in Jean's analysis, he estimated
that soil moisture could be measured to an accuracy of 5
to 10 percent by weight under ideal conditions. Kroll
[84] compared measurements over Chickasha, Oklahoma and
Weslaco, Texas acquired in 1973 to Jean's measurements with
comparable results.

Schmugge et al. [85] reports data in 1972 and 1973
acquired at an agricultural test site in Phoenix, Arizona at
19.4 GHz and 1.42 GHz. Figure III-7 compares the response
of the 19.4 GHz radiometer to soil moisture in the top
centimeter of soil for light soils (sandy loam and loam)
and heavy soils (clay loam). Although there is a linear
decrease of antenna temperature with soil moisture, the
depression of antenna temperature for a given moisture
content is less for heavy soils than for the light soils.
This is apparently a result of the fact that the clay
soils maintain a higher percent soil moisture than the loam
soils for the same matric potential. The details of this
explanation were contained in Chapter II. Since field
capacity is related to matric potential, the difference in
the antenna temperature variations between the heavy
and light soils can be accounted for by plotting brightness
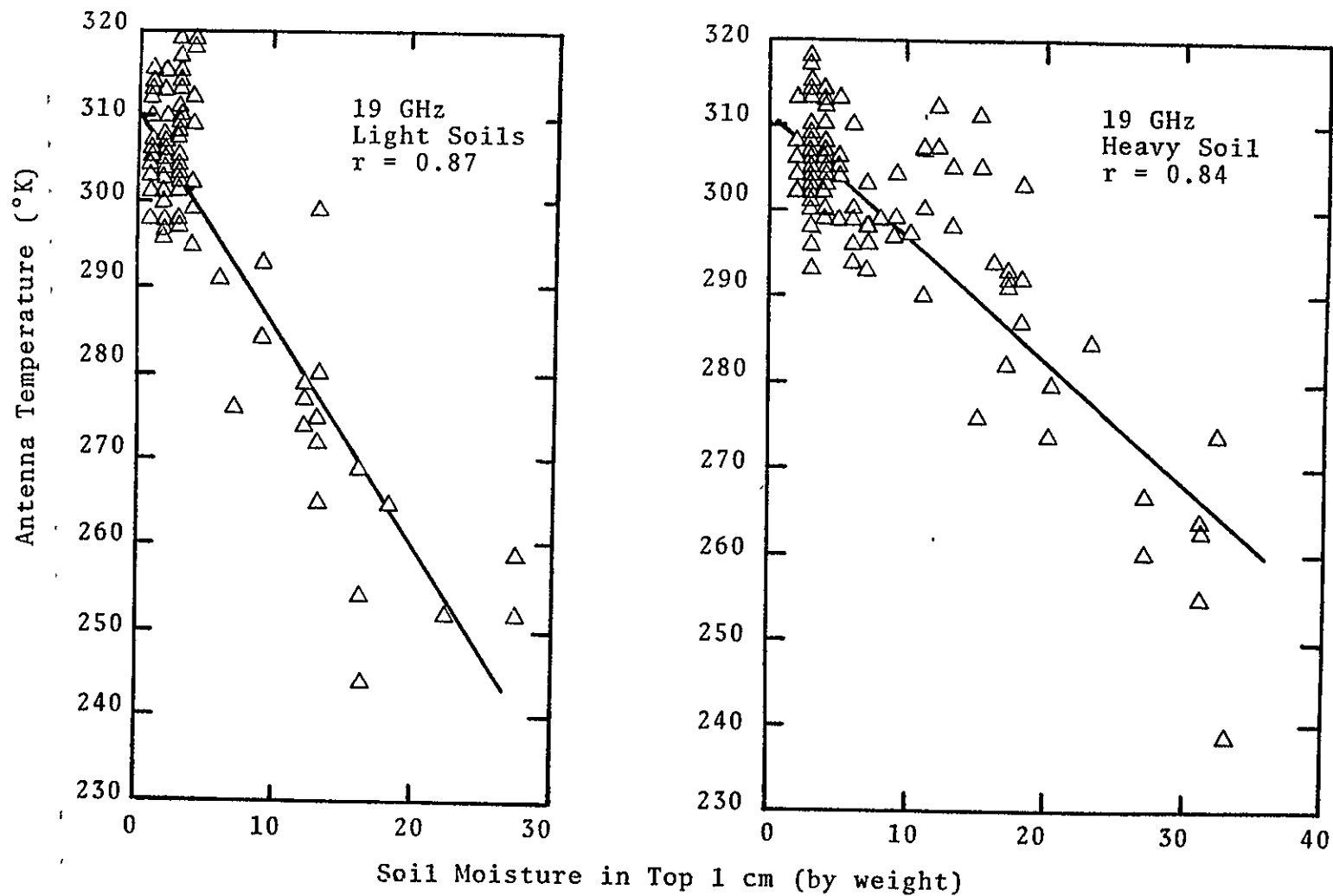
Figure III-7. Plot of 19 GHz measured antenna temperature versus soil moisture for light soils (sandy loam and loam) and heavy soils (clay loam) (after Schmugge et al. [85]).

temperature as a function of percentage field capacity instead of soil moisture (Figure III-8).

Schmugge et al. [85] shows that similar linear behavior is observed for the antenna temperature obtained with the 1.42 GHz radiometer when plotted as a function of percentage field capacity in the top centimeter (Figure III-9). However, when antenna temperature is plotted versus percentage field capacity in the top 2.5 cm layer, there appears to be a "flat region" out to about 50 percent field capacity where the linear decrease begins (Figure III-10). The flat region extends out even further when the antenna temperature is compared to the percentage field capacity of the top 5 cm of soil. These results lead Schmugge et al. to conclude that the 1.42 GHz radiometer was primarily responding to soil moisture in the top 1 to 2 centimeters of soil.

Schmugge et al. [86] reported the results of the first aircraft experiment that was flown as part of the currently on going Joint Soil Moisture Experiment that is being sponsored by the NASA Johnson Space Center. This experiment was flown in April, 1974, at the agricultural test site in Phoenix, Arizona using radiometers operating at 10.69 GHz and 1.4 GHz. The purpose of the experiment was to obtain data to quantify the effects of nonuniform vertical distribution of moisture, surface roughness, and soil type. The radiative transfer model described by Burke and Paris [32] was utilized in the analysis of these data.
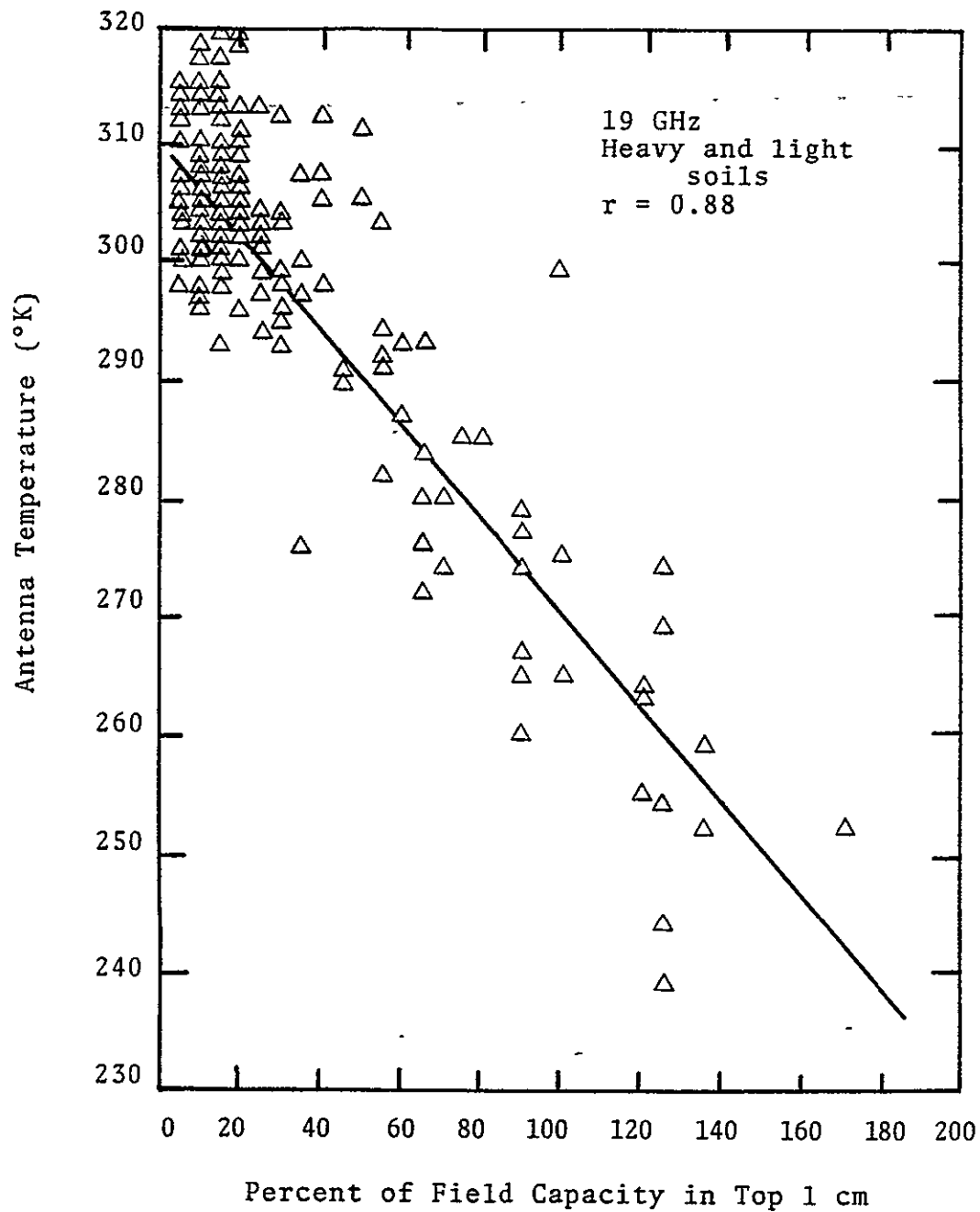
Figure III-8.   Plot of 19 GHz measured antenna temp-
                erature versus soil moisture in top 1 cm
                expressed as percent field capacity
                (after Schmugge et al. [85]).
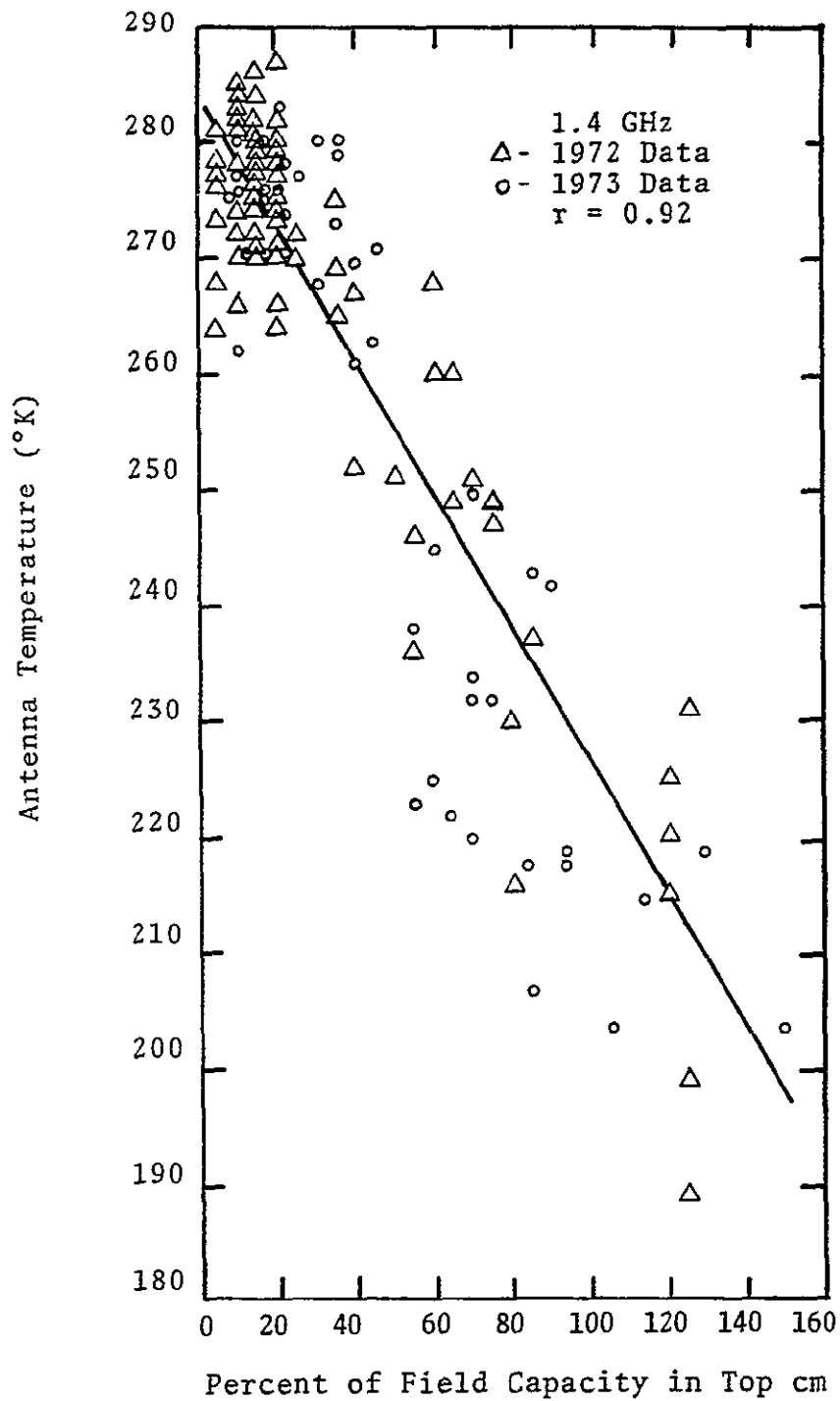
Figure III-9. Plot of 1.4 GHz measured antenna temperature versus soil moisture in top 1 cm expressed as a percent of field capacity (after Schmugge et al. [85]).
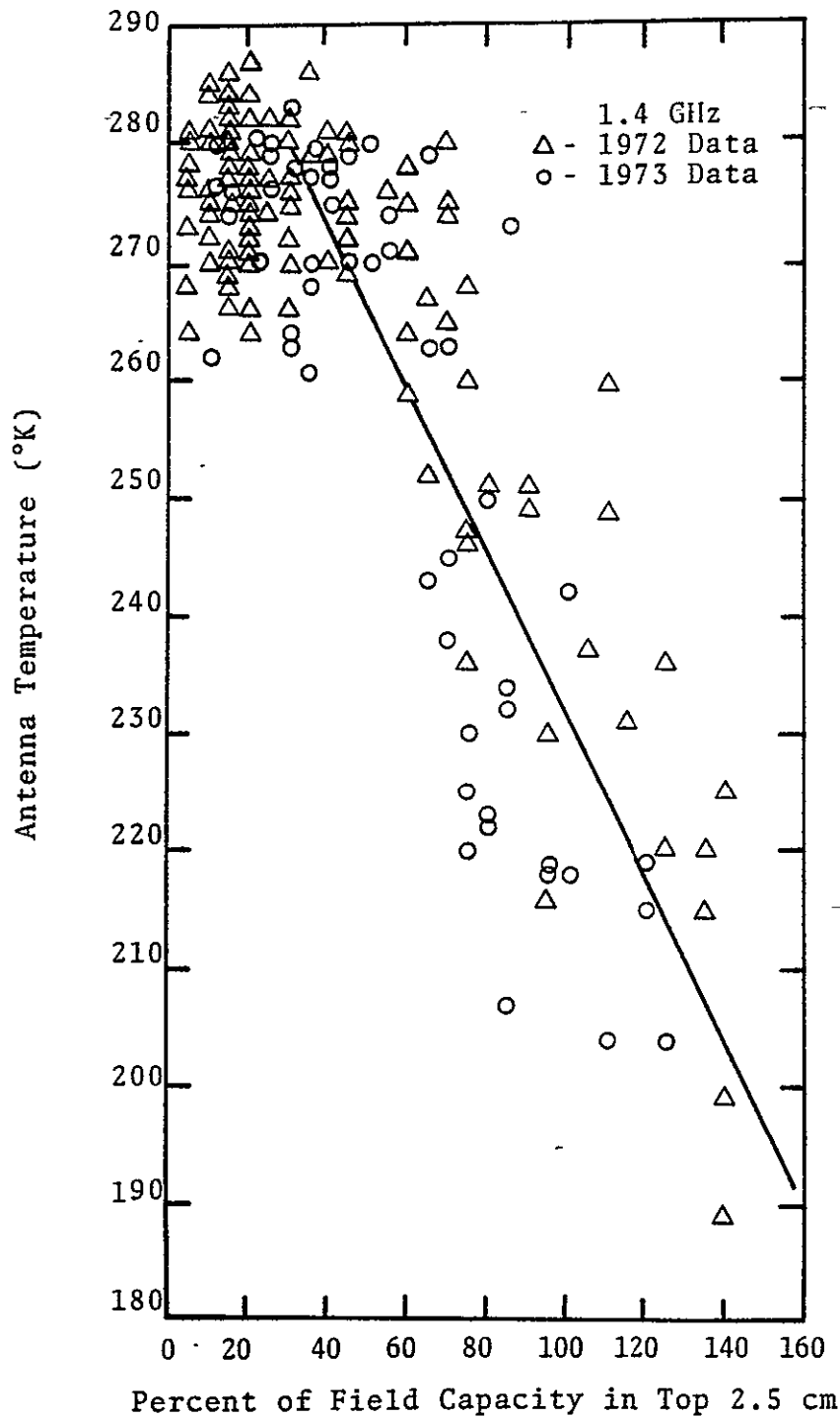
Figure III-10. Plot of 1.4 GHz measured antenna temperature
versus soil moisture expressed as a percent
of field capacity in the top 2.5 cm (after
Schmugge et al. [85]).

X-band data were acquired at an incident angle of 49°. L-band data were acquired at 40° incidence. Since the Burke and Paris [32] radiative transfer model is a smooth surface model, and since most of the Phoenix fields were listed, Schmugge et al. [86] assumed that the primary effect of surface roughness was to change the effective look direction of the antenna. With this assumption, Schmugge et al. concluded that surface roughness effects can be separated by comparing two parameters; a parameter denoted by P which is one-half of the sum of the vertical and horizontal apparent antenna temperatures, and a parameter denoted by Q which is the difference of the vertical and horizontal apparent antenna temperatures. These parameters are the first two Stokes parameters, where P is related to intensity of emission and Q is related to the polarization of the emission. Schmugge et al. also concluded that the microwave signature of the surface rewetting effect described by Jackson [87] is an increase in the polarization of emission. This conclusion was based on the fact that the Q observed at dawn was greater than that observed at midday for the same fields at 10.69 GHz. In addition, they concluded that the L-band radiation comes from much deeper in the soil than the X-band radiation. However, they further concluded that surface soil moisture (0-2 cm) dominates over the subsurface soil moisture gradient at both frequencies.

Passive Ground-Based Measurements

Measurement programs utilizing ground-based radio-
meters have been performed for a number of years for the
purpose of basic research in several areas. They include
programs executed by researchers at the Aerojet-General
Corporation, Jet Propulsion Laboratory, and Texas A&M
University, who performed ground-based experiments to
acquire data to determine the relationship between radia-
tion from soil and soil moisture. Results of these measure-
ment programs are described below.

Bare soil - Richerson [34] and Jean et al. [88] re-
ported measurement of coarse sand made at 31.4 GHz at
Texas A&M University in 1971. Comparison of measurements
of smooth sand, made immediately after wetting, to theoretical
predications were satisfactory. However, measurements made
of the same scene an hour after irrigation had a much less
well defined relationship to soil moisture. This problem
was a result of the formation of a dry layer above the
wet subsurface. Measurements of wet rough sand were less
sensitive to soil moisture than measurements of the smooth
sand.

Other measurements demonstrating the effect of soil
moisture layering are reported by Blinn and Quade [89],
and Blinn et al. [90]. Their measurements demonstrate the
effect of varying the depth of a very sharply defined dry

layer of sand over a wet layer of sand. It is shown that
such a worst case soil layering situation can cause the
emission to oscillate as the depth of the layer is varied
(Figure III-11). In addition, Blinn and Quade demon-
strated the depth of penetration of 1.4 GHz, 10.69 GHz
and 31.6 GHz emission for a number of sands and gravels
as a function of particle size and moisture content. Figure
III-12 shows the penetration depth for sand as a function
of moisture and frequency. The depth of emission at 1.4 GHz
is shown to be greater than 15 cm for dry sand and from
5 to 7 cm for wet sand (15 percent moisture by weight).

Lee [91] and Newton et al. [92] reported measure-
ments of bare smooth and rough soil surfaces as a function
of soil moisture. These measurements were made at 1.4 GHz
and 10.6 GHz with the sensor described in Chapter V. Their
measurements demonstrate that surface roughness decreases
the sensitivity of the emission to soil moisture. As shown
in Figure III-13, the emission from dry soil is approximately
independent of surface roughness. However, for wet soil
the emission is greater from the rough surface. This
phenomenon is also evident in measurements made by Blinn
and Quade [89] of smooth and raked sand (Figure III-14).

Poe et al. [93] report a series of measurements
made at 37 GHz, 13.6 GHz, 5.0 GHz and 1.4 GHz of bare soil
in Tempe, Arizona. These measurements further demonstrate
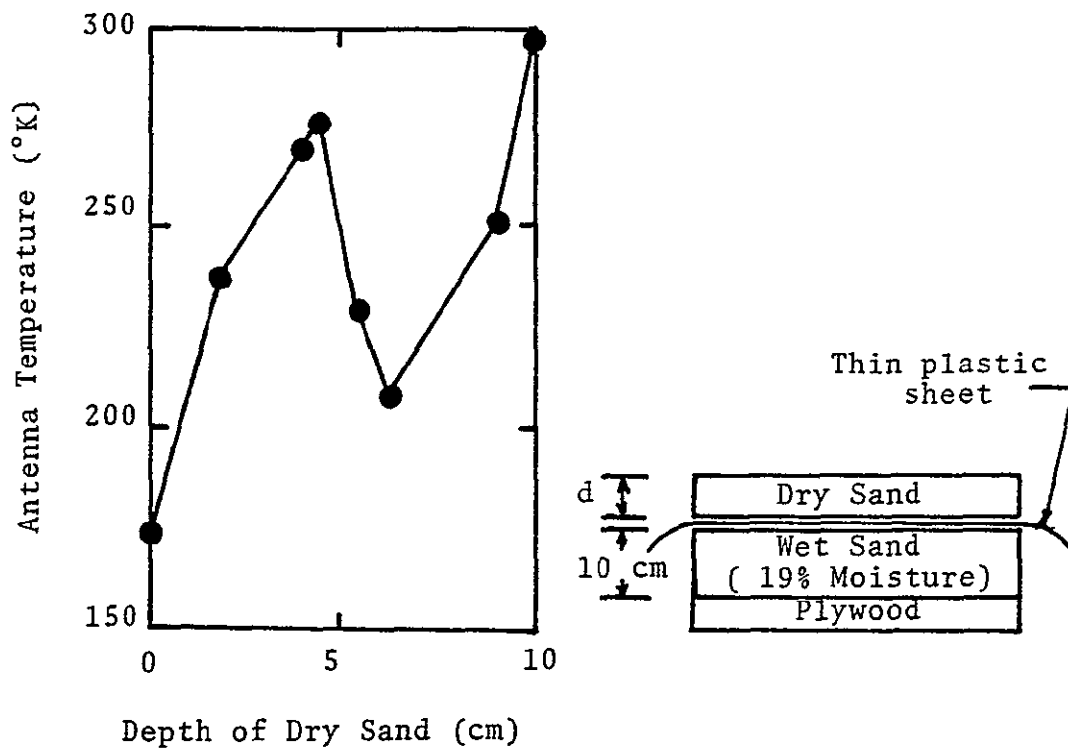
Figure III-11. The 21 cm response for dry and overlying wet sand (after Blinn et al. [90]).
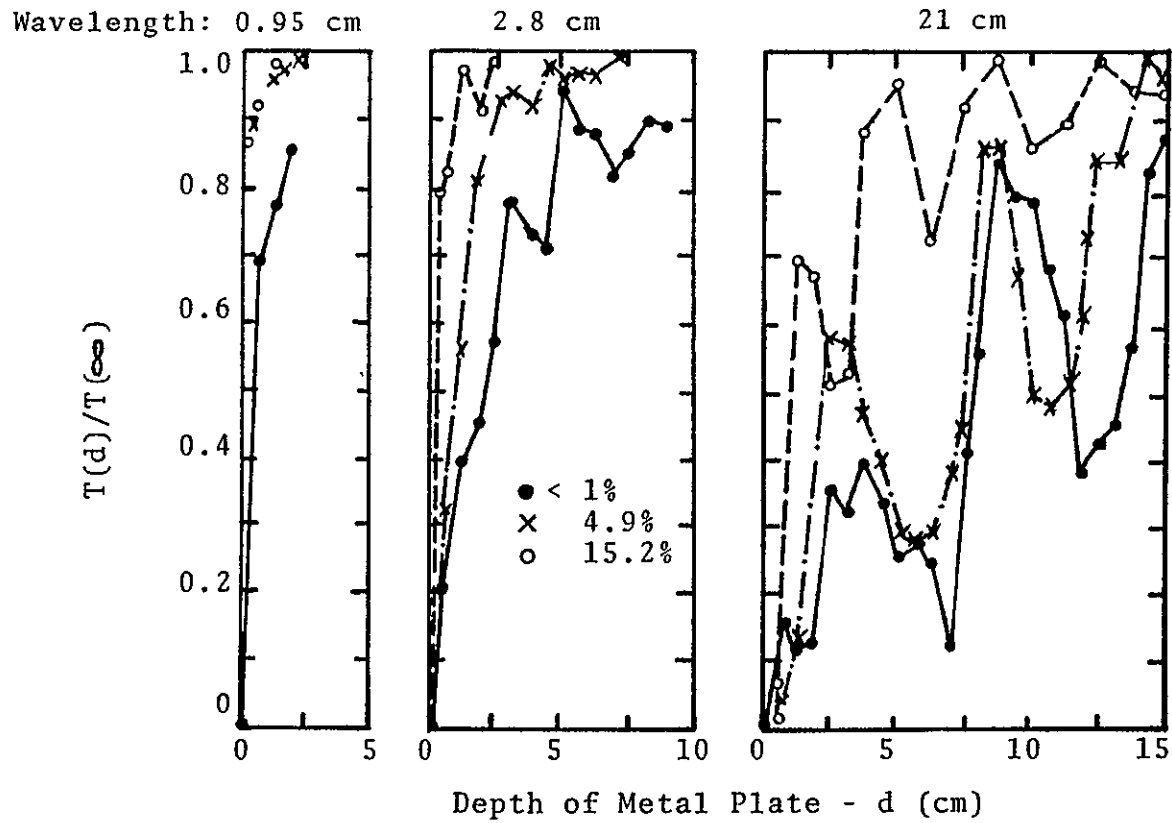
Figure III-12. Plate measurements of moist sand (after Blinn et al. [90]).
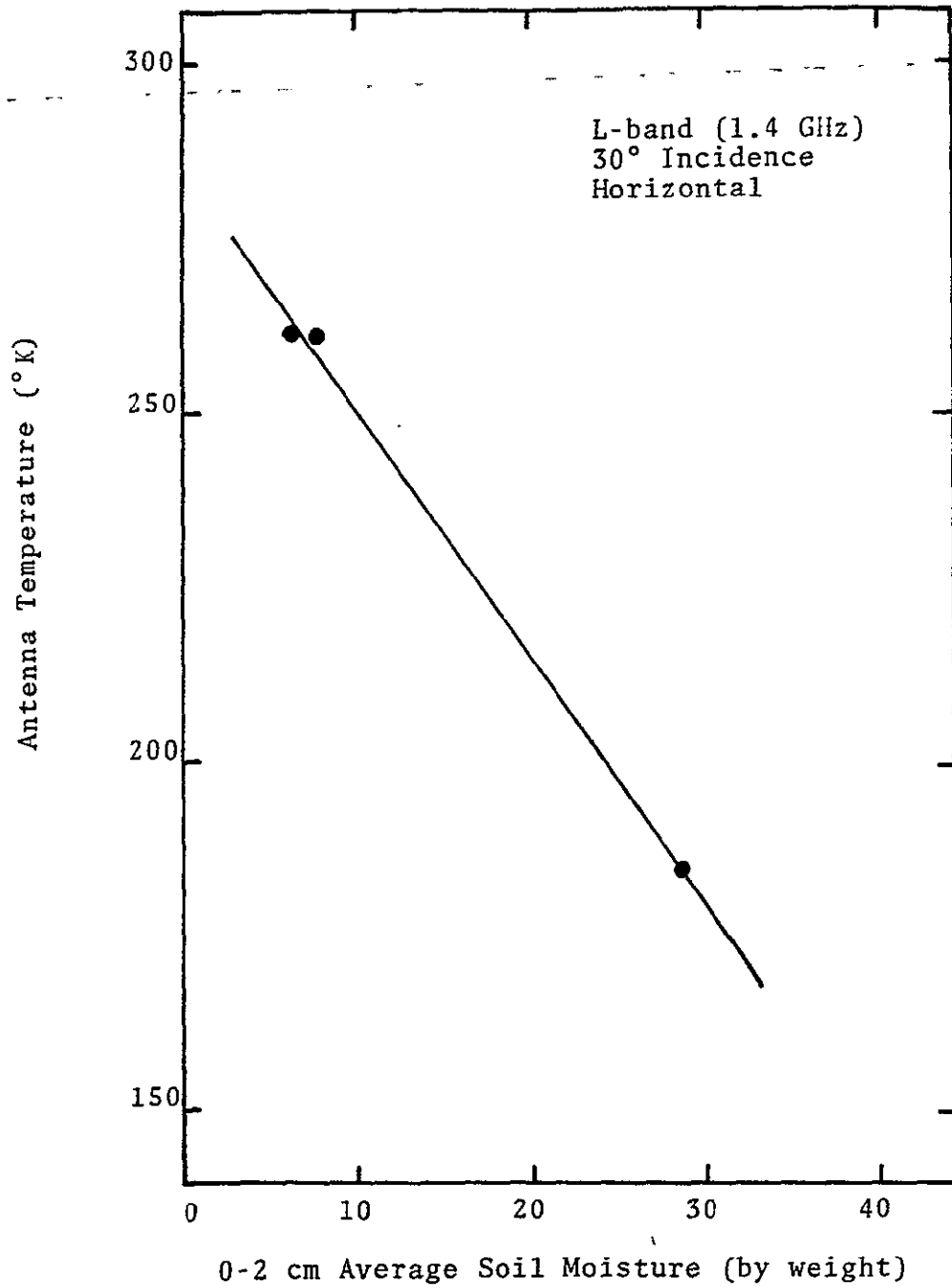
Figure III-13. Antenna temperature versus soil moisture for a smooth bare field (after Lee [91]).
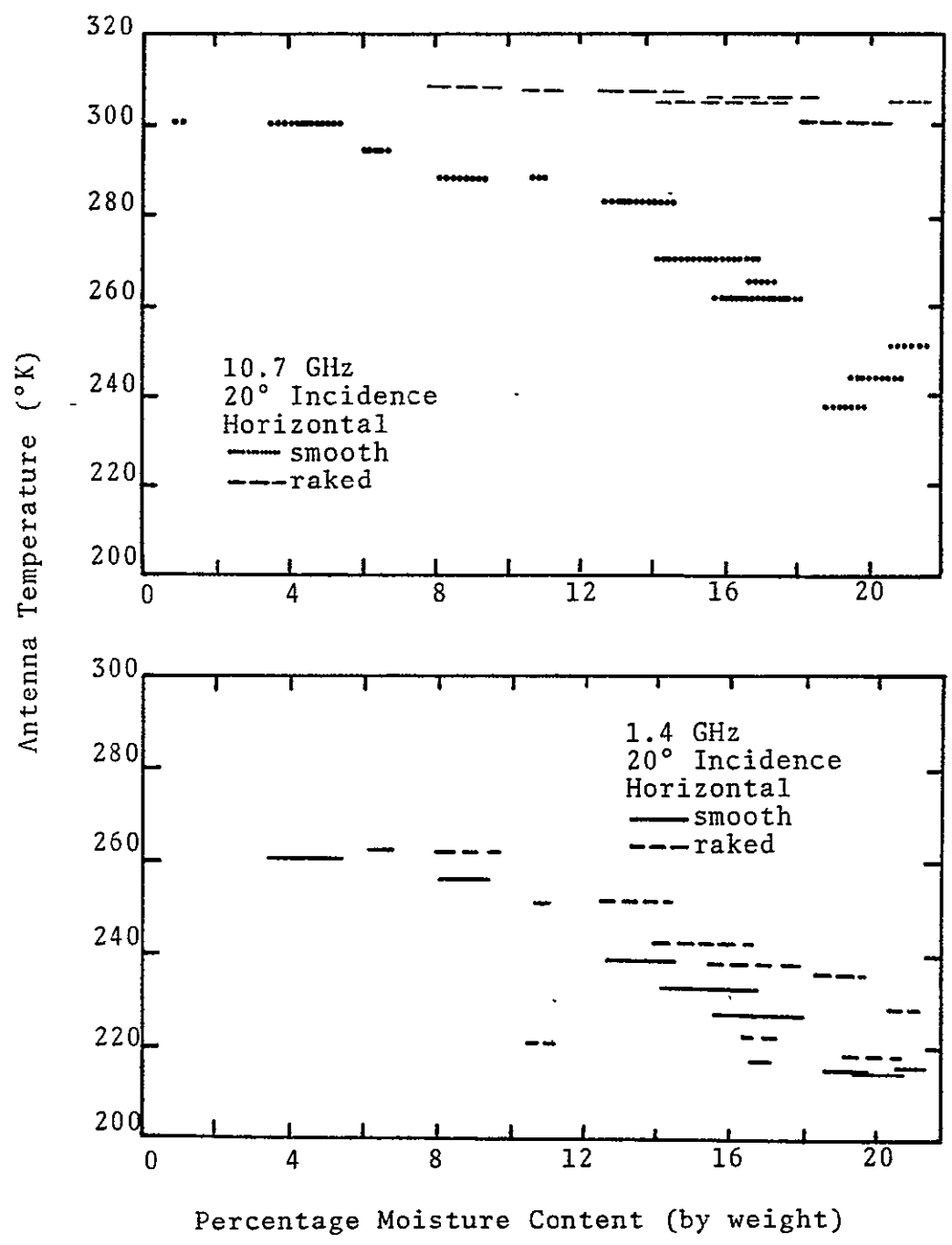
Figure III-14. Moisture effects for smooth and rough junction sand (after Blinn and Quade [89]).

that the lower frequencies have a greater sensitivity to soil moisture than the higher frequencies, and that the sensitivity for horizontal polarization is greater than for vertical polarization. An algorithm is presented which permits a calculation of the vertical profile of the total volume of water per unit area using measured horizontally polarized antenna temperature which have been normalized by the surface soil temperature. The model is based on the intuitive feeling by the authors that it is the total mass of water per unit area lying between the surface and the skindepth which determines the·brightness temperature, rather than the specific details of the distribution of moisture. Although the model produced reasonable results for very wet soil conditions, it produced poor results for dry conditions. Generally, soil moisture distribution with depth is fairly uniform for wet conditions. The poor estimates produced by the algorithm for dry conditions indicates that the basic assumption made by Poe et al. that the soil moisture distribution has a minimal effect is invalid.

Vegetated soil - Very few ground-based passive microwave measurements of vegetated soil have been published in the literature. Riegler [94] reports limited measurements of alfalfa, oats and wheat using passive and active microwave systems at X-band. The data are, however, too sparse to

draw any conclusions concerning the effect of vegetation on the ability to remotely measure soil moisture. Lee [91] and Newton et al. [92] also report measurements of vegetated smooth and rough surfaces. The vegetation used in these studies was 0.4 meter high oats planted in a uniform cover. Lee's results show that the vegetation acted as an attenuator at 1.4 GHz, and that it exhibited a masking effect at 10.63 GHz regardless of the surface roughness. Although the vegetation acted as an attenuator at 1.4 GHz, the soil moisture dependence was only slightly affected. In addition, good agreement was found between the vegetation model developed by Sibley [75] and experimental results.

Applicability of Published Literature

A considerable number of authors have reported either airborne or ground-based passive microwave measurements, however, a review of these measurements show that they are disjoint in terms of the scenes measured and the frequencies and incident angles utilized. Many of the measurements are useful for comparing the effects of specific combinations of scene and sensor parameters. However, there are too few microwave measurements reported in the literature to be of use in any systematic analysis of soil emission to determine the effects of volume inhomogenities, surface roughness and vegatative cover.

CHAPTER IV

MODELS

Introduction

Chapter III contains a review of previously published
approaches to modeling the soil-vegetation complex.   In
that review the scene was decomposed into three categories;
the soil volume, the surface and the vegetation cover.
This same approach to modeling the soil-vegetation complex
will be used in this chapter. The rationale, development
and interpretation of the models used to describe each
scene component in this study will be given, as well as
the rationale for choosing the models.

Only models that describe emission from the soil-
vegetation complex are discussed. This radiation will be
termed brightness temperature. The total emission from
a scene consists not only of the brightness temperature
of the scene, but also of emission from several other
sources (Figure III-1). These components include thermal
microwave emission of the intervening atmosphere between
the scene and measurement system, emission of the sky
reflected from the scene into the receiving antenna

aperture, manmade sources and reflections of point sources
such as the sun into the receiving aperture. The total
emission from a scene will be termed the apparent tempera-
ture of the scene. A radiometer responds to the apparent
temperature of a scene and will be termed antenna tempera-
ture. Although most of the components of the apparent
temperature of a scene may be considered negligible in many
cases, they must sometimes be considered when comparing
antenna temperature measurements to model predictions of
scene brightness temperature. Such a comparison will be
left to Chapter VI.

The model presented to describe the brightness tempera-
ture of the soil-vegetation complex is a composite of three
individual models. Certain assumptions are required in
order to use these individual models in conjunction with
one another as a model of the composite soil-vegetation
complex. For instance, the soil volume will be modeled
by assuming that it is composed of horizontally homogeneous
layers. However, this model will be used in conjunction
with an independent model of the surface. As a result,
an assumption must be made concerning the location of the
reference datum that will describe the planar top layer of
the soil volume model. The mean surface height will be

used as this reference datum (Figure IV-1). A similar
assumption must be made for the interface between the
vegetation model and the surface model. In fact, the
same reference datum will be used for this interface as
shown in Figure IV-1.

Soil Volume

Model Description

Modeling options - It was pointed out in Chapter III
that the classical approach to modeling the emission from
soil has been the Peake approach [29]. This approach re-
lates the emissivity of a scene to the integral of the
differential scattering coefficients defined for the top
side of the surface. As a result, the Peake approach re-
sults in a composite model of the soil volume and soil
surface. It cannot be used to model the soil volume
independently of the soil surface. In addition, the
Peake approach is a special case of a more general formu-
lation (as is shown in the next section) and is only
strictly valid for uniform soil moisture and uniform soil
temperature profiles.

Stogryn [30] derived a general formulation for the
emitted radiation intensity of a volume. Stogryn's only
assumptions were that the volume was horizontally uniform
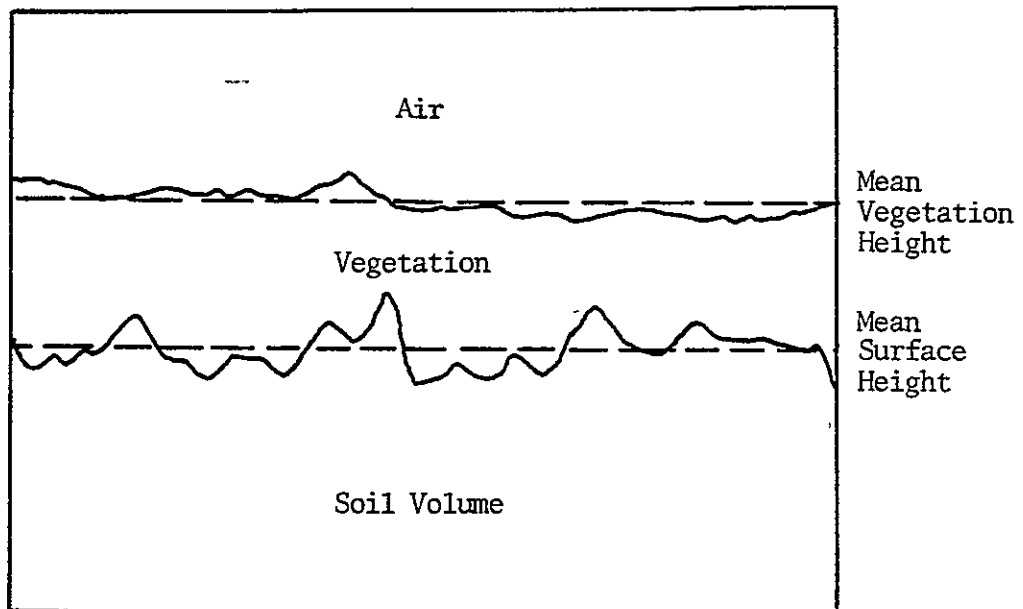
Figure IV-1. Soil surface and vegetation surface
reference datums.

and had a smooth surface. Stogryn points out that the number of permittivity profiles for which explicit, exact or even approximate solutions can be obtained using this formulation is very limited. Stogryn outlines a numerical procedure for evaluating his formulation for arbitrary permittivity variations. However, he noted that "this approach requires a considerable amount of computation which is not directly related to the desired results" [30]. In addition, Stogryn states that "such a procedure can be expected to consume a large amount of time on a high speed digital computer when results are required for a number of angles." More importantly this approach does not provide results that can be interpreted in terms of a single parameter related to the soil moisture profile.

For the case where permittivity varies slowly with depth, Stogryn [30] and Tsang et al. [31] demonstrate that their formulation is identical to the integral radiative transfer equation for a semi-infinite, plane, non-scattering, stratified volume in thermodynamic equilibrium. Further, the radiative transfer approach to modeling the emission from a layered horizontally plane homogeneous soil volume approaches Stogryn's exact solution as the layers become infinitely thin.

Ground data measurements of soil moisture and soil temperature profiles made in /support of the microwave emission measurements reported in Chapter V could only be obtained for specific depth increments. As a result, the soil permittivity profiles used in conjunction with a model of emission from a soil volume will be assumed to be piecewise continuous. This assumption eliminates the advantage of using an exact formulation, such as those by Stogryn [30] and Tsang et al. [31], to model the radiation intensity emitted from the soil volume. A radiative transfer approach will be adequate.

Radiative transfer equations - England [43] demonstrated that scattering within the soil volume had negligible effects on the emission of moist soil. As a result the radiative transfer approach of Burke and Paris [32] is adequate to effectively model the radiation intensity emitted by a soil volume.

The basic derivation of the Burke and Paris [32] approach will be reviewed in order to demonstrate the assumptions underlying the model. The soil volume is modeled as a horizontally plane stratified medium with each layer consisting of a non-scattering homogeneous soil (Figure IV-2). Soil permittivity and soil temperature are assumed to be constant across any given layer of soil. The soil surface and the layer interfaces are assumed to be
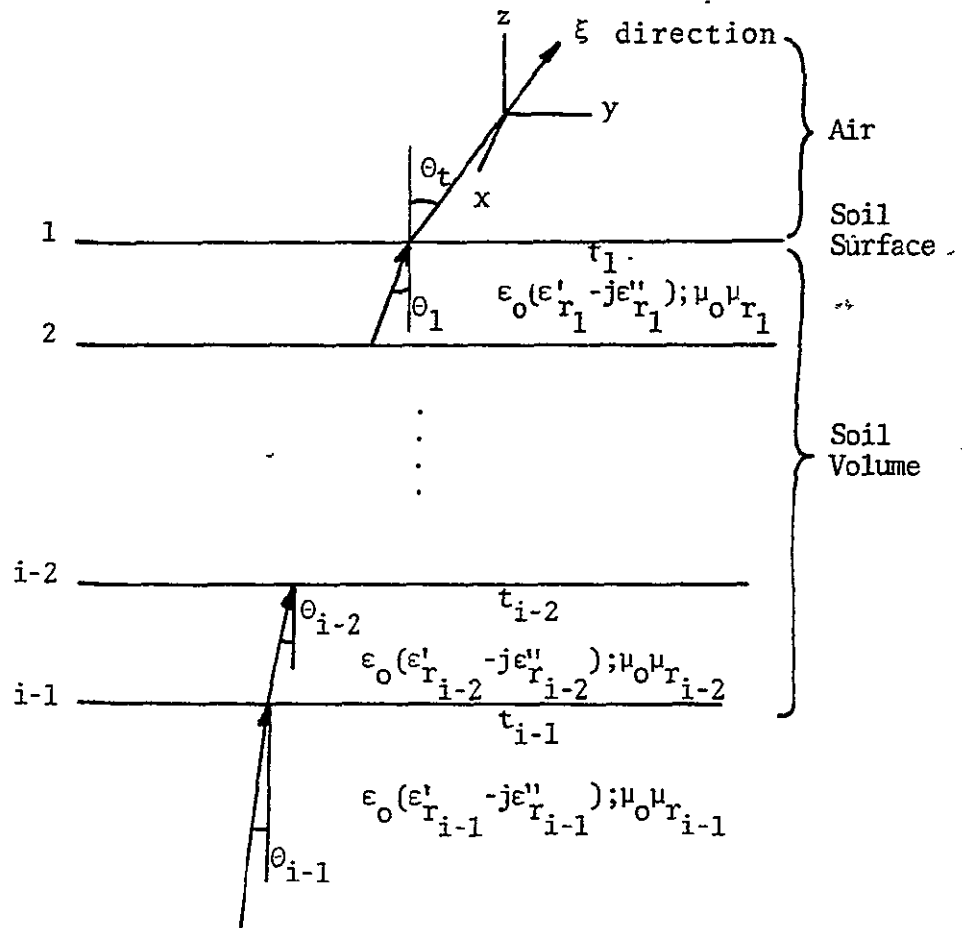
t_i - physical soil temperature of each layer

ε_o - permittivity of free space

μ_o - permeability of free space

$\varepsilon'_{r_i} - j\varepsilon''_{r_i}$ - relative permittivity of each layer

μ_{r_1} - relative permeability of each layer (≈ 1.0)

Figure IV-2. Soil volume geometry used in the radiative transfer model of soil emission.

smooth. The power intensity transmitted across each layer
interface can be calculated in terms of the Fresnel trans-
mission coefficients.

The transfer of radiation within the soil volume is
described by the basic equation of radiative transfer as
given by Chandrasekhar [95].

$$\frac{d\, I_\omega(z)}{d\, z} = -\gamma_\omega(z)\, I_\omega(z) + \gamma_\omega(z)\, I_\omega(z) \tag{IV-1}$$

In (IV-1) $I_\omega(z)$ is the intensity of the radiation propa-
gating upward as denoted in Figure IV-2. It is only
dependent on the z coordinate since each layer is uniform
in x and y. $J_\omega(z)$ is the radiation source function of the
soil. It is constant within each layer and is given by
Planck's emission law as noted below. Both $I_\omega(z)$ and
$J_\omega(z)$ are power intensities and have units of watts per
m^2 steradian. The subscript ω denotes dependence on
frequency.

$\gamma_\omega(z)$ is the power absorption coefficient of the soil.
It is also constant within each layer and is dependent on
frequency. Generally, $\gamma_\omega(z)$ is given as the mass absorp-
tion coefficient times the density of the medium. For a

non-scattering media, it is

$$\gamma_\omega (z) = 2 \alpha (z) \quad .$$

$(IV-2)$

where $\alpha(z)$ is the electric field attenuation coefficient.

Goody [96] has shown that the emission of a body is Planckian if the population of energy levels is due primarily to collisions among molecules. Therefore, even without the restriction of local thermodynamic equilibrium, the source function is given by Planck's emission law:

$$J_\omega (t) = \frac{2 h \nu^3}{c^2} \left(\frac{1}{e^{h\nu/kt} - 1} \right)$$

$(IV-3)$

where

    h - Planck's constant (6.63×10^{-34} Joule-second)

    k - Boltzman's constant (1.38×10^{-23} Joule/°K)

    c - speed of light

    t - temperature

    ν - frequency

For microwave frequencies it can be shown that the source function given by (IV-3) is directly related to the temperature of the medium. At microwave frequencies $h\nu/kt \ll 1$. Expanding the second term of (IV-1) and neglecting terms above the first order yields:

$$J_\omega(t) = \frac{2h\nu^3}{c^2}\left[\frac{1}{(1+\frac{h\nu}{kt})-1}\right]$$
(IV-4)

or

$$J_\omega(t) = \frac{2kt}{\lambda^2}$$

where free space wavelength is given by

$$\lambda = \frac{c}{\nu}$$

The result of (IV-4) is generally known as the Rayleigh-Jeans approximation [95]. Equation (IV-4) describes the total radiation energy. Assuming random polarization, this energy can be divided equally into orthogonal polarization states:

$$J_\omega(t)_v = J_\omega(t)_h = \frac{kt}{\lambda^2}$$
(IV-5)

where

v - vertical polarization

h - horizontal polarization

The source function in (IV-1) is directly related to the temperature of the medium. It is therefore reasonable to define an effective temperature of emission, T_e, that is directly proportional to $I_\omega(z)$. $I_\omega(z)$ and T_e are polarization dependent, however.

Subscripts denoting polarization will be suppressed in the following equation development and the energy in each polarization state will be assumed to be uncorrelated. Adopting this terminology and considering a narrow range of frequencies near ω and one polarization, (IV-1) can be rewritten as

$$\frac{d T_e(z)}{d z} = -2\alpha(z) T_e(z) + 2\alpha(z) t(z) \qquad \text{(IV-6)}$$

where

T_e - effective temperature of emission at one polarization

t - temperature of the medium

For the horizontally homogeneous plane stratified medium defined in Figure IV-2; α, T_e, and t are all constant for a given layer.

Since electrical properties of the soil volume have been defined to be piecewise continuous in depth, (IV-6) can only be evaluated within individual layers. The discontinuities at each interface must be handled separately. The effective temperature of emission within a layer can be obtained by integrating (IV-6) over the layer thickness. For the first layer (IV-6) is integrated from a point just below the surface to a point just above the second interface. This integration results in

$$T_e(1^-) = t_1(1 - e^{-2\alpha_{z_1} \Delta z_1}) + T_e(2^+) e^{-2\alpha_{z_1} \Delta z_1} \qquad \text{(IV-7)}$$

The argument, 1^-, denotes a point just below the surface (interface 1) and 2^+ denotes a point just above the second interface (Figure IV-2). The thickness of the layer between the surface (interface 1) and interface 2 is given by Δz_1. The attenuation constant, α, is dependent only on the depth z, hence the notation α_{z_1}.

In (IV-7) the energy emitted in layer 1 is given by

$$t_1(1 - e^{-2\alpha_{z_1} \Delta z_1})$$

while the upwelling radiation from the soil volume below interface 2 is given by $T(2^+)$. The exponential coefficient multiplying $T(2^+)$ in (IV-7) describes the attenuation that the upwelling energy from below interface 2 experiences as it propagates through layer 1.

The upwelling radiation referenced to a point just above interface 2 is given by

$$T_e(2^+) = \overline{R}_2 \, t_1 \left(1 - e^{-2\alpha_{t_1} \Delta z_1}\right) + T_e(2^-) \, T_2 \qquad \text{(IV-8)}$$

The first term on the right of (IV-8) represents that portion of the energy emitted in layer 1 that is reflected from interface 2 back toward the surface. $\overline{R}_2$ represents the power reflection coefficient in the negative z direction at interface 2. (Hereafter "bars" over a power transmission or reflection coefficient denotes that they correspond to the negative z direction). The second term on the right of (IV-8) is simply the upwelling energy from below interface 2 transferred across interface 2 using the power transmission coefficient corresponding to interface 2, T_2.

The form of the equation defining $T_e(1^-)$ can be visualized by substituting (IV-8) into (IV-7)

$$T_e(1^-) = t_i\left(1 - e^{-2\alpha_{z_1}\Delta z_1}\right) + e^{-2\alpha_{z_1}\Delta z_1}$$

$$\left[\bar{R}_2 t_i(1 - e^{-2\alpha_{z_2}\Delta z_1}) + T_e(2^-)T_2\right]$$

By repeating this procedure for N layers, a series can be defined to represent $T_e(1^-)$:

$$BT_{volume} = T_e(1^-) = T_{e_1}\left(1 + e^{-2\alpha_{z_1}\Delta z_1}\bar{R}_2\right)$$

$$+ \sum_{i=2}^{N} T_{e_i}\left(1 + e^{-2\alpha_{z_i}\Delta z_i}\bar{R}_{i+1}\right) \cdot \qquad \text{(IV-9)}$$

$$e^{-2\sum_{k=1}^{i-1}\alpha_{z_k}\Delta z_k} \prod_{j=2}^{i} T_j$$

where

$$T_{e_i} = t_i\,(1 - e^{-2\alpha_{z_i}\Delta z_i})$$

N - number of layers

$R_N + 1 = 1.0$

Δz_N = infinity

Equation (IV-9) defines the effective temperature of
emission for the soil volume just below the surface.
$T_e(1^-)$ will be defined as the radiometric brightness
temperature of the soil volume, BT_{volume}.

$T_e(1^-)$ is dependent on the angle θ_1 at which the
energy is approaching the surface from below (Figure IV-2).
This is a result of the dependence of the power transmission
coefficients, power reflection coefficients, and attenua-
tion constants on angle. For a uniform soil permittivity
profile the transmission coefficients go to unity and the
reflection coefficients go to zero, but the attenuation
constant is still dependent on angle, θ_1.

For the case of a smooth soil surface, the brightness
temperature of the soil is given by simply multiplying
(IV-9) by the power transmission coefficient for a smooth
surface.

$$BT_{soil} = T_e(1^+) = T_e(1^-) \cdot T_1 = BT_{volume} \cdot T_1 \qquad \text{(IV-10)}$$

The technique of handling rough surfaces will be presented
in the next section.

To complete the formulation, equations defining α_{z_i}, T_i, and $\overline{R}_i$ must be provided. A formulation for α_{z_i} will first be derived, then a technique of obtaining T_i and $\overline{R}_i$ will be discussed.

<u>Attenuation constant (α_z)</u> - In order to evaluate (IV-9) an expression is needed for the attenuation constant, α_z. Most electromagnetic textbooks [39], [97], [98] give an expression for the attenuation constant that is independent of the direction of propagation. In using such an expression the direction from which energy is incident on each layer interface is taken into account in the reflection and transmission coefficients at each interface. However, the evaluation of (IV-9) is more convenient (as will be pointed out below) if the direction of propagation is included in the expression for the attenuation constant.

An expression for the z component of the attenuation constant is derived below. It will be seen that the resulting expression is dependent on the direction of propagation. In deriving α_z a plane wave harmonic in time traveling in the ξ_i direction and independent of the x coordinate will be assumed (Figure IV-2). This wave will have the form:

$$\overline{E}_i(y, z, t) = \overline{E}_i \, e^{j k_i \xi_i} \, e^{j \omega t} \qquad \text{(IV-11)}$$

where

$$\xi_i = \overline{n}_i \cdot \overline{r}$$

$\overline{n}_i$ - unit vector defining the direction of propagation in the ith layer

$\overline{r}$ - position vector

t - time

For a general medium, k_i is complex and takes the form:

$$k_i = \beta_i + j\alpha_i \qquad \text{(IV-12)}$$

Therefore (IV-11) may be written:

$$\overline{E}_i(y,z,t) = \overline{E}_i e^{j(\beta_i + j\alpha_i)\xi_i} e^{j\omega t} \qquad \text{(IV-13)}$$

The rectangular coordinates of ξ_i are:

$$\xi_{x_i} = 0$$

$$\xi_{y_i} = y \sin \theta_i \qquad \text{(IV-14)}$$

$$\xi_{z_i} = z \cos \theta_i$$

Using these in (IV-13) yields:

$$\overline{E}_i(y, z, t) = \overline{E}_i \, e^{-\alpha_i \Delta \xi_i} \cdot$$

$$e^{j(\beta_i y \sin \theta_i + \beta_i z \cos \theta_i)} \, e^{j \omega t} \qquad \text{(IV-15)}$$

The x, y, and z coordinate components of β_i are given by

$$\beta_{x_i} = 0$$

$$\beta_{y_i} = \beta_i \sin \theta_i \qquad \text{(IV-16)}$$

$$\beta_{z_i} = \beta_i \cos \theta_i$$

At any interface, Snell's law requires that the phase velocity parallel to the interface must be equal in the two media that define the interface, thus, the y components of the phase velocities must match across the interfaces.

$$\beta_{y_i} = \beta_{y_{i+1}} \qquad \text{(IV-17)}.$$

So

$$\beta_{y_1} = \beta_{y_i}$$

$$\qquad \text{(IV-18)}$$

$$\beta_1 \sin \theta_1 = \beta_{y_i}$$

In addition, the boundary conditions at each interface require that the parallel components of the electric field be equal at the interface. This condition requires that

$$\overline{E}_i \sin \theta_i = \overline{E}_{i+1} \sin \theta_{i+1} \tag{IV-19}$$

be independent of the y dimension. It is obvious from (IV-15) that this can only occur if

$$\alpha_{y_i} = 0 \tag{IV-20}$$

It is known that [97], [98]

$$K_i^2 = \omega^2 \mu_i (\varepsilon_i' - j \varepsilon_i'') \tag{IV-21}$$

where

$$\mu_i = \mu_o \mu_{r_i}$$

$$\varepsilon_i' = \varepsilon_o \varepsilon_{r_i}'$$

$$\varepsilon_i'' = \varepsilon_o \varepsilon_{r_i}''$$

μ_o - permeability of free space ($4\pi \times 10^{-7}$ henrys/meter)

ε_o - permittivity of the space (8.85×10^{-12} farads/meter)

From (IV-12)

$$k_i^2 = (\cancel{\beta_{x_i}^2}^{0} + \beta_{y_i}^2 + \beta_{z_i}^2) - (\cancel{\alpha_{x_i}^2}^{0} + \alpha_{y_i}^2 + \alpha_{z_i}^2) + 2j\beta_i\alpha_i \qquad \text{(IV-22)}$$

Equating the real and imaginary parts of (IV-21) and (IV-22) yields

$$\beta_{y_i}^2 + \beta_{z_i}^2 - \alpha_{z_i}^2 = \omega^2 \mu_0 \mu_{r_i} \varepsilon_0 \varepsilon_{r_i}' \qquad \text{(IV-23a)}$$

$$-2\beta_i\alpha_i = \omega^2 \mu_0 \mu_{r_i} \varepsilon_0 \varepsilon_{r_i}'' \qquad \text{(IV-23b)}$$

Substituting (IV-18) into (IV-23a) yields

$$\beta_{z_i}^2 - \alpha_{z_i}^2 = \omega^2 \mu_0 \epsilon_0 \left(\epsilon_{r_i}' - (\beta_1 \sin \theta_1)^2 \right) \qquad \text{(IV-24)}$$

where [93]

$$\mu_{r_i} \approx 1.0$$

$$\beta_1 = \left[\frac{\epsilon_{r_1}'}{2} \left(1 + \sqrt{1 + \left(\frac{\epsilon_{r_1}''}{\epsilon_{r_1}'}\right)^2} \right) \right]^{1/2}$$

while (IV-23b) reduces to

$$-2\beta_{z_i} \alpha_{z_i} = \omega^2 \mu_0 \epsilon_0 \epsilon_{r_i}'' \qquad \text{(IV-25)}$$

Solving (IV-24) and (IV-25) simultaneously

$$\beta_{z_i} = \frac{\omega^2 \mu_0 \epsilon_0 (\epsilon_{r_i}' - (\beta_1 \sin \theta_1)^2)}{2} \left[1 + \sqrt{1 + \left(\frac{\epsilon_{r_i}''}{\epsilon_{r_i}' - (\beta_1 \sin \theta_1)^2}\right)^2} \right]$$

$$\text{(IV-26)}$$

$$\alpha_{z_i} = -\left(\omega^2 \mu_0 \epsilon_0 \epsilon_{r_i}'' \right) \Big/ 2\beta_{z_i}$$

Equation (IV-26) describes the z component of the electric field attenuation, α_z, and phase, β_z, constants. Note that these quantities are constant across any given layer. The use of these quantities for calculating the power transmission coefficients is discussed below.

Power transmission and reflection coefficients - Analytical descriptions of the power transmission and reflection coefficients are also needed in order to evaluate (IV-9). The layer interfaces defined in Figure IV-2 are assumed to be smooth. As a result, the transmission and reflection of electric fields at these interfaces can be described using the Fresnel electric field transmission and reflection coefficients given in most electromagnetic textbooks [39], [97], [98]. Since the derivation of these coefficients is well known, it will not be repeated here. However, the relationship between these coefficients and the power transmission and reflection coefficients required in (IV-9) will be presented.

Given the complex vector electric, $\overline{E}$, and magnetic, $\overline{H}$, field intensities, the average power density can be computed using Poynting's theorem [97].

$$\overline{P}_{average} = \frac{1}{2} \, Real\left(\overline{E} \times \overline{H}^{*}\right) \tag{IV-27}$$

For the geometrical arrangement shown in Figure IV-3, the power density transmitted across area S is given by

$$P_{t_{avg.}} = \frac{1}{2} \text{Real} (E_t H_t^*) \cos \theta_t \qquad (IV\text{-}28)$$

where E_t and H_t are the transmitted field intensities. The relationship between the magnetic and electric field intensities is given by

$$H_t = E_t / \eta_1 \qquad (IV\text{-}29)$$

where η_1 is the intrinsic impedence of the medium.

$$\eta_1 = \sqrt{\frac{\mu_0 \mu_{r_1}}{\varepsilon_0 (\varepsilon_{r_1}' - j \varepsilon_{r_1}'')}} \qquad (IV\text{-}30)$$

The Fresnel transmission coefficient for the electric field intensity will be denoted by t_e. Incorporating this notation into (IV-28) yields
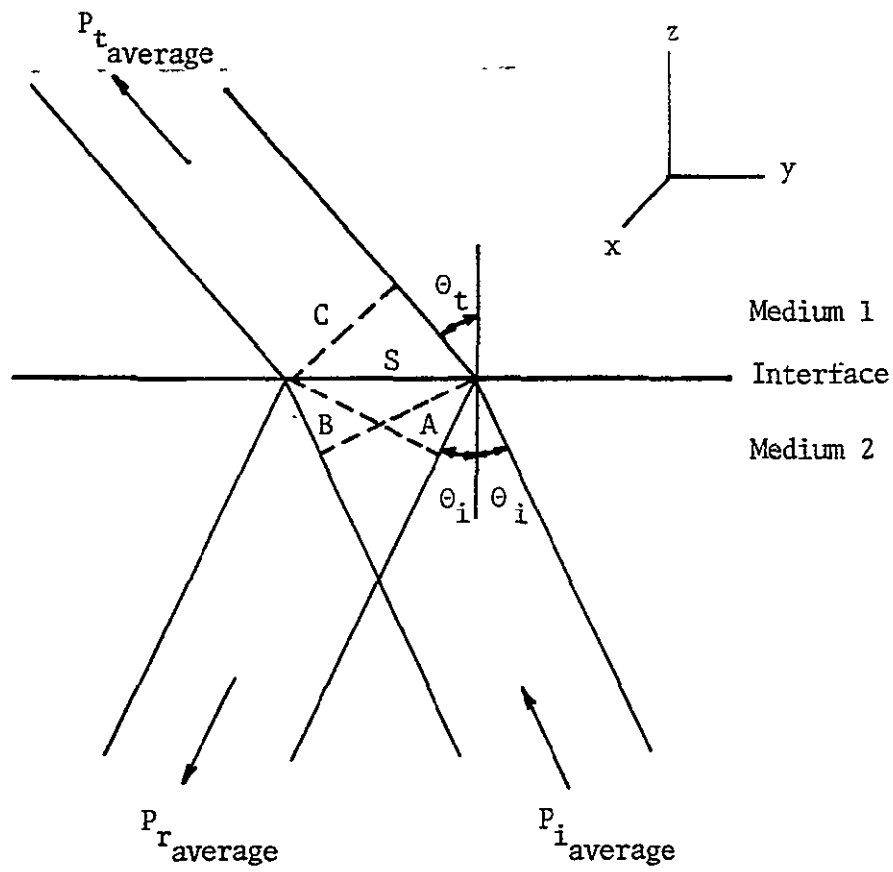
$$\text{area A} = \text{area B}; \quad \frac{\text{area A}}{\text{area S}} = \cos \Theta_i; \quad \frac{\text{area C}}{\text{area S}} = \cos \Theta_t$$

Figure IV-3.   Geometry used to describe the relationship between incident, reflected, and transmitted power density.

$$P_{t_{avg}} = \frac{1}{2} |t_e|^2 |E_i|^2 \text{Real}\left(\frac{1}{\eta_1^*}\right) \cos \theta_t \qquad \text{(IV-31)}$$

The power transmission coefficient is defined as the ratio of transmitted power density to incident power density. The power density incident on area S is

$$P_{i_{avg}} = \frac{1}{2} |E_i|^2 \text{Real}\left(\frac{1}{\eta_2^*}\right) \cos \theta_i \qquad \text{(IV-32)}$$

so that the power transmission coefficient is given by

$$T = |t_e|^2 \frac{\cos \theta_t}{\cos \theta_i} \sqrt{\frac{\varepsilon_{r_1}'}{\varepsilon_{r_2}'}} \qquad \text{(IV-33)}$$

It can similarly be shown that the power reflection coefficient is equivalent to the square of the magnitude of the electric or magnetic field Fresnel reflection coefficient:

$$R = |\rho_e|^2 = |\rho_h|^2 \qquad \text{(IV-34)}$$

ρ_e is the Fresnel reflection coefficient for the electric field intensity and ρ_h is for the magnetic field intensity.

Applying the conservation of energy requirement at the interface, an equation relating power transmission to Fresnel reflection coefficients can easily be derived. At the interface the power density transmitted plus the power density reflected must equal the incident power density.

$$P_{i_{avg.}} \cos \theta_i = P_{r_{avg}} \cos \theta_i + P_{t_{avg.}} \cos \theta_t \qquad \text{(IV-35)}$$

Substituting (IV-27) and (IV-29) into (IV-35) yields:

$$\frac{|E_t|^2}{|E_i|^2} = \left(1 - \frac{|E_r|^2}{|E_i|^2}\right) \sqrt{\frac{\varepsilon'_{r_2}}{\varepsilon'_{r_1}}} \; \frac{\cos \theta_i}{\cos \theta_t} \qquad \text{(IV-36)}$$

Since the square of the magnitude of the Fresnel electric field transmission and reflection coefficients is given by

$$|t_e|^2 = \frac{|E_t|^2}{|E_i|^2}$$

and

$$|\rho_e|^2 = \frac{|E_r|^2}{|E_\lambda|^2}$$

then (IV-36) reduces to

$$|t_e|^2 \frac{\cos\theta_t}{\cos\theta_\lambda}\sqrt{\frac{\epsilon'_{r_1}}{\epsilon'_{r_2}}} = \left(1 - |\rho_e|^2\right) \tag{IV-37}$$

Combining (IV-33) and (IV-37), it is seen that the power transmission coefficient is related to the Fresnel electric field reflection coefficient by

$$T = \left(1 - |\rho_e|^2\right) \tag{IV-38}$$

Equation interpretation - Equations (IV-9), (IV-26), and (IV-33) or (IV-38) define the radiative transfer model of emission from a soil volume. A note of caution is in order in applying these equations. It was shown that a

plane wave propagating in the soil medium is only attenu-
ated in the z direction. As a result, the planes of
constant amplitude are parallel to the xy plane, and not
parallel to planes of constant phase. The planes of
constant phase are perpendicular to the direction of
energy flow. Since only the z component of the attenua-
tion and phase constants are of concern, and the z direc-
tion is perpendicular to the planes defining the interfaces
between the layers, the Fresnel reflection coefficients in
(IV-34) and (IV-38) must be of the form:

$$\rho_{h_i} = \frac{k_{z_i} - k_{z_{i-1}}}{k_{z_i} + k_{z_{i-1}}}$$

$$\rho_{v_i} = \frac{\varepsilon_{r_{i-1}} k_{z_i} - \varepsilon_{r_i} k_{z_{i-1}}}{\varepsilon_{r_{i-1}} k_{z_i} + \varepsilon_{r_i} k_{z_{i-1}}}$$

(IV-39)

where

$$k_{z_i} = \beta_{z_i} + j\alpha_{z_i}$$

$$\varepsilon_{r_i} = \varepsilon'_{r_i} - j\varepsilon''_{r_i}$$

v   - vertical polarization

h   - horizontal polarization

Note that the angular dependence is contained in β_{z_i} and α_{z_i} and not in the reflection coefficients.

Since the Fresnel reflection coefficients are calculated using (IV-39), one does not have to contend with complex angles of refraction that occur for imperfect dielectrics. This is the advantage of deriving the radiative transfer model in terms of only the z components of the attenuation and phase constants.

It can be seen in Figure IV-2 that only medium 0, air, and the Nth medium are semi-infinite in extent. As a result, the power transmission coefficients for all interfaces except the first must be calculated for a layered media. Likewise the power reflection coefficients in the negative z direction must be calculated for a layered media, except for the last interface. This can be done by using the impedence matching technique described by Tyrus [39] and Ramo et al. [98] to calculate the Fresnel reflection coefficients used in (IV-34) and (IV-38).

Only small errors are observed, however, if the reflection coefficient for each interface is calculated assuming semi-infinite media on each side of the interface. Under this assumption, the reflection coefficient at any interface is independent of the incident direction, so

$$\overline{R}_i = R_i$$

for all i, where i denotes the interface. Since

$$T_i = 1 - R_i$$

(IV-9) reduces to a slightly simpler form. This assumption
was used for the calculations in the remainder of this
report.

Demonstration of the Model

Comparison to accepted procedures - An in-depth
derivation and discussion on the applicability of the
integral equations describing radiative transfer is given
by Chandrasekhar [95]. Further discussion on this approach
is provided by Paris [40]. Equation (IV-9) is simply a
numerical approximation to the integral equation of
radiative transfer. The integral equation is given by

$$T_e(1^-) = \int_{0^-}^{\infty} 2\alpha_z(z) T(z) e^{-\int_{-z}^{0^-} 2\alpha_z(s)ds} dz \qquad \text{(IV-40)}$$

The limit of the integrals, 0^-, denotes integration
from or to just below the surface. In this case, $\alpha_z(z)$ is a

smoothly varying function of depth as is T(z), which is
the source function given by Planck's law of emission.
In the limit as the thickness of the individual layers is
decreased, (IV-9) approaches (IV-40).

Calculated soil volume brightness temperatures - The
effect of moisture and temperature profiles on the radia-
tion emitted from the soil volume can be demonstrated using
(IV-9). Note, however, that these calculations do not
include effects of the surface-to-air interface, but are
calculations of the radiation impinging on the surface
from below. The radiation is referenced to the mean surface
height reference datum shown in Figure IV-1. There are
three cases that are of interest:

1) uniform temperature and
   uniform moisture

2) nonuniform temperature and
   uniform moisture

3) uniform temperature and
   nonuniform moisture

For the case of uniform moisture and temperature pro-
files, the brightness temperature of the soil volume,
BT_{volume}, calculated using (IV-9) is simply equivalent to
the soil temperature. In addition, it is independent of
the angle at which the radiation is impinging on the surface
from below, i.e., it is isotropic. This can be seen by

simplifying (IV-9). Under the uniform moisture and uniform temperature assumption (IV-9) reduces to

$$BT_{volume} = t_2 \left(1 - e^{-2\alpha_2 \Delta z_2} \right)$$ (IV-41)

where

t_2 - soil temperature

α_2 - attenuation constant of the soil

Δz_2 - depth of soil

Since the soil is semi-infinite in extent, Δz_2 is infinity and (IV-41) reduces to

$$BT_{volume} = t_2$$ (IV-42)

This result is interesting since it demonstrates that for uniform moisture and temperature profiles, the dependence of the brightness temperature on soil moisture is controlled totally by the surface boundary effects.

An explanation for the above phenomena can be found by examining (IV-9). Even though the moisture and temperature

profiles are assumed to be uniform, (IV-9) can be evaluated
as written. In doing this, the maximum depth below which
at least one percent of the total radiation originates can
be determined (Figure IV-4). For uniform profiles of 15%,
25% and 35% moisture by volume, this depth for 1.4 GHz is
26 cm, 20 cm, and 16 cm, respectively. Since the emission
from each layer decreases as the soil moisture decreases,
the maximum depth of emission has to increase to maintain
the same brightness temperature. However, it is of interest
to note that although the maximum depth of emission in-
creases, the equivalent depth of water for each soil
moisture (calculated using (II-8)) is not equal. For 15%,
25%, and 35% soil moistures it is 3.9 cm, 5.0 cm, and
5.6 cm, respectively. This demonstrates that the emission
from a soil volume is not dependent on equivalent volumes
of soil water for a given frequency.

For a nonuniform temperature profile and uniform soil
moisture profile, it can be shown that the radiation
impinging on the surface from below is not isotropic. It
is a function of the transmission angle, θ_1 (Figure IV-2),
i.e., the direction from which energy is incident on the
surface from below. This is a result of the fact that the
distance energy must travel from its point of origin to
reach the surface increases as the transmission angle, θ_1,
increases. In effect, the temperature profile along the

Percentage Contribution to Total Volume Emission From Individual Subsurface Layers
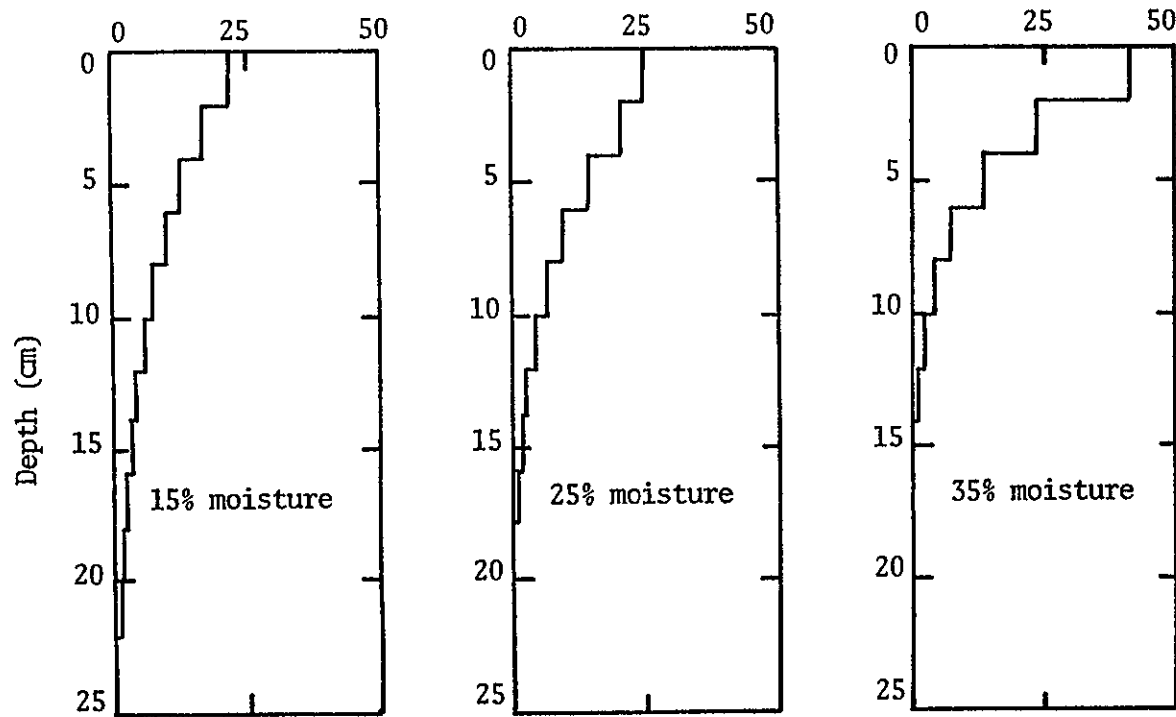
Figure IV-4. Percentage contribution of two centimeter soil layers to the total volume emission calculated at 1.4 GHz for uniform soil moisture and temperature profiles.

ray path changes as the transmission angle is changed.

It is of interest to note that the energy impinging on the surface from below is not polarization dependent as long as the soil moisture profile is uniform. This can be seen in Figure IV-5. Figure IV-5 is the brightness temperature of the volume calculated using (IV-9) for two uniform moisture profiles of 15% and 35%, and the two non-uniform temperature profiles shown in Figure IV-6. The only polarization dependent terms in (IV-9) are the transmission and reflection coefficients. For uniform soil moisture profiles the reflection coefficients are zero for all angles θ_1 and the transmission coefficients are unity.

Figure IV-5 again demonstrates the effect of moisture on the depth from which the volume emission originates. For a 15% uniform moisture profile and transmission angles less than 46°, it is seen that temperature profile A produces less volume emission than temperature profile B. Figure IV-6 shows that temperature profile B is cooler than profile A near the surface and warmer for depths greater than 3.5 cm. This indicates that for 15% moisture and angles less than 46°, a major percentage of emission is originating below 3.5 cm. Figure IV-7(a) demonstrates this for θ_1 equal to zero degrees. Since the emission due to temperature profile A is greater than that due to temperature profile B for transmission angles greater than 46°,
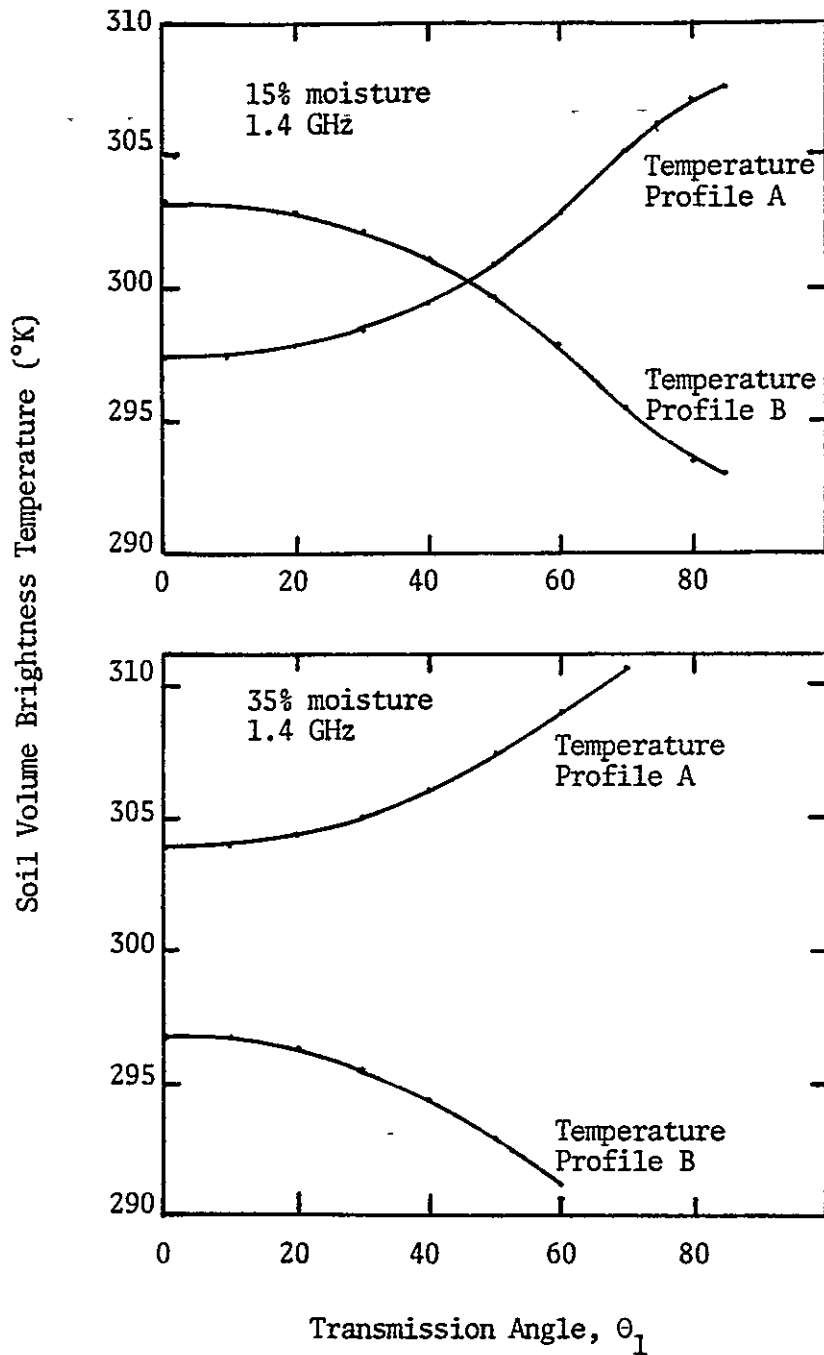
Figure IV-5. Brightness temperature of a soil volume
for uniform moisture and nonuniform
temperature profiles. Each curve repre-
sents both vertical and horizontal
polarizations.
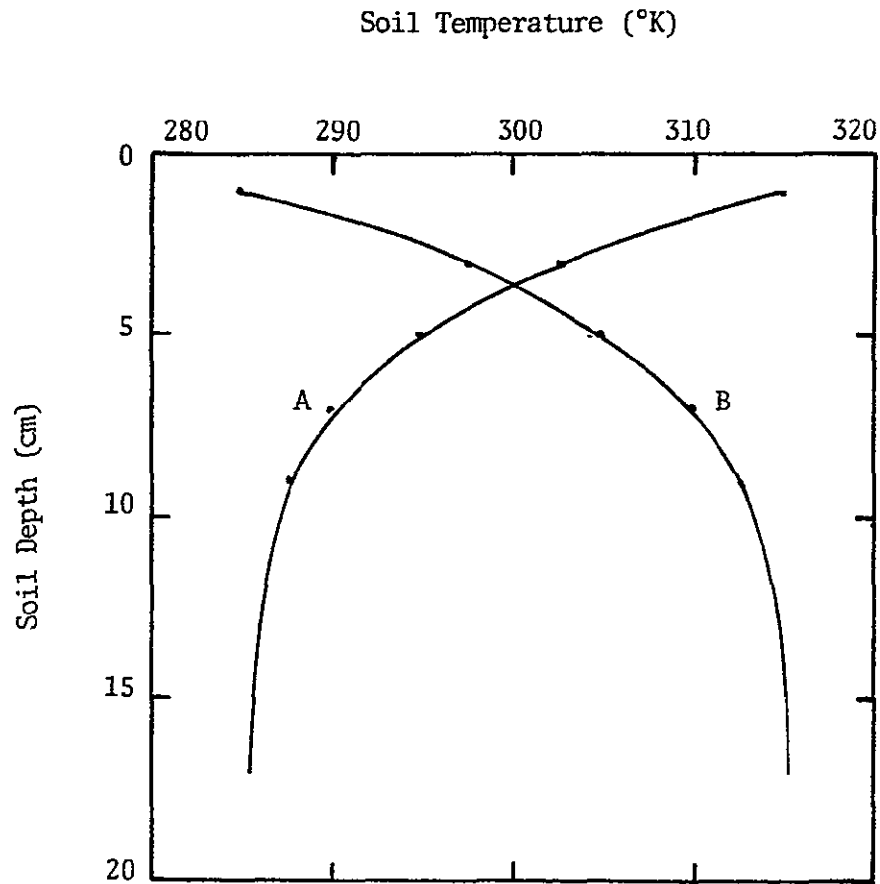
Soil Temperature (°K)

Figure IV-6. Soil temperature profiles used to demonstrate that the emission from a soil volume is not isotropic for nonuniform temperature profiles (Figure IV-5).

Brightness Temperature of Each Layer (°K)

BT$_{volume}$ = 297.4°K

15% Soil Moisture

Temperature Profile A

$\Theta_1 = 0°$

1.4 GHz

BT$_{volume}$ = 303.3°K

15% Soil Moisture

Temperature Profile B

$\Theta_1 = 0°$

1.4 GHz
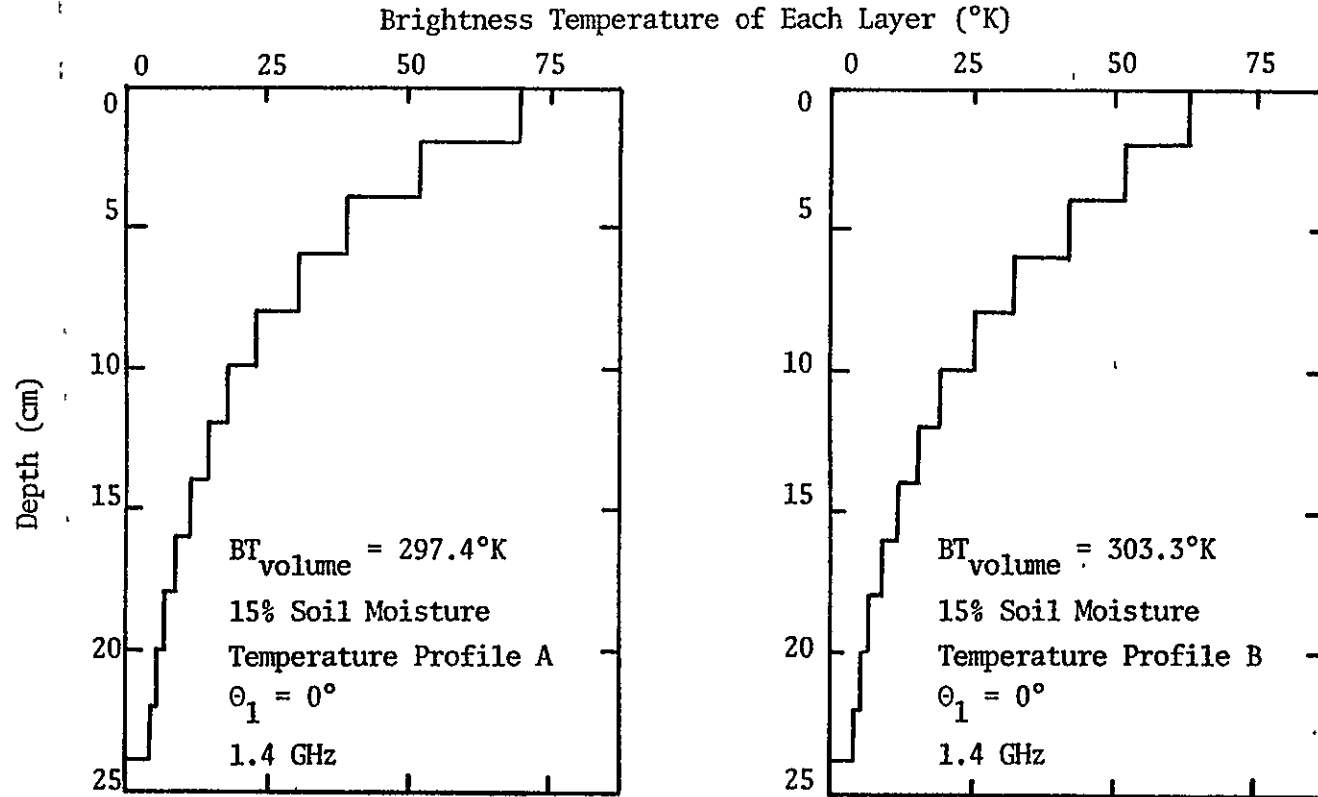
Figure IV-7(a).   The contribution of two centimeter soil layers to the total volume brightness temperature for soil temperature profiles A and B of Figure IV-6.

Brightness Temperature Contribution of Each Layer (°K)

Depth (cm)

$BT_{volume} = 303.9°K$

35% Soil Moisture

Temperature Profile A

$\Theta_1 = 0°$

1.4 GHz

$BT_{volume} = 296.8°K$

35% Soil Moisture

Temperature Profile B

$\Theta_1 = 0°$

1.4 GHz
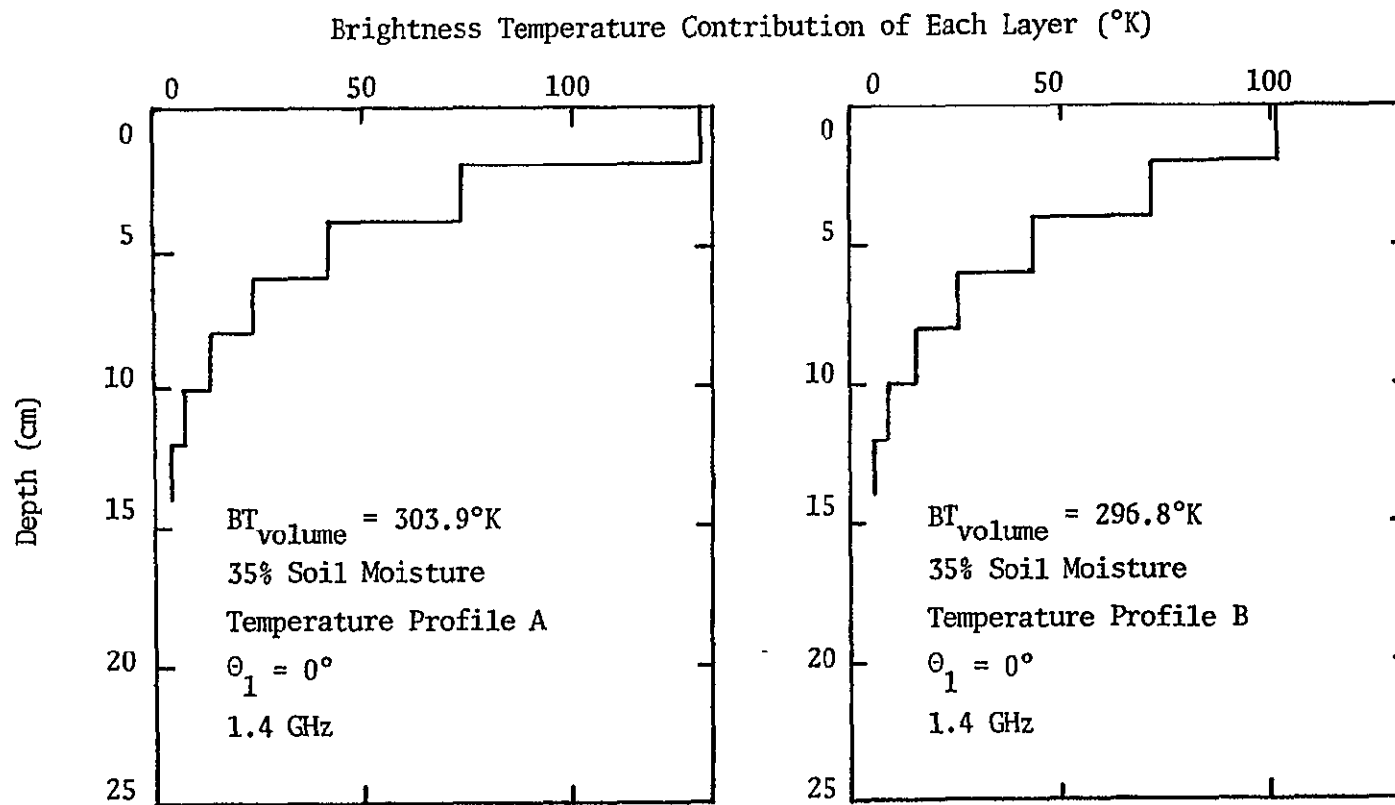
Figure IV-7(b). The contribution of two centimeter soil layers to the total volume brightness temperature for soil temperature profiles A and B of Figure IV-6.

then the depth from which the majority of the emission originates decreases as the transmission angle increases.

At 35% moisture, Figure IV-5 demonstrates that the temperature in the top few centimeters dominates. This is simply due to the fact that the maximum depth of emission is much shallower at 35% moisture than it is at 15% moisture. Figure IV-7(b) demonstrates the contributions of each soil layer to the total emission for a 35% uniform moisture profile at a transmission angle of zero degrees.

The third case of interest is a uniform temperature profile and nonuniform moisture profile. Since the moisture changes between layers, the reflection and transmission coefficients for each layer interface are not zero and one, respectively, as they were for uniform moistures. The reflection and transmission coefficients now depend on the permittivities of the layers forming the boundary, and on the transmission angle θ_1. The attenuation constant also depends on the permittivity of the soil and the transmission angle. As a result, the radiation impinging on the surface from below is not isotropic, but varies with angle θ_1. In addition, the radiation is polarization dependent.

The statements made above can be demonstrated using the soil moisture profiles of Figure IV-8. Figure IV-9 is the resulting volume brightness temperature, BT_{volume},

Percent Soil Moisture (vol)
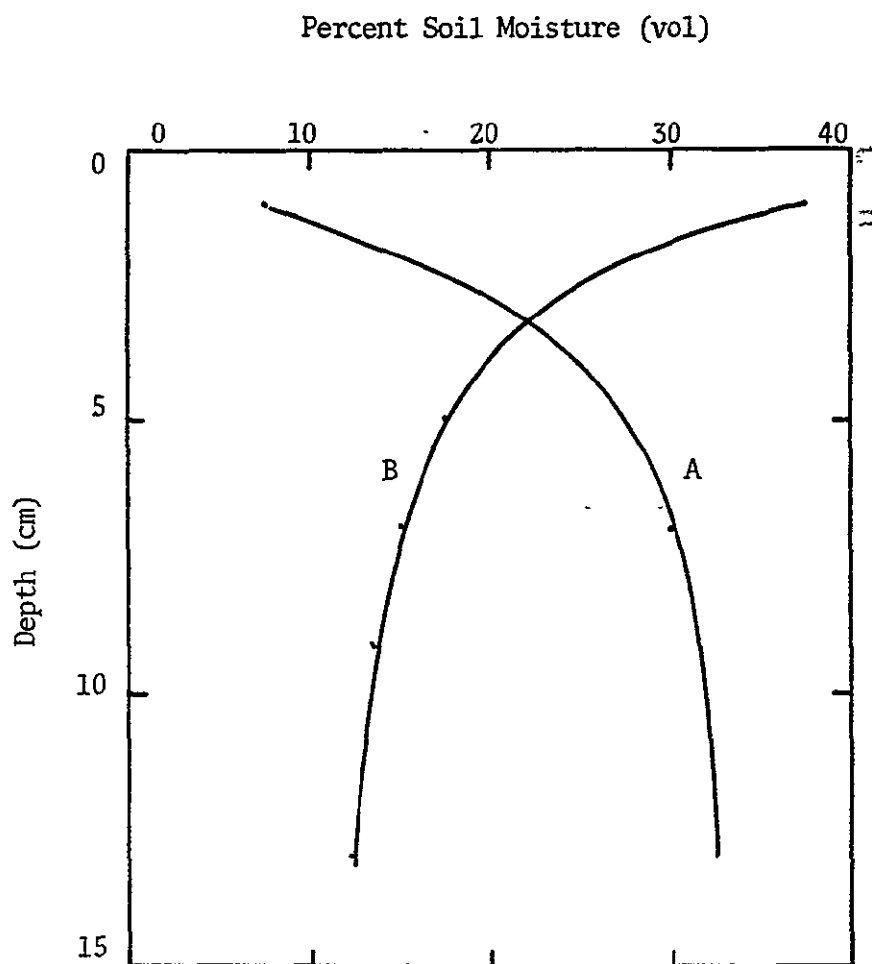
Figure IV-8. Soil moisture profiles used to
demonstrate that the emission
from a soil volume is not iso-
tropic for nonuniform moisture
profiles.
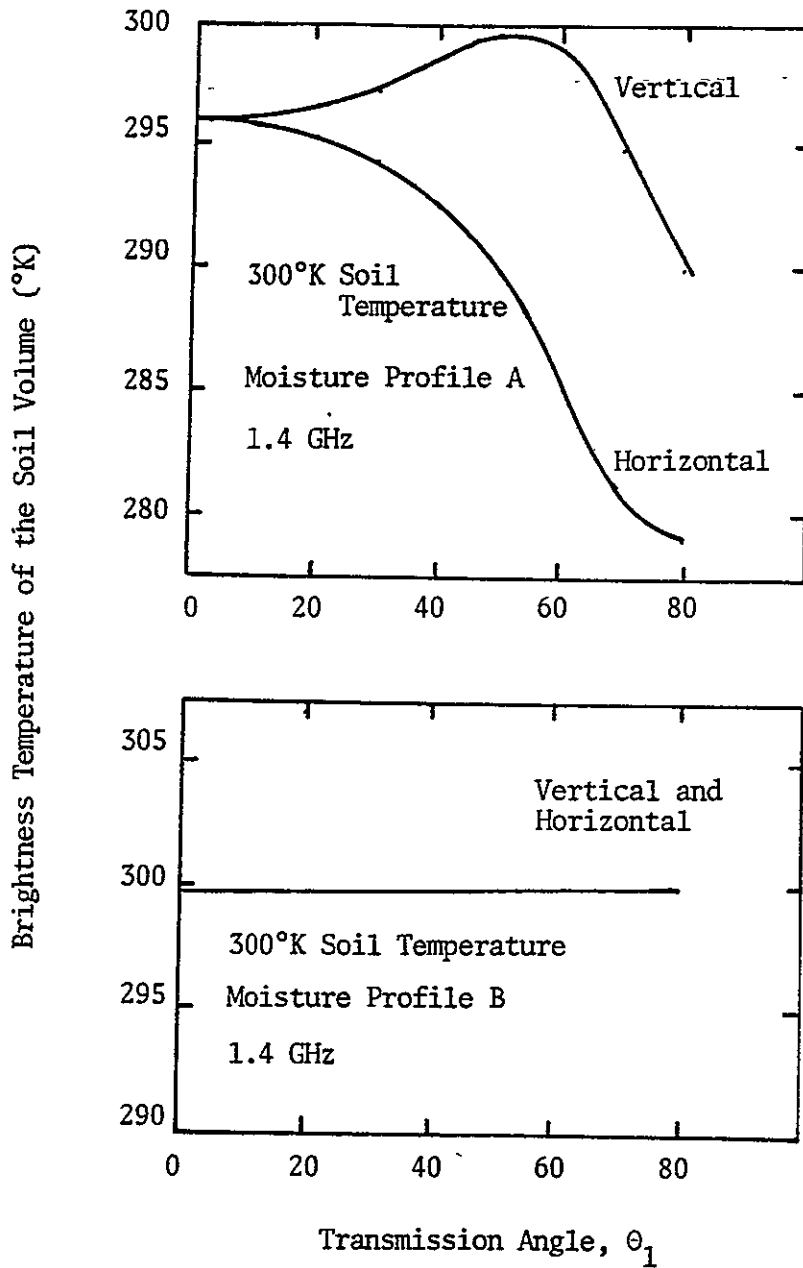
Figure IV-9. Calculated brightness temperatures of the soil volume for nonuniform soil moisture profiles.

calculated for these profiles as a function of θ_1 using (IV-9) and assuming a uniform soil temperature of 300°K. Moisture profile A produces a volume emission that has a dependence on θ_1 that is characteristic of the smooth interface power transmission coefficient. However, moisture profile B, which is wetter at the surface than below, does not. This is due to the fact that the greatest percentage of energy originates in the top layer. As seen in (IV-9) the energy originating in this layer is not directly modified by a transmission coefficient.

Figure IV-10 demonstrates the contribution of each soil layer for both profiles at a transmission angle of zero degrees. It is seen that the first layer contributes the majority of energy for moisture profile B. As the transmission angle increases, the percentage contribution of the first layer (for moisture profile B) also increases.

In summary, the effects of moisture and temperature profiles on the brightness temperature of the soil volume have been demonstrated. Uniform soil moisture and soil temperature profiles produce isotropic emission from the soil volume. However, for uniform conditions the maximum depth for which emission is influential depends only on the soil moisture, and the magnitude of the total soil volume emission depends only on the soil temperature. A nonuniform temperature profile causes the emission from

Brightness Temperature Contribution of Each Layer (°K)
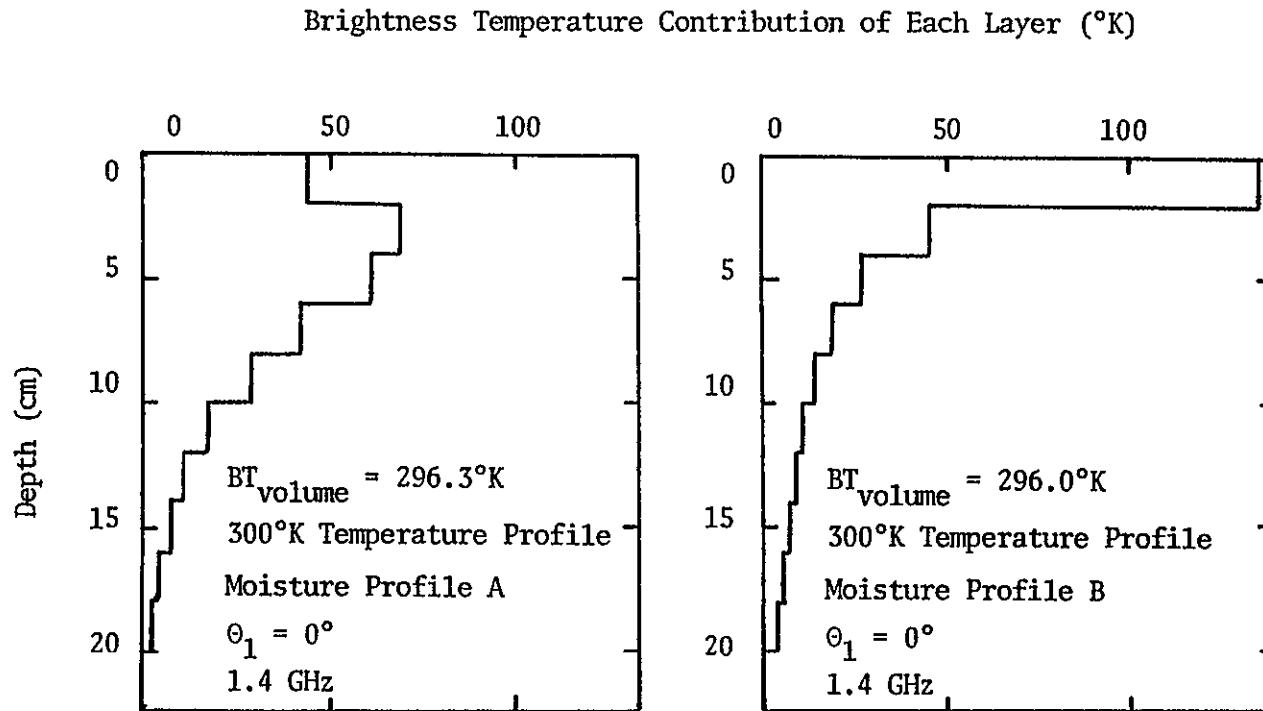
Figure IV-10.   The contribution of two centimeter soil layers to the total
volume brightness temperature for soil moisture profiles
A and B of Figure IV-8.

the soil volume to be nonisotropic, but not polarization
dependent. A nonuniform moisture profile causes the
emission from the soil volume to be nonisotropic and
polarization dependent.

Surface Roughness

Model Development

Peake approach - Most of the approaches to modeling
the emission from rough surfaces that are described in the
literature stem from the Peake approach. They model the
surface emission utilizing bistatic scattering coefficients
defined for the top side of the surface. Inherent in this
approach is the assumption that the soil is in thermo-
dynamic equilibrium with blackbody (isotropic) radiation
impinging on the surface from the hemisphere above the
surface. Due to this assumption, the Peake approach is
not strictly valid for the cases in which the energy
impinging on the surface from below is not isotropic. As
was shown in the last section, a nonuniform soil moisture
or soil temperature profile produces nonisotropic volume
radiation. As a result, the Peake approach is only a
special case of a more general solution to emission from
soil surfaces.

Transmission scattering - A more general formulation
than the Peake approach is required for describing the
emission of moist soils. This is due to the fact that the
soil moisture and soil temperature profiles are very
dynamic and are very seldom uniform with depth, thereby
violating the assumption of isotropic radiation. For the
purposes of this report, the soil moisture and soil tempera-
ture profiles will be assumed to be constant over the area
within the antenna footprint. With this assumption, a
general formulation for the emission of soil can be ob-
tained by describing the transmission of energy from the
soil volume across the soil surface. This formulation
does not require that the radiation be isotropic, that is,
it does not require the assumption of thermodynamic
equilibrium.

The radiation intensity incident on the surface from
below as a function of soil permittivity and soil tempera-
ture profile is described by the radiative transfer equa-
tions. It is now necessary to develop equations that
describe transmission of that energy across an arbitrary
surface.

It is convenient to describe the effect of the surface
in terms of differential transmission coefficients. These
differential transmission coefficients describe the power
that is transmitted into an increment of solid angle, $d\Omega_t$,

defined above the surface. This transmitted power is due to energy incident on the surface from below through an increment of solid angle, $d\Omega_1$, defined below the surface.

The differential transmission coefficients can be described by considering an infinite surface forming, on the average, a plane, although over small regions it may have complexity of structure (Figure IV-11). If a differential element of radiation of intensity $I_1 d\Omega_1$ impinges on the surface from below at an angle of incidence (transmission angle), θ_1 and azimuth angle ϕ_1, on an element of surface area A, and the differential intensity of scattered radiation from A to a point a distance R away in the direction (θ_t, ϕ_t) is $I_t d\Omega_t$, then the differential transmission coefficient will be defined by·

$$T(\theta_1, \phi_1; \theta_t, \phi_t) = \frac{4\pi R^2 I_t}{(I_1 \cos \theta_1) A} \qquad (IV-43)$$

Conceptually, energy impinges on the surface from below from all angle pairs (θ_1, ϕ_1). The total radiation transmitted into $d\Omega_t$ in the direction (θ_t, ϕ_t) results from energy impinging on the surface from all directions (θ_1, ϕ_1). The differential energy transmitted into $d\Omega_t$ in
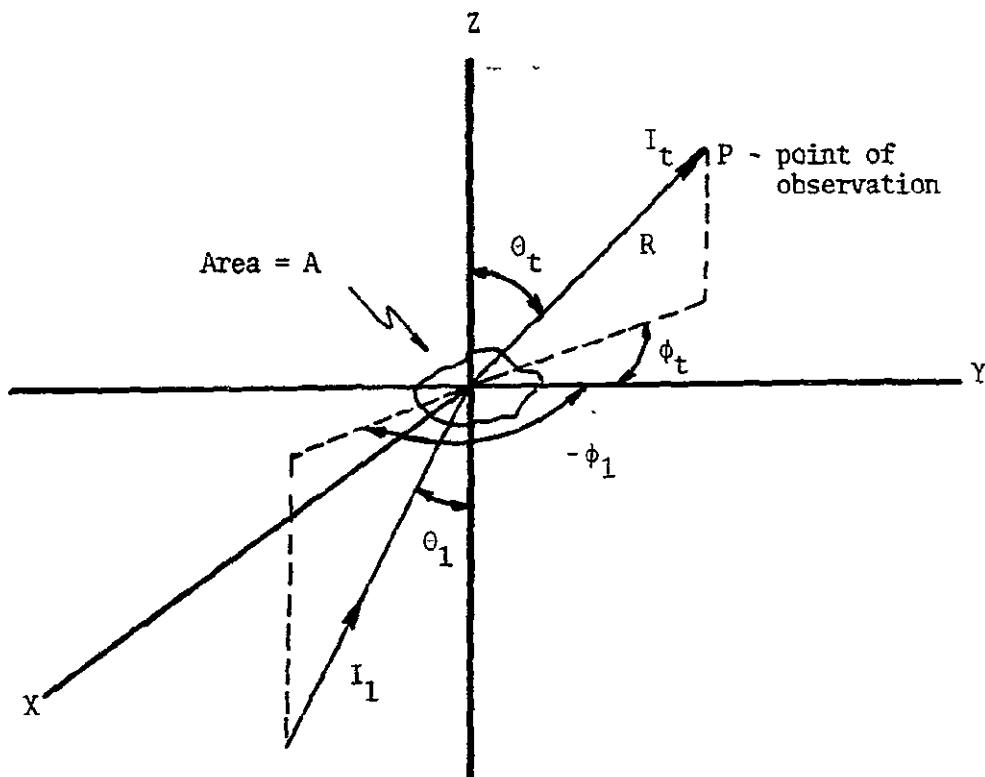
Figure IV-11. Geometry used to describe differential
transmission coefficients.

the direction (θ_t, ϕ_t), a distance R from the surface, caused by radiation impinging on the surface from below from $d\Omega_1$ in the direction (θ_1, ϕ_1) is

$$P_t(1,t) \, d\Omega_t \, d\Omega_1 = \frac{1}{4\pi} \, T(1,t) \left[I_1(1) \cdot \right.$$

(IV-44)

$$\left. A \cos \theta_1 \right] d\Omega_t \, d\Omega_1$$

where

$d\Omega = \sin \theta \, d\theta \, d\phi$

A - area on the surface through which energy is transmitted

Regarding the notation, P(1,t), the first letter in parenthesis denotes the angle pair from which radiation is incident (θ_1, ϕ_1). The second letter in the parenthesis denotes the angle pair describing the direction into which energy is transmitted (θ_t, ϕ_t). Integrating over all angle pairs (θ_1, ϕ_1) yields

$$P_t(t) \, d\Omega_t = A \, d\Omega_t \left[\frac{1}{4\pi} \int_0^{2\pi} \int_0^{\pi/2} \cos \theta_1 \, T(1,t) \, I_1(1) \, d\Omega_1 \right]$$

(IV-45)

The differential element of radiation incident on the surface from below and the differential element of transmitted radiation can be at orthogonal polarization states

with respect to one another. Thus, the differential transmission coefficients will be written in the form $\bar{\tau}_{ij}(1,\bar{t})$. The first subscript indicates the incident polarization state (vertical or horizontal) and the second indicates the transmitted polarization state. Equation (IV-45) can now be written in the form:

$$\left(P_t(t)\right)_i \, d\Omega_t = A\, d\Omega_t \left[\frac{1}{4\pi} \int_0^{2\pi} \int_0^{\pi/2} \cos\theta_i \cdot \right.$$

$$\left. \left(\tau_{ii}(1,t)\, I_i(1) + \tau_{ji}(1,t)\, I_j(1) \right) d\Omega_i \right] \qquad \text{(IV-46)}$$

where

$$\tau_{ji}(1,t) = \frac{4\pi R^2 \, I_{t_i}(\theta_t, \phi_t)}{A \cos\theta_i \, I_{i_j}(\theta_i, \phi_i)}$$

The differential element of energy transmitted into the direction (θ_t, ϕ_t) can also be written:

$$\left(P_t(t)\right)_i d\Omega_t = A \cos\theta_t \, I_{t_i}(\theta_t, \phi_t) \, d\Omega_t \qquad \text{(IV-47)}$$

Equating (IV-46) and (IV-47) yields:

$$A \cos \theta_k \, I_{t_k}(t) \, d\Omega_k = A \, d\Omega_k \left[\frac{1}{4\pi} \int_0^{2\pi} \int_0^{\pi/2} \right.$$

$$\left. \cos \theta_1 \left(\tau_{ii}(l,t) \, I_i(l) + \tau_{ji}(l,t) \, I_j(l) \right) d\Omega_1 \right] \tag{IV-48}$$

So

$$I_{t_k}(t) = \frac{1}{4\pi} \int_0^{2\pi} \int_0^{\pi/2} \frac{\cos \theta_1}{\cos \theta_k} \left(\tau_{ii}(l,t) \, I_i(l) + \tau_{ji}(l,t) \, I_j(l) \right) d\Omega_1 \tag{IV-49}$$

Equation (IV-49) is a general equation defining the power intensity emitted by a rough medium. Since the radiometric brightness temperature is directly related to radiation intensity, the brightness temperature of the soil is given by

$$BT_{SOIL} = \frac{1}{4\pi} \int_0^{2\pi} \int_0^{\pi/2} \frac{\cos \theta_1}{\cos \theta_k} \cdot \tag{IV-50}$$

$$\left(\tau_{ii}(l,t) \, BT_{volume_i} + \tau_{ji}(l,t) \, BT_{volume_j} \right) d\Omega_1$$

Equation (IV-50) can be transformed into:

$$BT_{soil_i} = \frac{1}{4\pi} \int_0^{2\pi} \int_0^{\pi/2} (T_{ii}(t,1) \, BT_{volume_i}$$

$$+ T_{ij}(t,1) \, BT_{volume_j}) \, d\Omega,$$

(IV-51)

through the use of the reciprocity relations [29]:

$$\cos \theta_1 \, T_{ij}(1,t) = \cos \theta_t \, T_{ji}(t,1)$$

(IV-52)

where i and j denote either polarization state.

To complete the formulation it is necessary to develop equations that describe the differential transmission coefficients.

Differential transmission coefficients - The various techniques of modeling electromagnetic scatter from rough surfaces were described in Chapter III. In that discussion, the ranges of validity of the various techniques were presented. Geometrical or ray tracing techniques are valid only for surfaces with very large radii of curvature compared to a wavelength. Small perturbation theory is valid only for surfaces with very small rms surface height fluctuations with respect to a wavelength.

Most soil surfaces do not fit either one of these criteria, nor do they strictly fit the criteria of the Kirchhoff approximation. Generally, the criteria for the Kirchhoff approximation is, however, closer to real soil surfaces than the others. In addition, it has been pointed out by Beckmann and Spizzichino [58] that the Kirchhoff approximation works reasonably well for surfaces not strictly fitting its surface criteria.

The Kirchhoff approach was utilized in conjunction with the Stratton-Chu integral as modified by Silver [99] to develop an expression for the differential transmission coefficients. This derivation is presented in Appendix A. However, the results of this derivation did not yield the expected results. There are no other expressions for transmission through a rough surface presented in the literature. Therefore, there were no corresponding derivations with which to check the results of Appendix A.

Since a suitable expression for the differential transmission coefficients was not obtained, it was necessary to develop an equivalent expression to (IV-50). An equivalent expression is developed below in terms of the bistatic scattering coefficients of the underside of the surface.

Conversion to scattering coefficients - Since expressions for bistatic scattering coefficients are available in the literature, it is convenient to write (IV-50) in

terms of scattering coefficients. A transmission function will be defined that describes the energy transmitted across a rough boundary. This function will be defined in terms of the energy incident on the surface from below and the bistatic scattering coefficients of the underside of the surface. It relates the energy transmitted into an increment of solid angle above the surface, $d\Omega_t$, in terms of the energy incident on an equivalent smooth surface from an increment of solid angle below the surface, $d\Omega_1$.

For a smooth surface, the energy transmitted across the surface can be written in terms of the energy incident on the surface through $d\Omega_1$, and the energy reflected from the surface through $d\Omega_r$ (Figure IV-12). The directions associated with $d\Omega_1$, $d\Omega_t$, and $d\Omega_r$ are related through Snell's law.

$$P_i \, d\Omega_i = P_t \, d\Omega_t + P_r \, d\Omega_r$$

$$P_t \, d\Omega_t = P_i \, d\Omega_i - P_r \, d\Omega_r \qquad \text{(IV-53)}$$

but

$$d\Omega_i = d\Omega_r \qquad \text{(IV-54)}$$
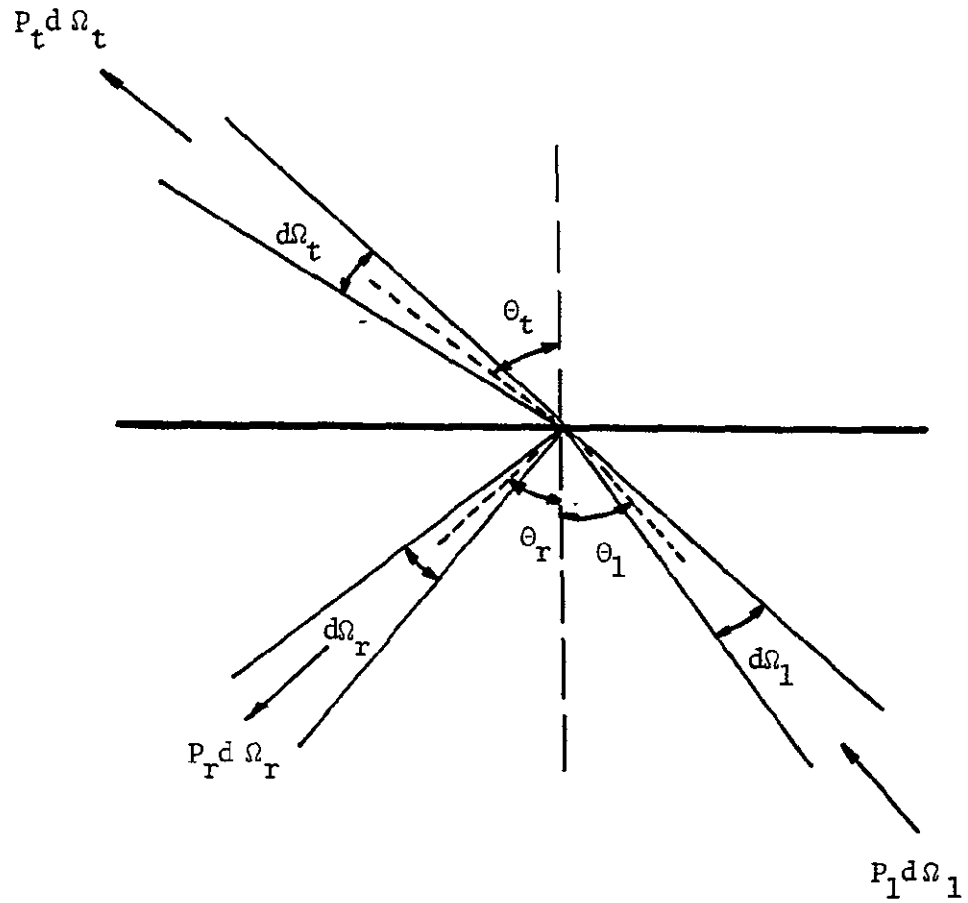
Figure IV-12. Geometry used to describe the transmission and reflection of energy at a smooth interface.

so

$$P_t \, d\Omega_t = P_1 \, d\Omega_1 - P_r \, d\Omega_1 \qquad \text{(IV-55)}$$

Equation (IV-55) is based on the boundary condition at the surface. The tangential electric fields must be equal on either side of the surface.

Rough surfaces can be modeled as an effective smooth surface. In doing this, (IV-53) is still valid. However, the energy reflected from the rough surface into $d\Omega_r$ must be substituted into (IV-53) rather than the energy reflected from a smooth surface as done previously. Also, the transmitted energy will be related to the incident energy by a transmission function.

$$P_t \, d\Omega_t = T(\theta_t, \phi_t) \, P_1 \, d\Omega_1 \qquad \text{(IV-56)}$$

where

$$P_1 \, d\Omega_1 = A \cos \theta_1 \, I_1(\theta_1, \phi_1) \, d\Omega_1 \qquad \text{(IV-57)}$$

For a rough surface, the energy reflected into $d\Omega_r$ can be obtained using bistatic scattering coefficients. Energy is reflected into $d\Omega_r$ as a result of energy incident on the subsurface from all incident angles. The bistatic scattering coefficients, $\gamma(s,r)$, describe the energy that is scattered into $d\Omega_r$ as a result of energy incident on the surface from any arbitrary solid angle increment $d\Omega_s$ from the direction (θ_s, ϕ_s), as shown in Figure IV-13.

$$P_r \, d\Omega_r \, d\Omega_s = A \cos \theta_s \, I_1(s) \, \frac{\gamma(s,r)}{4\pi} \, d\Omega_r \, d\Omega_s \qquad \text{(IV-58)}$$

where

$$\gamma(s,r) = \frac{4\pi R^2 I_r(\theta_r, \phi_r)}{A \cos \theta_s \, I_1(\theta_s, \phi_s)}$$

$I_r(\theta_r, \phi_r)$ — intensity reflected into $d\Omega_r$ as a result of energy impinging on the surface from $d\Omega_s$

Equation (IV-58) is integrated over all increments of solid angle $d\Omega_s$ to obtain the total energy reflected into $d\Omega_r$ as a result of energy incident on the surface from all angle pairs (θ_s, ϕ_s).
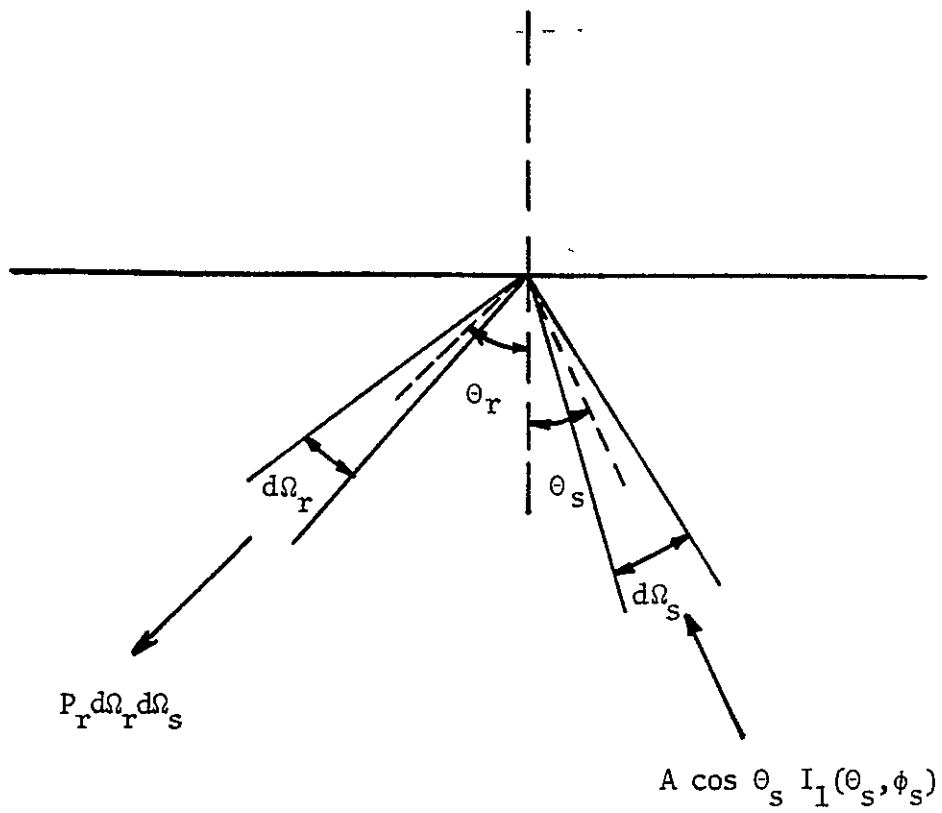
Figure IV-13. Geometry used to describe bistatic scattering coefficients.

$$P_r \, d\Omega_r = \frac{A \, d\Omega_r}{4\pi} \int_0^{2\pi}\int_0^{\pi/2} \cos\theta_s \, \Upsilon(s,r) \, I_1(s) \, d\Omega_s \qquad \text{(IV-59)}$$

Substituting (IV-56), (IV-57) and (IV-59) into (IV-53) yields the transmission function of the surface.

$$\Upsilon(\theta_t,\phi_t) \, P_1 \, d\Omega_1 = P_1 \, d\Omega_1 - \frac{A \, d\Omega_r}{4\pi} \int_0^{2\pi}\int_0^{\pi/2} \cos\theta_s \cdot$$

$$\Upsilon(s,r) \, I_1(s) \, d\Omega_s$$

$$\text{(IV-60)}$$

$$\Upsilon(\theta_t,\phi_t) = 1 - \frac{\dfrac{d\Omega_r}{4\pi} \displaystyle\int_0^{2\pi}\int_0^{\pi/2} \cos\theta_s \, \Upsilon(s,r) \, I_1(s) \, d\Omega_s}{\cos\theta_1 \cdot I_1(1) \, d\Omega_1}$$

Since (IV-60) describes an effective smooth surface, then

$$d\Omega_1 = d\Omega_r$$

$$\cos\theta_1 = \cos\theta_r$$

$$\Upsilon(s,r) = \Upsilon(s,1) \qquad \text{(IV-61)}$$

$$\phi_r = \pi + \phi_1$$

Substituting (IV-61) into (IV-60) yields:

$$\Upsilon(\theta_t, \phi_t) = 1 - \frac{1}{4\pi} \int_0^{2\pi} \int_0^{\pi/2} \frac{\cos\theta_s}{\cos\theta_r} \Upsilon(s,r) \frac{I_1(s)}{I_1(l)} \, d\Omega_s \qquad \text{(IV-62)}$$

Relying on the reciprocity relationships:

$$\cos\theta_s \, \Upsilon(s,r) = \cos\theta_r \, \Upsilon(r,s) \qquad \text{(IV-63)}$$

and the fact that $\cos\theta_1 = \cos\theta_r$, then (IV-61) becomes

$$\Upsilon(\theta_t, \phi_t) = 1 - \frac{1}{4\pi} \int_0^{2\pi} \int_0^{\pi/2} \Upsilon(l,s) \frac{I_1(s)}{I_1(l)} \, d\Omega_s \qquad \text{(IV-64)}$$

Equation (IV-64) can now be used to describe the energy transmitted into $d\Omega_t$ as a result of energy incident on the surface from below from all directions.

$$P_t \, d\Omega_t = \Upsilon(t) P_1 \, d\Omega_1$$

$$A \cos \theta_t \, I_t(t) \, d\Omega_t = \Upsilon(t) \, A \cos \theta_1 \, I_1(1) \, d\Omega_1$$

$$I_t(t) \, d\Omega_t = \left[\Upsilon(t) \, I_1(1) \, \frac{\cos \theta_1}{\cos \theta_t} \right] d\Omega_1 \qquad \text{(IV-65)}$$

Demonstration of the Model

Comparison to the Peake approach - It was shown that for a uniform soil moisture profile the radiation impinging on the surface from below is isotropic. With this assumption (IV-64) reduces to

$$\Upsilon(\theta_t, \phi_t) = 1 - \frac{1}{4\pi} \int_0^{2\pi} \int_0^{\pi/2} \Upsilon(1, s) \, d\Omega_s$$

and

$$I_t(\theta_t, \phi_t) = \frac{\cos \theta_1}{\cos \theta_t} \cdot$$
$$\left[1 - \frac{1}{4\pi} \int_0^{2\pi} \int_0^{\pi/2} \Upsilon(1, s) \, d\Omega_s \right] I_1(\theta_1, \phi_1) \qquad \text{(IV-66)}$$

Equation (IV-66) is equivalent to Peake's result which was derived under the assumption of thermodynamic equilibrium. Note that the derivation of (IV-66) did not require the assumption of thermodynamic equilibrium.

The equivalent Peake equation is given by

$$I_t(\theta_t, \phi_t) = \left[1 - \frac{1}{4\pi} \int_0^{2\pi} \int_0^{\pi/2} \gamma'(1,s) \, d\Omega_s'\right] I_1(\theta_1, \phi_1) \qquad (IV-67)$$

where $\gamma'(1,s)$ and $d\Omega_s'$ are defined in the upper hemisphere. Figure IV-14 demonstrates the definition of the solid angle increments. Equations (IV-66) and (IV-67) describe the relationship between the bistatic scattering coefficients defined in each hemisphere.

$$1 - \frac{1}{4\pi} \int_0^{2\pi} \int_0^{\pi/2} \gamma'(1,s) \, d\Omega_s' = \frac{\cos \theta_1}{\cos \theta_t} \cdot$$

$$\left[1 - \frac{1}{4\pi} \int_0^{2\pi} \int_0^{\pi/2} \gamma(1,s) \, d\Omega_s\right]$$

or

$$\gamma'(\theta_t, \phi_t) = \frac{\cos \theta_1}{\cos \theta_t} \gamma(\theta_t, \phi_t) \qquad (IV-68)$$

$$\frac{\sin\Theta_1}{\upsilon_{soil}} = \frac{\sin\Theta_1'}{\upsilon_{air}}$$
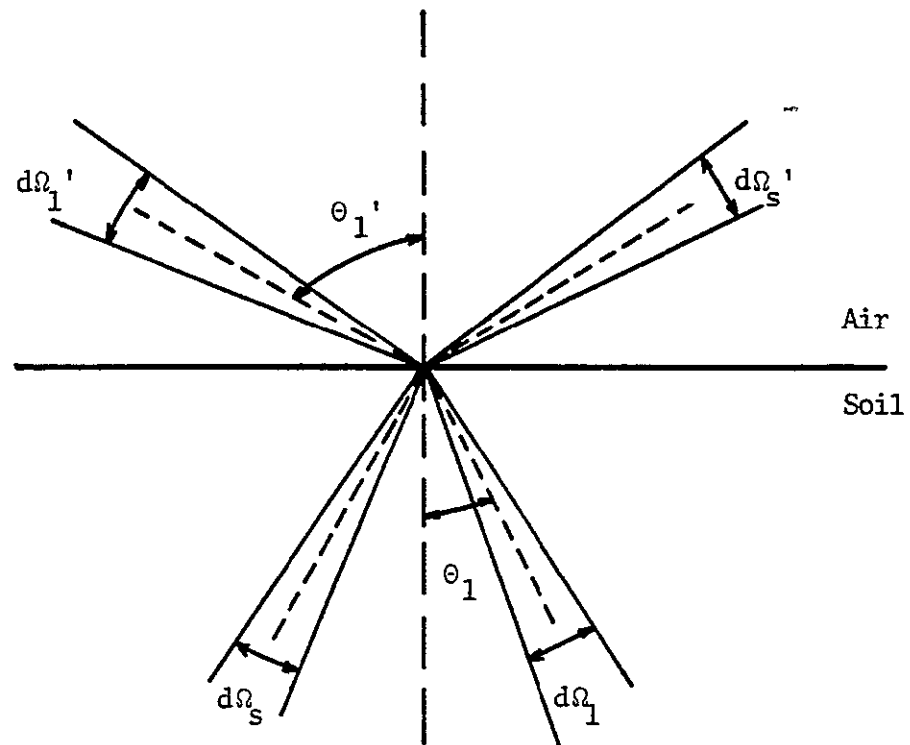
υ - phase velocity

Figure IV-14. Geometry used to relate the bistatic scattering coefficients in the hemisphere above the soil surface to the bistatic scattering coefficients in the hemisphere below the soil surface.

It is also of interest to note that for a smooth surface and uniform soil moisture profile that

$$\Upsilon(1,s) = |\rho(1,s)|^2 \, \delta(\theta_1) \, \delta(\phi_1)$$

where

$\rho(1,s)$ - Fresnel reflection coefficient

$\delta(\ )$ - Dirac delta function

So that (IV-64) becomes

$$\Upsilon(\theta_t, \phi_t) = 1 - \frac{1}{4\pi} \int_0^{2\pi} \int_0^{\pi/2} |\rho(1,s)|^2 \, \delta(\theta_1) \delta(\phi_1) \, d\Omega_s$$

(IV-69)

$$\Upsilon(\theta_t, \phi_t) = 1 - |\rho(\theta_1, \phi_1; \theta_s, \phi_s)|^2$$

as would be expected based on the Peake approach.

Computed effects of roughness - The soil moisture and surface roughness dependence of energy emitted from a soil surface can be demonstrated using (IV-65). In doing this, analytical expressions for the bistatic scattering coefficients are required. One technique of

obtaining the bistatic scattering coefficients is to use the physical optics approach to determine the scatter from a rough surface.

Leader [61] has solved the Stratton-Chu integral as modified by Silver [99] for the power reflected from a rough surface due to power incident on that surface from a particular direction. Performing an ensemble average over the surface height deviations, Leader found that

$$\frac{I_{r_i}(\theta_r,\phi_r)}{I_{i_i}(\theta_i,\phi_i)} = \left\langle \left(\frac{E_r(\theta_r,\phi_r) E_r^*(\theta_r,\phi_r)}{E_i(\theta_i,\phi_i) E_i^*(\theta_i,\phi_i)} \right) \right\rangle$$

$$(IV-70)$$

$$= \frac{2\pi A}{(4\pi R)^2} \left(a_i - \frac{m_y}{m_z} a_{y_i} \right)^2 \frac{Q m_z^2}{\left(m_z^4 + Q m_y^2 \right)^{3/2}}$$

where

$I_r(\theta_r,\phi_r)$ - average power intensity reflected into $d\Omega_r$ due to energy incident on the surface from $d\Omega_1$

A - area illuminated

R - distance to the point under consideration

$n_y = \sin \theta_r - \sin \theta_1$

$n_z = \cos \theta_r + \sin \theta_1$

i - vertical or horizontal polarization

And

$$Q_i = -\cos \theta_r \left(1 + \rho_i(\theta_i, \theta_r) \right) + \cos \theta_i \left(1 - \rho_i(\theta_i, \theta_r) \right)$$

$$Q_{y_i} = \sin \theta_i \left(1 - \rho_i(\theta_i, \theta_r) \right) + \sin \theta_r \left(1 + \right.$$

$$\left. \rho_i(\theta_i, \theta_r) \right) - \left(\cos \theta_r + \cos \theta_i \right) \frac{\partial \rho_i(\theta_i, \theta_r)}{\partial z_y} \Bigg|_{\substack{z_x = 0 \\ z_y = 0}}$$

(IV-71)

where

$\rho_i(\theta_1, \theta_r)$ - Fresnel reflection coefficient for
vertical or horizontal polarization

z_j - surface slope in the x or y direction

Equation (IV-70) is dependent on the surface statistics
through the roughness parameter Q.

$$Q = \left[k \, C'(\tau_0) \, \sigma_z^2 \right]^{-2}$$

(IV-72)

where

k - wave number

$C'(\tau_o)$ - derivative of the autocorrelation function

of the surface evaluated at τ_o

τ_o - point of expansion of $C(\tau)$ in deriving (IV-70)

σ_z^2 - surface height variance

In deriving (IV-70), Leader made the following assumptions

1) The incident wave is plane and linearly polarized.

2) Multiple interaction of irregularities such as shadowing and multiple scattering may be neglected.

3) The observation point is in the far field.

4) The Stratton-Chu integral is applied over a finite portion of a closed surface.

5) The surface can be approximated at any point as an infinite plane.

6) Only energy in the plane of incidence is considered.

Leader's [61] result, (IV-70), can be converted to a differential scattering coefficient in the following manner. The differential scattering coefficients are defined as:

$$\gamma(\theta_i,\phi_i; \theta_r,\phi_r) = \frac{4\pi R^2 I_r(\theta_r,\phi_r)}{A\cos\theta_i\, I_i(\theta_i,\phi_i)} \qquad \text{(IV-73)}$$

Separating (IV-73) into orthogonal polarization state gives:

$$\gamma_{ii}(\theta_i,\phi_i; \theta_r,\phi_r) = \frac{4\pi R^2 I_{r_i}(\theta_r,\phi_r)}{A \cos\theta_i \, I_{i_i}(\theta_i,\phi_i)}$$

(IV-74)

$$\gamma_{ji}(\theta_i,\phi_i; \theta_r,\phi_r) = \frac{4\pi R^2 I_{r_i}(\theta_r,\phi_r)}{A \cos\theta_i \, I_{i_j}(\theta_i,\phi_i)}$$

However, Leader showed that under his assumptions,

$$\gamma_{ji}(\theta_i,\phi_i; \theta_r,\phi_r) = 0$$

(IV-75)

In addition, since only energy in the plane of incidence is considered,

$$\gamma_{ii}(\theta_i,\phi_i; \theta_r,\phi_r) = \gamma_{ii}(\theta_i; \theta_r)\,\delta(\phi_i)$$

(IV-76)

where $\delta(\phi_1)$ is the Dirac delta function.

Combining (IV-70), (IV-74), (IV-75), and (IV-76) gives:

$$\gamma_{ii}(\theta_i,\phi_i;\theta_r,\phi_r) = \left[\frac{4\pi R^2}{A\cos\theta_i}\right]\frac{2\pi A}{(4\pi R)^2} \cdot$$

$$\left(a_i - \frac{m_y}{m_z}a_{y_i}\right)^2 \frac{Q m_z^2}{(m_z^4 + Q m_y^2)^{\frac{3}{2}}}\delta(\phi_i) \qquad (IV-77)$$

Noting that (IV-77) is defined for the hemisphere below the soil surface, it can be combined with (IV-64) to yield an expression for the surface transmission function.

$$\Upsilon_L(\theta_t,\phi_t) = 1 - \frac{1}{4\pi}\int_0^{\pi/2}\left[\frac{1}{2\cos\theta_i}\cdot\right.$$

$$\left.\left(a_i - \frac{m_y}{m_z}a_{y_i}\right)^2 \frac{Q m_z^2}{(m_z^4 + Q m_y^2)^{3/2}}\right]\frac{I_i(s)}{I_i(1)}\,d\theta_s \qquad (IV-78)$$

Equation (IV-78) defines that fraction of power incident on the surface from $d\Omega_1$ below the surface that is transmitted across the surface into $d\Omega_t$. Combining (IV-78) with (IV-65) provides a description of the energy emitted from the soil at the ith polarization into the direction (θ_t,ϕ_t); that is,

$$I_{k_i}(\theta_k, \phi_k) = T_i(\theta_k, \phi_k) \, I_{1_i}(\theta_1, \phi_1) \frac{\cos \theta_1}{\cos \theta_k}$$

$$BT_{soil_i}(\theta_k, \phi_k) = T_i(\theta_k, \phi_k) \, BT_{volume_i}(\theta_1, \phi_1) \frac{\cos \theta_1}{\cos \theta_k}$$

$$(IV-79)$$

In order to perform example calculations using (IV-78) and (IV-79), appropriate values of the roughness parameter, Q, must be defined. The point, τ_0, about which the derivative of the autocorrelation function is expanded increases with transmission angle, θ_t. Therefore, as seen in (IV-77), Q decreases with transmission angle, θ_t. The distribution of Q changes as the surface roughness changes. It is therefore necessary to define a Q distribution that is appropriate for each surface roughness of interest. The Q distributions that correspond to the smooth, medium and rough surfaces described in Chapter V are determined in Chapter VII (Table VII-6). These distributions are used below to demonstrate the effects of surface roughness.

Assuming uniform soil moisture and soil temperature profiles, the radiation impinging on the surface from below is isotropic. Under this condition (IV-78)

reduces to

$$T_i(\theta_t, \phi_t) = 1 - \frac{1}{4\pi} \int_o^{\pi/2} \left[\frac{1}{2\cos\theta_i} \cdot \right.$$

$$\left. \left(a_i - \frac{m_y}{m_z} a_{y_i}\right)^2 \frac{Q m_z^2}{(m_z^4 + Q m_y^2)^{3/2}} d\theta_s \right. \qquad \text{(IV-80)}$$

Using (IV-80) and (IV-79), a normalized brightness temperature can be defined as

$$NBT_i = \frac{I_{t_i}(\theta_t, \phi_t)}{I_{i_i}(\theta_i, \phi_i)} = T_i(\theta_t, \phi_t) \frac{\cos\theta_i}{\cos\theta_t} \qquad \text{(IV-81)}$$

This normalized brightness temperature corresponds to emissivity as defined by Peake [29] for the special case of uniform soil moisture and soil temperature profiles.

The effect of soil moisture for uniform profiles will be demonstrated with (IV-80) and (IV-81) or (IV-79) using the Q distributions defined in Chapter VII. Figures IV-15 and IV-16 show the emitted radiation intensity for a smooth surface at 1.4 GHz as a function of transmission angle and soil moisture. These calculations were performed assuming uniform moisture and temperature profiles. Note that transmission angle is equivalent to the definition of incident angle that is normally used to describe radar
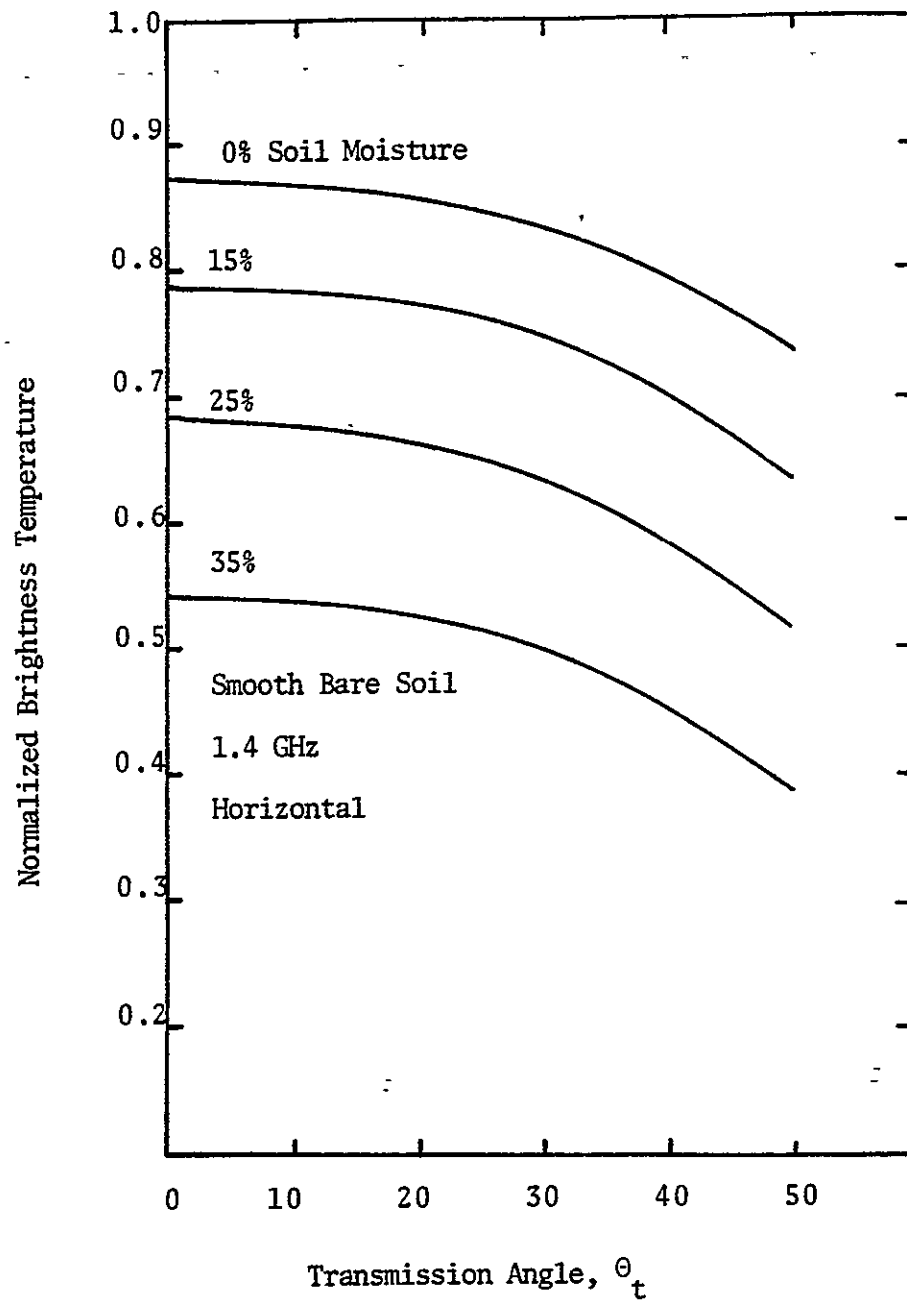
Figure IV-15. Calculated horizontally polarized emission of smooth bare soil as a function of volumetric soil moisture and transmission angle.
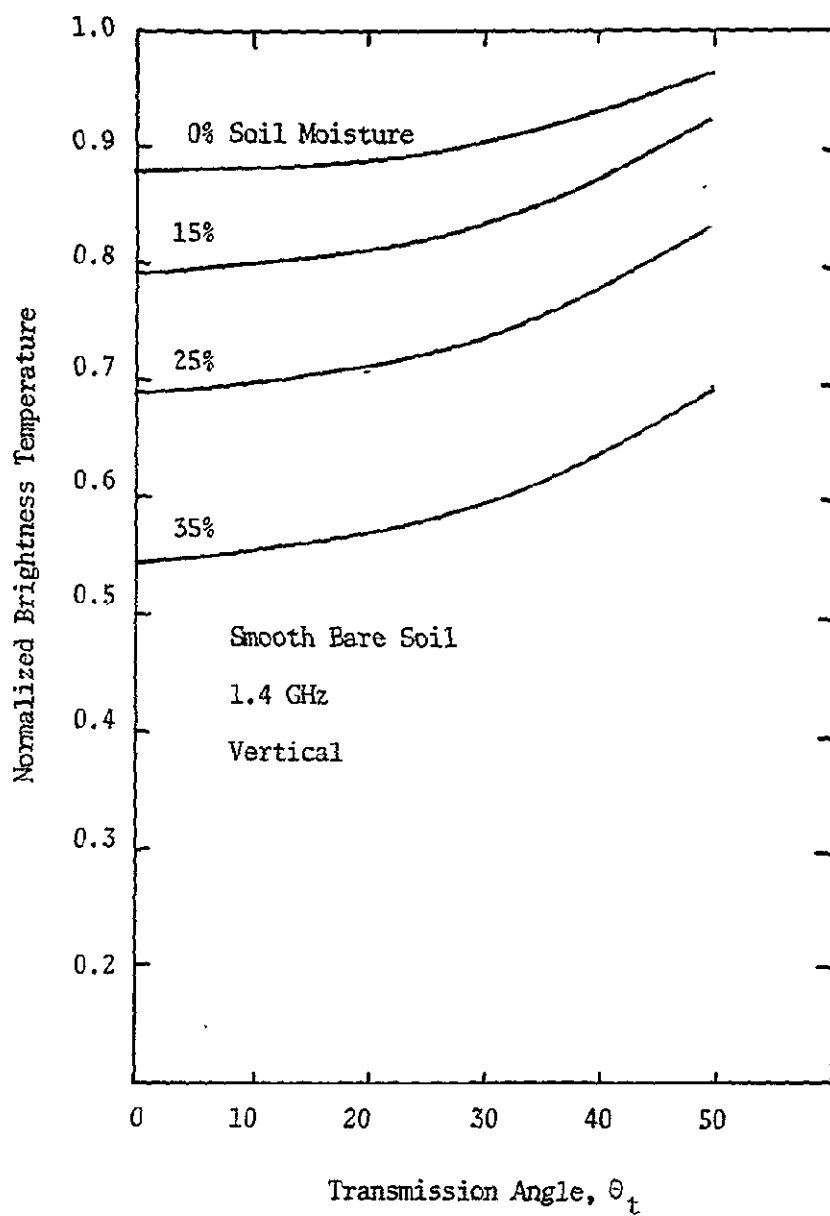
Figure IV-16. Calculated vertically polarized emission
of smooth bare soil as a function of
volumetric soil moisture and transmis-
sion angle.

backscatter. The change in emission as a function of soil

moisture for a smooth surface at nadir can be more clearly

seen in Figure IV-17. It is seen that on the average,

the emitted radiation intensity at nadir changes approxi-

mately 2.8°K per percent volumetric moisture for a smooth

surface, assuming a soil temperature of 300°K. As the

angle of transmission is increased, this slope will de-

crease for vertical polarization and slightly increase

for horizontal polarization (Figure IV-18).

The effect of surface roughness can now be demonstrated

and compared to the soil moisture and soil temperature

response of a smooth surface. For uniform soil moisture

and uniform soil temperature profiles, the emitted radia-

tion intensity is directly proportional to the soil

temperature. Since the transmission function $T_i(\theta_t, \phi_t)$

is not dependent on soil temperature, the effect of

surface roughness on the soil emission is unchanged for

different soil temperatures. However, the effect of

surface roughness does change with soil moisture. Figures

IV-19 and IV-20 show calculations of soil brightness

temperature as a function of the transmission angle

and roughness for both polarizations, a uniform soil

temperature of 300°K and a uniform soil moisture of

35 percent.
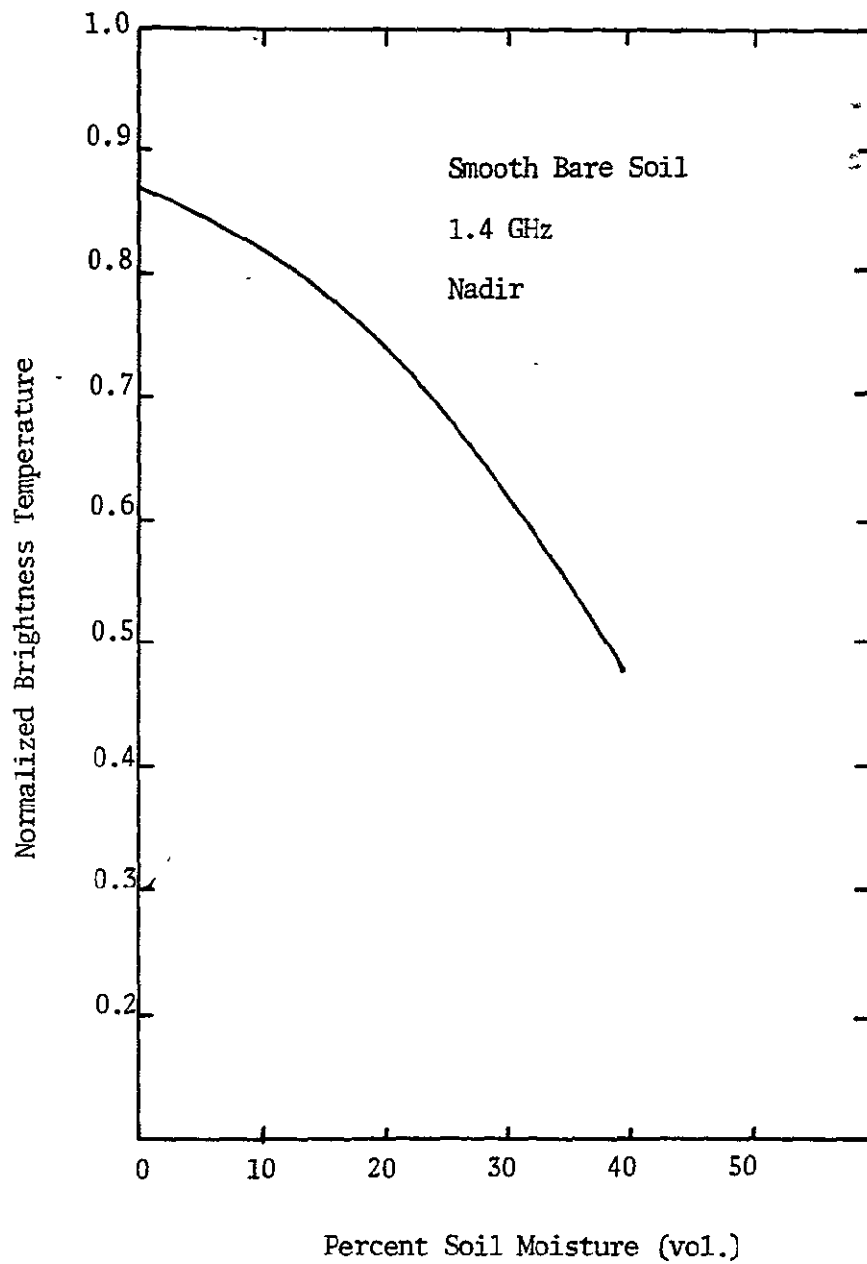
Figure IV-17. Calculated change in emission of smooth bare soil as a function of volumetric soil moisture.
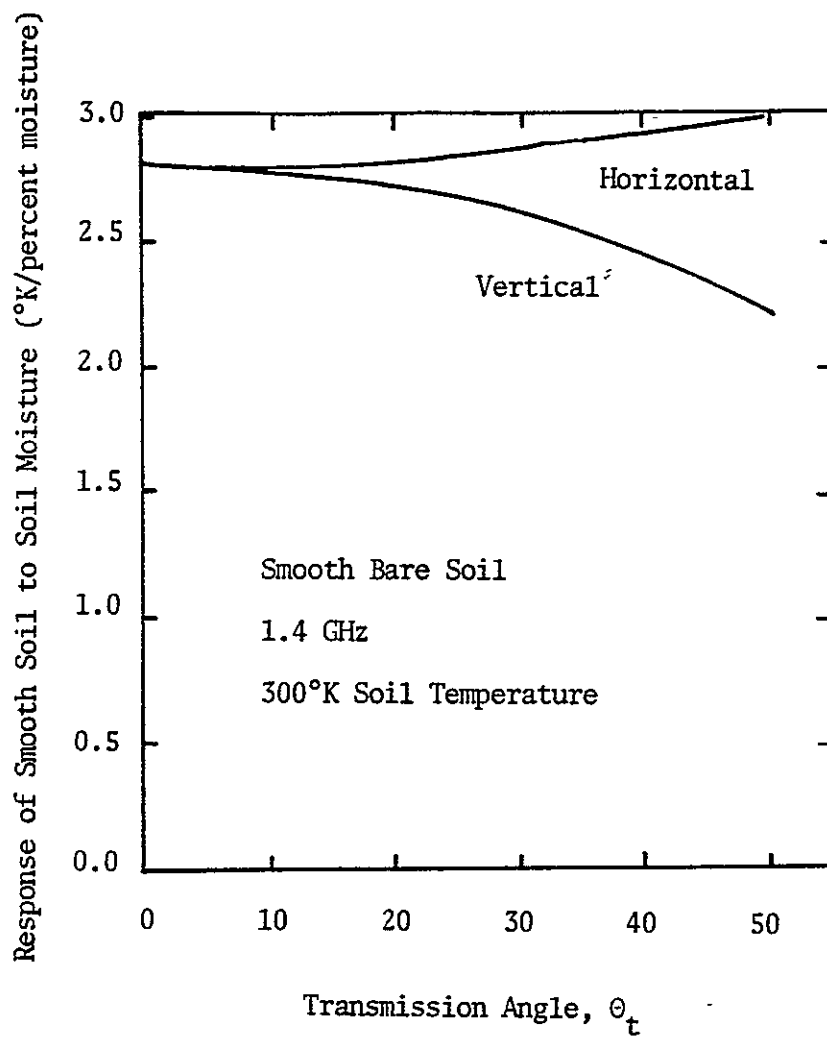
Figure IV-18. Calculated response of smooth bare
soil to volumetric soil moisture as
a function of transmission angle.
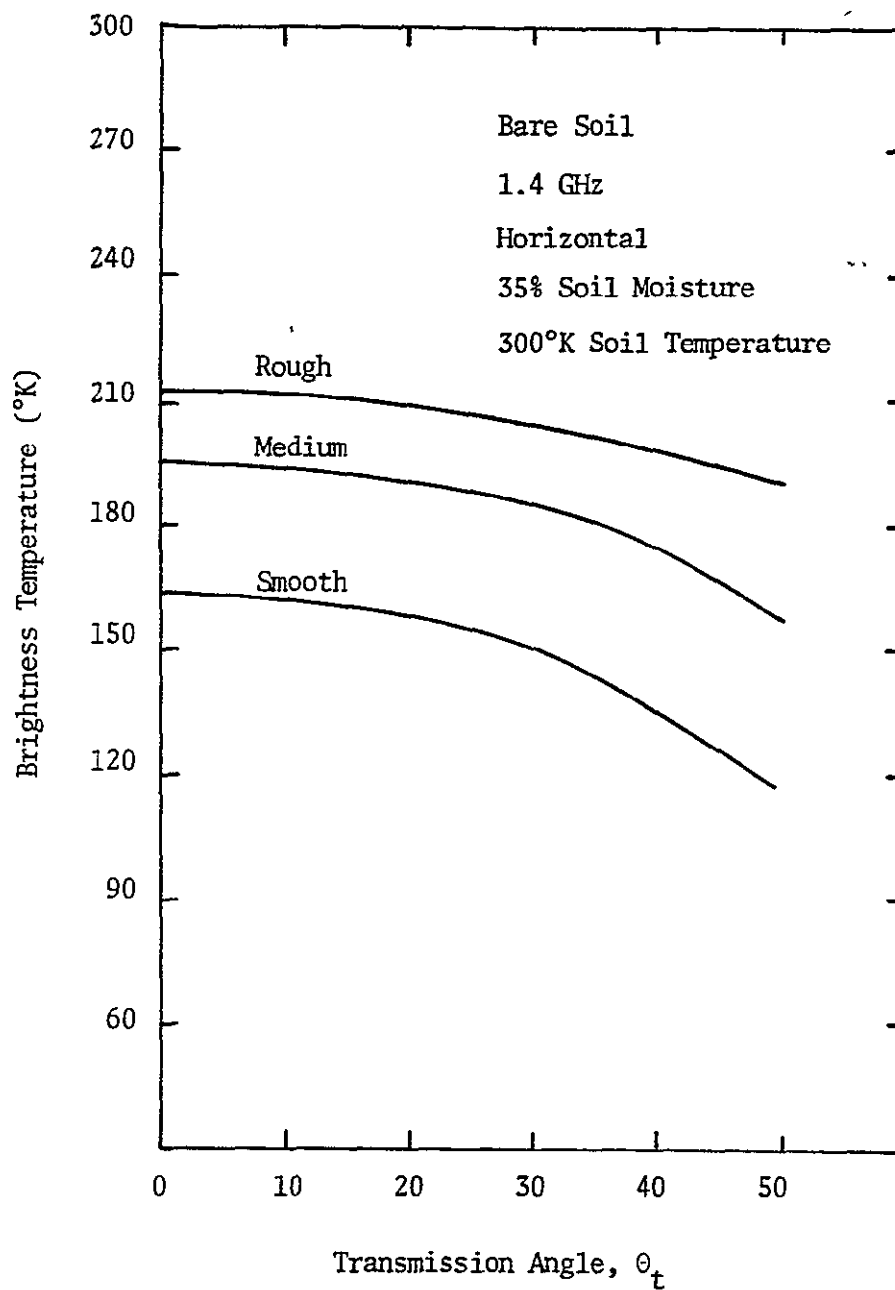
Figure IV-19. Calculated horizontal brightness
temperature of bare soil as a
function of roughness and trans-
mission angle.
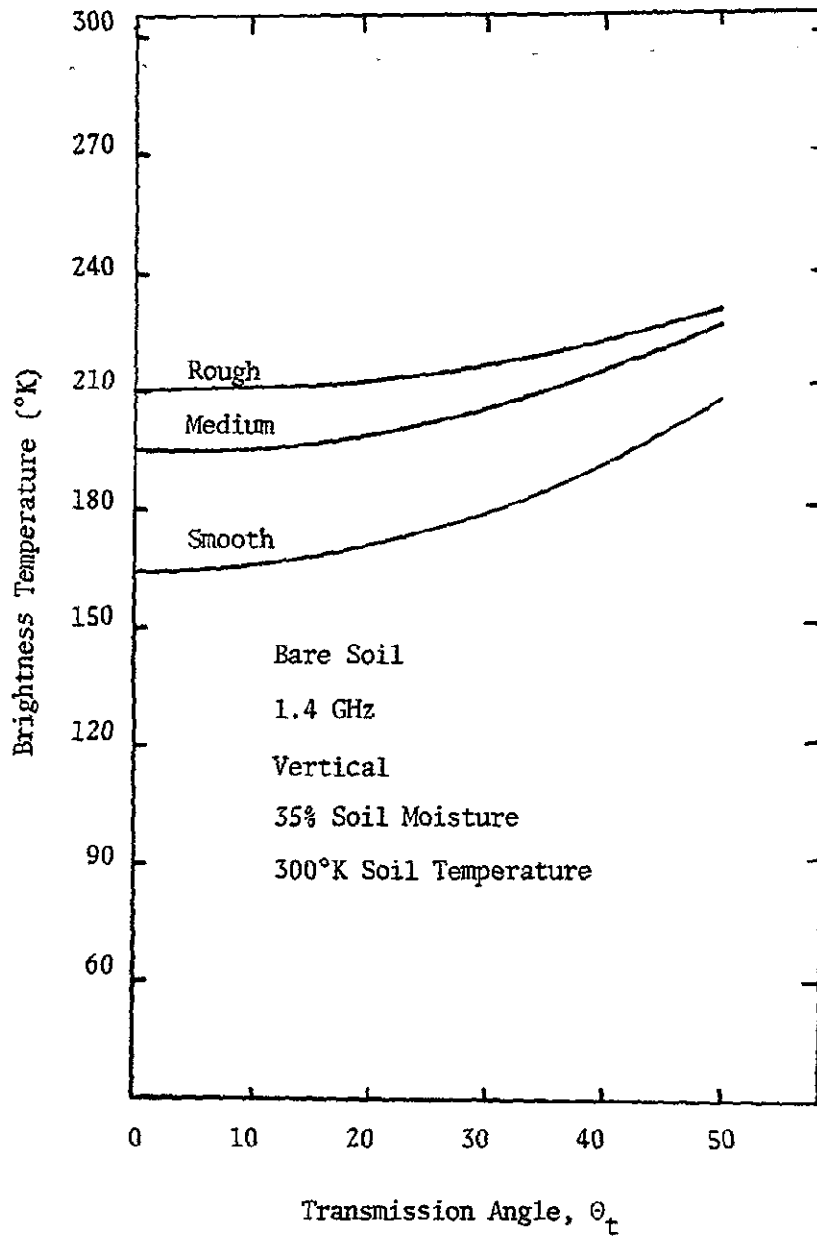
Figure IV-20. Calculated vertical brightness temperature of bare soil as a function of roughness and transmission angle.

The effect of soil moisture can be seen more clearly by plotting brightness temperature versus soil moisture at one transmission angle. Figure IV-21 is such a plot at nadir. Note that the effect of roughness is not simply a shift in brightness temperature, as is the case for soil temperature, but the roughness actually changes the response to soil moisture. As surface roughness increases, the brightness temperature increase is greater the higher the soil moisture. So, as the surface gets rougher, the response to soil moisture decreases. This is demonstrated at nadir in Figure IV-22. Figure IV-22 is a plot of the average slopes of the curves in Figure IV-21 as a function of rms surface height.

Vegetation

Model Description

Two models describing emission from vegetation were briefly presented in Chapter III, one by Sibley [75] and one by Basharinov and Shutko [78]. Each modeled the vegetation as a planar dielectric slab overlying the soil surface. Sibley modeled the transmission through the slab and Basharinov and Shutko modeled the emissivity of the slab based on the effective reflection coefficient. The main difference between the two approaches lies in their
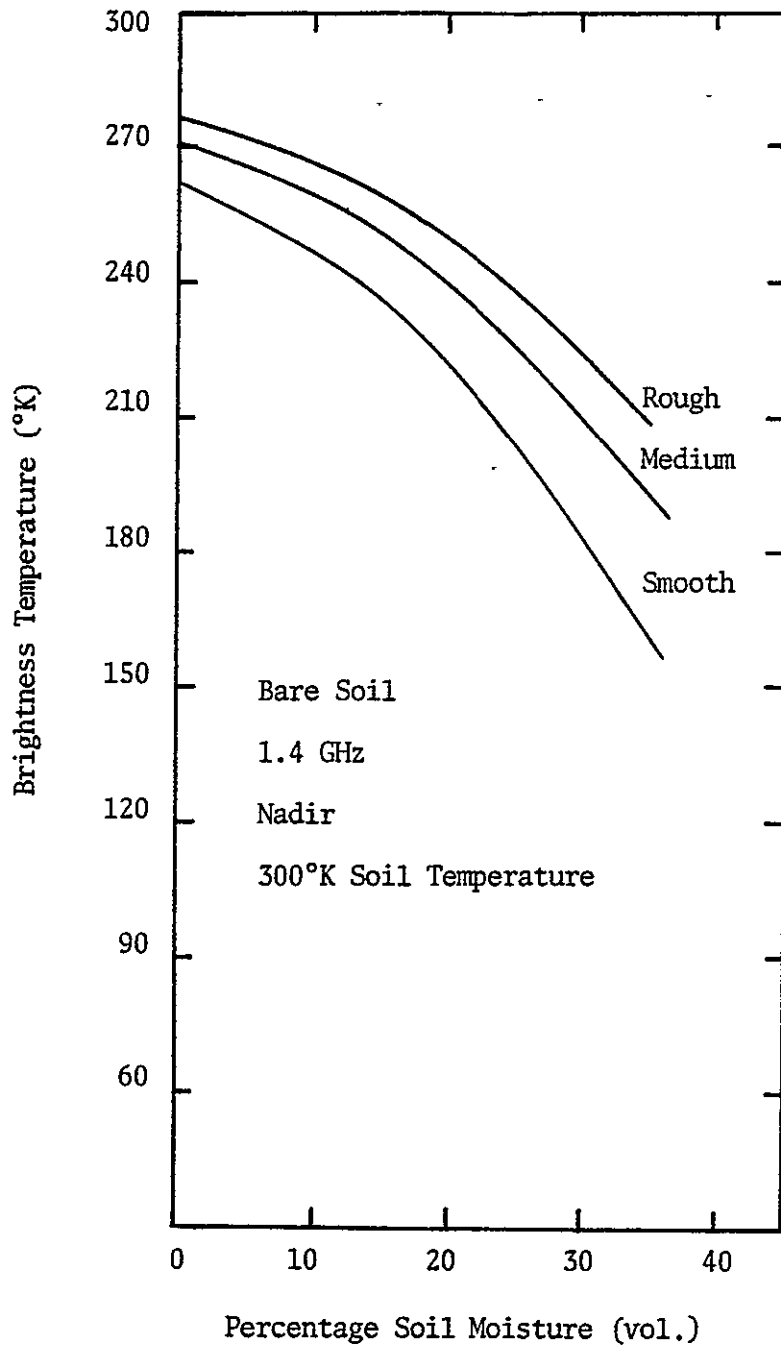
Figure IV-21. Calculated brightness temperature
of bare soil as a function of
roughness and soil moisture.
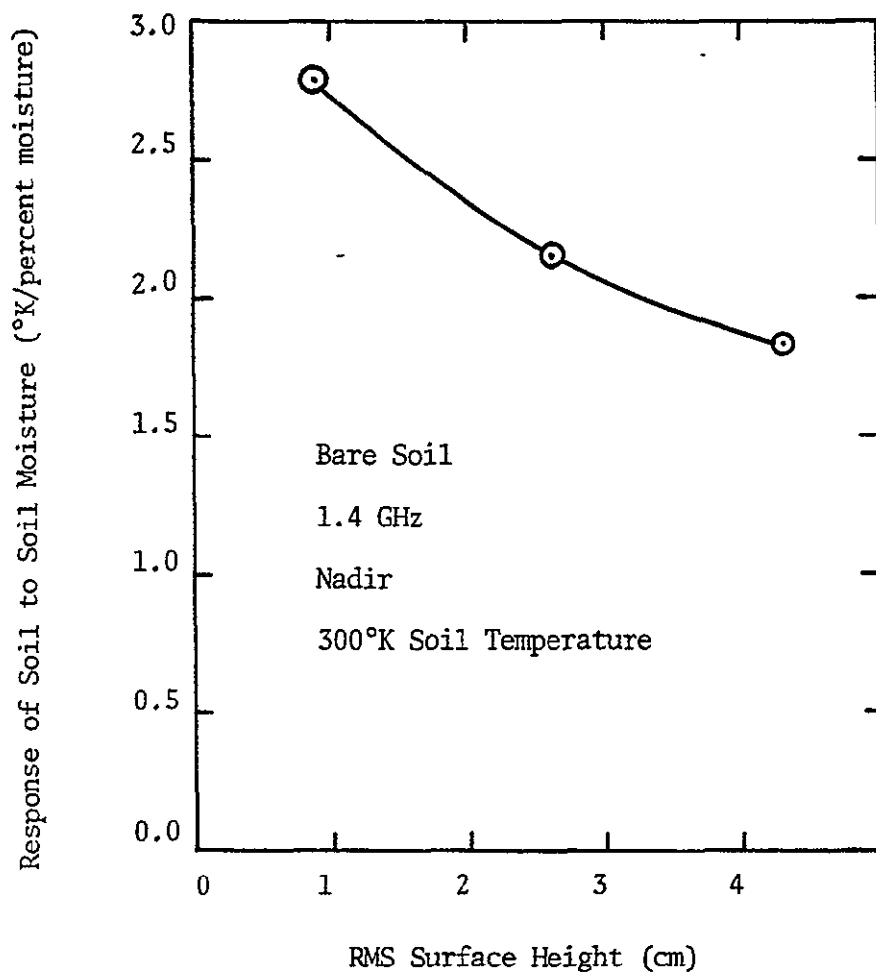
Figure IV-22. Change in the response of bare soil emission to soil moisture as a function of surface roughness.

respective techniques of determining the propagation properties of the slab.

Basharinov and Shutko [78] modeled the optical depth of the vegetation slab by assuming that the water in the plant volume was either a fog or precipitated water. Sibley [75] calculated the permittivity of the vegetation based on a mixing formula. He then used this permittivity to calculate the attenuation of energy emitted from the soil as it propagated through the vegetation, and to calculate the emission of the vegetation.

It has been shown by Lee [91] and Newton et al. [92] that Sibley's approach is sufficient to describe the general effects of vegetation. In addition, Waite and Cook [74] concluded that scattering within the vegetation canopy could be neglected. As a result, Sibley's approach will be utilized in this document.

Sibley's [75] vegetation model is based on the fact that energy is radiated from a soil volume, across the surface boundary and through the vegetation canopy. The radiative transfer model describes the emission from the soil volume,and the surface model presented in the previous section describes the effects of the surface. These two models together describe the brightness temperature of the soil.

For vegetated surfaces the brightness temperature
of the soil is simply modified to account for propagation
through the vegetation layer. This requires calculating
the attenuation coefficient of the planar vegetation slab.
Only the permittivity of the vegetation slab must be
specified in order to calculate this coefficient.

Sibley [75] used the Weiner model for a dielectric
mixture as presented by Evans [76] to calculate the
permittivity of the vegetation slab. In doing this,
Sibley postulated that the vegetation was a mixture of
vegetation (primarily water) and air. The resulting
equation for the permittivity of the vegetation canopy
is:

$$\epsilon_m = \frac{\epsilon_v (1 + pu) + u(1-p)}{\epsilon_v (1-p) + p + u} \qquad (IV-82)$$

where ϵ_v is the relative permittivity of the vegetation,
p is the fraction of the canopy volume which is occupied
by vegetation, and u is a parameter called the Formzhal
which describes the dispersion of one medium within the
other.

The selection of u is not critical and is generally
assumed to be in the range of 10 to 25. Peake and
Oliver's [77] formulation of the permittivity of vegetation
was used in the dielectric mixture calculation. It is
given as

$$\varepsilon_v = \frac{F}{2} \, \text{Real}(\varepsilon_w) + j\frac{F}{2} \, \text{Imaginary}(\varepsilon_w)$$ (IV-83)

where F is the fraction of water by weight in the plant
and ε_w is the relative permittivity of water. The Debye
form of the permittivity of water was used and is given
by [100], [101].

$$\varepsilon_w = \varepsilon_\infty + \frac{\varepsilon_s - \varepsilon_\infty}{1 + j\left(\frac{f}{f_0}\right)}$$ (IV-84)

The parameter ε_∞ is generally chosen to be 5.5 while

$$\varepsilon_s = 87.7 - 0.4(t - 273)$$ (IV-85)

and

$$f_0 = 9.0 + 0.405(t - 273)$$

t is the temperature of the canopy in degrees Kelvin and f is frequency.

Uniformly vegetated surface - It will first be
assumed that the soil is covered by a homogeneous
dielectric layer with permittivity described by (IV-82).
Neglecting atmospheric effects, there are two processes
through which the emission of bare ground is modified by
a vegetation layer. The emission from the bare ground,
described by (IV-79) is attenuated as it propagates
through the canopy. Also, thermal radiation from the
canopy augments the radiation from the soil surface.

The magnitude of a field having propagated a distance
H through a lossy dielectric is

$$ E = E_o e^{-\alpha H \sec \theta_t} \qquad \text{(IV-87)} $$

where E_o is the initial field strength, θ_t is the trans-
mission angle, and α is the attenuation constant given by

$$ \alpha = \left[\frac{\mu_o \mu_{r_v} \varepsilon_o \varepsilon_{r_v}}{2} \sqrt{1 + \left(\frac{\varepsilon''_{r_v}}{\varepsilon'_{r_v}}\right)^2} - 1 \right]^{1/2} \qquad \text{(IV-88)} $$

where

μ_{r_v} - relative permeability of the vegetation (≈ 1.0)

ϵ'_{r_v} - real part of the relative permittivity of the vegetation

ϵ''_{r_v} - imaginary part of the relative permittivity of the vegetation

Average power density is proportional to the square of the magnitude of the electric field, and the brightness temperature of the soil is proportional to emitted power density. As a result, the component of the brightness temperature of the soil-vegetation complex that is due to the brightness temperature of the soil passing through the vegetation is

$$\left(BT_{soil-vegetation}\right)_{soil\ component} = BT_{soil}\ e^{-2\alpha H \sec \theta_t}$$

(IV-89)

In addition to the attenuation of the emission from the soil, the vegetation layer also contributes to the total brightness temperature of the soil-vegetation complex. Assuming that all points within the canopy emit radiation

equally, the canopy contribution can be derived from the
general expression for the radiation intensity of a
dielectric layer of thickness H.

$$BT_v = \int_0^H B(h) \, e^{-\int_h^H a(z) \sec \theta_t \, dz} \sec \theta_t \, dh \qquad \text{(IV-90)}$$

where

BT_v - brightness temperature of the vegetation

$B(h)$- differential source function

$a(z)$- power attenuation constant at height z;

$\qquad a(z) = 2 \, \alpha(z)$

Sibley [75] assumed that the source function in the
vegetation is equal to

$$B(h) = t(h) \, \varepsilon_s(h) \qquad \text{(IV-91)}$$

where

t(h) - temperature of the canopy at height h

ε_δ(h) - differential emission coefficient at height
h (radiation per unit length)

Assuming that the temperature, attenuation constant, and source function are constant with the canopy, (IV-90) reduces to

$$BT_v = t_v \left(\frac{\varepsilon_s}{2\alpha}\right)\left(1 - e^{-2\alpha H \sec \theta_t}\right)$$

(IV-92)

Sibley [75] points out that if the system is in thermal equilibrium, the differential emission coefficient is equal to the absorption coefficient, 2α. Since the condition is often violated in a plant canopy, Sibley assumes that the emission coefficient is equal to

$$\varepsilon_\delta = f\, 2\alpha$$

(IV-93)

where f is an energy transfer factor. Thus,

$$BT_v = t_v\, f\left(1 - e^{-2\alpha H \sec \theta_t}\right)$$

(IV-94)

If f<1 the canopy is gaining energy, and if f>1 the canopy is loosing energy.

The total brightness temperature of the soil-vegetation complex (for a uniform cover of vegetation) can now be written as

$$BT_{soil-vegetation} = BT_{soil} \, e^{-2\alpha H \sec \theta_t} + BT_v \qquad \text{(IV-95)}$$

Calculations based on these equations will be given below.

Row crops - Sibley [75] also developed the equations that describe the effect of row planted vegetation on the emission of soil. The equations describing the emission and attenuation characteristics of uniform vegetation were simply modified to account for the geometry of the rows. The rows are assumed to consist of uniform vegetation with a rectangular cross section. Figure IV-23 denotes the geometry of the situation. The direction from which the scene is observed is denoted by θ_t, the incident angle, and ϕ_t, the azimuth angle. Both θ_t and ϕ_t can only assume values less than or equal to $\pi/2$. The direction $\theta_t = 0°$ is normal to the surface, and $\phi_t = 0°$ is perpendicular to the rows.
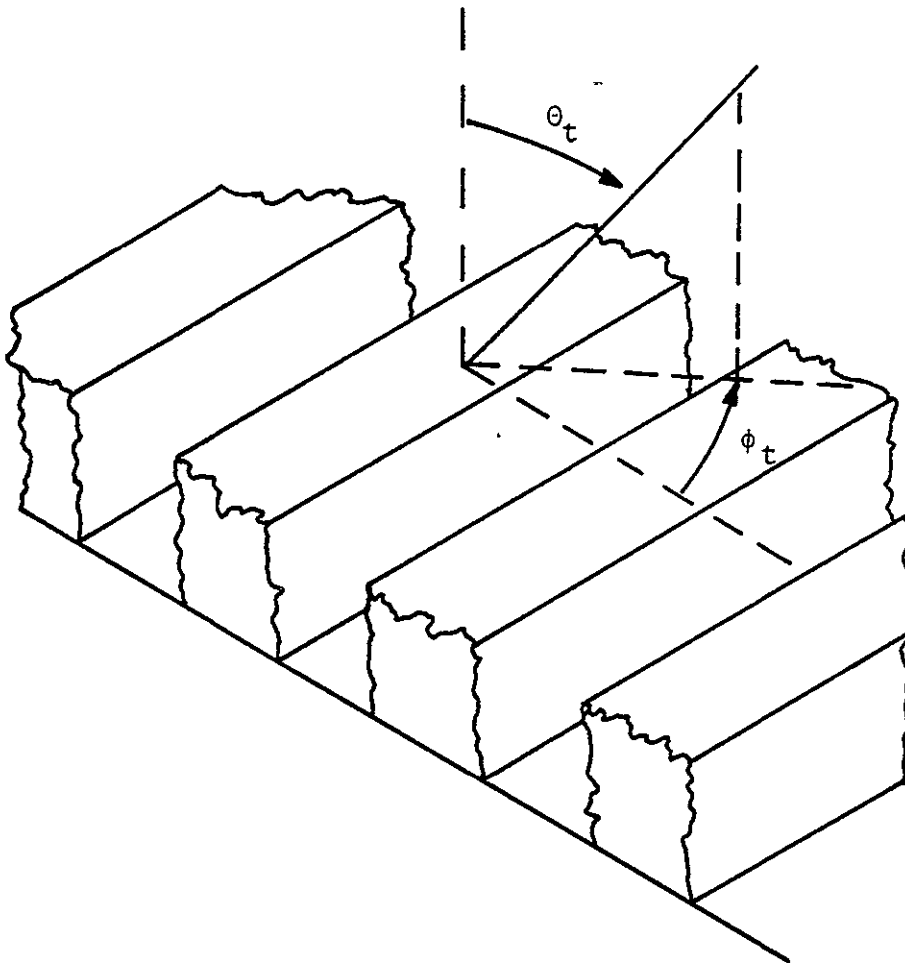
Figure IV-23. Geometry for radiation from row
vegetation (after Sibley [75]).

A cross-sectional view of the rows is given in Figure IV-24. The height and width of the rows are denoted by H and W, respectively. The width of the non-vegetated space between the rows is denoted by A. The dimension B is denoted on Figure IV-24 and also on Figure IV-25. It is given as

$$B = H \tan \theta_t \cos \phi_t \qquad \text{(IV-96)}$$

Note that the length (A + W), the row period, may be considered a unit length. The power radiated into direction (θ_t, ϕ_t) by any region of length (A + W) is the same. As a result, the brightness temperature of an entire field with uniform row spacing is given by the average power radiated from any region (A + W) long.

If B < A only a portion of the power radiated from the soil experiences attenuation. The <u>average</u> length of path the energy must traverse through the vegetation canopy is used as the length over which the radiation experiences attenuation. This average distance is determined by first projecting the cross sectional area of the canopy into the plane of incidence as shown in Figure IV-26(a). This projected cross sectional area is

$$H W \sec \theta_t \qquad \text{(IV-97)}$$

B < A

B > A
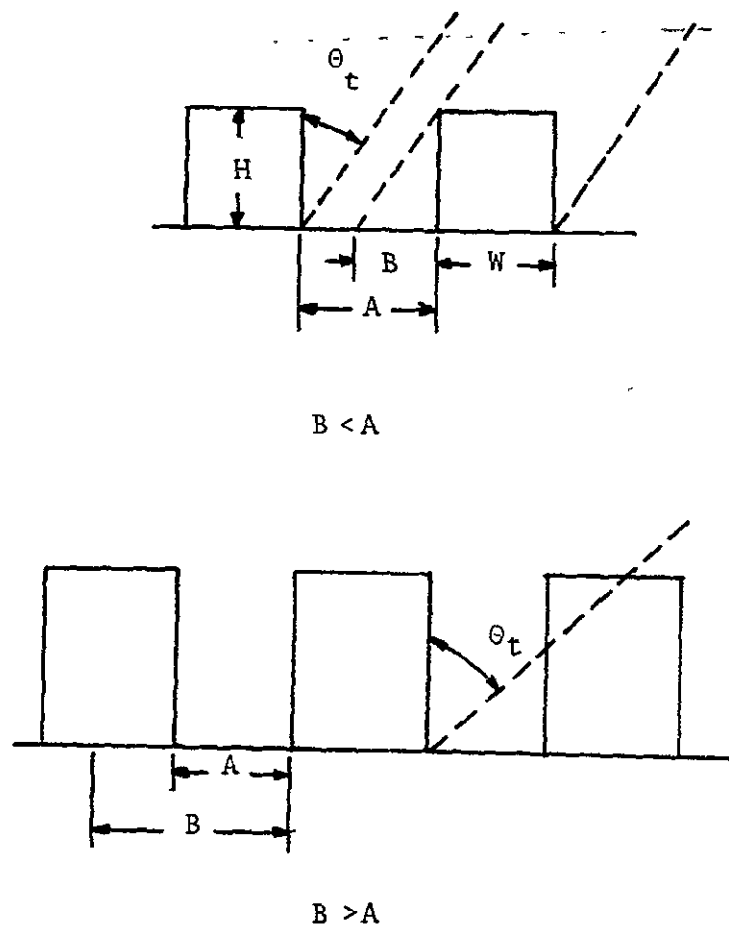
Figure IV-24. Geometry for emission perpendicular
to rows (after Sibley [75]).
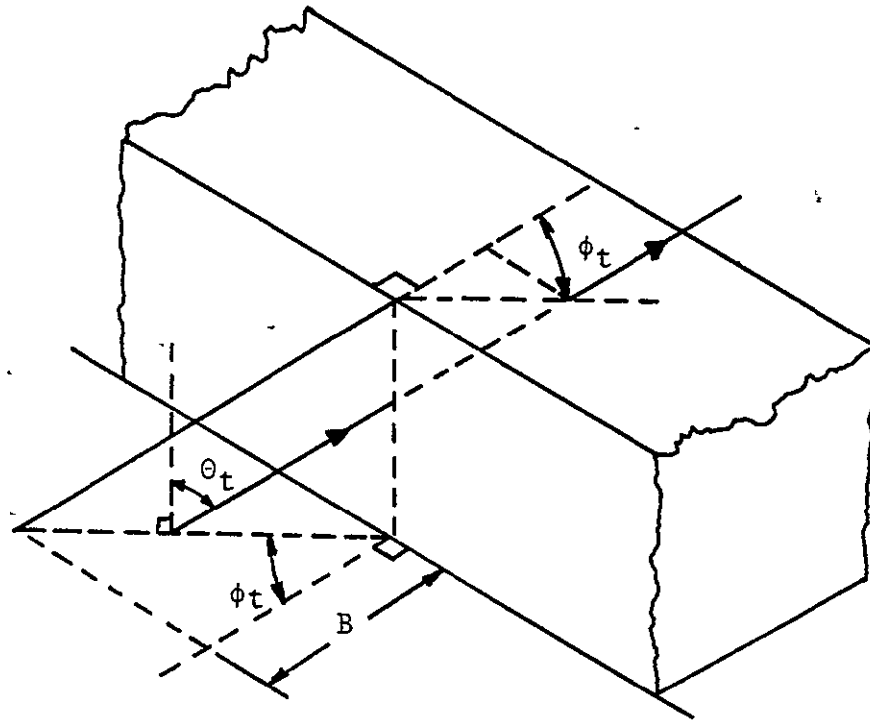
Figure IV-25. Geometry for propagation through a row canopy at an arbitrary azimuth angle (after Sibley [75]).

(a)

(b)
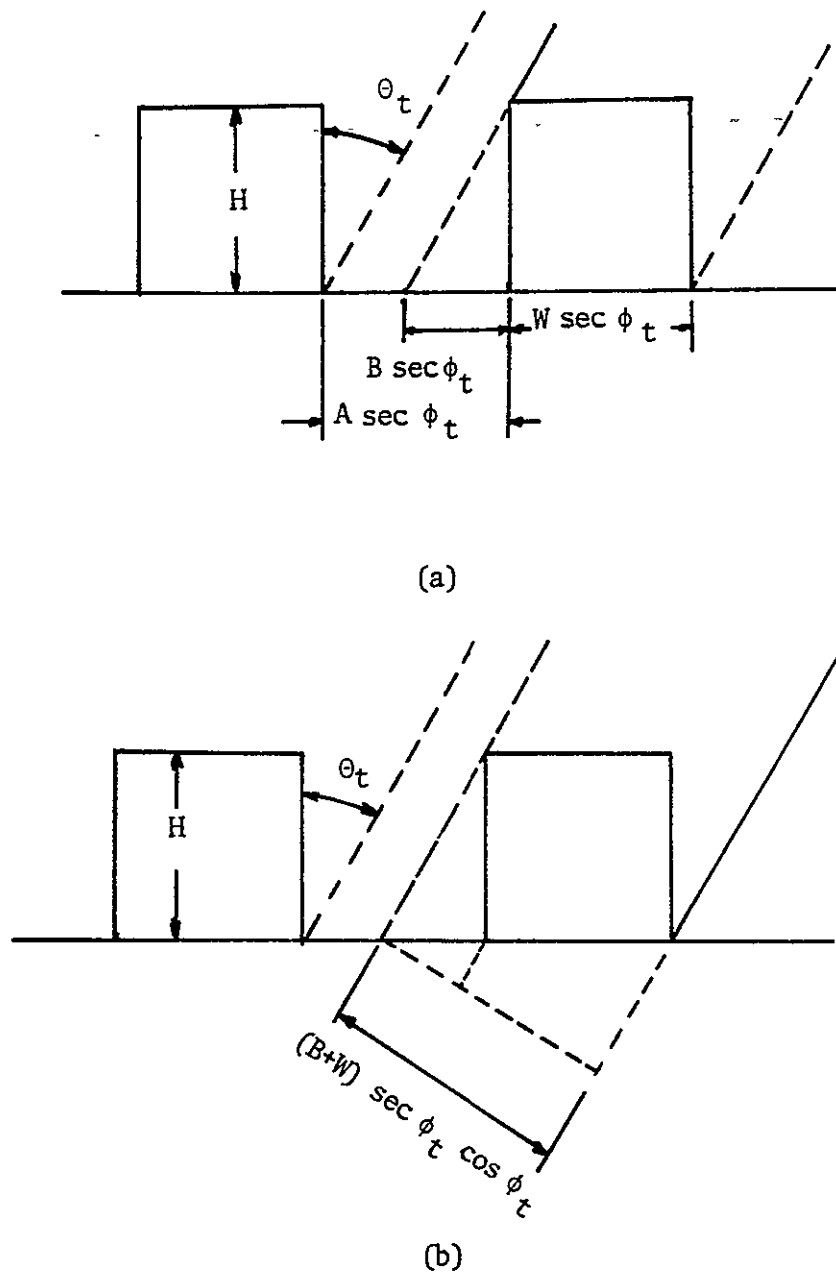
Figure IV-26. Geometry used to aid in the explanation of the average distance the soil emission must traverse through a row canopy for arbitrary azimuth and transmission angles.

Secondly, the projection of (B+W) onto the plane of incidence,

$$(B+W) \sec \phi_t \qquad \text{(IV-98)}$$

is projected onto the plane perpendicular to the direction of propagation (Figure IV-26(b)). This projection is

$$(B+W) \sec \phi_t \cos \theta_t \qquad \text{(IV-99)}$$

Dividing (IV-97) by (IV-99) results in the average distance the radiation must traverse through the vegetation for the case B < A.

$$d = \frac{HW \sec \phi_t}{(B+W) \sec \phi_t \cos \theta_t} \qquad \text{(IV-100)}$$

If B > A all of the soil is either covered or shadowed by vegetation. For this case the average attenuation distance is

$$d = \frac{HW}{(A+W) \cos \theta_t} \qquad \text{(IV-101)}$$

For simplicity, a special function will be defined to account for the differences in the two cases, $B > A$ and $B < A$.

$$L(A,B) = B \quad \text{when} \quad B < A$$

$$L(A,B) = A \quad \text{when} \quad B \geq A \tag{IV-102}$$

Utilizing this function, the apparent temperature of row crops is given by

$$BT_{row} = \frac{[A - L(A,B)] BT_{soil} + [L(A,B) + W] BT_{soil-vegetation}}{A + W} \tag{IV-103}$$

where BT_{soil} is defined by (IV-79), and $BT_{soil-vegetation}$ is defined by (IV-95). However, the average attenuation distance is now given by

$$d = \frac{HW}{(L(A,B) + W) \cos \theta_t} \tag{IV-104}$$

Model Demonstration

Uniform vegetation - Sibley's [75] formulation for
a uniform cover of vegetation over smooth soil (with
uniform temperature and moisture profile) is demonstrated
in Figure IV-27. These data show that as vegetation
density is increased, the apparent temperature also in-
creases until eventually the dependence of the apparent
temperature on soil moisture is completely masked. This
effect is also apparent if vegetation density is held
constant and frequency is increased (Figure IV-28).
Therefore, as the frequency of the measurement is increased,
the ability to detect soil moisture deteriorates. Figure
IV-28 also demonstrates the effect of a temperature dif-
ference between the soil and vegetation canopy.

As evidenced by Figures IV-27 and IV-28, computations
based on Sibley's [75] formulation indicate that the
sensitivity of apparent temperature to variations in
moisture content depend on several parameters. For a
uniform canopy of 100% coverage over a smooth surface,
the vegetation volumetric density, vegetation height,
frequency, and transmission angle affect the sensitivity
to moisture. Since there are several parameters that
affect the sensitivity in the same manner, there are
numerous equivalent states. However, it was determined
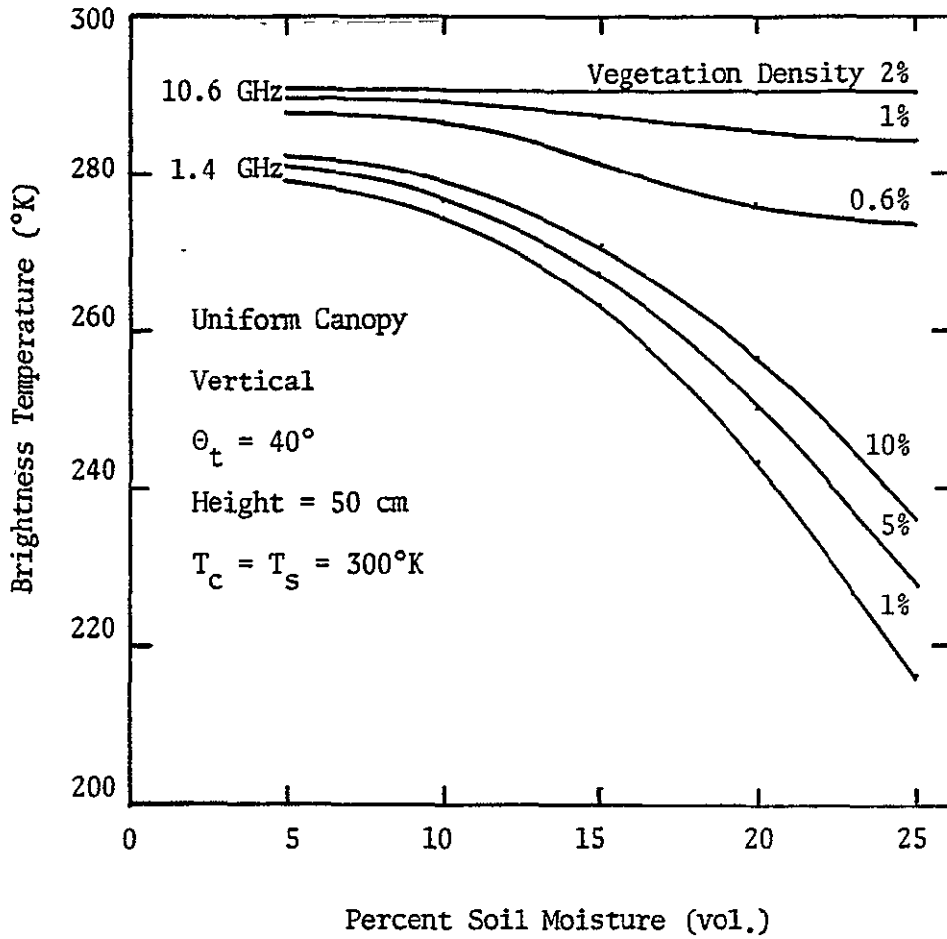
Figure IV-27. Vertically polarized brightness
temperature of a uniform canopy
as a function of soil moisture
and vegetation density.
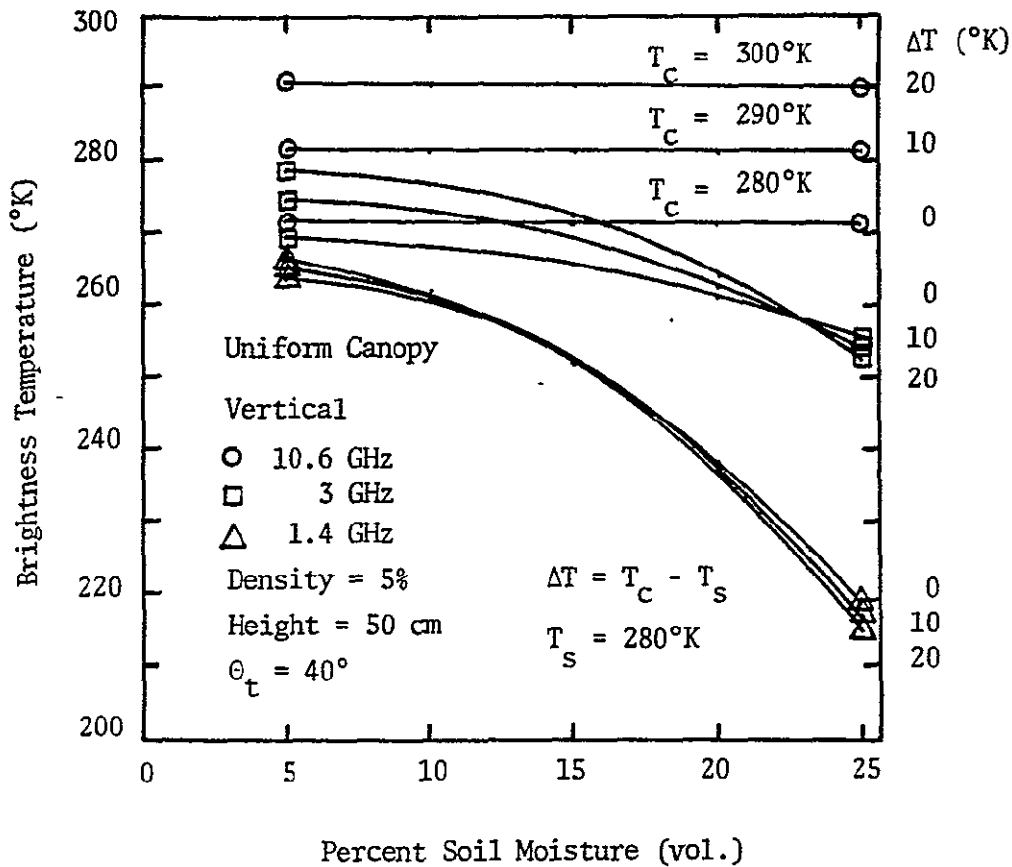
Figure IV-28. Vertically polarized brightness temperature of a uniform canopy as a function of soil moisture for three combinations of vegetation and soil temperatures.

that equivalent states have approximately equal vegeta-
tion height-density products. It was also determined that
equivalent states were independent of transmission angle.

Figure IV-29 is a plot of measured soil moisture
content (based on Sibley's formulation) against height-
density product. As the height-density product increases,
the apparent soil moisture that could be measured using
an airborne radiometer decreases. In addition, the rate
of decrease is higher as the frequency of the measurement
increases. However, it is of significance to note that
in the L-band frequency region it appears that there is a
potential of measuring soil moisture in the presence of
normal vegetation.

Row vegetation - Calculations based on the equation
for row crops (Figures IV-30 and IV-31) show that the
sensitivity to changes in moisture are highly dependent
on the azimuth angle as would be expected. Figures IV-32
and IV-33 illustrate this dependence for uniform soil
moisture of 20% and several transmission angles. As
expected, the lower the transmission angle the smaller the
effect of the azimuth angle. As a result, the optimum
transmission angle for remote sensing soil moisture through
vegetation is nadir for both uniform and row planted
vegetation.
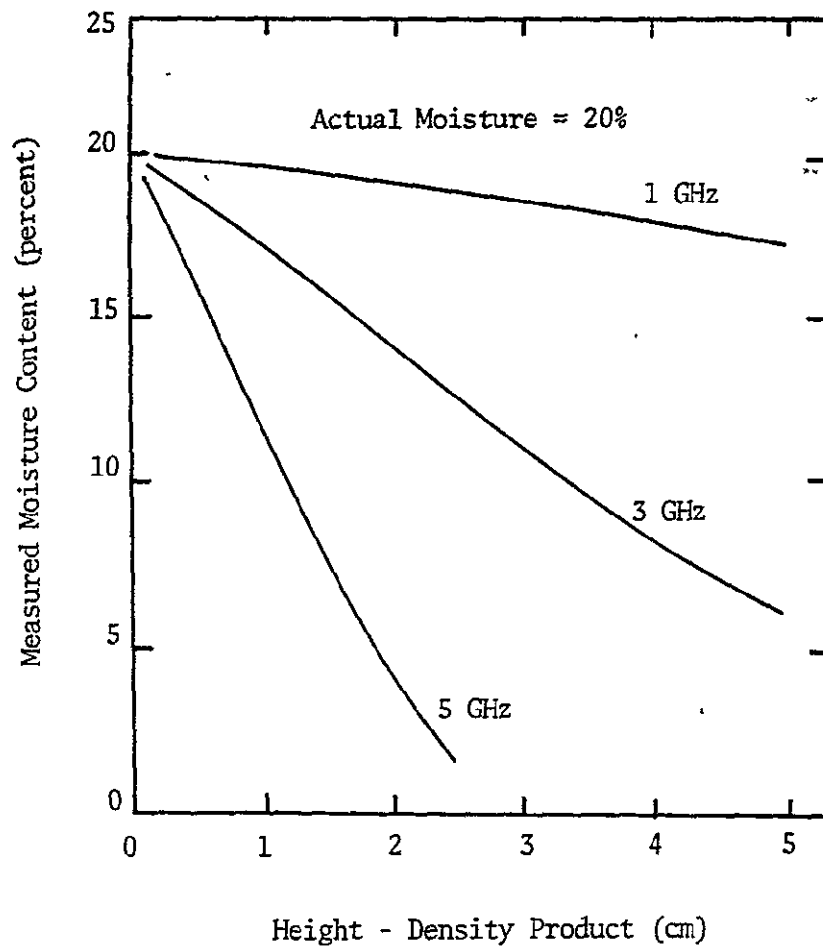
Figure IV-29. Moisture content determined from
apparent temperature of vegetated
soil (after Sibley [75]).
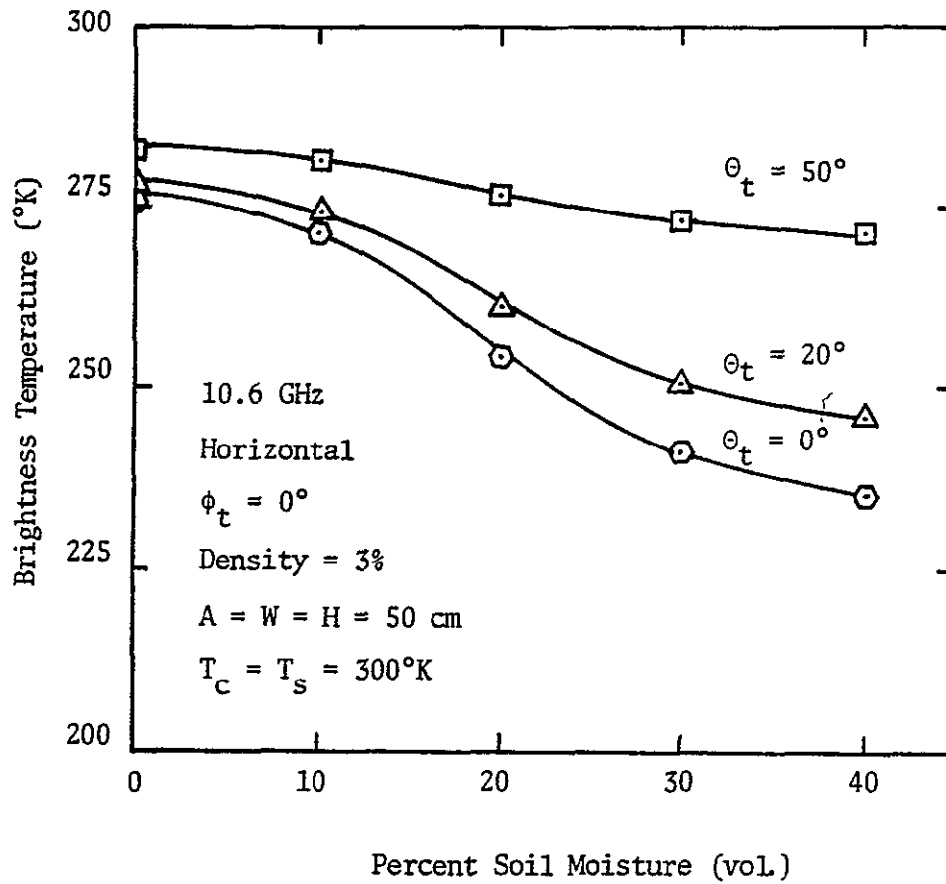
Figure IV-30. Brightness temperature of row
vegetation at 10.6 GHz as a function
of soil moisture and transmission
angle looking perpendicular to the
rows.
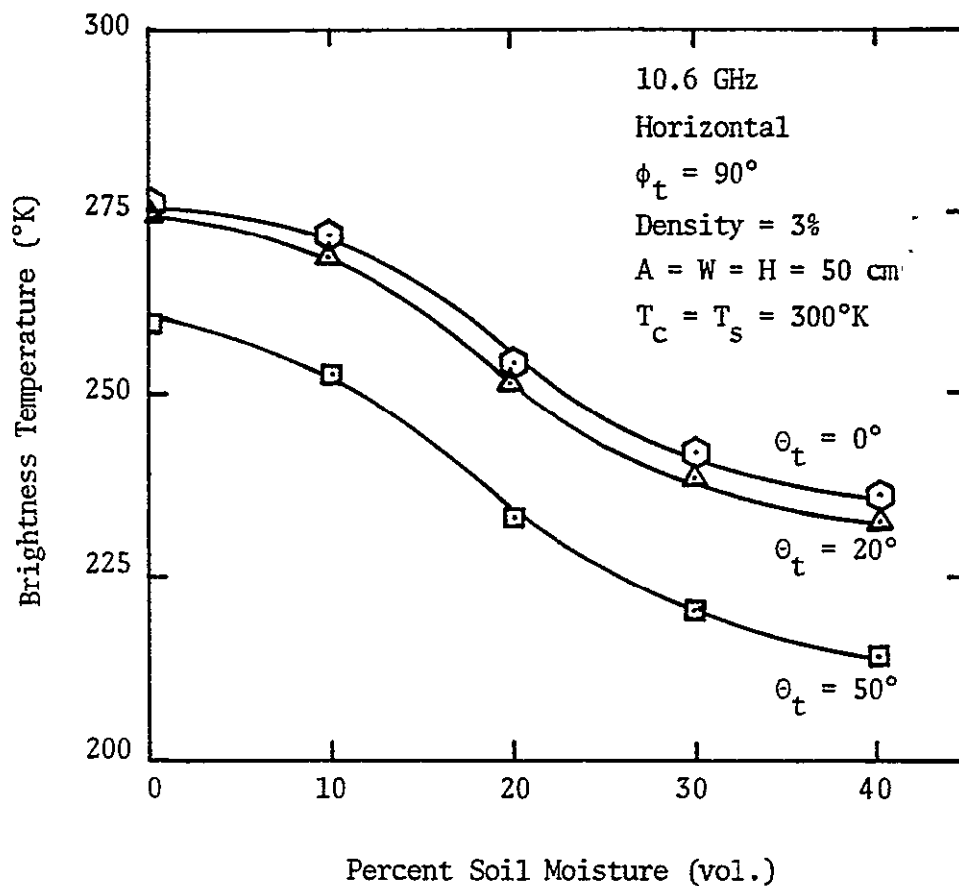
Figure IV-31. Brightness temperature of row vegetation
at 10.6 GHz as a function of soil moisture
and transmission angle looking parallel
to the rows.
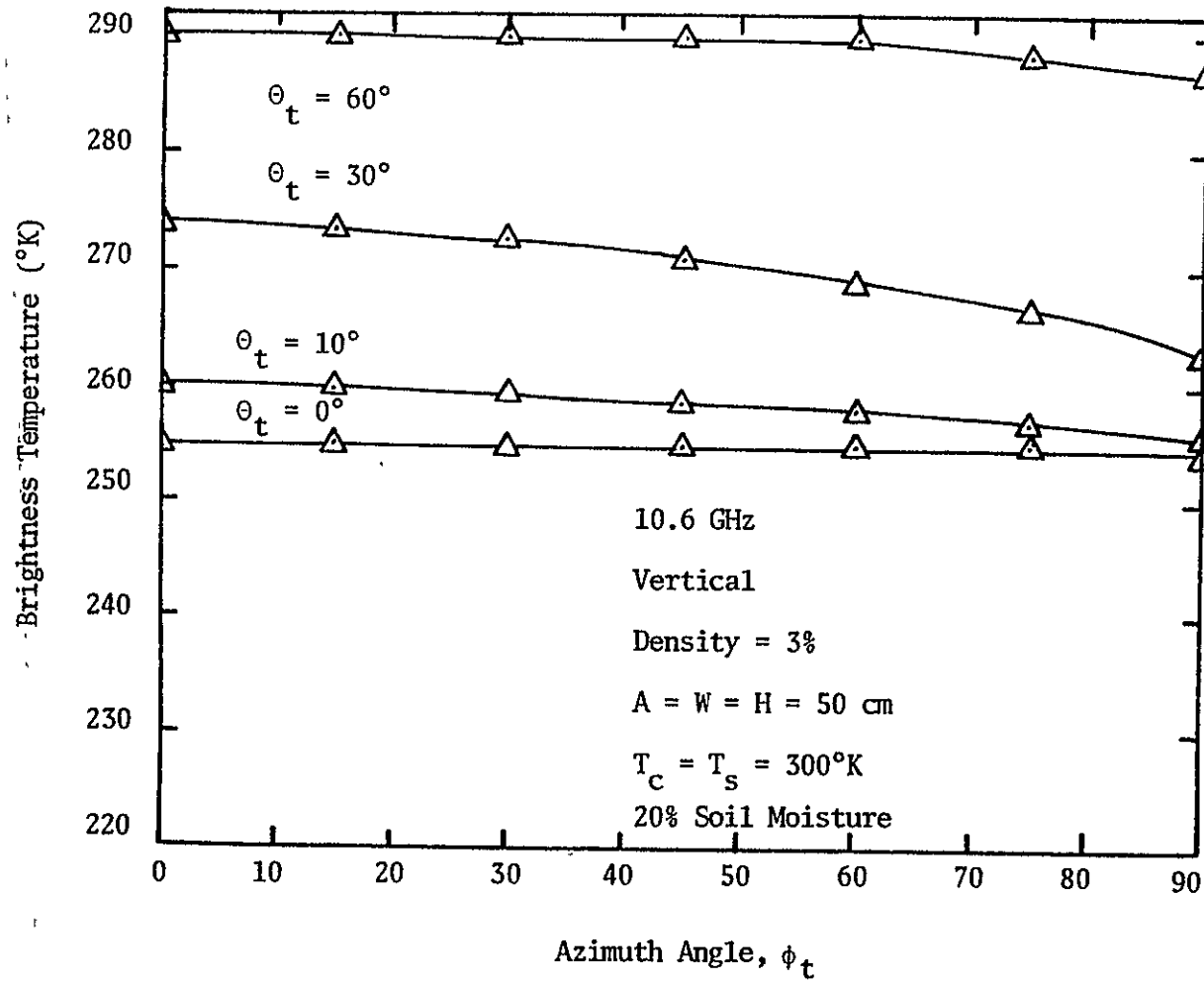
Figure IV-32. Vertical brightness temperature of row vegetation as a function of transmission and azimuth angles.
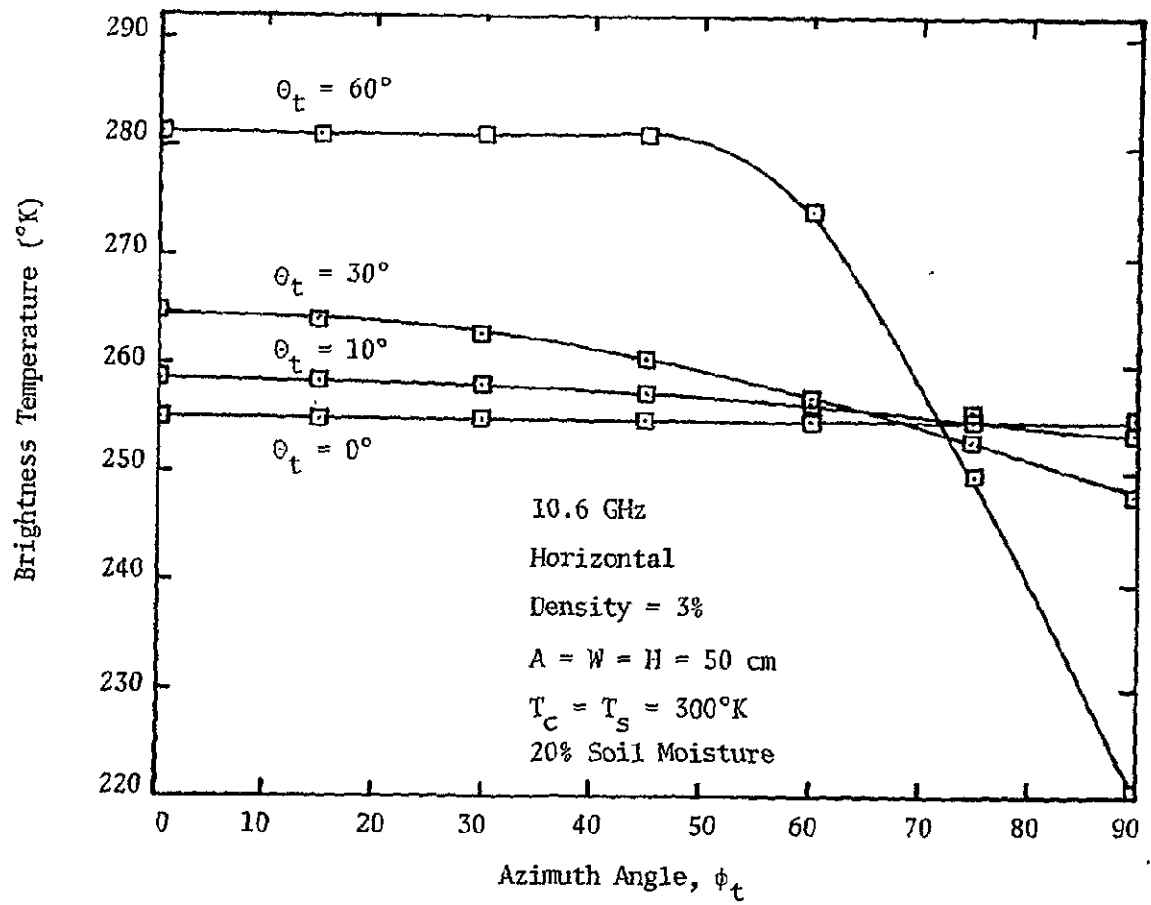
Figure IV-33. Horizontal brightness temperature of row vegetation as a function of transmission and azimuth angles.

CHAPTER V

MEASUREMENT PROGRAM

An on-going systematic measurement program designed
to measure the effects of scene parameters such as soil
moisture, soil temperature, surface roughness and vegetation
cover on the microwave emission of soil was initiated by
Texas A&M University (TAMU) in 1973. This program has been
funded by the NASA Johnson Space Center (JSC) as part of
the NASA Johnson Space Center Joint Soil Moisture Experiment
(JSME). The objective of the JSME is to verify that a
useful measure of soil moisture can be obtained remotely
using active and/or passive microwave sensors.

The measurements reported in this document were
acquired by Texas A&M University as part of the JSME.
In acquiring these data, the NASA/JSC two frequency truck
mounted radiometer·system was utilized. This system is
described in the following section. The individual ex-
periments involving the use of this system are described
after the system description, and general comments are
made concerning microwave data reduction and accuracy.

Microwave Signature Acquisition System

Background

In 1971 the Earth Observation Division of the NASA
Johnson Space Center wrote specifications for procurement

of a five frequency radiometer system. AIL, a division of
Cutler Hammer received the contract to build the system.
Due to funding restrictions, only two of the original five
frequencies were constructed by AIL, 1.4 GHz and 10.6 GHz.
The resulting system, termed the Microwave Signature
Acquisition System (MSAS) by NASA, was subsequently de-
livered to NASA in late 1972 and mounted on two vehicles
in the spring of 1973. The receiver and RF hardware were
mounted on a hydraulic boom capable of obtaining a height
of 65 feet (Figure V-1). The controller, tape drive, and
minicomputer were mounted in an air-conditioned van
(Figure V-2). The antenna mount is configured such that
the incident angle can be varied from nadir to zenith.
The antennas can also be rotated about their major axis
to change the receiver polarization with respect to the
plane of incidence.

MSAS Description

The MSAS consists of basically three subsystems as
detailed in Figure V-3:
1) RF Subsystem
2) Receiver Subsystem
3) Data Processing Subsystem
The L-band RF and receiver subsystems are essentially the
same as the S194 radiometer that was flown aboard Skylab.
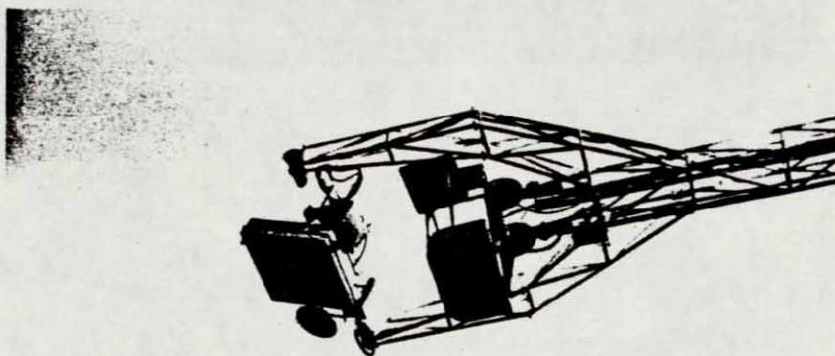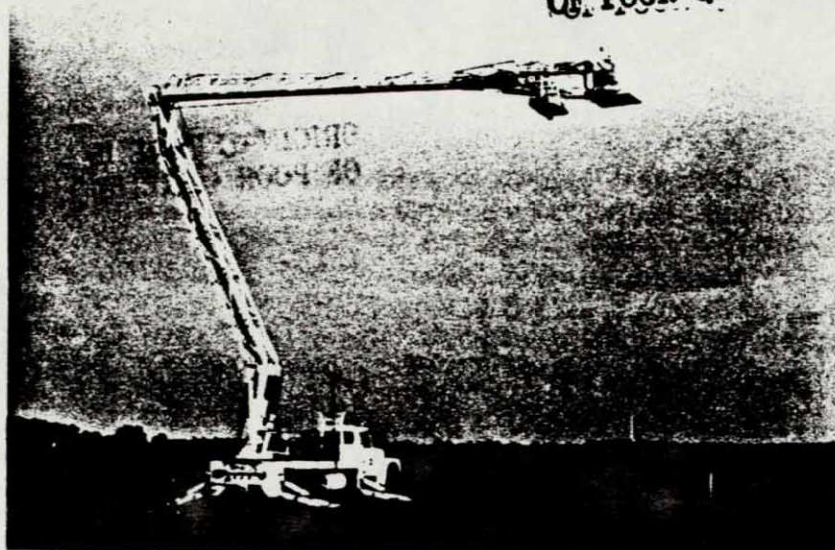
Figure V-1. Boom truck with the radiometer mounted
at the end of the boom (top). Close-up
showing details of the radiometer antennas
and truss structure (bottom).

Figure V-2. Van that houses the radiometer
control and data processing
electronics.

Figure V-3(b). Block diagram of the MSAS subsystems.
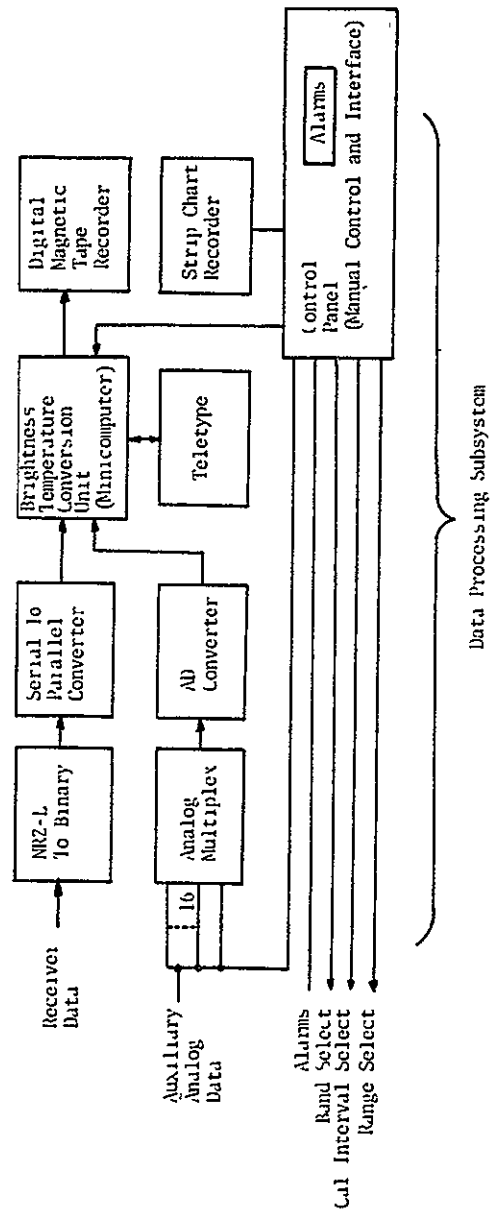
These radiometers are of the "Dicke" type which modulates
the incoming power against a stable reference source.

In a standard Dicke type receiver, a Dicke switch,
driven by a reference oscillator, alternately connects
the output of the antenna port and a reference source to
the input of the RF amplifier. If the antenna temperature
differs from the temperature of the reference source, a
square wave modulated signal is produced. The modulated
signal is then processed to yield a dc voltage proportional
to the temperature difference of the known reference and
the equivalent antenna temperature.

The MSAS is constructed such that the gain of the
receiver is also modulated in synchronism with the Dicke
switch rate. This modulation is accomplished through the
use of a digital attenuator that forces the receiver output
corresponding to the reference source input to be equal to
the receiver output corresponding to the antenna input.
The attenuator value is directly related to the radiometric
antenna temperature. Since the Dicke switch rate is
105 Hz, it is assumed that the system gain does not fluc-
tuate within one cycle of the switch.

For internal calibration purposes, the MSAS has two
internal reference noise generators. One has an equivalent
noise temperature of approximately 383°K and the other has
an equivalent noise temperature of 272°K. These sources

provide a means of periodically measuring the equivalent noise temperature of the receiver.

RF subsystem - As presently configured, the RF subsystem consists of a modular X-band RF head built in a separate temperature controlled enclosure with a waveguide connection to the 10.6 GHz antenna. It has already been noted that the L-band RF hardware is contained within the receiver enclosure. The L-band frequencies of operation are within the 1 to 2 GHz passband of the receiver, therefore, it is essentially a tuned radio frequency amplifier and, hence, does not use a mixer or local oscillator. The L-band RF hardware performs the switching operation between the antenna and the reference noise generators (RNG's), protection filtering and preamplification.

In contrast, the X-band output must be down-converted from a center frequency of 10.63 GHz to a center frequency of 1.5 GHz in order to be within the receiver passband. The X-band RF head performs the RF switching between the antenna and the RNG's, filtering, down-conversion, and IF preamplification.

Contained within the RF hardware of the X-band head and the L-band RF hardware are the two RNG's, each set of which were specifically designed for a particular frequency band of operation. The warmer RNG is used as the reference for comparison to the antenna output port; both are used for internal calibration. The stability and the uncertainty

in measuring the temperature of the RNG's has a major effect on the ultimate accuracy of the radiometer. The design and construction of these RNG's are discussed in detail by Hornbostel [102].

Receiver subsystem - The receiver subsystem consists of a broadband IF input square law detector, low noise and low offset dc amplifier, Y-factor measurement circuitry, timing and control circuitry for Dicke switch operation and synchronism, alarm and band selector logic, and the data multiplexer. The essential part of the receiver subsystem is the Y-measurement circuitry. This circuitry performs the digital attenuation that enables the radiometer to act as a form of gain-modulated switched radiometer.

The Y-measurement system can be simply depicted as in the block diagram of Figure V-4. As previously stated, it uses a gain modulation technique that automatically changes the gain of the radiometer system in synchronism with the switching between the antenna and the hot RNG. The gain is automatically adjusted to satisfy the equality

$$G_a(T_{ant} + T_e) = G_h(T_h + T_e) \qquad \text{(V-1)}$$

T_{ant}

G_a

1

1 2

2

T_{out}

G_h

2

T_h

T_c
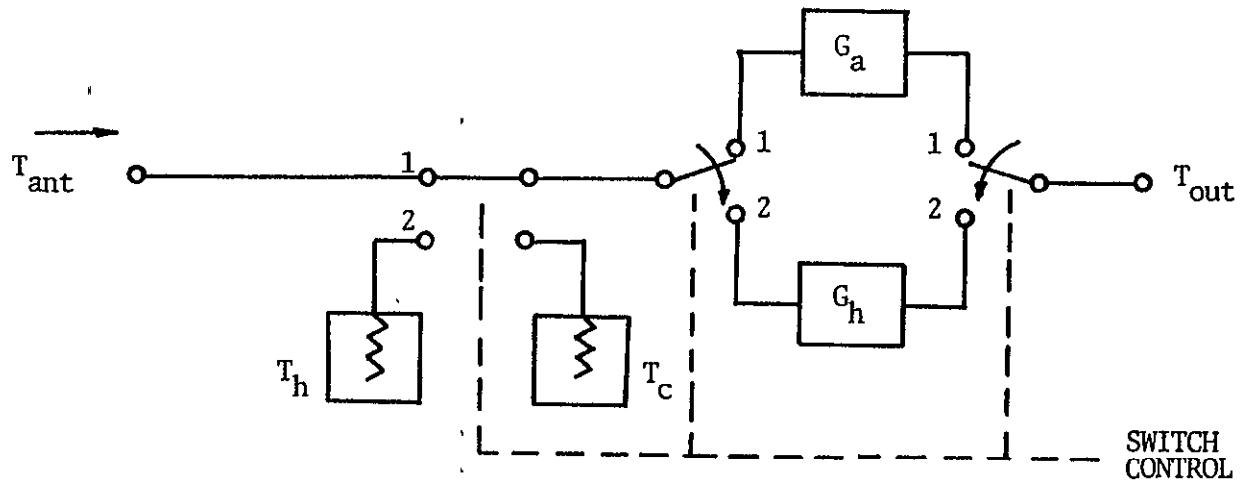
SWITCH
CONTROL

Switch Position	T_{out}
1	$G_a \, (T_{ant} + T_e)$
2	$G_a \, (T_h + T_e)$

Figure V-4.   Block diagram descriptive of the gain modulation technique.

where

G_a - gain of the receiver when looking at the antenna

G_h - gain of the receiver when looking at the hot RNG

T_{ant} - radiometric antenna temperature

T_e - noise temperature of the receiver

T_h - noise temperature of the hot RNG

T_c - noise temperature of the cold RNG

The gain adjustment is accomplished through the use of a digital attenuator that forces the receiver output voltage that corresponds to the hot RNG to be equal to the dc voltage out of the receiver when the input is from the antenna. The setting of the attenuator is termed a Y-factor and is defined as:

$$G_a = Y G_h \qquad \text{(V-2)}$$

therefore,

$$Y = \frac{G_a}{G_h} = \frac{T_h + T_e}{T_{ant} + T_e} \qquad \text{(V-3)}$$

and

$$T_{ant} = \frac{T_h + T_e(1 + Y)}{Y} \qquad (V-4)$$

Equation (V-4) demonstrates that the system output, T_{ant}, is independent of gain.

T_e is the equivalent noise temperature of the receiver and is measured periodically through the use of both the hot and cold RNG's. This is accomplished by replacing the antenna input by that of the cold RNG. Equation (V-4) then becomes:

$$T_e = \frac{T_c Y - T_h}{1 - Y} \qquad (V-5)$$

Since the radiometer output is independent of gain variations, the gain stability of the system need only be sufficient to prevent loss of signal below the sensitivity threshold of the detector. About 10 dB of automatic gain control (AGC) is included in the receiver to compensate for long-term aging effects, thus assuring near optimum gain.

Data Processing Subsystem - The data processing sub-
system performs the functions of radiometer control, input
data formatting, system performance monitoring, and
furnishes malfunction alarms for the radiometer system.
The hardware for this includes a ruggedized Rohm mini-
computer, a teletype with paper punch and reader, a mag-
netic tape unit, and a system control panel.

The minicomputer is used for system performance
monitoring, data formatting, and as the teletype and mag-
netic tape interface. It was also designed to be used for
real-time data reduction, however, this function was
inoperative until recently. Data reduction techniques
were implemented on Texas A&M University computers and are
described in detail by Newton [103] and Newton and Tesch
[104]. Modifications to the MSAS software for real-time
data reduction are described by Clark and Newton [105].

Radiometer alarms are activated and displayed directly
at the control panel by the data processing subsystem if
any system malfunctions are detected. The radiometer
receiver is controlled through the teletype or manual
operator inputs selectable at the control panel.

Radiometric data in the form of a serial digital
data train is formatted in the receiver and output to the
computer in 16-bit parallel data transfers. Simultaneously,
the computer accepts 16 channels of analog input via an

input multiplexer and 10-bit AD converter. These analog channels are for supplemental or auxiliary data and are formatted together with the radiometric data and output to a seven track computer compatible (Univac 1108) magnetic tape. In addition, these analog signals may be selected in groups of four for real-time analog strip chart recording.

Experiments

A series of three experiments have been performed with the MSAS at Texas A&M University. The first of this series was completed in 1973 and was a joint effort between NASA Johnson Space Center, Texas A&M University, and Lockheed Electronics Co., Inc. The results of this experiment are reported by Lee [91] and Newton et al. [92]. Data tabulations are contained in the document by Lee [91] and will not be presented in this document. Experiments were also performed in 1974 and 1975 at Texas A&M University. The data from these experiments are largely the basis for this work. Both of these experiments are described below.

Measurement Program in 1974

The 1974 experiment was conducted at the Texas A&M University Research Farm from June 26 through July 21. University of Kansas, NASA/JSC, and Lockheed Electronics Co., Inc. personnel also participated in the experiment.

The purpose of the experiment was to obtain simultaneous active and passive microwave data of well controlled bare and vegetated soil as a function of soil moisture and uniform surface roughness similar to flat tilled agricultural fields. The NASA/JSC L-band (1.4 GHz) and X-band (10.6 GHz) radiometer (MSAS) and the University of Kansas 2-8 GHz radar spectrometer were used to obtain the microwave data. Tabulated passive microwave data and summary tabulations of corresponding ground truth data were documented by Newton [103] and will not be duplicated here. Details of the raw data reduction of the passive microwave data are also presented by Newton [103]. The corresponding active microwave data are reported by Batlivala and Cihlar [106], and a complete listing of ground truth data are reported by Newton and Lee [107].

Ground truth and microwave data were obtained from ten plots of land in the TAMU Research Farm in Burleson County, Texas. Figure V-5 shows the field layout. It should be pointed out that Newton and Lee [107] describe the soil within the test field as 16% sand, 35% silt and 49% clay. However, those numbers were based on one textural analysis. Several later textural analyses revealed that a closer estimate of the average field texture is 3% sand, 35% silt and 62% clay. The soil was uniform across the test fields and is classified as Miller clay.

Field D

Field C

Field B

Field A

Sorghum hybrid
planted in rows

Bare

Sorghum hybrid
planted 3 weeks
prior to the
experiment

Sorghum hybrid
planted 5 weeks
prior to the
experiment

9 — 43 — 12 — 43 — 12 — 43 — 12 — 43

Row
Direction

Smooth

Smooth

Smooth

15

Medium Rough

Medium Rough

Medium Rough

15

Rough

Rough

Rough

15

6

6

Shallow Ditch

Access Road

N

Ditch

■ →Active System Data Acquisition Location

▲ →Passive System Data Acquisition Location

All dimensions are in meters

Figure V-5.   Layout of the 1974 experimental plots.

Nine of the ten plots shown in Figure V-5 were 15 m by 46 m (sets A, B, C) and one was 46 m square (plot D). The nine smaller plots were in sets of three with each set having one plot prepared with a smooth surface, one with a medium rough surface, and one with a rough surface. Set C was bare while sets A and B were uniformly planted in a sorghum hybrid. Set A was planted approximately five weeks prior to the field measurements and set B was planted three weeks before. Two densities of vegetation were thereby available for the experiment. However, the vegetation did not grow well on the rough fields of sets A and B. Consequently, the vegetation densities on these fields were different from the density of vegetation on the corresponding smooth and medium rough fields. Plot D was also planted in sorghum hybrid approximately six weeks before the experiment, but in rows running north and south.

Figure V-6 through V-8 show the three magnitudes of surface roughness. The smooth had an rms surface height of 0.88 cm, the medium 2.6 cm, and the rough 4.3 cm. Figure V-9 shows an example of the uniform vegetation. The vegetation in set B was approximately 125 cm high, while in set A it was approximately 188 cm high. Figure V-10 shows the vegetation planted in rows. It averaged 252 cm in height.

Each of the field sets were consecutively sprinkle irrigated until they were saturated (12-14 hours). Active
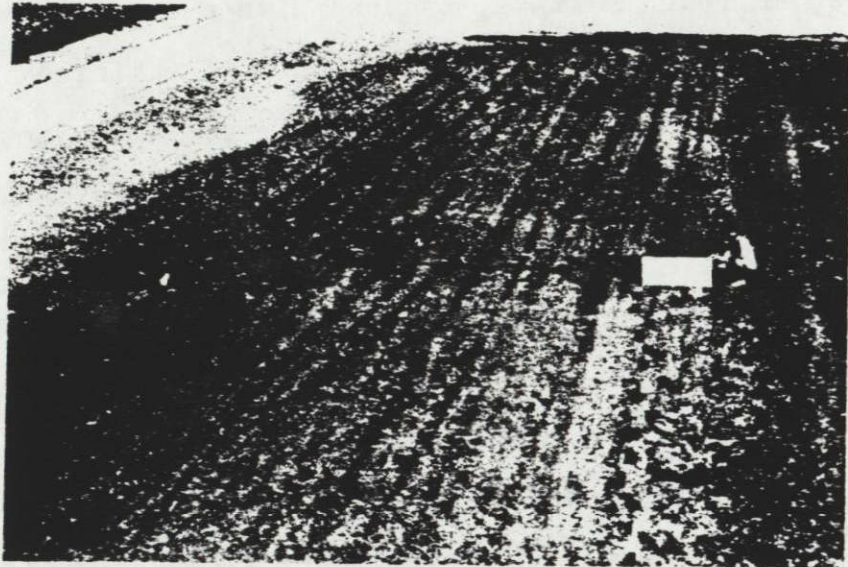
Figure V-6.   Smooth field used in the 1974
             measurements program.
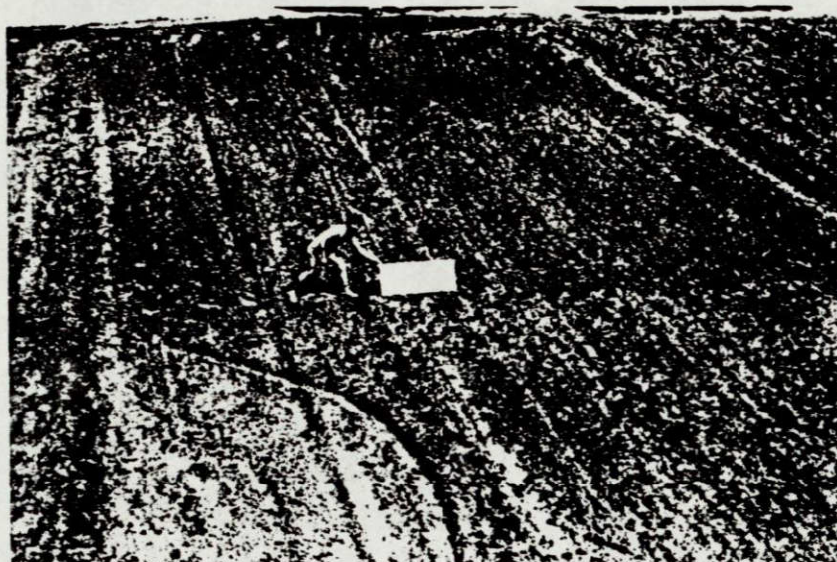
Figure V-7. Medium rough field used in
the 1974 measurements program.

Figure V-8. Rough field used in the 1974
measurements program.
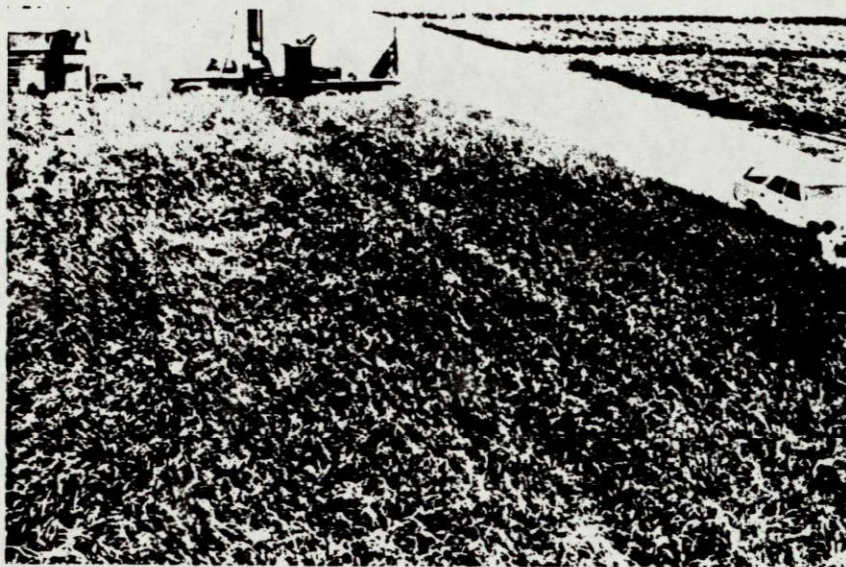
Figure V-9. Example of the uniform vegetation
covers used in the 1974 measurements
program.

Figure V-10.   Row planted vegetation used in
the 1974 measurements program.

and passive data were recorded simultaneously at each plot (except for plots A and B rough) as a function of soil moisture, transmission angle, polarization, and frequency. Measurements of plot D were made both parallel and perpendicular to the rows. Figure V-5 indicates the relative positions of the active and passive systems during data acquisition. Passive data were acquired at 0°, 20°, 35°, and 50° transmission (i.e. incident) angles for both horizontal and vertical polarizations at 1.4 GHz and 10.6 GHz. Sky temperature measurements were also made at zenith periodically during data acquisition. Data were taken on a twenty-four hour schedule, therefore, both day and night measurements were acquired.

Soil moisture and soil temperature profile measurements were made simultaneously with the microwave measurements. Soil moisture samples were obtained from 0-1 cm, 1-2 cm, 2-5 cm, 5-9 cm, and 9-15 cm layers. Soil temperature measurements were made with probes at the mid-point of each of these layers. These measurements were made at four locations equally spaced along both edges of each field, since the ground truth personnel had to remain out of the antenna field of view. Soil bulk density profiles, surface roughness, and vegetation height and density were obtained at numerous locations throughout the experiment.

Measurement Program in 1975

The 1975 experiment was conducted at the TAMU Research
Farm from July 13 through July 25, very near the site of
the 1973 and 1974 experiments. The purpose of the experi-
ment was to obtain passive microwave data of well-controlled
row tilled bare and vegetated soil to demonstrate the
effects of soil moisture and row direction. The NASA/JSC
L-band and X-band MSAS was used to acquire the microwave
data. Tabulations of the microwave data and corresponding
ground truth data are reported by Newton and Tesch [104].
Newton and Tesch also provide detailed ground truth and
experiment descriptions.

Two adjacent fields each approximately 45 m by 41 m
were used as test fields. The soil within these fields
was Miller clay. A drawing of the two field layouts and
ground truth sampling sites is shown in Figure V-11.
Field A was bare soil and field B was cotton that had an
average height of 61 cm and an average width of 60 cm
at the start of the measurements. Both fields were plowed
with rows running east-west and separated with a zone of
cotton approximately 3.05 meters in width. Average height
and width for a row in field A was 20 cm and 95 cm, re-
spectively. For a row in field B the typical height and
width were 13 cm and 90 cm, respectively.
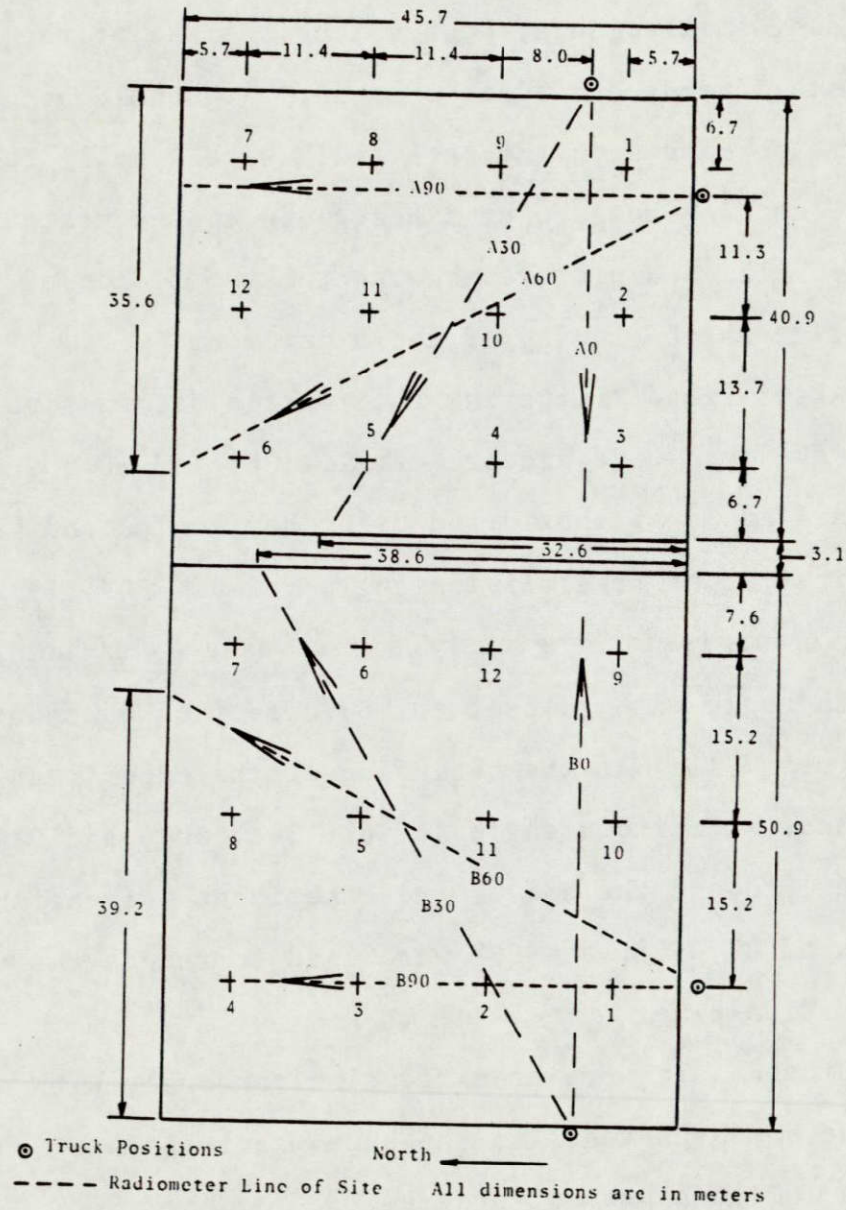
Figure V-11. Layout of the 1975 experimental plots.

The cotton in field B was planted approximately 7 1/2 weeks before the measurements were started. At the time of the measurements the cotton was in good health. Before the measurements were started, the bare field was weeded of small plants, however, by the end of the experiment small weeds had again emerged. It should be noted that measurements of the bare field were usually taken in the morning because of a heavy dew on the cotton plants. Figure V-12 is a picture showing the two fields as they looked at the beginning of the experiment.

After flood irrigating the two fields, passive microwave data were acquired at 1.4 GHz and 10.6 GHz for fields A and B as they dried using horizontal and vertical polarization at transmission angles of 0°, 20°, 35°, and 50°. Transmission angle scans were made as a function of azimuth angle with respect to row direction as denoted in Figure V-11. At the beginning of the experiment scans were made at azimuth angles of 0°, 30°, 60°, and 90°. However, toward the end of the experiment only azimuth angles of 0°, 45°, and 90° were used to reduce the data acquisition time.

Ground data were acquired simultaneously with the microwave measurements in the same manner as was done in the 1974 measurement program.
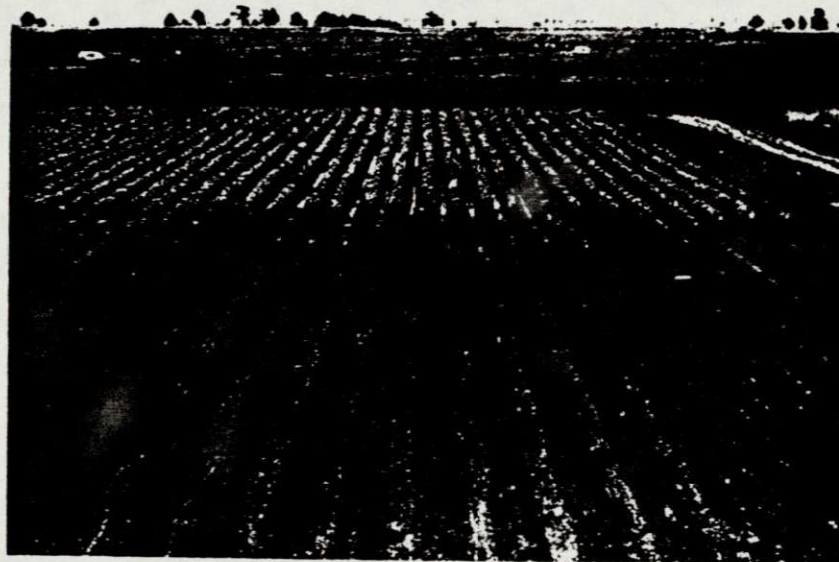
Figure V-12.   Field layout used in the 1975
measurements program.

Microwave Data Reduction

The techniques of reducing raw radiometer data to apparent antenna temperature in degrees Kelvin is fully explained by Newton [103]. The derivation of the equations used to reduce the raw data is provided by Paris [108]. Only a summary of data reduction equations and calibration constants will be given here. Figure V-13 is a functional block diagram of the MSAS. Figure V-13 is useful in understanding the data reduction equations that are given by Newton. A summary of these equations is provided below:

$$\overline{T}_m = \frac{T_{AA} - (1 - L_{AA})\, t_{AA}}{L_{AA}} \tag{V-6}$$

$$T_{AA} = \frac{T_{SA} - r\left(t_d\, L_{CAA} + (1 - L_{CAA})\, t_{CAA}\right)}{1 - r} \tag{V-7}$$

$$T_{SA} = C_3 T_{SH} + (C_2 - C_3)\, t_d + (1 - C_2)\, t_{CAA}$$
$$- \frac{A_H - A_A}{A_H' - A_c'} \left[C_3 T_{SH}' - C_1 T_{SC}' + (C_1 - C_3)\, t_d' \right] \tag{V-8}$$

$$r = \left[\frac{R_A - 1}{R_A + 1} \right]^2$$

$$C_1 = \frac{L_{CC}}{L_{CAA} L_{CAB}}$$

where

$\overline{T}_m$ - mean weighted radiometric temperature of the scene (antenna temperature).

T_{AA} - radiometric temperature at the output of the antenna.

L_{AA} - transmittance of the antenna.

t_{AA} - physical temperature of the antenna.

T_{SA} - radiometric temperature on the receiver side of the impedance mismatch at the antenna input port.

L_{CAA} - transmittance of the cable connecting the antenna to the receiver enclosure.

t_{CAA} - physical temperature of the antenna-receiver cable.

t_d - physical temperature of the receiver enclosure.

r - power reflection coefficient of the antenna-cable mismatch.

R_A - voltage standing wave ratio of the antenna-
cable mismatch.

L_{CH} - transmittance of the cable connecting the Dicke
switch to the hot reference noise generator
(RNG).

L_{CC} - transmittance of the cable connecting the
Dicke switch to the cold reference noise
generator (RNG).

L_{CAB} - transmittance of the cable inside the receiver
enclosure connecting the Dicke switch to the
external antenna cable.

T_{SH} - radiometric temperature of the hot RNG.

T_{SC} - radiometric temperature of the cold RNG.

A_H - attenuator setting in counts when the input
to the receiver is the hot RNG.

A_C - attenuator setting in counts when the input
to the receiver is the cold RNG.

A_A - attenuator setting in counts when the input
to the receiver is from the antenna.

The quantities that are primed denote measurements that
are made during the internal calibration sequence.

Equations (V-1) through (V-3) are used to reduce the
MSAS attenuator setting, A_A, to the measured
antenna temperature of the scene. The system constants
that must be determined in order to use these equations

are L_{AA}, r, C_1, C_2, and C_3. Values for constants L_{AA}, r, and C_2 (which are the antenna transmittance, the power reflection coefficient between the antenna and the cable connecting the antenna to the receiver or RF head enclosure, and the loss factor of that cable) as given by Newton [103] were used to reduce both the 1974 and 1975 data sets. Constants C_1 and C_3 were estimated individually for each data set.

The constants C_1 and C_3 were estimated by comparing MSAS measurements of uniform scenes to theoretical calculations of the brightness temperature of those scenes. As a result, the absolute calibration of the reduced measurements is only as good as the theoretical models used to estimate the emission of the scene. Measurements of the atmosphere at zenith, of smooth water, and smooth soil (for 1974 data) were used to calculate C_1 and C_3. These targets were chosen since a very accurate model of atmosphere emission was available from Paris [108], and smooth surfaces can be accurately modeled using Fresnel equations. However, at the 10.6 GHz wavelength, the surfaces assumed to be smooth were not ideally smooth.

Although the absolute accuracy of the measurements may not be precise, the precision of the measurements is good. At 1.4 GHz the standard deviation of the measurements based on a one second integration time was typically 0.6°K,

while at 10.6 GHz it was 1.7°K. Each data points used in
the following chapters are averages of 60 to 90 one second
measurements.

Other errors to be aware of arise from the pointing
accuracy of the antennas. The antenna positioning mechanism
was not optimum and pointing accuracies are estimated to
be ± 5° in incident and polarization angle. Periodically
higher inaccuracies occurred, but these measurements were
generally deleted.

CHAPTER VI

COMPARISON BETWEEN ANTENNA TEMPERATURE

AND BRIGHTNESS TEMPERATURE

The models described in Chapter IV will be used to
aid in the analysis of the antenna temperature measurements
described in Chapter V. As a result, it will be necessary
to compare radiometer antenna temperature measurements to
theoretical calculations of the brightness temperature of
the scene. The measured antenna temperature is not a
pure measurement of the brightness temperature of a scene,
but it is degraded by two phenomena. First, the apparent
radiation impinging on the antenna does not only consist
of the brightness radiation of the scene. It has components
due to sources other than the scene of interest as de-
scribed in the introductions to Chapter III and Chapter IV.
Secondly, the antenna beamwidth further degrades the
measurement.

Because of these non-ideal conditions, care must be
exercised when comparing theoretical calculations to
antenna measurements. Therefore, a discussion of the
response of an antenna to the brightness temperature of
a scene is provided before analyzing the antenna measure-
ments that were described in Chapter V. In this discussion
the relationships describing the measured antenna

temperature in terms of the apparent radiation incident on the antenna will be provided. Following that, the effects of the antenna beamwidth will be presented. Finally, the contribution of atmospheric radiation to the apparent temperature of a scene will be described.

Measured Antenna Temperature

Power Output of An Antenna

The purpose of this section is to describe the relationships between the apparent intensity impinging on an antenna and the output power of the antenna. In doing this the relationship between the apparent intensity and the brightness temperature of the scene as calculated using the models of Chapter IV will also be pointed out.

The apparent radiation intensity leaving a scene is the sum of several components as described in Chapters III and IV. The apparent radiation intensity leaving a scene can be described in terms of these components in the following manner

$$I_A = I_B + I_{RS} + I_{SE} + I_{IA} + I_P \qquad \text{(VI-1)}$$

where

I_A - apparent radiation intensity

I_B - brightness intensity (described analytically by the models in Chapter IV)

I_{RS} - reflected sky radiation

I_{SE} - radiation emitted by the system and reflected from the surface back into the antenna aperture

I_{IA} - radiation emitted by the intervening atmosphere between the scene and the antenna

I_P - point source radiation directed toward the antenna aperture

Only the reflected sky radiation and the self emitted radiation need be seriously considered as degrading factors in measuring the brightness temperature using a ground-based system.

In the microwave region of the spectrum the emitted radiation intensity of a scene is proportional to the temperature of the scene. However, intensity is defined as electromagnetic energy leaving or approaching a differential element of area on an imaginary plane within the time interval t + dt and having a direction of propagation contained in a differential solid angle dΩ whose central direction is normal to the imaginary plane [109]. Intensity has dimensions

$$\text{Intensity} \Rightarrow I \Rightarrow \frac{\text{energy}}{\text{area time steradian}} \Rightarrow \frac{\text{watts}}{m^2 \ Hz \ rad^2 \ sec^2}$$

It is extremely important to note that intensity is invariant along its propagation path. That is, the radiation leaving a surface will be characterized by the same value of intensity at any distance from its origin.

Flux is the radiant energy leaving or approaching an imaginary plane within a time interval t + dt in all directions in a hemispherical solid angle bounded by the imaginary plane [109]. Flux is the total rate of energy flow and has dimensions

$$Flux \Rightarrow q \Rightarrow \frac{energy}{area\ time} \Rightarrow \frac{watts}{m^2\ Hz\ sec}$$

The intensity vector describes the flux in any direction. The integration of intensity over the hemisphere will give flux, if a suitable correction is included to account for the projected area (Figure VI-1).

$$q = \int_0^{2\pi} \int_0^{\pi/2} I(\theta,\phi) \frac{dA'}{r^2} = \int_0^{2\pi} \int_0^{\pi/2} I(\theta,\phi) \cos\theta\, d\Omega \qquad (VI-2)$$

where

q - flux

$I(\theta,\phi)$ - intensity

dA' = cos θdA
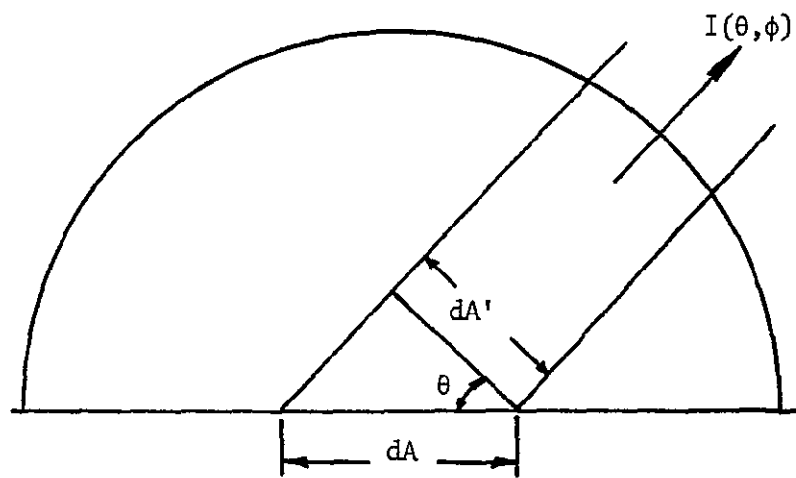
$$d\Omega = r^2 dA = r^2 \sin\theta\, d\theta\, d\phi$$

$$dA' = \cos\theta\, dA$$

Figure VI-1. Geometry used to demonstrate the proper integration of intensity to obtain flux.

dA' - element of area perpendicular to the direction

  of intensity (Figure VI-1)

dA - element of area on the plane bounding the

  hemisphere through which the flux is passing

So, given the intensity of emission from a scene, the flux can be computed for a given direction. Knowing the area over which this flux crosses allows one to calculate the total power emitted from the area.

A review of the equations that define the power output of an antenna is required in order to relate intensity of emission to the measurements made by a radiometer. The apparent intensity impinging on the antenna is I_A (watts/m^2 steradian), assuming that the system is integrating over some finite time and bandwidth. This intensity is interpreted as watts per unit antenna aperture area per steradian. For an area extensive homogeneous scene within $d\Omega$, I_A is that intensity passing through dA' which is associated with $d\Omega$ (Figure VI-2). Since $d\Omega$ is independent of distance, the same power density (i.e., $I_A d\Omega$ watts/Hz m^2) is observed at the antenna aperture as is observed at dA'. The power received by an antenna is

$$W_k = \iint_{4\pi} \iint_{\substack{Antenna \\ Aperture}} \left(I_A(\theta, \phi) \right)_k \, d\Omega \, dA_e \qquad \text{(VI-3)}$$
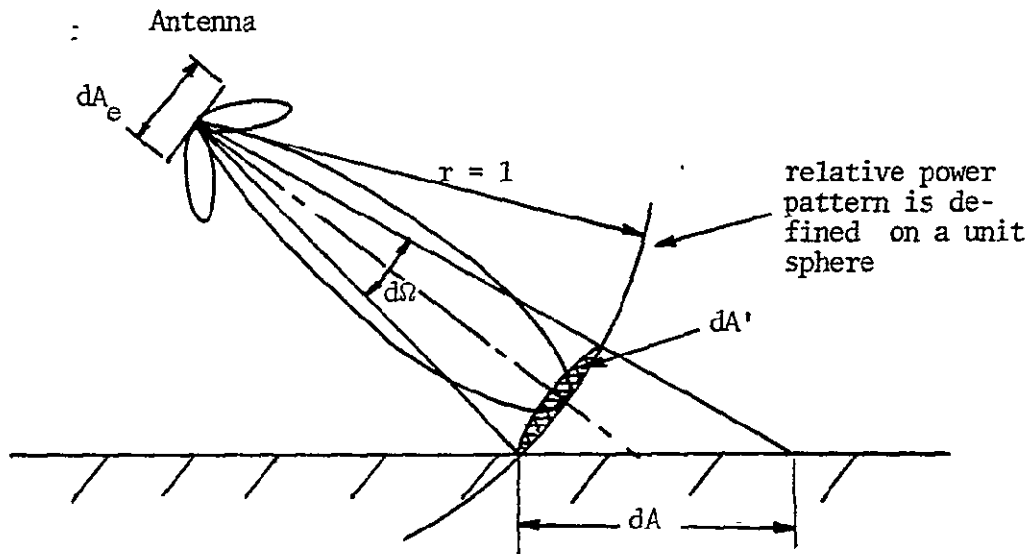
Figure VI-2. Representation of an antenna beamwidth.

where

W_k - power output (watts), where subscript k denotes polarization relative to the antenna coordinate system

$(I_A(\Theta,\phi))_k$ - apparent intensity of radiation (watts/m^2 ster Hz) in the direction (Θ,ϕ) at the kth polarization with respect to the antenna coordinate system

$d\Omega = \sin\Theta d\phi d\phi$

dA_e - effective antenna aperture in the direction (Θ,ϕ) with respect to the antenna major axis

Assuming that the cross polarized antenna power pattern is negligible, then

$$dA_e = dA_{e_K}$$

Equation VI-2 can be integrated over the antenna aperture to yield

$$W_k = \iint\limits_{4\pi} \left(I_A(\Theta,\phi)\right)_k A_{e_K}(\Theta,\phi) \, d\Omega \qquad \text{(VI-4)}$$

The effective aperture of an antenna is given by

$$A_{e_k}(\theta, \phi) = \frac{\lambda^2}{4\pi} \, g_{d_k}(\theta, \phi) \qquad (VI-5)$$

where

A_{e_k} - effective antenna aperture for the kth polarization

g_{d_k} - directive gain for the kth polarization (for a lossless antenna directive gain is equal to power gain [110])

λ - wavelength

and

$$g_{d_k}(\theta, \phi) = \frac{4\pi \, P_k(\theta, \phi)}{\iint\limits_{4\pi} P_k(\theta, \phi) \, d\Omega} \qquad (VI-6)$$

where

$$\frac{P_k(\theta, \phi)}{\iint\limits_{4\pi} P_k(\theta, \phi) \, d\Omega}$$

is the one way relative power pattern of the antenna. So

$$A_{e_k}(\theta,\phi) = \frac{\lambda^2\, P_k(\theta,\phi)}{\displaystyle\iint_{4\pi} P_k(\theta,\phi)\, d\Omega} \tag{VI-7}$$

Substituting (VI-7) into (VI-4) yields:

$$W_k = \iint_{4\pi} (I_A(\theta,\phi))_k \left[\frac{\lambda^2\, P_k(\theta,\phi)}{\displaystyle\iint_{4\pi} P_k(\theta,\phi)\, d\Omega} \right] d\Omega \tag{VI-8}$$

Since one is generally only interested (or only able to compute) energy impinging on the antenna through its main lobe, (VI-8) can be written

$$W_k = \frac{\lambda^2}{\displaystyle\iint_{4\pi} P_k(\theta,\phi)\, d\Omega} \left[\iint_{\substack{main\\lobe}} (I_A(\theta,\phi))_k\, P_k(\theta,\phi)\, d\Omega \right.$$

$$\left. + \iint_{\substack{remaining\\\Omega}} (I_A(\theta,\phi))_k\, P_k(\theta,\phi)\, d\Omega \right] \tag{VI-9}$$

Assuming that the side lobes and back lobes are negligible, (VI-9) reduces to

$$W_k = \frac{\lambda^2}{\iint\limits_{4\pi} P_k(\theta,\phi)d\Omega} \iint\limits_{\substack{main \\ lobe}} \left(I_A(\theta,\phi)\right)_k P_k(\theta,\phi)\,d\Omega \qquad \text{(VI-10)}$$

The assumptions involved in deriving (VI-10) were that
the cross polarized antenna power pattern is negligible
and that the side lobes and back lobes of the like polarized
power pattern are also negligible. Under these assumptions,
(VI-10) describes the power output of an antenna at the
k^{th} polarization with respect to the antenna coordinate
system due to a polarized intensity I_A incident on its
aperture. However, the models in Chapter IV describe the
polarization of emission from the scene with respect to
the plane of transmission rather than the antenna coordinate
system. This problem of inconsistency in polarization
definition is discussed later in the chapter.

Apparent Antenna Temperature

It is now of interest to convert the power measured
by the antenna to antenna temperature. By doing this the
relationship between measured antenna temperature and scene
brightness temperature can be illustrated.

The power measured by a radiometer is related to
temperature based on the equation describing the thermal
noise power in a resistive element.

$$W = kTB \qquad \text{(VI-11)}$$

where

    k - Boltzman's constant

    B - Bandwidth

    T - Temperature of the resistive element in degrees
       Kelvin

If W represents the power output of a radiometer antenna,
T will be termed the measured antenna temperature and will
be denoted T_m.

In the microwave region the Rayleigh Jean's approxi-
mation to Planck's emission law [95] can be used to relate
the apparent intensity of emission from a scene to the
apparent temperature of the scene. In this case the
apparent temperature contains the polarization dependence.
Note that this polarization dependence is with respect to
the plane of incidence and is denoted by i. The apparent
temperature is defined as the temperature a blackbody
would have to be in order to emit radiation equal to the
polarized apparent radiation of the scene.

$$I_{A_i} = \frac{k T_{A_i}}{\lambda^2} \qquad \text{(VI-12)}$$

where

T_{A_i} - apparent temperature of the scene at the ith polarization

λ - wavelength

Letting k denote a polarization state with respect to the antenna coordinate system (IV-10) becomes

$$W_k = k T_{m_k} B$$

$$= \frac{\lambda^2}{\iint\limits_{4\pi} P_k(\theta,\phi)d\Omega} \iint\limits_{\substack{main \\ lobe}} \left[\int_{\nu_1}^{\nu_2} \frac{k T_A}{\lambda^2} d\nu \right] P_k(\theta,\phi) \, d\Omega \qquad \text{(VI-13)}$$

where

ν - frequency (ν_2 - ν_1 defines the bandwidth of interest)

Assuming that the radiation intensity is constant over the bandwidth

$$T_{m_k} = \frac{1}{\iint\limits_{4\pi} P_k(\theta,\phi)d\Omega} \iint\limits_{\substack{main \\ lobe}} (T_A(\theta,\phi))_k \, P_k(\theta,\phi) \, d\Omega \qquad \text{(VI-14)}$$

Equation IV-14 describes the relationship between the measured antenna temperature and the apparent temperature of the scene. Utilizing (VI-1), the apparent scene temperature in (VI-14) can be broken down into its respective components to demonstrate the effect of its various components on the measured antenna temperature. Equation VI-14 expands to

$$T_{m_k} = \frac{1}{\underset{4\pi}{\iint} P_k(\theta,\phi)d\Omega} \left[\underset{\substack{main \\ lobe}}{\iint} \left(T_B + T_{RS} + T_{SE} + T_{IA} + T_P \right)_k \cdot P_k(\theta,\phi) \, d\Omega \right] \qquad (VI-15)$$

where

T_B - brightness temperature of the scene

T_{RS} - reflected sky temperature

T_{SE} - self emitted temperature reflected from the surface back into the antenna aperture

T_{IA} - temperature of the intervening atmosphere

T_P - point source radiation incident on the antenna aperture

Note that since each of the components are additive, their contributions can be calculated independently. Only the contributions due to the reflected sky temperature and the

self emission will be discussed further in this report.
The reflected sky radiation is discussed later in this
chapter and the self emission is discussed in Appendix D.
The other contributions are insignificant as far as this
work is concerned.

Effects of Beamwidth

Theoretical models like those described in Chapter
IV provide estimates of emitted radiation in terms of
power density per unit angle. However, antenna temperature
measurements are actually averages over some finite range
of angles due to the antenna beamwidth. An idealized
antenna with an infinitely narrow beamwidth would be
required to measure an apparent scene temperature without
averaging over a range of transmission angles.

In addition to this averaging effect, the polariza-
tion of calculated brightness temperatures is defined with
respect to the plane of transmission while the antenna
power pattern is defined for each of two orthogonal
polarization states with respect to the antenna reference
frame. Since the antenna receives energy from a finite
beamwidth, an antenna temperature measured at one of the
antenna polarizations actually consists of components of
both of the surface polarizations.

Peake [111], Claassen and Fung [112], and Grody [113] discuss in detail the problem associated with inverting a measured antenna temperature to the apparent temperature of a scene. Such a detailed discussion will not be provided here, but examples of the amount of degradation that can be expected due to the averaging effects and the polarization mixing effect will be presented.

Polarization Mixing

Equation (VI-14) describes the measured antenna temperature in terms of the apparent temperature of the scene. In this equation, the subscript k denotes that polarization is defined with respect to the antenna coordinate system. However, the models developed in Chapter IV were developed such that polarization was defined with respect to the plane of transmission of radiation from the surface toward the antenna. This polarization state was denoted by i. Figure VI-3 denotes the antenna and ground coordinate systems.

As a result of the inconsistency in defining polarization, the measured antenna temperature at polarization k is actually a mixture of the two surface polarizations states defined with respect to the plane of transmission. Dropping the assumptions made in deriving (VI-14), a general expression describing this polarization mixing
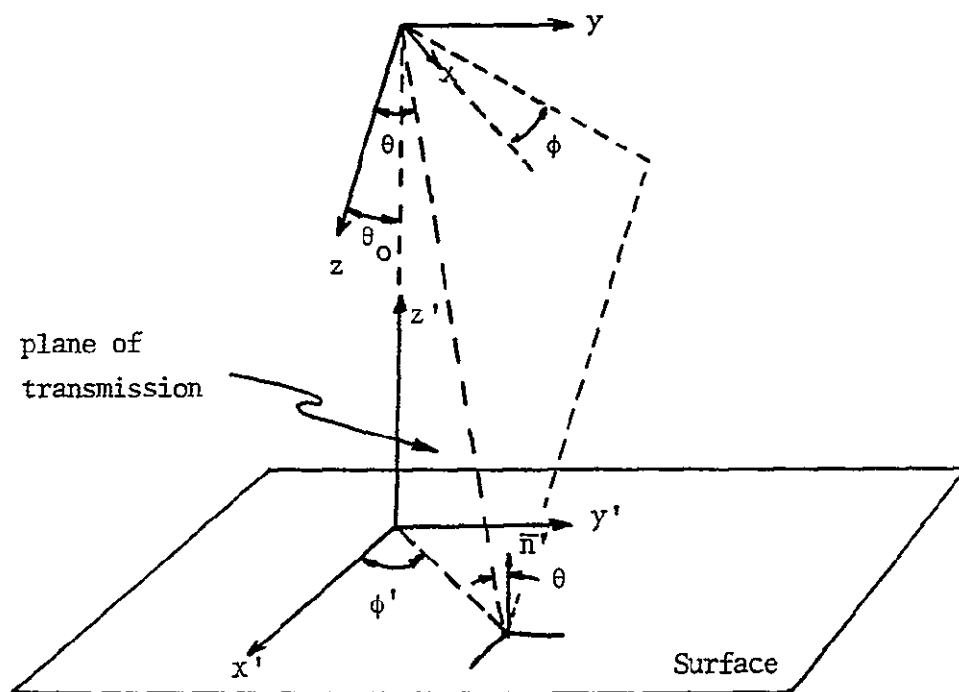
θ_o - transmission angle at which the major axis of
the antenna is viewing the surface

Figure VI-3.   Relationship between the antenna
and surface coordinate systems.

can be obtained by expanding (VI-14). In expanding (VI-14), a. linearly polarized antenna is assumed. The two polarization states will be denoted by "v" for vertical and "h" for horizontal (Figure VI-4). With the aid of the geometry shown in Figure VI-4 the antenna temperature can be written in terms of the two surface polarizations.

$$T_{A_V} = \sin^2\psi \, T'_{A_h} + \cos^2\psi \, T'_{A_V}$$

$$T_{A_h} = \cos^2\psi \, T'_{A_h} + \sin^2\psi \, T'_{A_V}$$

(VI-16)

The prime denotes polarization defined with respect to the plane of transmission. The general form of (VI-14) for a horizontally polarized antenna is [112]:

$$T_{m_h}(\theta_o) = \frac{1}{D} \iint_{4\pi} \left[P_v(\theta,\phi) \left(\sin^2\psi \, T'_{A_h} + \cos^2\psi \, T'_{A_V} \right) \right.$$

$$+ P_h(\theta,\phi) \left(\cos^2\psi \, T'_{A_h} + \sin^2\psi \, T'_{A_V} \right)$$

(VI-17)

$$\left. + \left(T'_{A_V} - T'_{A_h} \right) P_v(\theta,\phi) P_h(\theta,\phi) \sin 2\psi \, \cos\beta \right] d\Omega$$
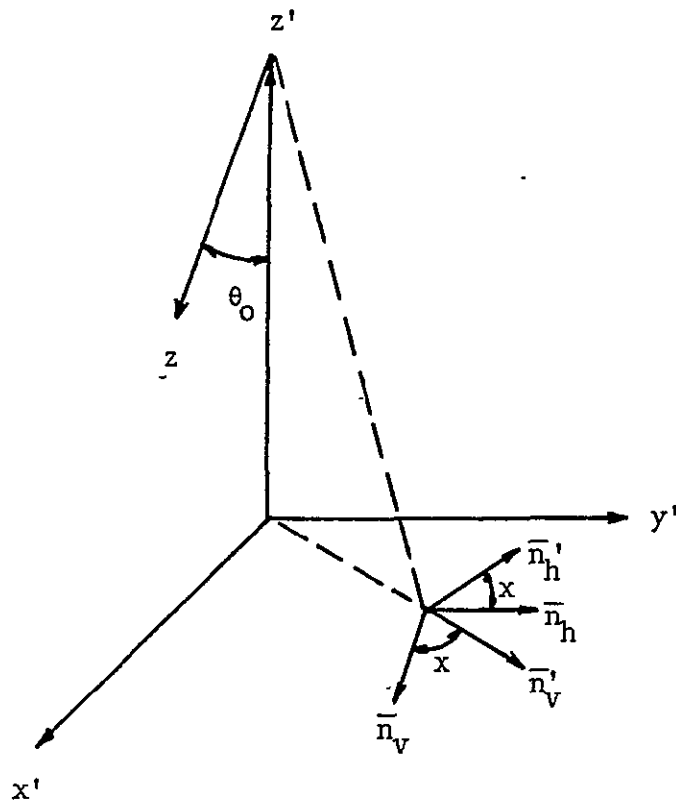
$\overline{n}_h'$ and $\overline{n}_v'$ - projections of the unit vectors defining the surface polarization onto the surface plane

$\overline{n}_h$ and $\overline{n}_v$ - projections of the unit vectors defining the antenna polarizations onto the surface plane

Figure VI-4. Relationship between the surface and antenna polarization vectors.

where

$$D = \iint_{4\pi} \left(P_v(\theta,\phi) + P_h(\theta,\phi) \right) d\Omega$$

$P_v(\theta,\phi)$ - cross polarized antenna power pattern

$P_h(\theta,\phi)$ - like polarized antenna power pattern

β - relative phase between the antenna polarization components [112]

The angle ψ is denoted in Figure VI-4 and is defined in the surface coordinate system. Its dependence on θ and ϕ in the antenna coordinate system must be taken into account when (VI-17) is integrated.

Equation (VI-17) can be used to demonstrate the effect of polarization mixing of the like polarized components and the cross polarized components.

Like polarization - To demonstrate the degradation due to only the like polarized antenna pattern, the cross polarized pattern will be neglected. It will also be assumed that the apparent temperature impinging on the antenna is constant over the beamwidth of the antenna. With the above assumptions and neglecting side and back lobes, (VI-17) reduces to

$$T_{m_h}(\theta_0) = \frac{1}{D} \left[T'_{A_h} \iint_{\substack{main \\ lobe}} P_h(\theta,\phi) \cos^2\psi \, d\Omega \right.$$

$$\left. + T'_{A_v} \iint_{\substack{main \\ lobe}} P_h(\theta,\phi) \sin^2\psi \, d\Omega \right]$$

(VI-18)

The terms H and V defined by

$$H = \frac{1}{D} \iint\limits_{\substack{main \\ lobe}} P_h(\theta, \phi) \cos^2 \psi \, d\Omega$$

(VI-19)

$$V = \frac{1}{D} \iint\limits_{\substack{main \\ lobe}} P_h(\theta, \phi) \sin^2 \psi \, d\Omega$$

are measures of the relative amount of energy received by
the antenna from the surface horizontal and vertical
polarizations, respectively.

$$T_{m_h} = H T_{A_h}' + V T_{A_v}'$$

(VI-20)

The terms H and V describe the polarization mixing due to
the antenna beamwidth. Note that the sum of H and V must
always equal unity.

For a linear vertically polarized antenna, H describes
that fraction of the horizontally polarized (surface
coordinate system) energy that is being measured by the
antenna. The worst case condition within the framework of
the above assumptions can be illustrated by assuming that
the antenna has a uniform unity power pattern over the main

lobe. With this assumption, the terms H and V can be calculated for different antenna beamwidths and the transmission angle at which the antenna is viewing the surface. Figure VI-5 are the results of these computations [113]. Note that the degradation is most severe at nadir, and it gets worse as the beamwidth gets larger.

The beamwidth between half-power points for the 1.4 GHz antenna is approximately 20° while for the 10.6 GHz antenna it is approximately 6°. Figure VI-5 and calculations of the brightness temperature of a smooth surface (Figures IV-19 and IV-20) were used to calculate the degradation that can be expected in the 1.4 GHz radiometer measurements (Figure VI-6). Since the 1.4 GHz system has the largest beamwidth, Figure VI-6 is the worst case condition that should be observed with the MSAS. Although the beamwidth of the antenna is large, the degradation in the measurement is small since the vertical and horizontal brightness temperatures approach each other as the transmission angle gets near zero.

Cross polarization - Following Grody [113], the effects due to cross polarization can be demonstrated by assuming that the cross polarized power pattern of the antenna is related to the like polarized power pattern by a constant factor.
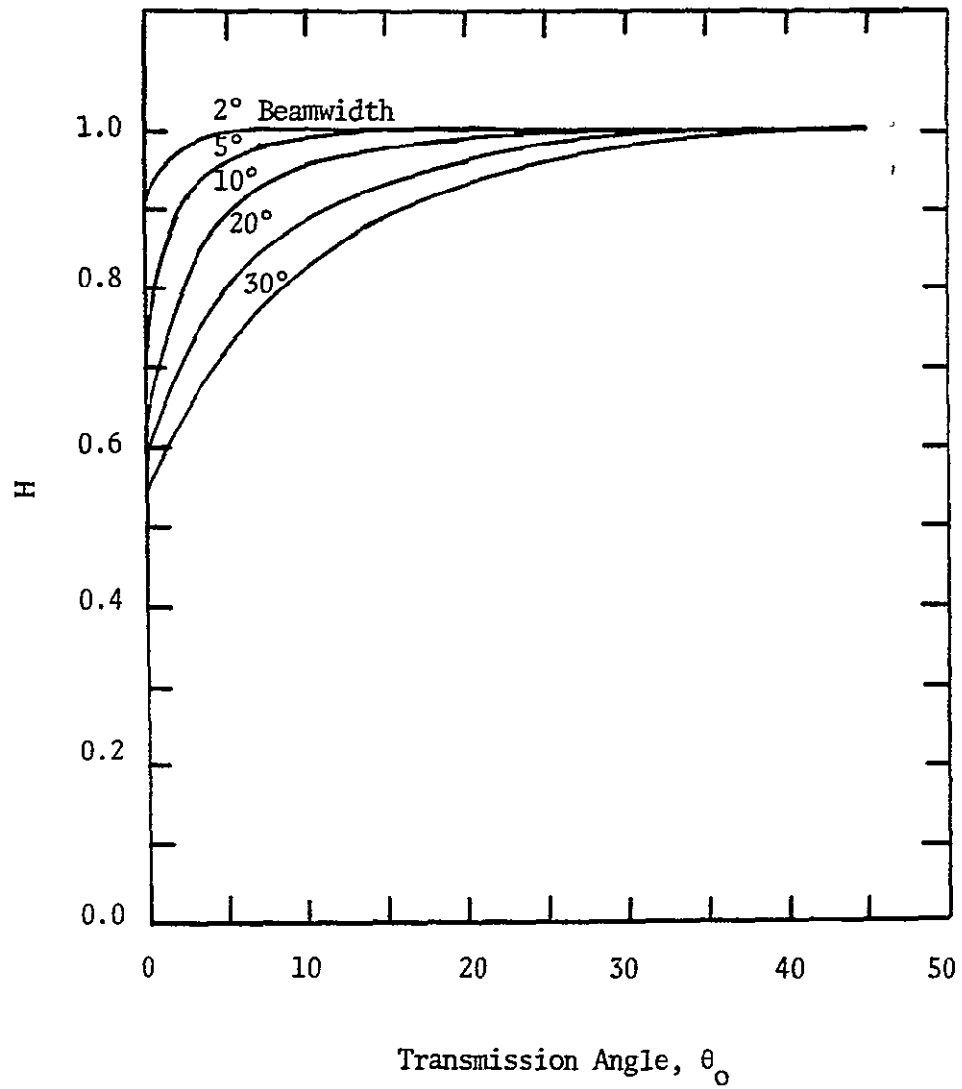
Figure VI-5. Normalized power received in horizontal polarization as a function of transmission angle, θ_o, for different beamwidths (after Grody [113]).
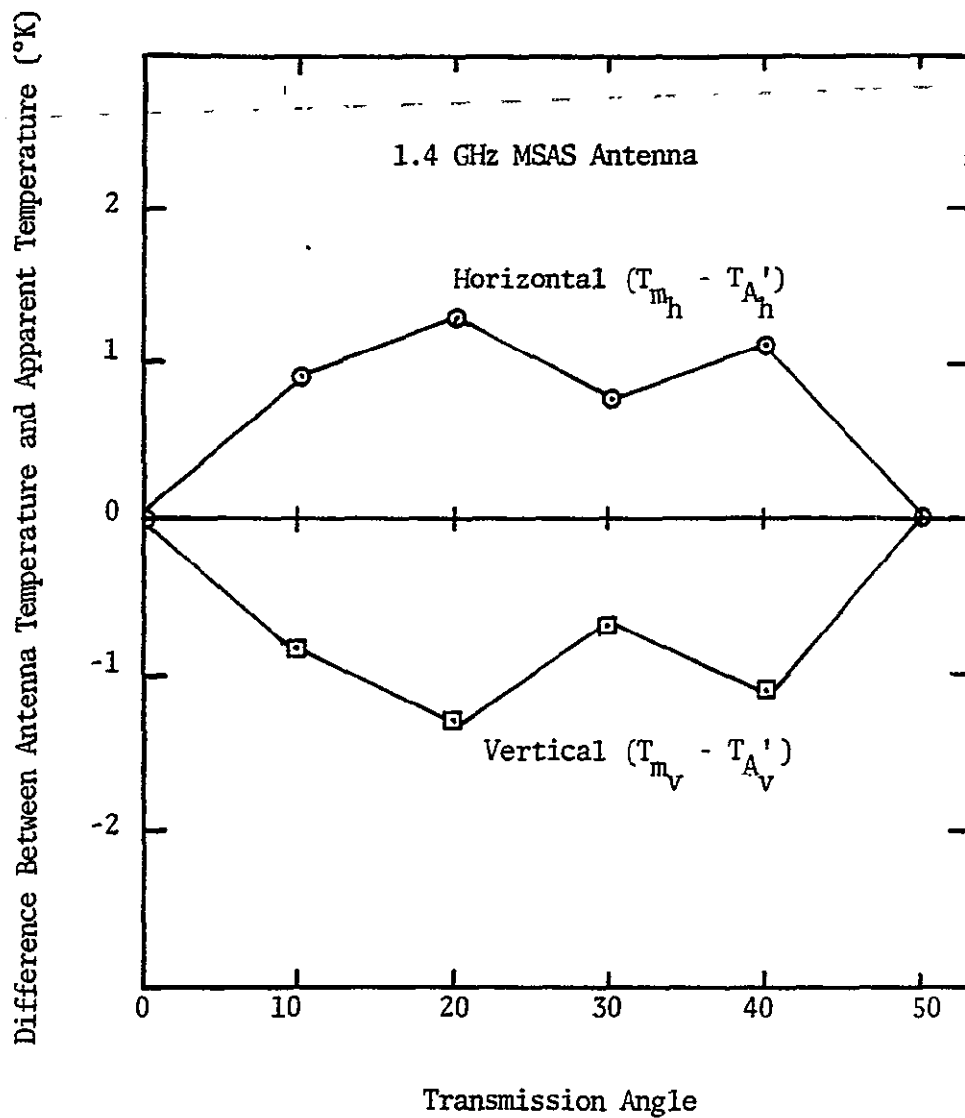
Figure VI-6. Comparison of measured antenna temperature to the corresponding apparent temperature.

$$P_v(\theta,\phi) = \frac{P}{1-P} P_h(\theta,\phi) \tag{VI-21}$$

As before a linear horizontally polarized antenna has been assumed. Substituting (VI-21) into (VI-17) and neglecting the third term in the integral of (VI-17)

$$H_{cross} = P + (1-2P) H \tag{VI-22}$$

Assuming a uniform unity like and cross polarized antenna power pattern across the main lobe only, H is given by (VI-19).

For angles larger than the beamwidth, it is observed from Figure VI-5 that H is approximately unity. For this condition

$$H_{cross} \approx 1 - P$$

$$\tag{VI-23}$$

$$V_{cross} \approx P$$

For this case H_{cross} and V_{cross} replace H and V in (VI-20).

However, both of the MSAS antennas have cross polarized power patterns greater than 25 dB down from the like polarized pattern. This corresponds to a p of less than 0.01. As a result, the cross polarized degradation is negligible even at scan angles less than the antenna beam-width.

Transmission Angle Averaging

In the above discussion on polarization mixing the apparent temperature of the scene was assumed to be con-stant over the beamwidth of the antenna. This was assumed so that the effects polarization mixing could be discussed independently of the antenna averaging effect. Averaging occurs over a finite range of transmission angles defined by the antenna beamwidth and look direction of the antenna.

The effects of transmission angle averaging will now be discussed independently of polarization mixing. To do this the beamwidth of the antenna will have to be assumed very narrow in the dimension perpendicular to the plane of transmission. This assumption, although unrealistic in terms of the real antenna beamwidths of the MSAS, will provide estimates of the worst case condition.

Again neglecting side and back lobes, the cross polarized antenna power pattern, and assuming a linear

horizontally polarized antenna with the like polarized
antenna power pattern described above, (VI-18) becomes

$$\overline{T_{m_h}} = \frac{1}{D} \int_{\Theta_1}^{\Theta_2} T_{A_h}' \, P_h(\Theta,\phi) \sin\Theta \, d\Theta \qquad \text{(VI-24)}$$

where Θ_1 and Θ_2 define the beamwidth in the plane of
transmission. The apparent scene temperature is no longer
assumed constant over transmission angle. Equation (VI-24)
is used to demonstrate the degradation of the brightness
temperature resulting from antenna averaging. All com-
ponents to the apparent temperature except the brightness
temperature are neglected, and the antenna power pattern
is assumed to be unity and uniform over the main lobe.
Figure VI-7 is the resulting calculations of the measured
antenna temperature as a function of beamwidth and the
corresponding brightness temperature. The degradation
increases as the beamwidth gets larger. The half-power
beamwidth of the 1.4 GHz antenna MSAS is approximately
30°, while the half-power beamwidth of the 10.6 GHz
antenna is approximately 12°.

Atmospheric Radiation

It was stated earlier that, for a ground-based radiom-
eter system viewing the earth, the sky radiation and the
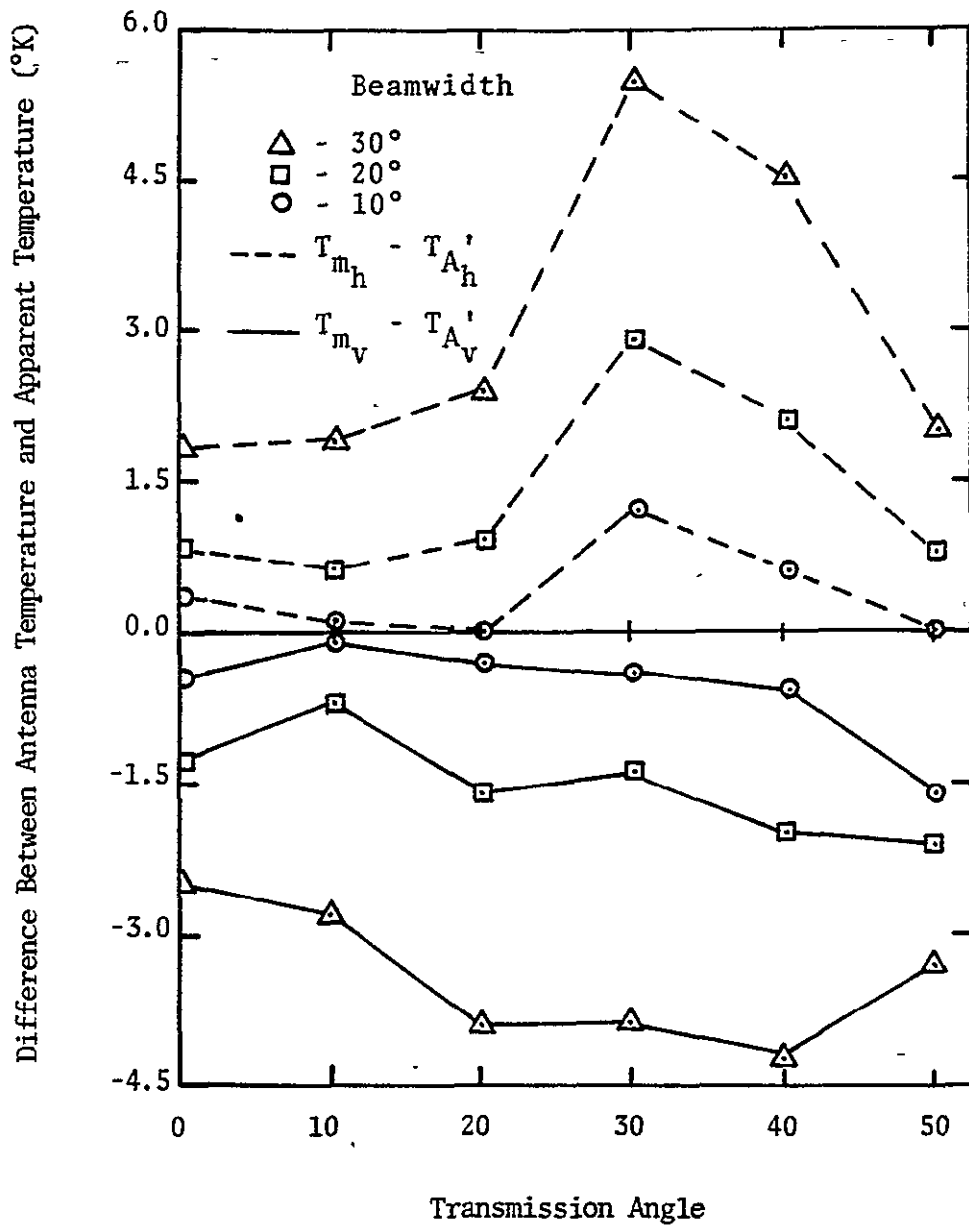
Figure VI-7. Degradation of measured antenna temperature due to transmission angle averaging.

self emitted radiation reflected from the surface were
the only potential contributions of any consequence to the
apparent temperature of the scene. A scheme for correcting
near-nadir antenna measurements for self emission is de-
scribed in Appendix B. The potential effects of reflected
sky radiation is discussed below.

Paris [40] provides a good discussion on the origin
and transfer of thermal microwave energy in the atmosphere.
Figure VI-8 is a plot of sky brightness temperature as a
function of zenith angle for both of the MSAS frequencies
assuming a standard atmosphere. These sky brightness
temperatures were calculated by Paris [114]. They are used
below to demonstrate the contribution of the atmosphere
to the apparent temperature of a scene.

Paris [40] also provides calculations to demonstrate
the extremes of the sky brightness temperature under various
conditions. The results of these calculations are provided
in Table VI-1 and Table VI-2. It is seen that the sky
brightness temperature at 1.4 GHz is affected little by
adverse conditions, however, at 10.6 GHz the sky brightness
temperature can change dramatically.

The bistatic scattering coefficients developed by
Leader [61] and presented in Chapter IV can be used to
calculate the sky radiation that is reflected into the
antenna aperture. The radiation from the atmosphere is
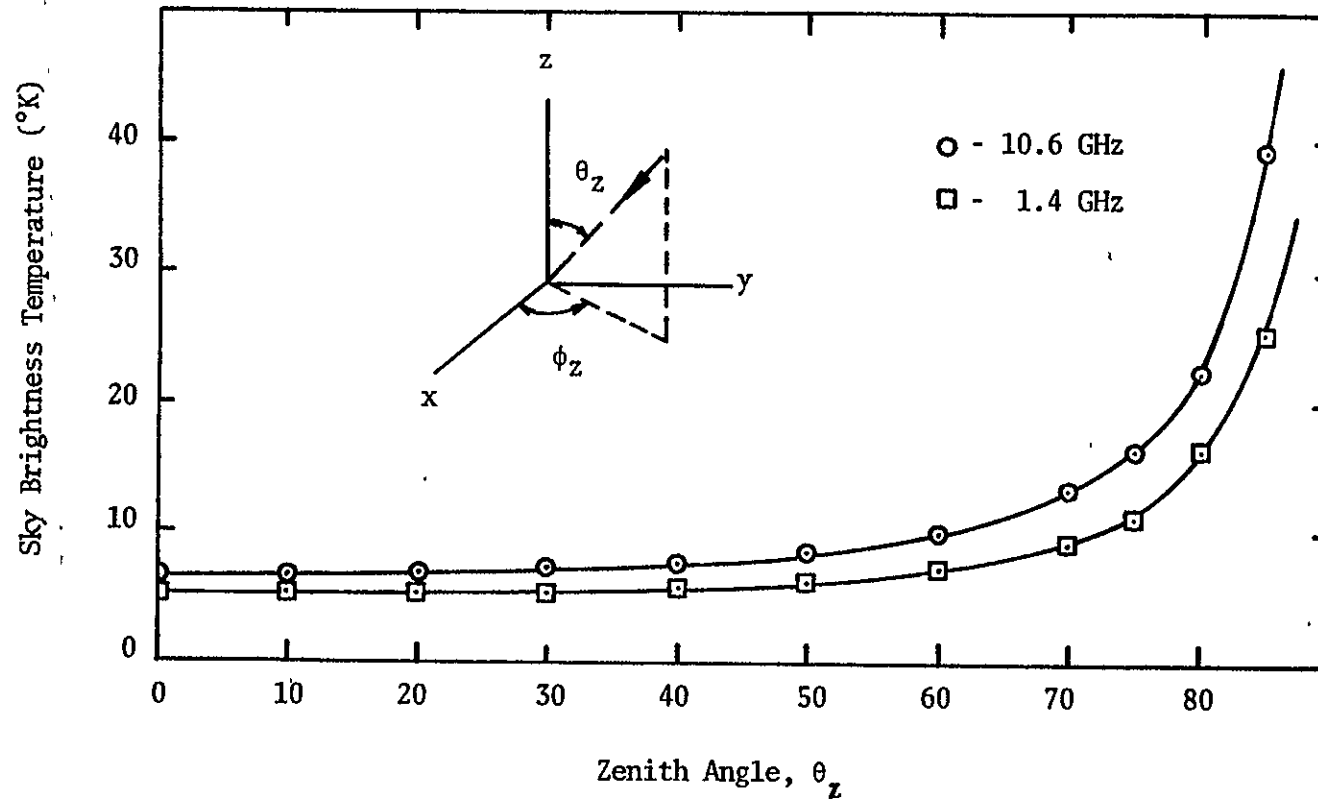
Figure VI-8. Sky brightness temperature for a standard atmosphere as computed by Paris [114].

TABLE VI-1

Ranges of Sky Brightness Temperature of the Atmosphere: $\theta_z=$ 0 deg. (after Paris [40])

Frequency (GHz)	Sky Brightness-temperature (°K)								
	Clear Sky			Clouds (No Rain)			Clouds and Rain		
1.42	2.1	(2.1)	2.2*	2.1	(2.2)	3.7	2.1	(2.3)	5.5
2.695	2.3	(2.3)	2.4	2.3	(2.7)	8.0	2.3	(3.1)	17.6
4.805	2.5	(2.6)	3.1	2.5	(3.7)	20.2	2.5	(5.4)	84.9
5.81	2.6	(2.8)	3.4	2.6	(4.4)	28.1	2.6	(7.1)	151.6
8.0	2.8	(3.2)	4.6	2.8	(6.3)	49.3	2.8	(13.4)	263.3
10.69	3.1	(4.1)	6.8	3.1	(9.7)	80.8	3.1	(26.3)	293.7
15.375	4.4	(7.6)	15.4	4.4	(19.5)	142.4	4.4	(57.9)	299.6
19.35	8.8	(20.7)	48.5	8.8	(43.2)	202.2	8.8	(88.5)	300.6
31.4	10.7	(20.9)	44.8	10.7	(62.0)	267.3	10.7	(164.0)	301.5
33.2	11.4	(21.6)	45.4	11.4	(66.0)	272.2	11.4	(173.0)	301.6
37.0	14.3	(25.0)	50.2	14.3	(76.7)	279.8	14.3	(191.3)	301.7
53.8	233.3	(252.0)	267.2	233.3	(264.0)	295.7	233.3	(282.6)	302.2

*The data are presented in the following format: Minimum Value (Value for Average Atmosphere, Cloud Condition, or Rain Condition) Maximum Value.

TABLE VI-2

Ranges of Sky Brightness Temperature of the Atmosphere: θ_z = 55 deg. (after Paris [40])

Frequency (GHz)	Sky Brightness-temperature (°K)								
	Clear Sky			Clouds (No Rain)			Clouds and Rain		
1.42	3.7	(3.7)	3.8*	3.7	(3.9)	6.4	3.7	(4.1)	9.5
2.695	4.0	(4.0)	4.2	4.0	(4.7)	13.7	4.0	(5.4)	30.0
4.805	4.4	(.4.5)	5.2	4.4	(6.5)	34.3	4.4	(9.3)	130.9
5.81	4.5	(4.8)	5.9	4.5	(7.6)	47.2	4.5	(12.3)	210.7
8.0	4.8	(5.6)	7.9	4.8	(11.0)	80.3	4.8	(23.0)	290.6
10.69	5.4	(7.1)	11.7	5.4	(16.7)	125.6	5.4	(44.3)	299.6
15.375	7.6	(13.0)	26.4	7.6	(33.1)	200.0	7.6	(93.3)	301.3
19.35	15.2	(35.1)	79.3	15.2	(71.1)	252.1	15.2	(148.5)	301.7
31.4	18.3	(35.5)	73.7	18.3	(99.2)	286.6	18.3	(221.8)	302.1
33.2	19.6	(36.6)	74.6	19.6	(104.9)	222.9	19.6	(230.0)	302.2
37.0	24.4	(42.2)	82.0	24.4	(120.0)	290.2	24.4	(245.3)	302.2
53.8	261.8	(280.5)	292.3	261.8	(284.8)	298.5	261.8	(290.2)	302.2

*The data are presented in the following format: Minimum Value (Value for Average Atmosphere, Cloud Condition, or Rain Condition) Maximum Value.

incident on the surface from all zenith angle pairs (Θ_z, ϕ_z). The radiation reflected from the surface into a particular direction is given by

$$T_{RS}(\Theta_t) = \int_0^{2\pi} \int_0^{\pi/2} \gamma_i(\Theta_z, \phi_z; \Theta_t, \phi_t) BT_{sky} \, d\Omega \qquad \text{(VI-25)}$$

where

γ_i - bistatic scattering coefficient of the surface at the ith polarization

BT_{sky} - sky brightness temperature

The bistatic scattering coefficients developed by Leader are only defined for the plane of transmission. In addition, the sky brightness temperature is assumed to be independent of the azimuth angle, ϕ_z.

Figures VI-9 through VI-12 are results of calculations using (VI-25) and the 1.4 GHz brightness temperature in Figure VI-8. It can be seen that the soil moisture has a considerable effect on the reflected sky radiation. The wetter the soil the higher the reflection. It can also be seen that the surface roughness affects the amount of radiation that is reflected. As the surface gets wetter the effects of surface roughness is exaggerated. Another observation that can be made is that as expected, more energy is reflected in horizontal polarization.
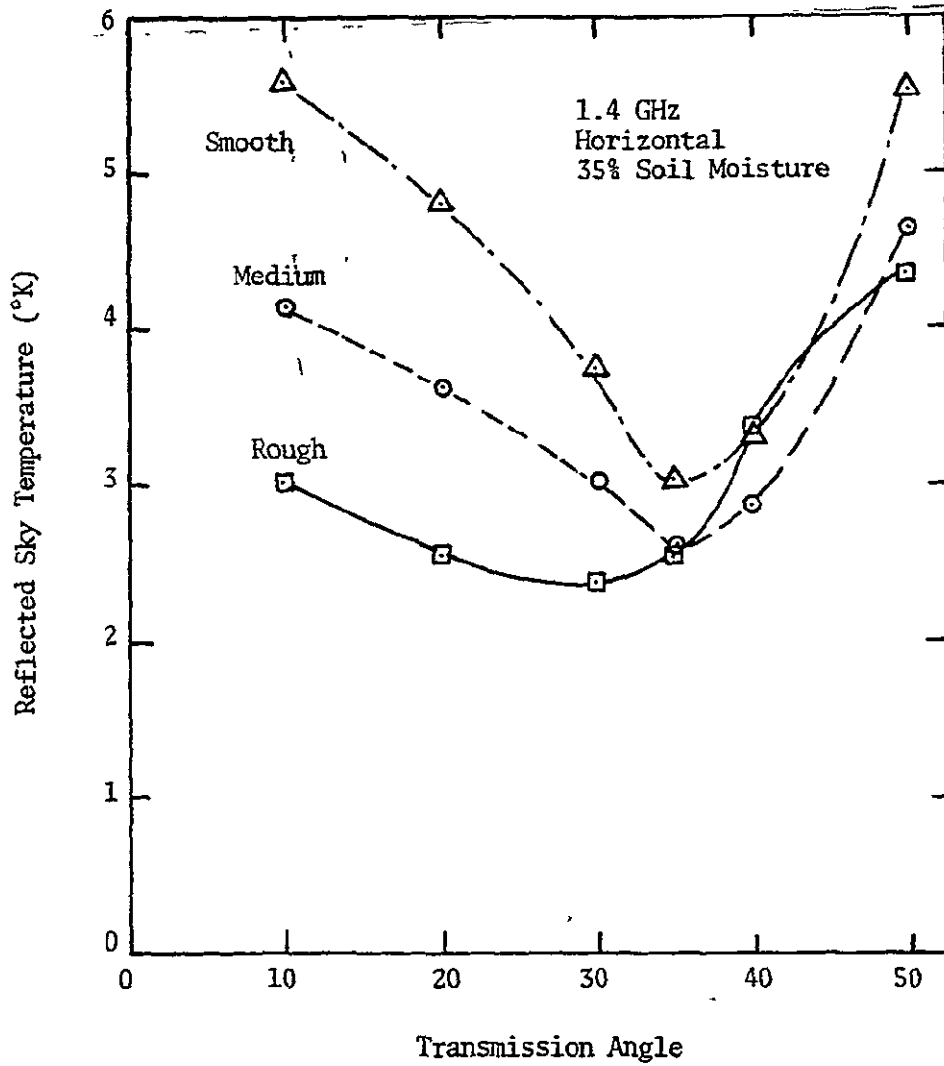
Figure VI-9. Reflected horizontally polarized sky brightness temperature for 35% soil moisture.
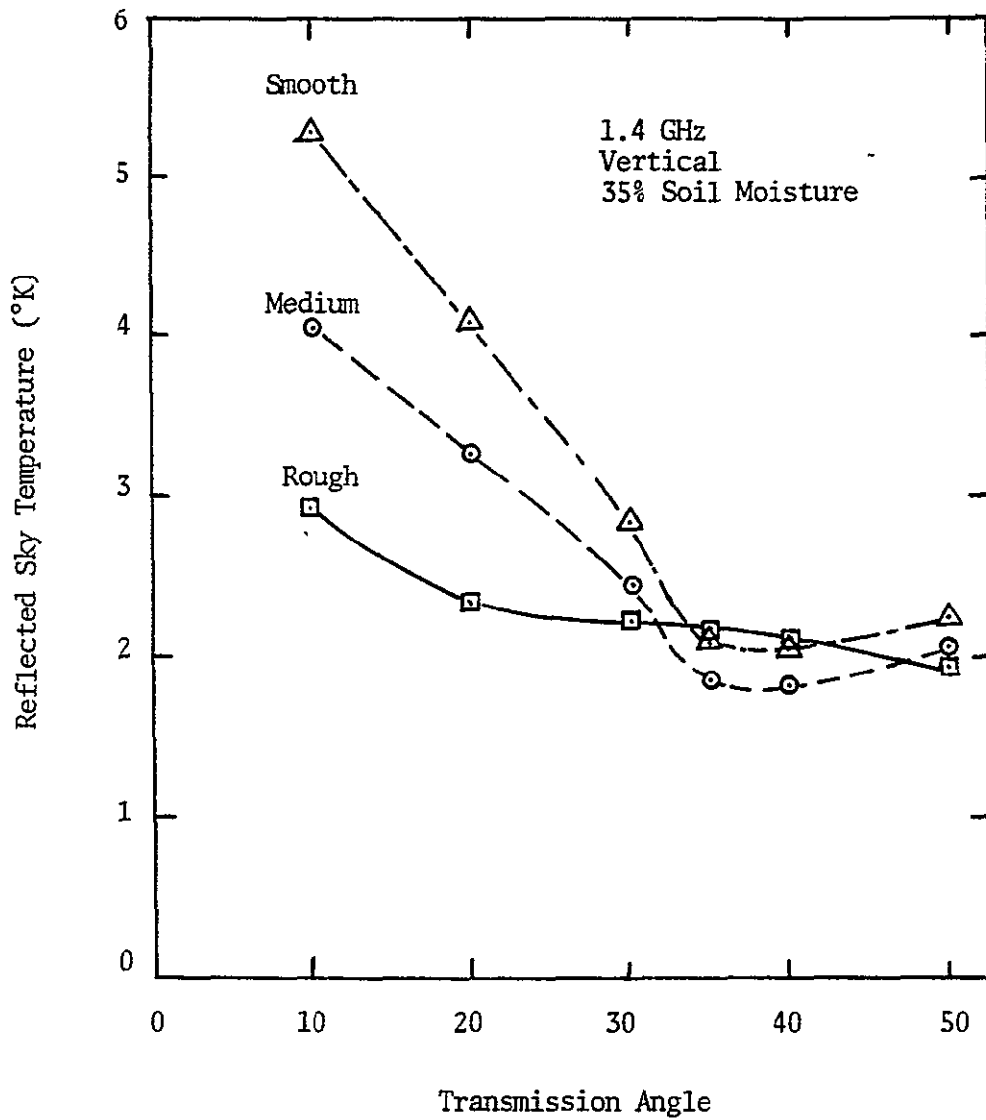
Figure VI-10. Reflected vertically polarized sky
brightness temperature for 35% soil
moisture.
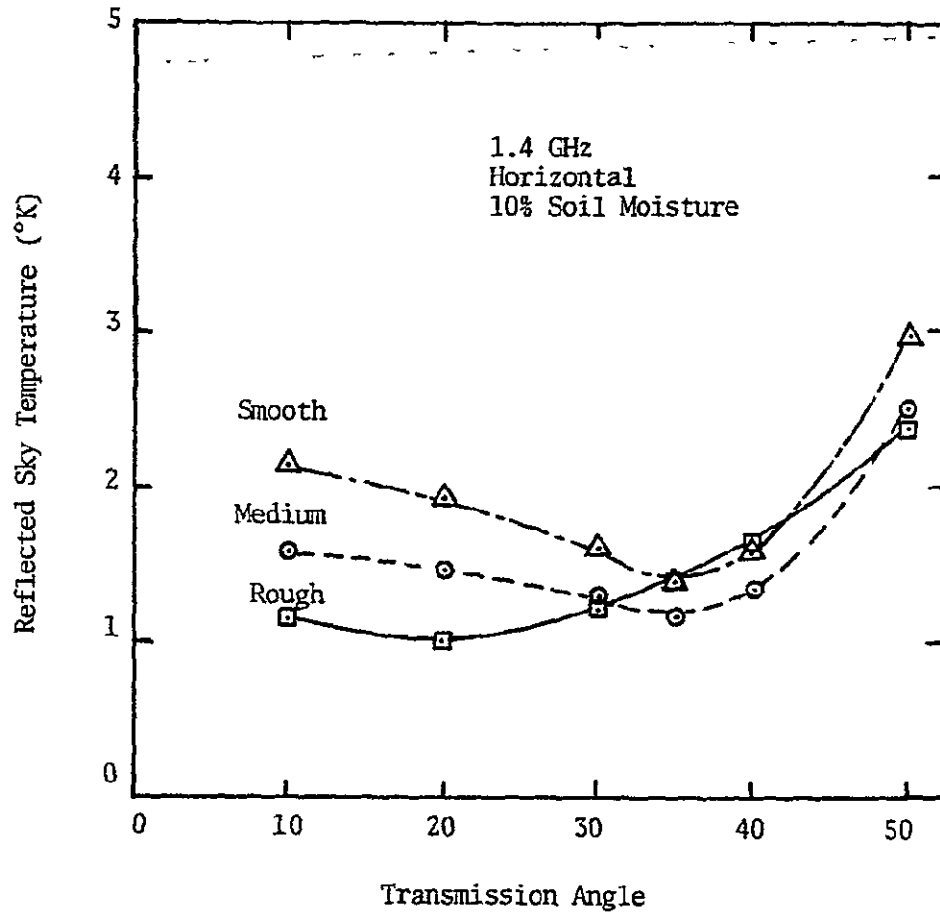
Figure VI-11. Reflected horizontally polarized sky
brightness temperature for 10% soil
moisture.
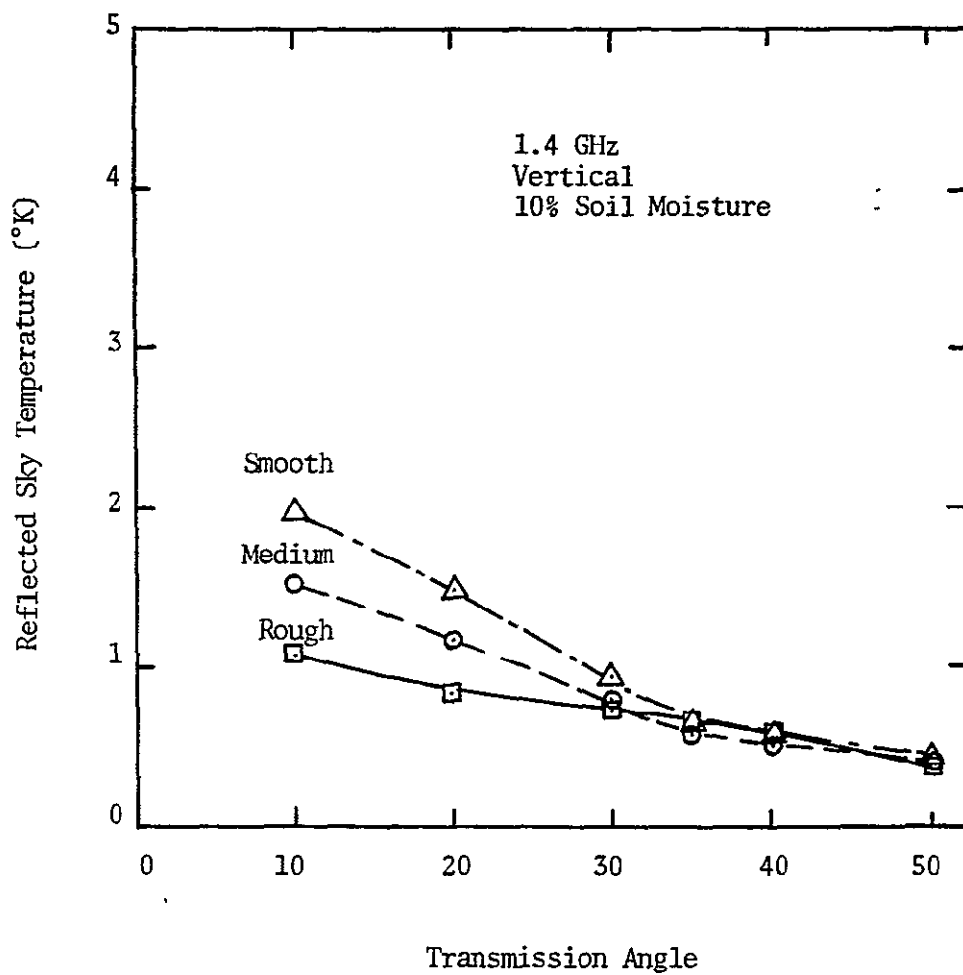
Figure VI-12. Reflected vertically polarized sky
brightness temperature for 10% soil
moisture.

CHAPTER VII

ANALYSIS OF MEASUREMENTS

Introduction

The ground based measurements of soil emission de-
scribed in Chapter V will be analyzed in this chapter to
determine the effects of soil moisture, surface roughness
and vegetative cover. The theme of this analysis will be
to determine the soil moisture information that can be
obtained from microwave radiometer measurements. The
analysis will involve comparisons between model predictions
and measured results. In addition, the models will be used
as tools in explaining the dependence of the measurements
on scene parameters.

All of the measurements that are analyzed in this
chapter were obtained at the Texas A&M Research Farms.
The experimental plots within this research farm area
consist of the same soil type (Miller clay). It was
pointed out in Chapter II that the permittivity of soil
was a function of soil matric potential, independent of
soil texture. However, since all of the measurements
analyzed in this chapter correspond to the same soil
texture, the conclusions that pertain to soil moisture
will apply equally to soil matric potential. As a result,

on a matric potential basis, the conclusions of this
chapter will apply to all soil textures.

The chapter is organized so that each scene parameter
can be addressed separately. First, the effects of soil
moisture and soil temperature profiles are discussed.
Following that, the effects of surface roughness are
addressed for both flat tilled and row tilled bare soil
surfaces. The effects of a vegetation cover over the soil
surfaces are then investigated. In the final section of
the chapter a procedure for estimating soil moisture
information using radiometer measurements is presented,
and the potential accuracy of this technique is discussed.

Quantification of Moisture and Temperature Profiles

It is clear that the microwave emission of a soil is
governed by the temperature of the soil and by the
permittivity of the soil, which is in turn governed by the
soil moisture, (or, more correctly, matric potential).
However, since the soil moisture and soil temperature are
not uniform with depth, the problem of estimating soil
moisture information from microwave data is greatly
complicated. Even after roughness effects are eliminated
there is a problem of interpreting the moisture information
that is obtained from the microwave data. Microwave energy

is emitted from some soil volume, not just a single layer.
As a result, the sensor is responding to a range of soil
moistures depending on the soil moisture profile and the
maximum depth from which radiation is emitted. In addition,
the temperature of the soil also affects the magnitude of
the radiation emitted from the soil. In order to interpret
microwave emission for soil moisture information, it is
necessary to; 1) determine a technique of compensating the
antenna temperature measurements for the effects of soil
temperature variations, 2) determine the effect of the
shape of the soil moisture profile on the sensor response,
3) determine a single parameter that will describe this
effect, and 4) determine the soil depth over which the
parameter describes the soil moisture. The microwave data
can then be interpreted in terms of this descriptive
parameter. Such a parameter will be developed and inter-
preted below. A technique of normalizing antenna measure-
ments to soil temperature will also be presented.

Soil Moisture Profile

Description of soil moisture parameters - There are
many techniques of defining a parameter that describes the
soil moisture distribution with depth. However, it is
difficult to develop a parameter that uniquely describes
the effect of each profile individually since the same

emission may be produced by more than one profile shape.
One of the earliest attempts at obtaining a single
parameter to describe a soil moisture profile was by
Lee [91]. Lee's technique was to calculate the electro-
magnetic attenuation profile of the soil based on the
permittivity profile, integrate the profile to determine
the skindepth and determine the equivalent uniform soil
moisture profile that would produce the same skindepth.
This parameter is termed the equivalent skindepth moisture
content and is denoted by m_S, It was subsequently compared
by Batlivala and Ulaby [115] along with two other param-
eters termed the equivalent incoherent reflection coef-
ficient moisture content and the equivalent coherent
reflection coefficient moisture content, to the moisture
at fixed depth increments.

The equivalent coherent reflection coefficient
moisture content was defined by Batlivala and Ulaby
[115] as the moisture content of a uniform soil medium
whose power reflection coefficient at the surface is
equal to the power reflection coefficient of a soil medium
with the nonuniform soil moisture profile. They
defined the equivalent incoherent reflection coefficient
moisture content as the moisture content of a uniform
soil medium whose power reflection coefficient is equal
to

$$R = 1 - E \qquad \text{(VII-1)}$$

where R is the power reflection coefficient of the non-uniform soil. The term denoted by E is an effective emissivity at nadir based on the relationship:

$$E = (1 - R_o)\left[\Gamma_1 P_1 + \sum_{i=2}^{n-1}\left(\Gamma_i P_i \prod_{j=1}^{i-1} Q_j\right) + \prod_{j=1}^{n-1} Q_j \right] \qquad \text{(VII-2)}$$

where

R_o - power reflection coefficient at the air soil interface

i - layer index (i = 1 is the surface layer and i = n is a semi-infinite homogeneous layer)

$\Gamma_i = 1 - 1/L_i$

$P_i = 1 + R_i/L_i$

$Q_i = (1 - R_i)L_i$

$L_i = \exp(\alpha_i d_i)$

R_i = power reflection coefficient at the interface between the i and i + 1 layers

α_i - attenuation coefficient of layer i (nepers/cm)

d_i - width of ith layer (cm)

Based on a comparison of the linear correlation coefficients calculated for $\sigma°$ and each of these equivalent moisture definitions, Batlivala and Ulaby [115] concluded that the equivalent incoherent reflection coefficient moisture content was the most appropriate in terms of the radar response to soil moisture. However, Batlivala and Ulaby grouped all the measurements of $\sigma°$ from the 1974 smooth, medium rough and rough fields (see Chapter V) together when calculating the correlation coefficients. The data should have been grouped by surface preparation. As a result, their correlation coefficient calculations are questionable.

For the passive case, the idea of equivalent moisture contents based on reflection coefficients is not advantageous since these do not generally conform to the physical phenomenon of the emission process. Such definitions of equivalent moisture content rely on the Peake [29] development of emissivity which is ambiguous for nonuniform temperature profiles. Even the equivalent incoherent reflection coefficient model described above is independent of the soil temperature profile, although the formulation of the effective emissivity, (VII-2), was adopted from the Burke and Paris [32] radiative transfer model.

A technique that is more soundly based on physical phenomenon is to calculate an equivalent incoherent soil moisture based on the percentage energy contribution of arbitrarily defined soil layers to the total emitted energy at the surface. In this case the percentage contribution of each layer is based on the emitted energy of each layer referenced to the soil surface. The equivalent incoherent soil moisture is then determined by summing the soil moisture of each layer, weighted by the percentage energy contribution of that layer at the soil surface. This summation is shown in (VII-3).

$$m_I = \sum_{i=1}^{N} \frac{SM(i) \cdot \Delta BT_{volume}(i)}{BT_{volume}} \qquad \text{(VII-3)}$$

where

m_I - equivalent incoherent soil moisture content (either volumetric or gravimetric)

SM(i) - soil moisture in each layer

$\Delta BT(i)$ volume - brightness temperature contribution of each layer referenced to the soil surface

BT volume - total brightness temperature of the soil volume

N - number of layers

It should be noted that m_I will be affected to a certain extent by the soil temperature profile since $BT(i)$ depends on the respective temperature of the ith layer.

Another parameter that has been used to describe an equivalent soil moisture is the attenuated soil moisture in a skindepth. This parameter is calculated by performing a weighted average of soil moisture down to a skindepth. In this case the weighting function is the attenuation constant of the soil from the ith layer to the surface. This summation is shown in (VII-4).

$$m_A = \sum_{i=1}^{N} \frac{SM(i) \cdot \exp\left(-\sum_{j=1}^{i} \alpha(j)\right)}{Skindepth} \qquad \text{(VII-4)}$$

where

m_A - attenuated soil moisture in a skindepth

$\alpha(j)$ - attenuation constant at each layer

$SM(i)$ - soil moisture in each layer

For off-nadir angles, m_A is calculated by assuming that the energy travels along a ray path determined by Snell's law of refraction. As in the case of the equivalent skindepth moisture content, the temperature profile has no effect on this parameter.

Optimization of the soil moisture description -

Several parameters have been set forth as descriptions
of the moisture in a soil volume. It is necessary to
choose only one of these parameters for the remaining
analysis. The chosen parameter should be the one that
best meets the needs of the applications of concern and
that is soundly based on physical reasoning. Physical
reasoning tends to direct the choice toward the equivalent
incoherent soil moisture, m_I. This statement is made
because m_I is based on the radiative transfer model which
is the best description to date of the actual emission
process from a soil volume.

Simple statistical methods and direct comparisons
between all of the parameters and the actual measured
soil moisture profiles will provide clues as to the best
choice for application purposes. Figure VII-1 is a plot
comparing the soil moisture profiles averaged over specific
depth increments for all of the profiles measured in field
CS (the 1974 smooth bare field, Figure V-5) to each of the
previously described parameters calculated for 1.4 GHz.
Only 1.4 GHz results are shown in Figure VII-1 since at
10.6 GHz the emission originates from very shallow skin-
depths and is of little utility in providing moisture at
depths below 2 cm. This will be demonstrated later.

It is obvious from Figure VII-1 that the attenuated
water content in a skindepth, m_A, is not directly related
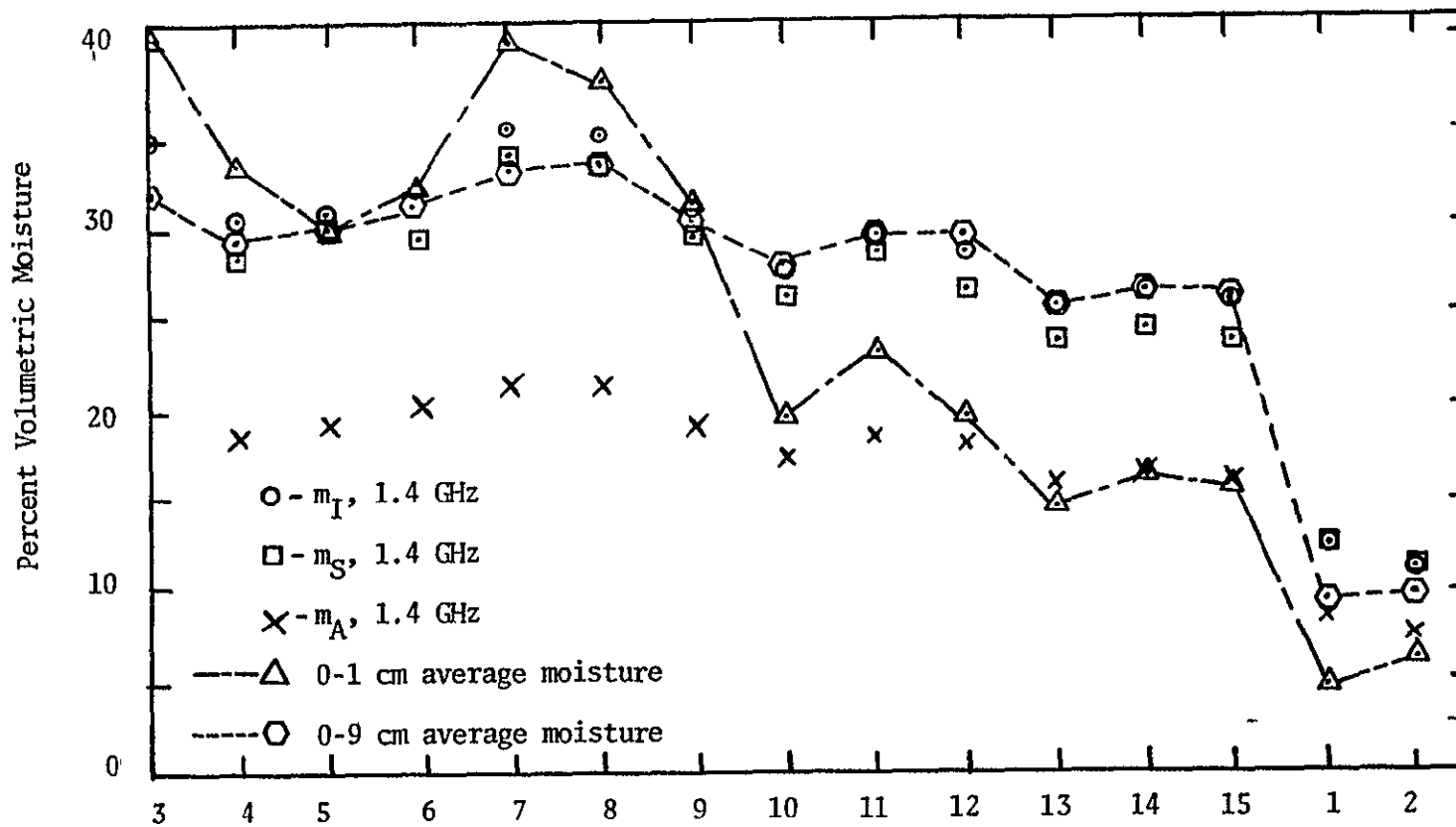
Ground Data Measurement Set - 1974 Smooth Bare Field (CS)

Figure VII-1. Comparison of calculated soil moisture parameters to the measured soil moisture averaged over depth.

to the measured soil moisture in any depth increment.
As a result, this parameter appears to be of little utility
at the present time. However, the equivalent incoherent
soil moisture and the equivalent skindepth soil moisture
does correspond to the measured moisture averaged over some
finite depth increment. As a result these parameters
contain information concerning the soil moisture profile
and will be of utility for certain applications.

More quantitative facts that are useful in determining
the optimum parameter to use in the subsequent analysis
of the microwave data are the correlation coefficient and
the covariance between the normalized antenna temperature
and each of the parameters. T_N is the normalized antenna
temperature. It is calculated by dividing the measured
antenna temperature in degrees Kelvin by the surface soil
temperature in degrees Kelvin. Table VII-1 contains a
tabulation of the normalized antenna temperature and the
three parameters of concern for field CS. The correlation
coefficient is defined in the standard manner [116]:

$$r = \frac{S_{xy}}{S_x S_y} \tag{VII-5}$$

TABLE VII-1

Data Used to Calculate Correlation Coefficients (Field CS)

Profile	Normalized Antenna Temperature (1.4 GHz, 20°, vertical) T_{N_v}	Equivalent Incoherent Soil Moisture; m_I (percent $\frac{grams}{cm^3}$)	Equivalent Skindepth Soil Moisture; m_S (percent $\frac{grams}{cm^3}$)	Attenuated Soil Moisture in a Skindepth, m_A (percent $\frac{grams}{cm^3}$)
CS 1	0.90	12.9	12.8	8.6
CS 2	0.92	11.3	11.7	7.4
CS 3	0.60	34.7	34.9	24.0
CS 4	0.72	30.4	28.5	18.9
CS 5	0.63	31.0	30.0	19.5
CS 6	0.62	32.2	29.6	20.2
CS 7	0.56	35.4	34.1	21.4
CS 8	0.60	35.2	33.8	21.6
CS 9	0.61	31.2	29.7	19.6
CS 10	0.69	27.3	26.1	17.4
CS 11	0.68	29.2	28.6	18.6
CS 12	0.78	28.6	26.4	18.1

TABLE VII-1 (Continued)

Profile	Normalized Antenna Temperature (1.4 GHz, 20°, vertical) T_{N_v}	Equivalent Incoherent Soil Moisture; m_I (percent $\frac{grams}{cm^3}$)	Equivalent Skindepth Soil Moisture; m_S (percent $\frac{grams}{cm^3}$)	Attenuated Soil Moisture in a Skindepth, m_A (percent $\frac{grams}{cm^3}$)
CS 13	0.79	25.3	23.8	16.1
CS 14	0.79	26.2	24.4	16.7
CS 15	0.81	25.7	23.9	16.3

where

S_{xy} - covariance between the given data points x and y

S_x - sample standard deviation of x

S_y - sample standard deviation of y

x - normalized antenna temperature

y - soil moisture parameter

Table VII-2 tabulates the results of the calculations.
Note that the correlation coefficient is approximately the
same for all three soil moisture parameters. Since S_x
is the same for all cases, it is more instructive to
compare the covariance calculations. If S_{xy} is zero
then the two variables are uncorrelated. As expected,
S_{xy} is largest for the equivalent incoherent soil moisture
and smallest for the attenuated soil moisture in a skin-
depth. These results coupled with physical intuition
indicate that m_I, the equivalent incoherent soil moisture,
should be used throughout the remainder of the analysis
as the parameter with which to correlate antenna
temperature measurements.

Interpretation of the equivalent incoherent soil
moisture - It is now instructive to interpret the parameter
m_I in terms of a measured soil moisture quantity. In
other words, assuming that this parameter could be estimated
without error from microwave antenna temperature measure-
ments. What soil moisture information does it provide?

TABLE VII-2

Results of the Correlation Analysis

Data Group	S_{xy}	r
T_{N_v} and m_I	-0.794	-0.912
T_{N_v} and m_S	-0.771	-0.914
T_{N_v} and m_A	-0.461	-0.911

This can most easily be seen in Figures VII-2 and VII-3 which are plots of soil moisture averaged to various depths for all of the soil profiles observed for the 1974 smooth bare field. Figure VII-2 contains a plot of m_I calculated for 10.6 GHz. Figure VII-3 contains a plot of m_I calculated for 1.4 GHz.

The parameter m_I for 10.6 GHz corresponds nearly exactly with the average soil moisture in the 0-1 cm layer for soil moistures above 25 percent. For soil moistures below 25 percent, it corresponds to a layer slightly deeper than 1 cm, although this depth is still closer to 1 cm than it is to 2 cm. It is evident that m_I corresponds to deeper layers the drier the soil moisture profile, although at 10.6 GHz these layers are very shallow.

At 1.4 GHz the same general trend occurs between m_I and the depth of the bottom of the layer containing the corresponding average soil moisture content. It is, however, much more pronounced and occurs at deeper layers, as would be expected. Figure VII-3 demonstrates that m_I calculated for 1.4 GHz generally corresponds to a layer between 0-5 cm and 0-15 cm, except for very wet conditions, above 35 percent soil moisture where it corresponds to a shallower layer.

It should be noted for interpretation purposes that the smooth bare field was irrigated just prior to acquiring
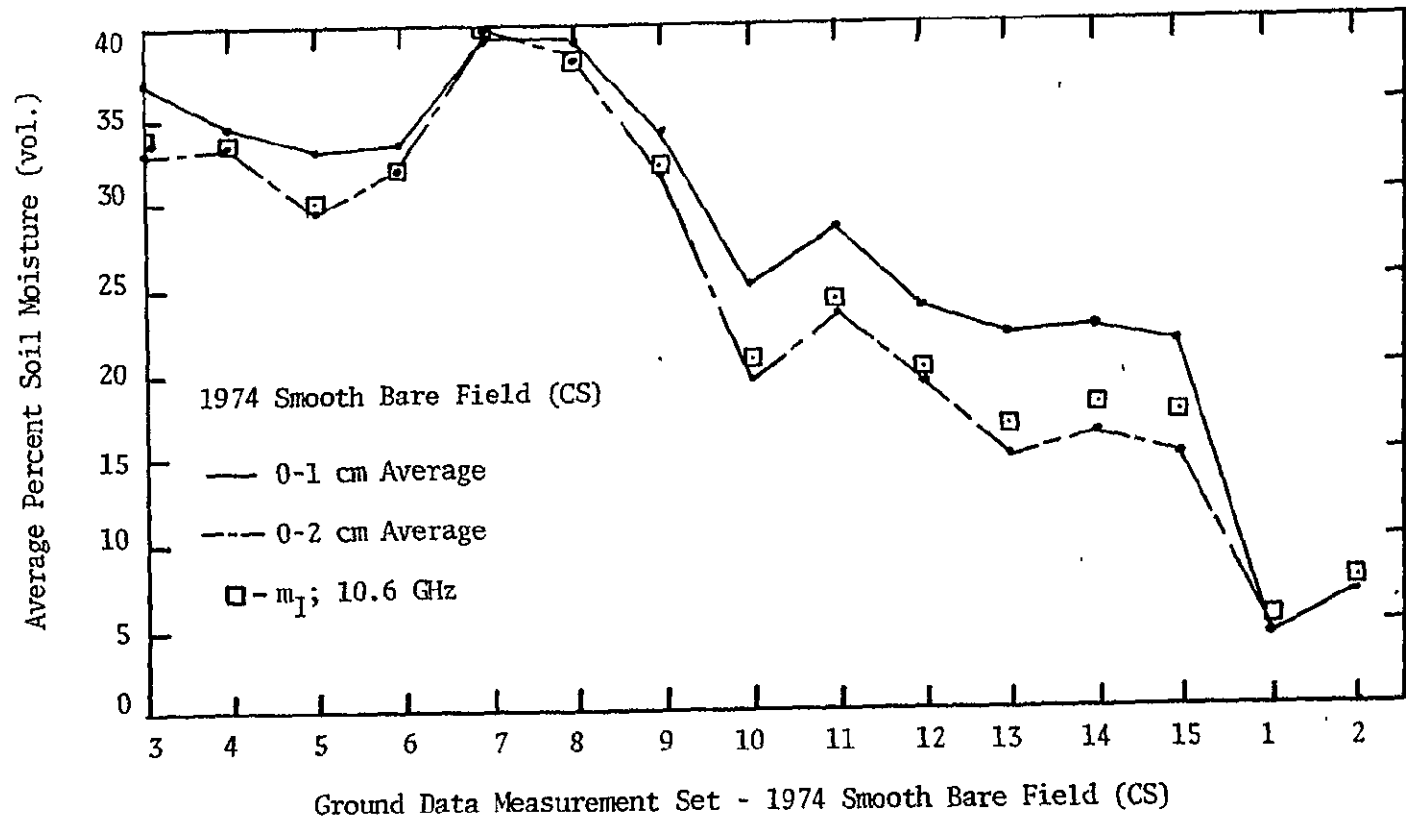
Figure VII-2. Comparison of equivalent incoherent soil moisture calculated at 10.6 GHz to measured soil moisture averaged over depth.
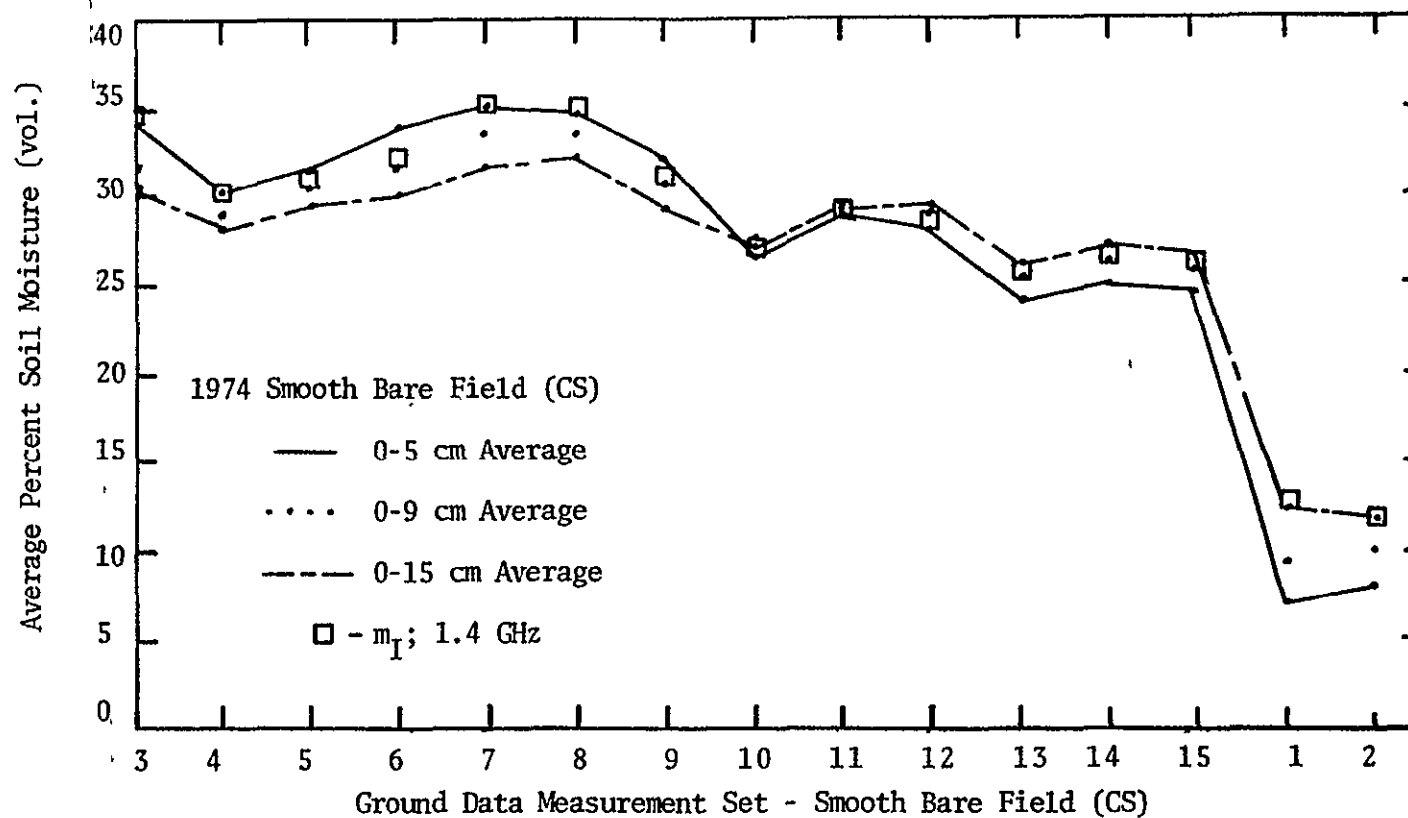
Figure VII-3. Comparison of equivalent incoherent soil moisture calculated at 1.4 GHz to measured soil moisture averaged over depth.

profile three. As a result, the surface 0-1 cm layer was wetter than the 0-2 cm layer from the time ground data measurement three was acquired until ground data measurement set seven was acquired. This is evident in Figure VII-2. Also, the 0-5 cm layer was wetter than the 0-9 cm layer which was wetter than the 0-15 cm layer between ground data set three and ground data set ten, when the order reversed. This can be seen in Figure VII-2. When the upper layers are wetter than the lower layers, the profile is said to be inverted. This condition occurs just after irrigation or a rain. Under this condition m_I corresponds to a shallower layer than when the profile is not inverted. However, the degree to which this is true still depends on the moisture in the lower 0-5 cm and 0-9 cm levels.

Since the m_I calculated for 10.6 GHz corresponds to the moisture in depths less than two centimeters for all profile situations, it will be assumed that 10.6 GHz only responds to 0-2 cm moisture hereafter. However, it is necessary to define the soil depth which corresponds to the m_I calculated for 1.4 GHz. The layer with which each m_I corresponds was calculated by linearly interpolating the average moisture contents. Figure VII-4 is the result of these calculations. They were done for the profiles of all three 1974 fields, CS, CM, and CR.
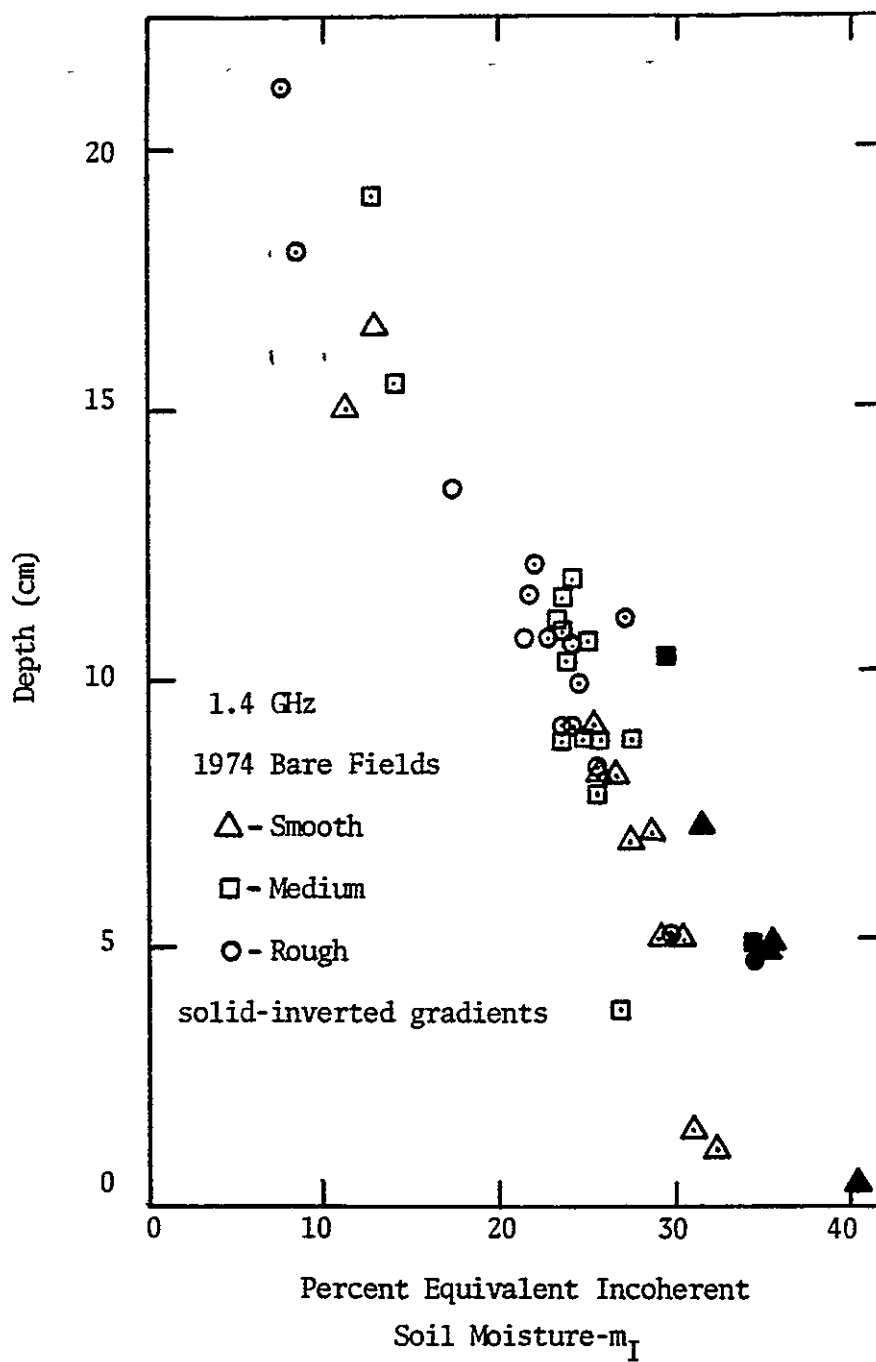
Figure VII-4. Comparison of equivalent incoherent
soil moisture (m_I) calculated at 1.4
GHz to the depth that corresponds to
an average soil moisture equal to m_I.

It is obvious from Figure VII-4 that there is a linear relationship between the equivalent incoherent soil moisture and the depth to the bottom of the corresponding soil layer, at least for m_I's below 25 percent. The apparent nonlinearity above 25 percent is a result of the actual soil moisture profile shape. There are three types of soil moisture profiles as depicted in Figure VII-5. Note that it is profile type B that generally causes the departure from a linear correlation with depth for m_I's above 25 percent (Figure VII-4). However, a linear least squares straight line fit to all of the data in Figure VII-4 yields a correlation coefficient of 0.92 and the following linear regression equation:

$$D = -0.58\ m_I + 23.64 \qquad \text{(VII-6)}$$

where D is the depth to the bottom of the layer in centimeters to which m_I corresponds.

A better estimate of the corresponding depth of measurement can be made by grouping the data of Figure VII-4 into three categories as denoted in Table VII-3. Table VII-3 inherently assumes that profile type A, an inverted profile, can be distinguished from the others.

Percent Soil Moisture

Type A
Inverted

Depth

Percent Soil Moisture

Type B

Depth

Percent Soil Moisture

Depth

Type C
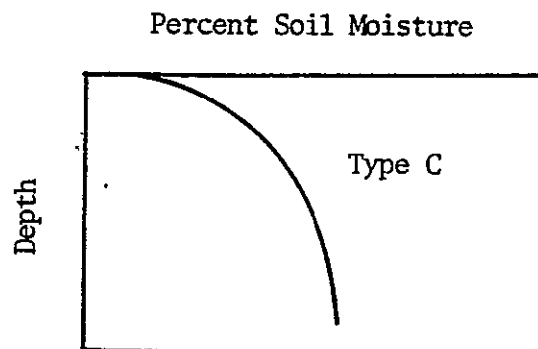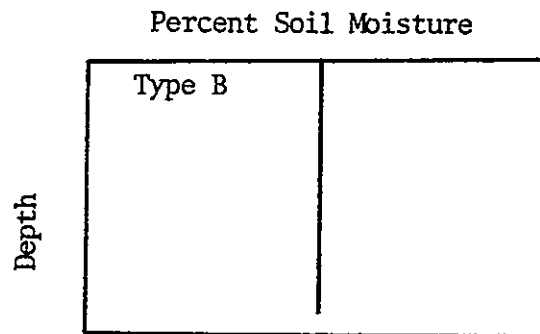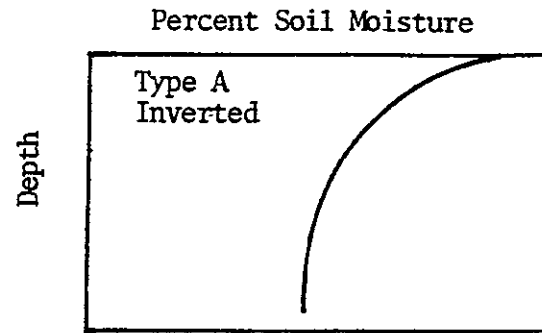
Figure VII-5. Definition of soil moisture
profile type.

TABLE VII-3

Separation of Profiles for Regression Analysis

Category	Definition
I	$m_I < 0.25$
II	$m_I > 0.25$ profile type A
III	$m_I > 0.25$ profile type B and C

It is felt that a soil moisture profile can be classified as type A simply by comparing the 10..6 GHz estimate of- — m_I to the 1.4 GHz estimate. If the 10.6 GHz estimate is larger, then the surface is wetter than the immediate subsurface and the profile is inverted. This result is of vital importance since the ability to distinguish inverted profiles from non-inverted profiles provides information on the recent history of water input to the soil system.

A linear least squares regression fit to the equivalent incoherent soil moisture categories given in Table VII-3 produce the results contained in Table VII-4. Figure VII-6 is a plot of these regression fits along with the 70 percent confidence intervals for each of the fits. In this linear regression analysis the basic assumptions are that the depths being estimated are normal uncorrelated random variables with equal variance and zero mean. Assuming that the equivalent incoherent soil moisture is measured without error, the 70 percent confidence intervals define the range of depths that will include the true mean depth with a 70 percent confidence.

The equivalent incoherent soil moisture, m_I, will be used in the remainder of this document to describe the soil moisture to which the antenna measurements are responsive. For convenience, it will be denoted by the acronym EQSM.

TABLE VII-4

Linear Regression Equations for Soil Profile

Categories I, II, and III

Category	Regression Line	Correlation Coefficient
I	$D = -0.569\ m_I + 23.77$	0.94
II	$D = -0.635\ m_I + 27.405$	0.92
III	$D = -1.055\ m_I + 35.79$	0.81
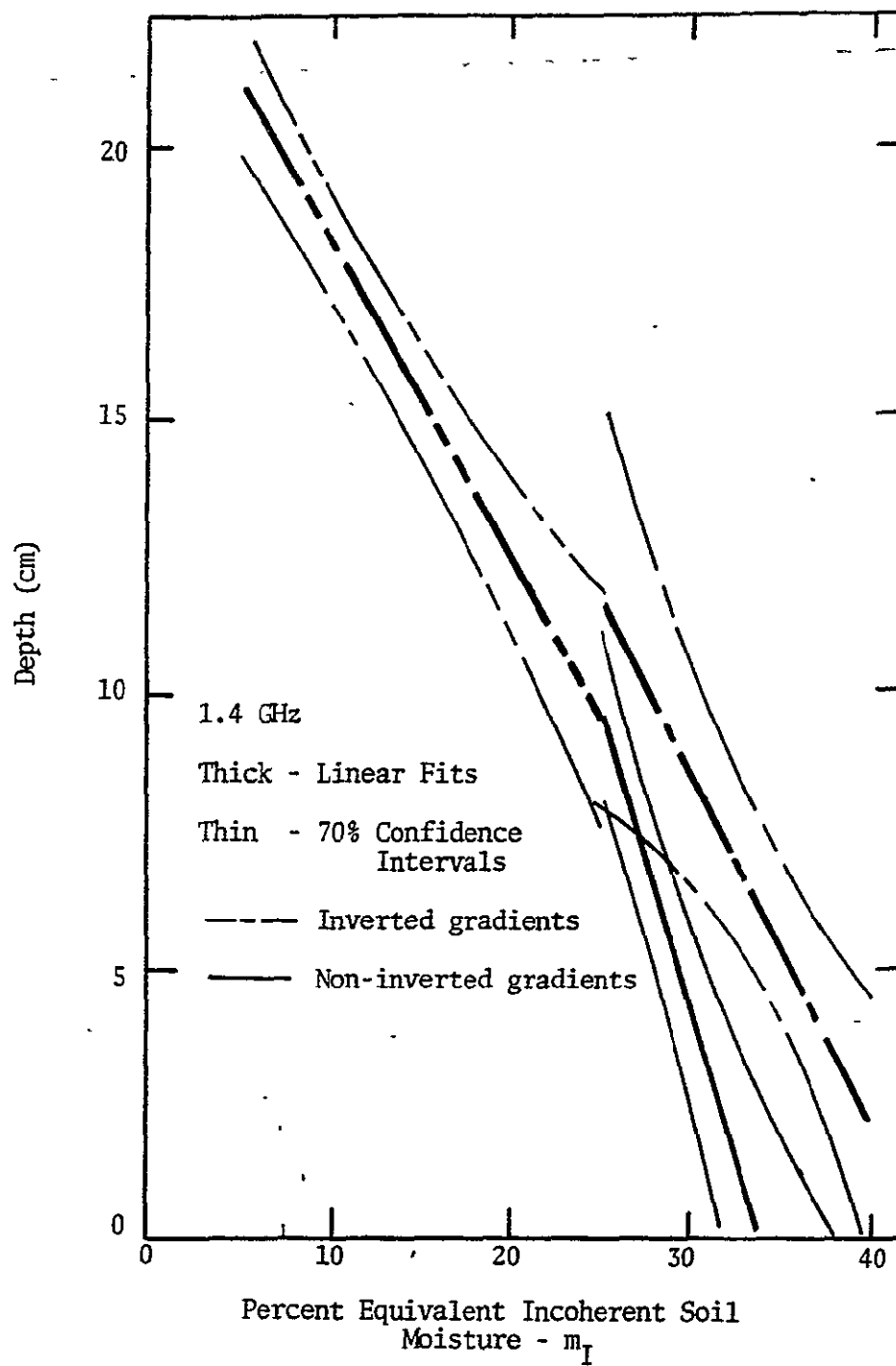
Figure VII-6. Linear regression fits and confidence
intervals for the data in Figure VII-4.

Appendix C contains calculations of EQSM for all of the
soil moisture profiles measured during the 1974 and 1975
measurement programs.

Soil Temperature Profile

The effect of the soil temperature profile was
demonstrated in Chapter IV. It was shown that emission
from the soil is dependent on the soil temperature
magnitude and the shape of the temperature profile. In
order to analyze antenna measurements for soil moisture
information without being biased by differences in soil
emission due to differences in the soil temperature
profile, it is necessary to normalize the antenna
temperature measurement to a soil temperature parameter.

Physical reasoning indicates that the best parameter
with which to normalize antenna temperature measurements
to eliminate differences due to the soil temperature
would be an equivalent incoherent soil temperature,
calculated using the same technique as is used to cal-
culate m_I, the equivalent incoherent soil moisture.
However, such a parameter cannot be utilized in a system
designed to remotely measure soil moisture since the
soil temperature profile is an unknown quantity. Surface
soil temperature is a remotely measurable quantity,
however, and can be used in such a system if required.

Therefore, as a compromise, the surface soil temperature will be used in the following analysis to normalize the measured antenna temperatures.

Normalized antenna temperatures calculated using surface soil temperatures compare very favorably with antenna temperatures normalized using an equivalent incoherent soil temperature, t_I.

$$t_I = \sum_{i=1}^{N} \frac{t(i) \cdot \Delta BT(i)_{volume}}{BT_{volume}} \qquad \text{(VII-7)}$$

where

t_I - equivalent incoherent soil temperature

$t(i)$ - soil temperature of each layer

ΔBT (i) - brightness temperature of each layer
volume
referenced to the soil surface

BT - total brightness temperature of the
volume
soil volume

For at least 97 percent of the 1974 measurements the antenna temperature normalized using the surface soil temperature is within 0.01 of the antenna temperature normalized using t_I. None differ by more than 0.02.

As with the equivalent incoherent soil moisture, the equivalent incoherent soil temperature will be

denoted by an acronym, EQST, in the remainder of this
report. It will not be used to normalize antenna
temperatures for analysis purposes, but it will be used
to describe the measured soil temperature. Appendix C
also contains tabulations of EQST for the soil temperature
profiles measured during the 1974 and 1975 measurement
programs.

Data Interpretation and Soil Moisture
Correlation

Antenna temperature measurements will be analyzed
in this section to demonstrate the soil moisture dependence,
and the effects of surface roughness and vegetation cover
on this dependence. The measured antenna temperatures
are not corrected for antenna beamwidth or reflected sky
temperature. It is doubtful that these measurement
deficiencies can easily be corrected in any system designed
for the purpose of making a usable estimate of soil
moisture. Rather, the system will have to be designed to
minimize such effects. The corrections were not made
for these particular deficiencies in order to demonstrate
that usable soil moisture information is contained in
the degraded soil brightness temperature measurement.
However, the reflected self emission component is a serious
effect for angles near nadir. Since this effect only

occurs as a serious problem in ground-based system measurements, all of the data measured at nadir have been corrected for this self emission component. Appendix B provides a detailed discussion of the self-emission effect and the scheme used to correct the measurements.

In the discussion that follows, the soil moisture dependence is first demonstrated using smooth bare soil measurements. Then, the effects of other scene parameters on this dependence are presented. The effects of surface roughness are presented first, then the effects of vegetation cover are discussed.

Smooth Surface Moisture and Angle Dependence

The effect of soil moisture is the largest for smooth bare soil surfaces. Surface roughness and vegetation cover tend to degrade this dependence. As a result, the soil moisture dependence will be presented first for a smooth bare soil surface. The effect of surface roughness and vegetation will be demonstrated later.

The experimental plots used in the 1974 measurement program contained a smooth bare field. Only 1.4 GHz data are used since the bare smooth field, field CS, did not appear smooth at the 10.6 GHz wavelength. The effect of transmission angle for a surface smooth at 10.6 GHz will be the same as will be demonstrated for the smooth surface at 1.4 GHz.

Normalized antenna temperature is plotted as a
function of transmission angle for four soil moisture
profiles in Figure VII-7. The measured antenna tempera-
tures were normalized using the 0-1 cm soil temperature
to eliminate effects of surface temperature variation.
It can be seen (Figure VII-7) that the change in the
vertical normalized antenna temperature with soil moisture
decreases as the transmission angle is increased (i.e.,
the response to soil moisture decreases as transmission
angle increases). It is not as obvious, but the response
to soil moisture for horizontal polarization increases
slightly with transmission angle.

Both of these phenomena are demonstrated in Figure
VII-8 through VII-14. These figures contain plots of
normalized antenna temperature as a function of soil
moisture for each transmission angle. A best fit straight
line has also been drawn through the points on each plot.
The slopes of the straight lines describe the average
sensitivity to soil moisture. The slope for horizontal
polarization shows a slightly increasing trend with
transmission angle while for vertical polarization it
shows a decreasing trend (Figure VII-15). In Figure
VII-15 the slopes are referenced to a ground temperature
of $300°K$ such that sensitivity in degrees Kelvin per percent
moisture can be plotted. The trends in Figure VII-15
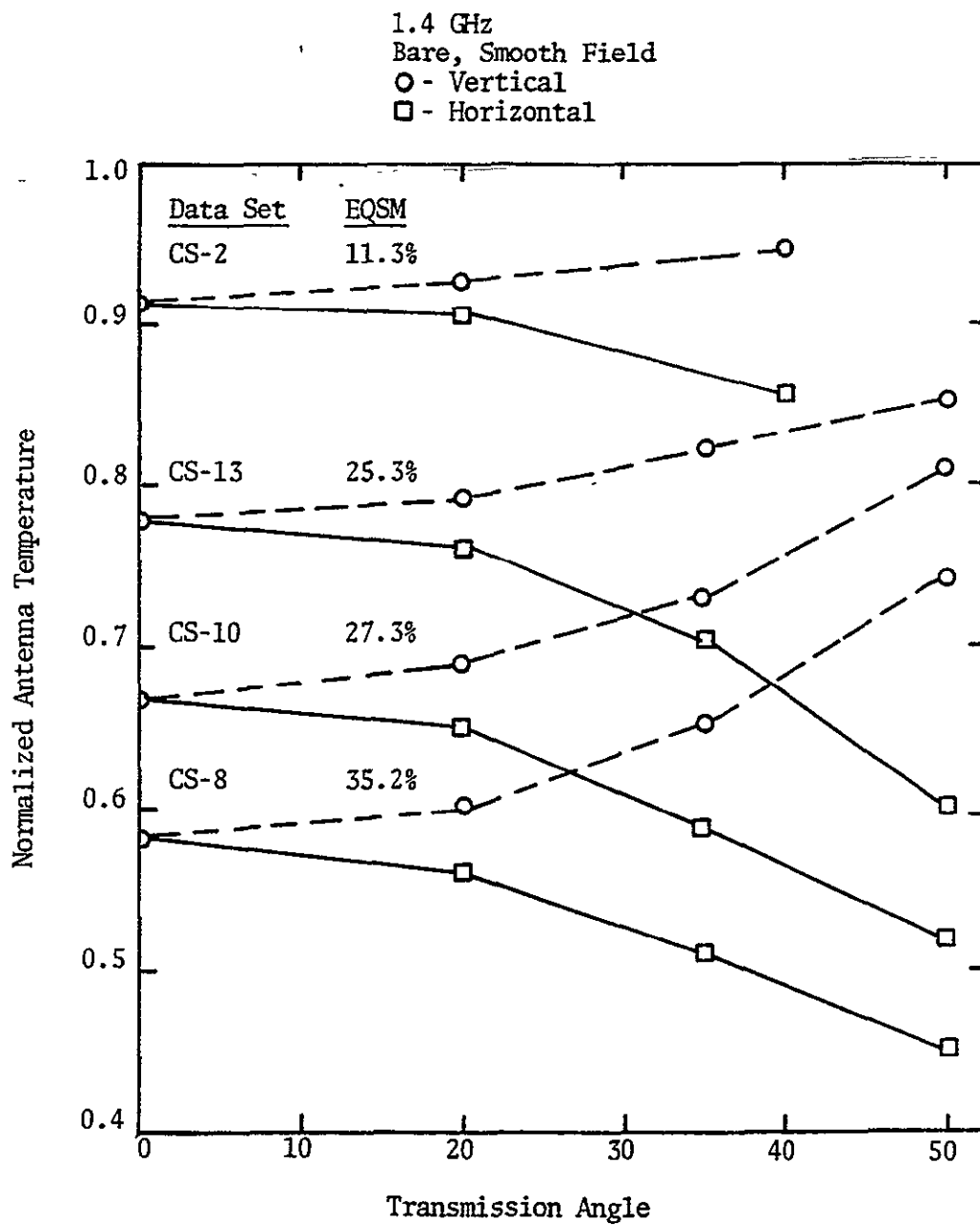
Figure VII-7. Measured 1.4 GHz emission as a
function of soil moisture and
transmission angle.
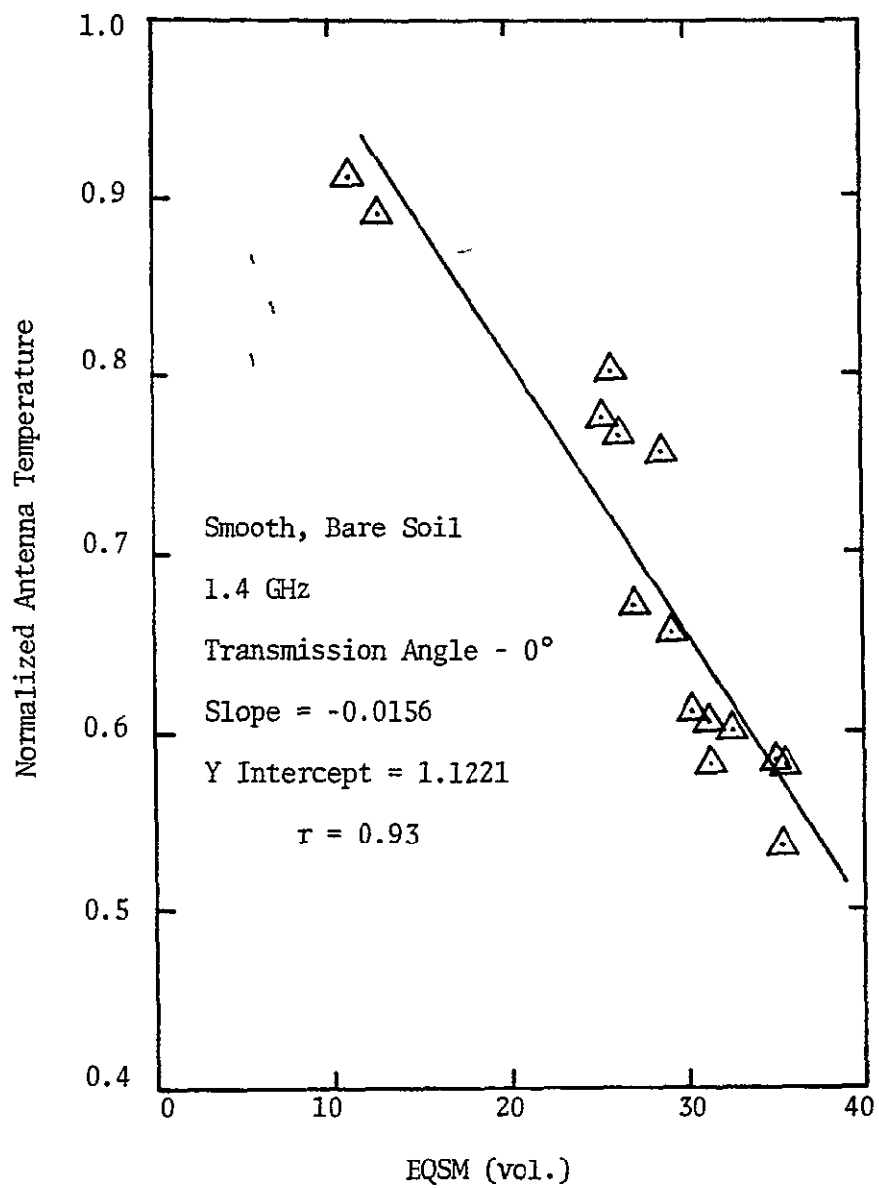
Figure VII-8. 1.4 GHz antenna temperature measurements of smooth, bare soil at nadir as a function of equivalent incoherent soil moisture.
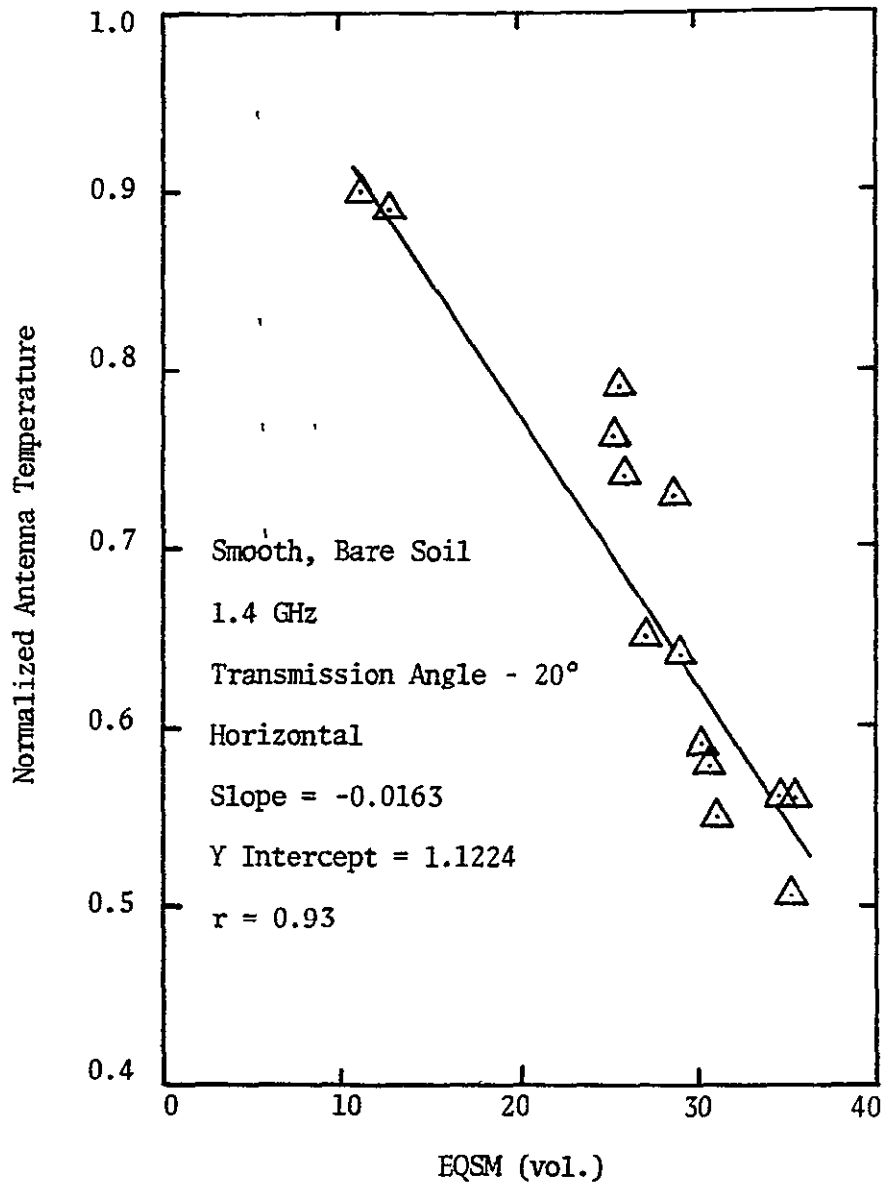
Figure VII-9. Horizontal 1.4 GHz antenna temperature
measurements of smooth, bare soil at
20° as a function of equivalent
incoherent soil moisture.
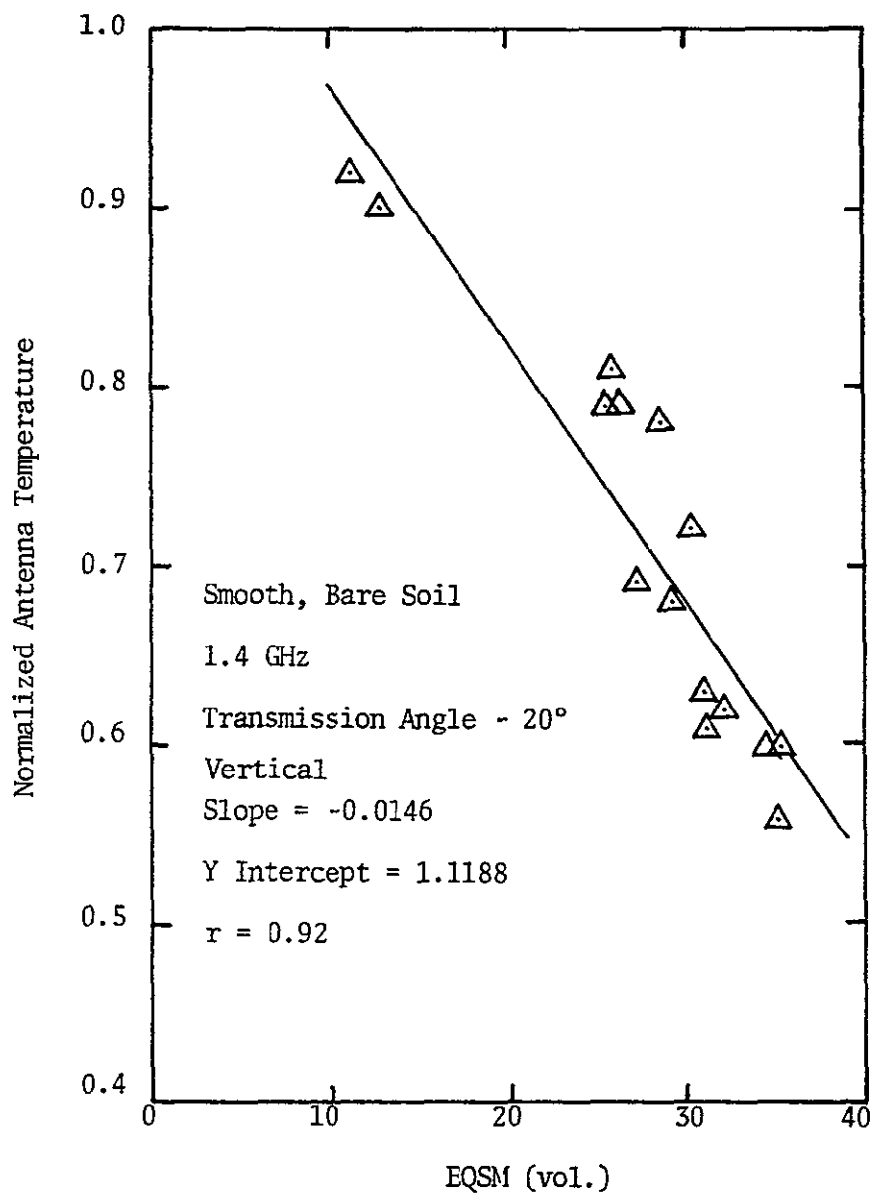
Figure VII-10. Vertical 1.4 GHz antenna temperature measurements of smooth, bare soil at 20° as a function of equivalent incoherent soil moisture.
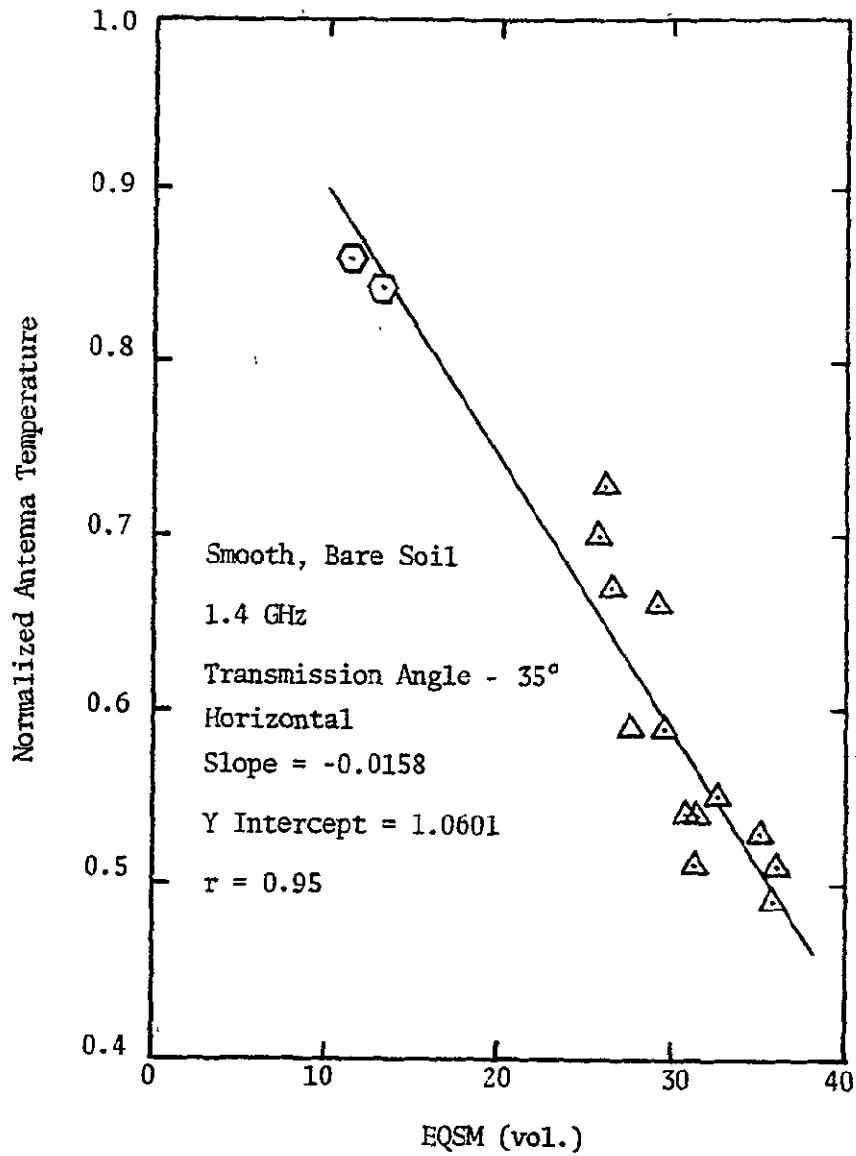
Figure VII-11. Horizontal 1.4 GHz antenna temperature
measurements of smooth, bare soil at
35° as a function of equivalent
incoherent soil moisture.
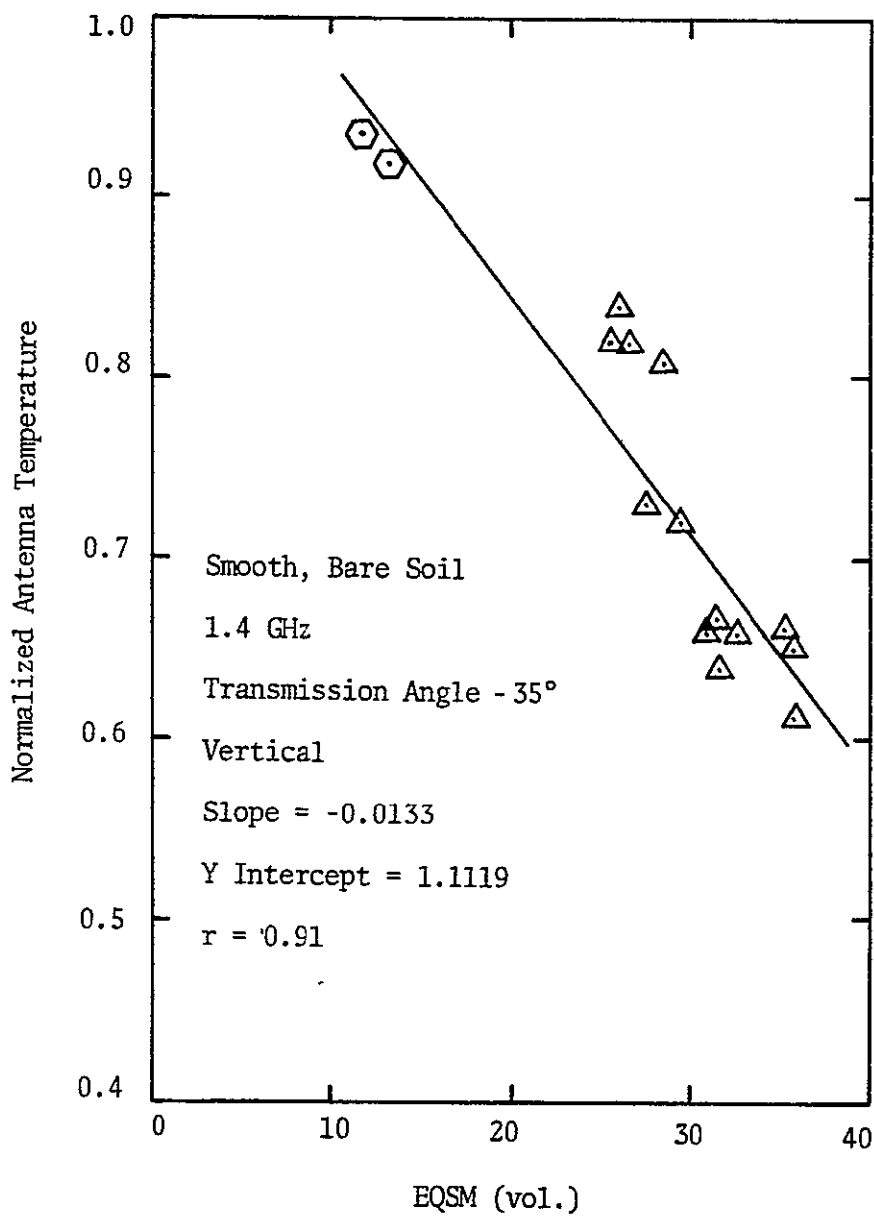
Figure VII-12.   Vertical 1.4 GHz antenna temperature
measurements of smooth, bare soil at
35° as a function of equivalent
incoherent soil moisture.
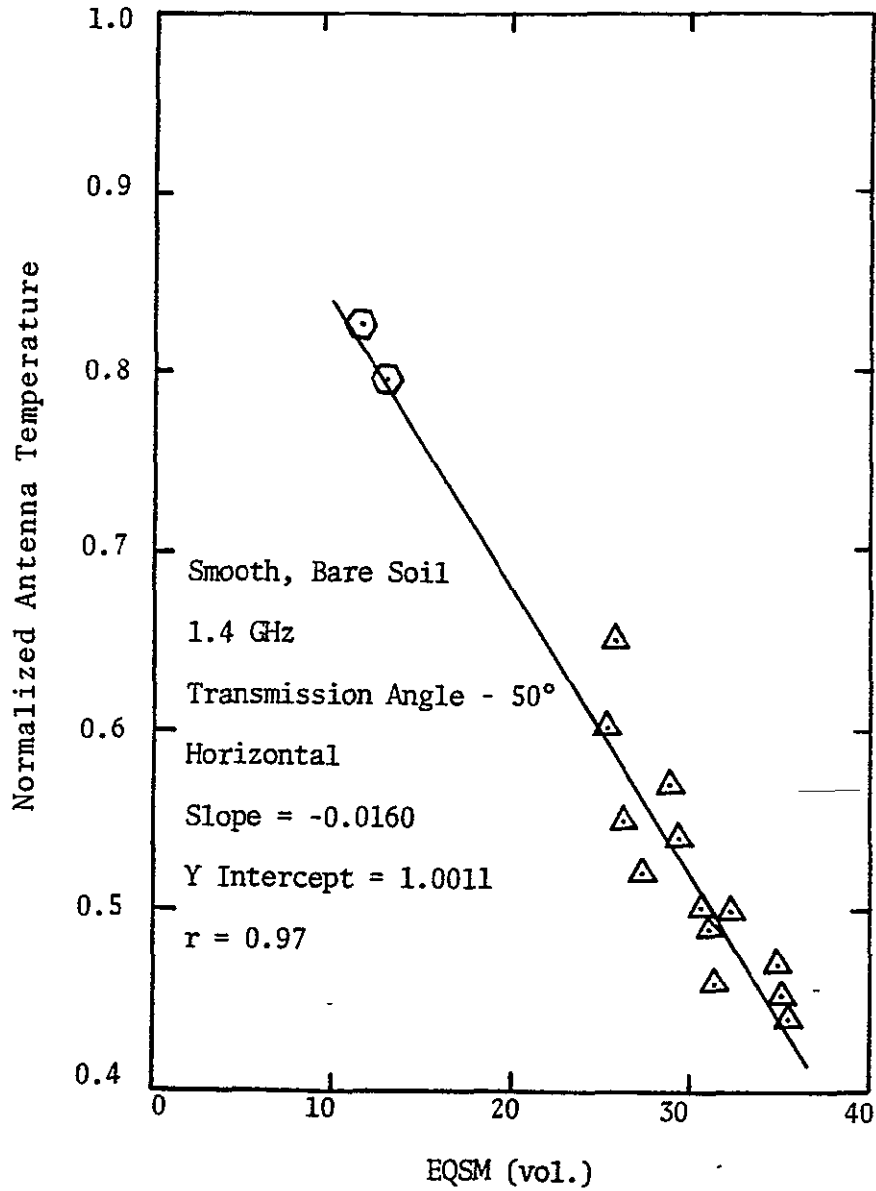
Figure VII-13. Horizontal 1.4 GHz antenna temperature measurements of smooth, bare soil at 50° as a function of equivalent incoherent soil moisture.
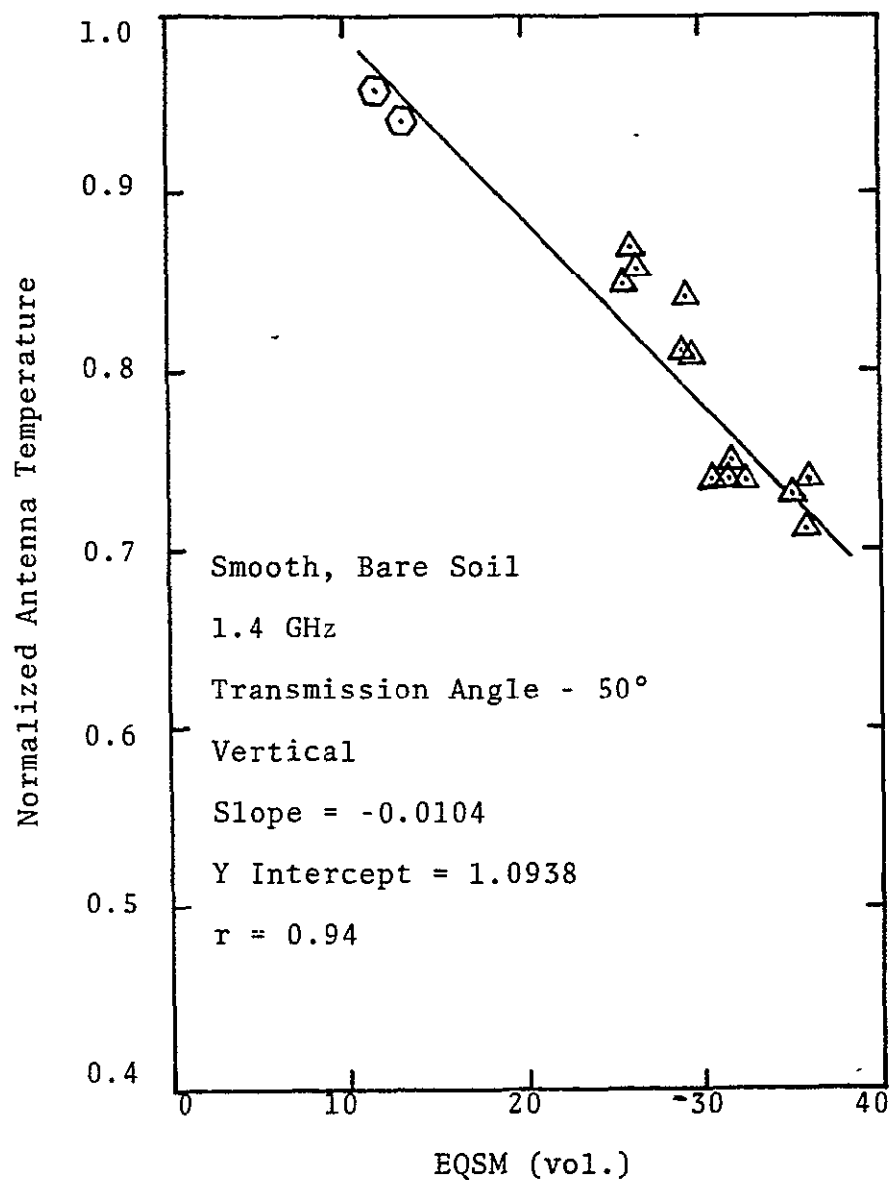
Figure VII-14. Vertical 1.4 GHz antenna temperature
measurements of smooth, bare soil at
50° as a function of equivalent
incoherent soil moisture.
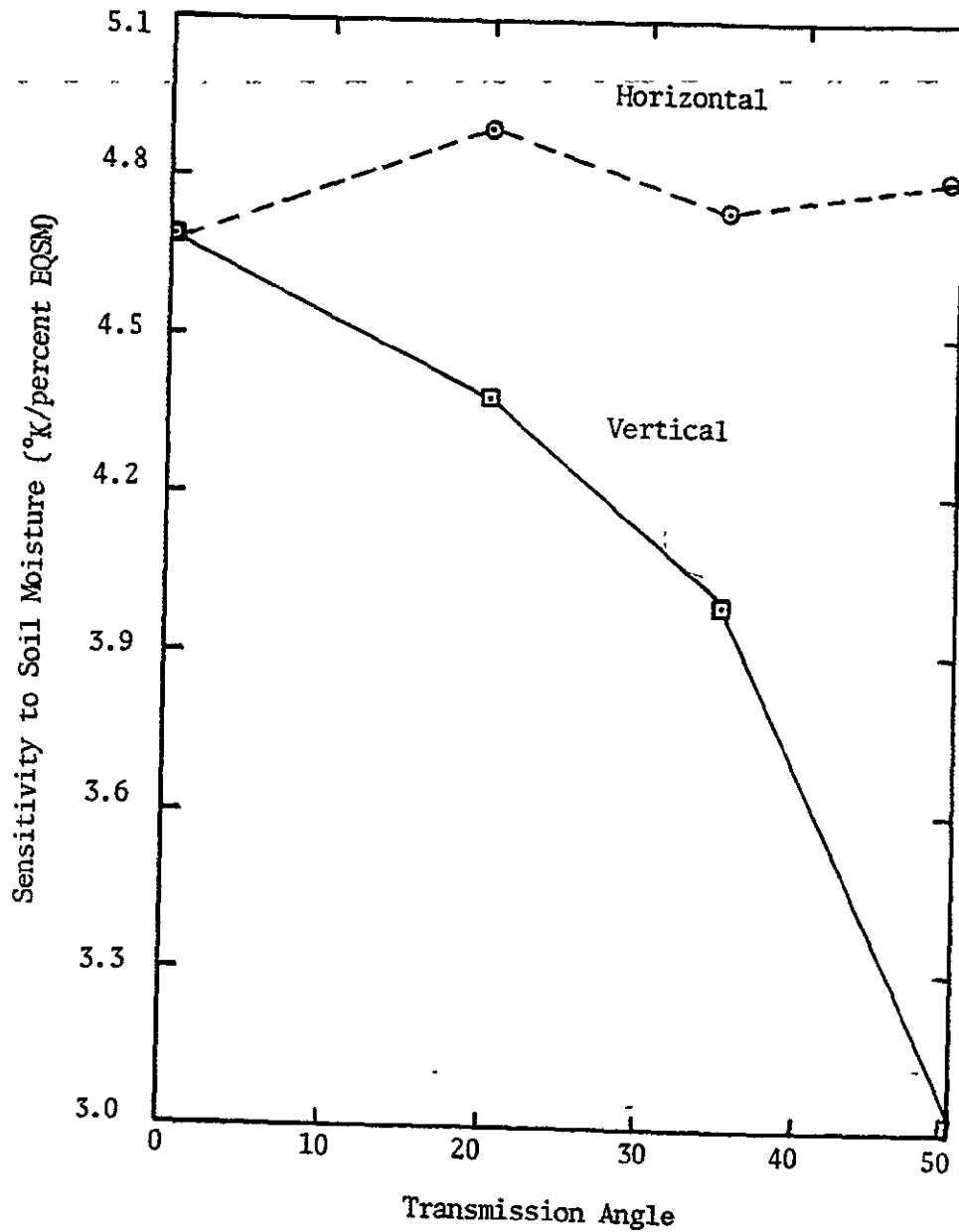
Figure VII-15.   Sensitivity of 1.4 GHz antenna
                 temperature measurements to soil
                 moisture of smooth, bare soil based
                 on linear regression fits.

were predicted in Chapter IV (Figure IV-18) using the model
for the emission from a smooth soil.

The predictions of this model indicate the rationale
behind the phenomenon. The sensitivity to vertically
polarized emission to soil moisture decreases with trans-
mission angle. This is due to the fact that the natural
angular response causes the vertical emission to increase as
the transmission angle increases. However, the brightness
temperature of emission can never exceed the physical
temperature of the soil. Thus, the allowable range over
which the vertical emission can change with soil moisture
decreases as the transmission angle increases. For
horizontal polarization the natural angular response causes
the emission to decrease with angle. Thus, as transmission
angle is increased the allowable range over which the emis-
sion can change with soil moisture is virtually unchanged.

In the discussion above, straight lines were fit to
the measurements in Figures VII-8 through VII-14 to
demonstrate the overall response to soil moisture.
However, the energy emitted from the soil is directly
dependent on the permittivity of the soil. This means
that normalized antenna temperature plotted versus soil
moisture should have a curvature that is the inverse of the
permittivity curve of Miller clay (Figure II-23). Cal-
culations based on the models presented in Chapter IV

demonstrate this phenomenon (Figure IV-17). The curvature of the plot in Figure IV-17 is inverse to the curvature of the plot of permittivity versus soil moisture for Miller clay (Figure II-23). The permittivity curve of Miller clay breaks at approximately 24 percent moisture. Although there are no antenna temperature measurements for moistures between 15 percent and 25 percent, the data plotted in Figures VII-8 through VII-14 indicate that 24 to 25 percent is the breakpoint.

In view of the discussion above, it is obvious that the points plotted in Figures VII-8 through VII-14 could be fitted with two straight lines. One for equivalent soil moistures ranging from 0 to 25 percent, and one for moistures ranging from 25 percent to saturation. Such a fit is demonstrated in Figure VII-16 using the predictions of the model.

It is interesting to compare the slopes of the best fit lines through the measurements presented in Figures VII-8 through VII-14 for moistures above 25 percent to the slopes of the lines through all of the points. This can be done by converting the slopes to sensitivity in degress Kelvin per percent moisture. The slopes of the linear regression lines fitted to all of the points were converted to a soil moisture sensitivity by multiplying them by a reference ground temperature of 300°K. The
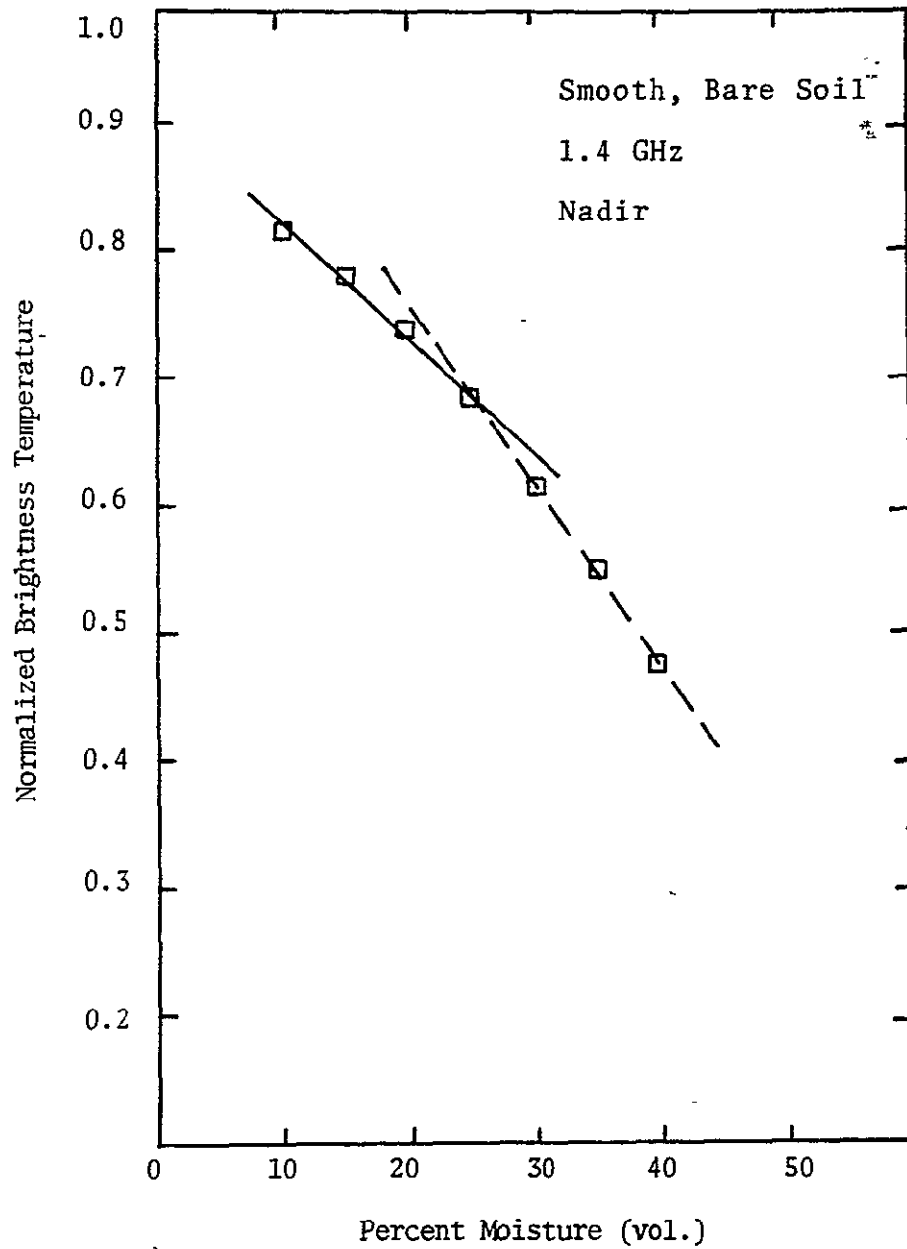
Figure VII-16. Calculated brightness temperature
of a smooth, bare soil as a function
of uniform soil moisture.

results are presented in Figure VII-15. The slopes of the linear regression lines fitted to the points above 25 percent soil moisture were converted to sensitivity in the same manner and plotted in Figure VII-17. A comparison of Figure VII-15 and Figure VII-17 demonstrate that the true response of antenna temperature measurements to variations in soil moisture for moistures above 25 percent is greater than the average response observed over the entire moisture range from dry to saturated.

Effects of Roughness

Antenna temperature measurements were made on two types of surface roughness during the 1974 and 1975 measurement programs. In 1974 the experimental plots were roughened as uniformly across the fields as possible. However, in 1975 the experimental plot was prepared in rows similar to the tillage practices used in the area near Phoenix, Arizona. This was done so that the effects of row direction could be investigated. As a result the discussion on roughness effects is divided into two parts; one on uniform roughness and one on the effects of row tillage.

Uniform roughness - It has been demonstrated that the emission from bare smooth soil is sensitive to changes in the shape and overall magnitude of the soil moisture
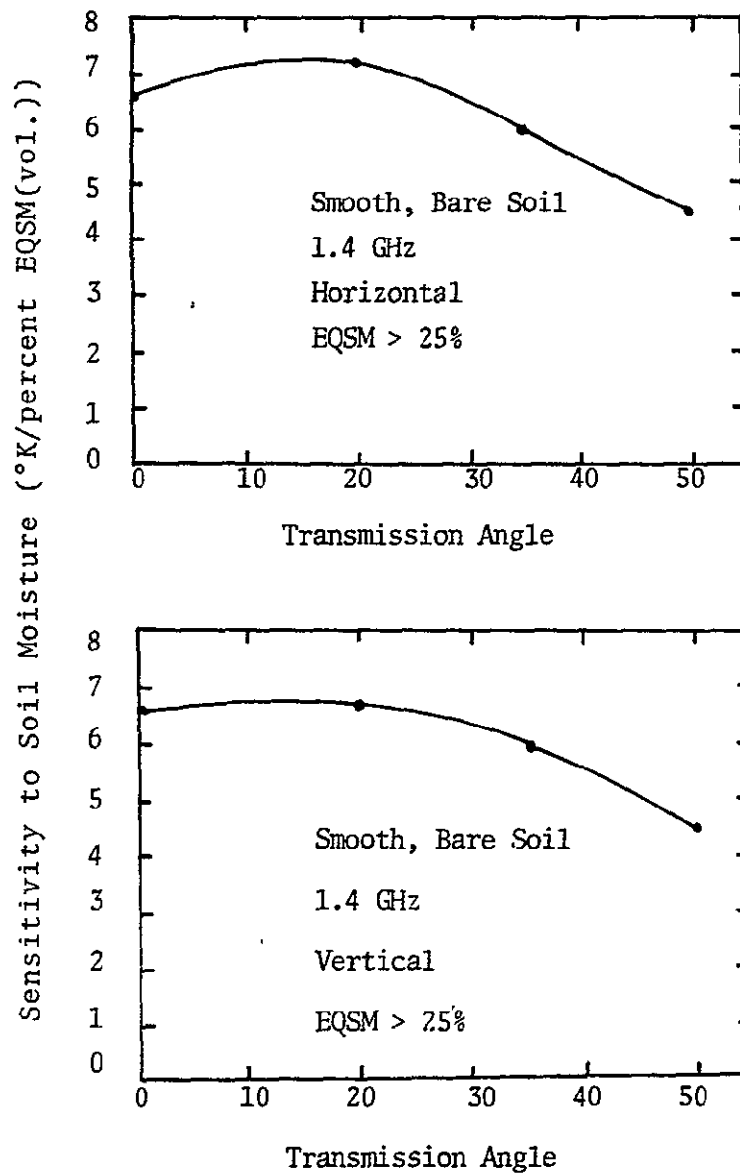
Figure VII-17. Sensitivity of antenna temperature measurements to soil moisture for average moistures greater than 25%.

profile. However, as the soil surface is roughened the sensitivity to soil moisture decreases. Naturally, the effect of a given surface roughness is dependent on the wavelength of the radiation. For 1.4 GHz at a transmission angle of 20°, Figure VII-18 demonstrates the reduction in the sensitivity of the emission to soil moisture due to the uniform roughness of the 1974 experimental plots. The smooth field (CS) had a rms surface height deviation of 0.88 cm, the medium rough (CM), 2.6 cm, and the rough (CR), 4.3 cm.

The fact that the response to soil moisture actually decreased with surface roughness was not expected at first. It was only after the model in Chapter IV was developed that a clear understanding of the emission phenomenon for rough surfaces was understood. In order to describe the emission from a rough surface using the model developed in Chapter IV, it was necessary to determine the values of Q, the roughness parameter distribution with transmission angle, that describe each of the surface preparations. The technique of obtaining the Q distributions for 1.4 GHz will be described, then a simple physical interpretation of the model predictions will be made.

Although the roughness parameter, Q, is defined in terms of the surface autocorrelation function and variance
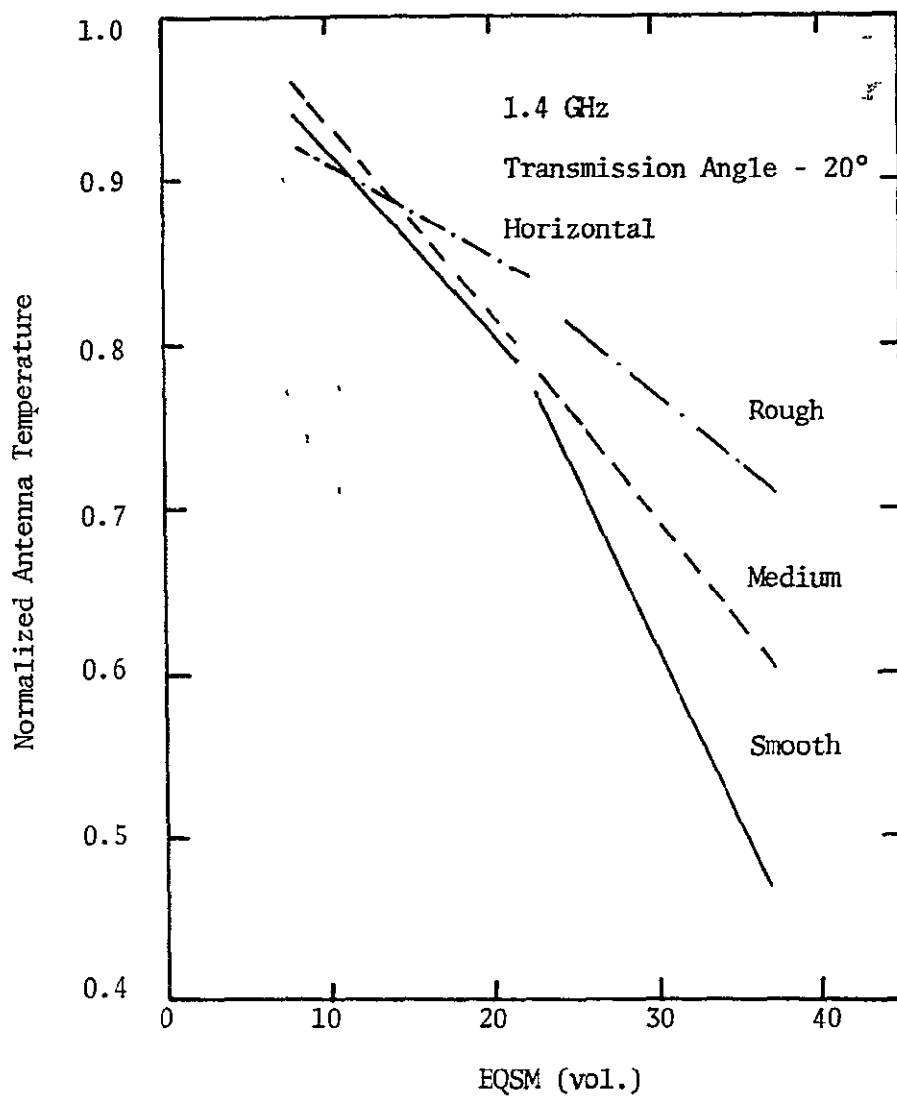
Figure VII-18. Normalized 1.4 GHz antenna
temperature measurements as
a function of soil moisture
for three surface roughness
conditions.

of the surface height distribution, (IV-72), it cannot

easily be obtained from a measurement of the surface

profile. Part of this problem arises from the difficulty

in properly choosing τ_o, the point about which the

derivative of the surface autocorrelation function is

evaluated. In order to get around this difficulty, the

Q distributions that define each of the surface prepara-

tions were obtained directly from the antenna temperature

measurements. However, this comparison was made at only

one soil moisture content. By forcing the antenna tempera-

ture measurements to fit the model predictions at only

one moisture content, the model prediction of the response

of the brightness temperature to soil moisture was left

unbiased.

The distributions of Q with transmission angle were

obtained by overlaying antenna temperature measurements

made at an EQSM of 35 percent with model calculations of

brightness temperature as a function of transmission angle.

In order to obtain antenna temperature measurements of

all three surfaces at 35 percent equivalent moisture, it

was necessary to perform a linear regression fit to the

antenna temperature measurements as a function of EQSM.

Table VII-5 contains the results of these fits. These

fits were then used to obtain the antenna temperatures

that correspond to 35 percent EQSM. Figure VII-19 is a

TABLE VII-5

Linear Regression Fits to the 1974 1.4 GHz Measurements

Field	Transmission Angle	Polarization	EQSM < 25			EQSM > 25		
			Slope	Intercept	r^2	Slope	Intercept	r^2
CS*	20	Hor	-0.011	1.025	0.99	-0.024	1.346	0.82
		Vert	-0.009	1.015	0.99	-0.022	1.358	0.83
	35	Hor	-0.012	1.001	1.00	-0.020	1.189	0.79
		Vert	-0.008	1.023	1.00	-0.020	1.328	0.80
	50	Hor	-0.017	1.019	1.00	-0.015	0.984	0.77
		Vert	-0.007	1.035	0.99	-0.015	1.230	0.84
CM	20	Hor	-0.014	1.116	0.90	-0.013	1.087	0.61
		Vert	-0.012	1.088	0.77	-0.011	1.054	0.52
	35	Hor	-0.015	1.106	0.86	-0.012	1.028	0.57
		Vert	-0.009	1.057	0.72	-0.011	1.087	0.61
	50	Hor	-0.019	1.142	0.83	-0.012	0.945	0.57
		Vert	-0.008	1.050	0.60	-0.009	1.076	0.72

Table VII-5 (Continued)

Field	Transmission Angle	Polarization	EQSM < 25			EQSM > 25		
			Slope	Intercept	r^2	Slope	Intercept	r^2
CR	20	Hor	−0.005	0.965	0.77	−0.009	1.057	0.84
		Vert	−0.005	0.960	0.64	−0.009	1.060	0.80
	35	Hor	−0.0053	0.940	0.57	−0.016	1.227	0.80
		Vert	−0.0045	0.957	0.62	−0.011	1.1165	0.88
	50	Hor	−0.007	0.942	0.61	−0.013	1.088	0.82
		Vert	−0.0037	0.9545	0.54	−0.010	1.118	0.95

*A point at 25% EQSM calculated using the regression for EQSM > 25% was used in determining the regression fit for EQSM < 25%
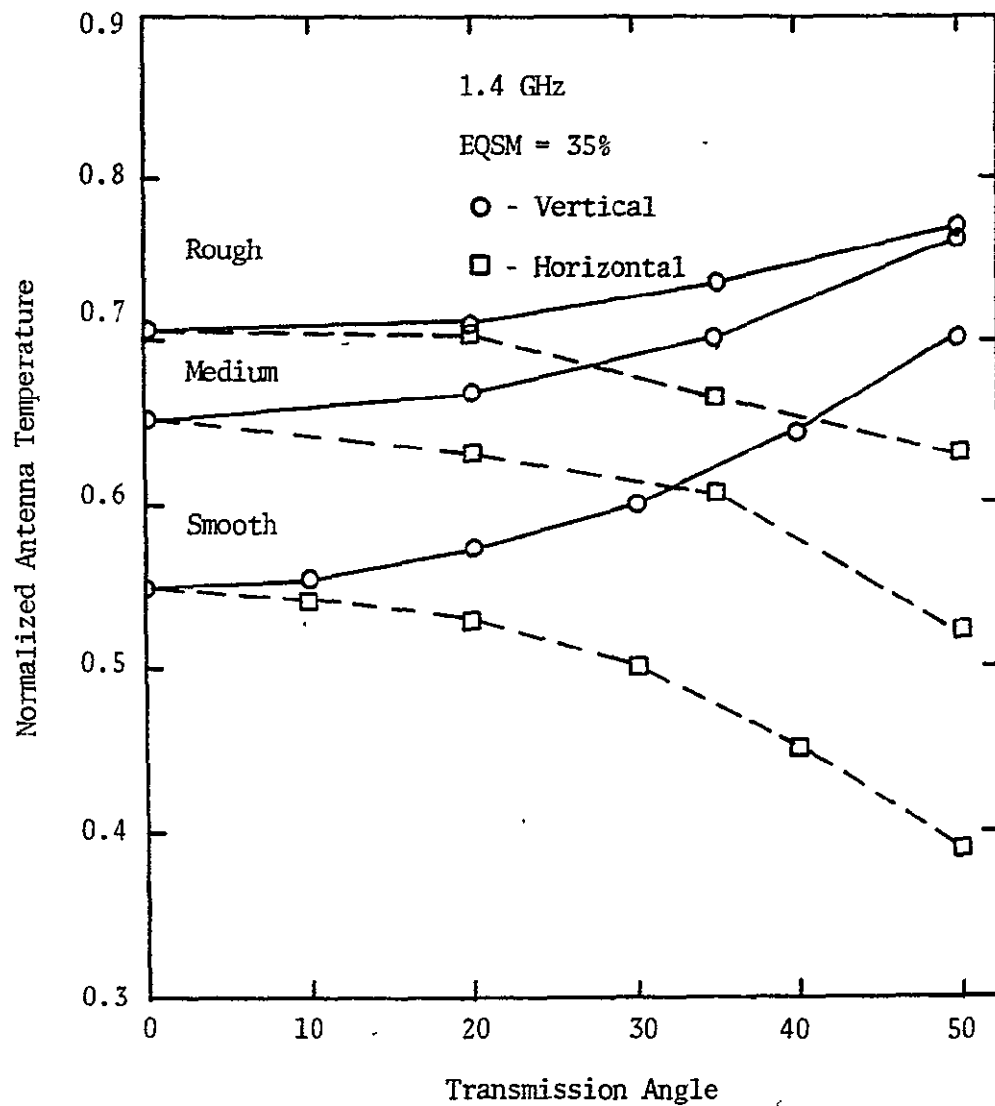
Figure VII-19. Normalized antenna temperatures corresponding to a 35% EQSM. These data were used in conjunction with Figures VII-20 and VII-21 to obtain the Q distributions for each surface.

plot of these antenna temperatures for each surface roughness. Actually the smooth surface in Figure VII-19 is described by a Fresnel surface rather than the antenna measurements. This was done to insure that the surface roughness model matched the Fresnel smooth surface model for the smooth surface Q distribution.

The data plotted in Figure VII-19 were simply overlaid on the model predictions contained in Figures VII-20 and VII-21 in order to obtain the Q distributions that describe each surface roughness. The proper Q for each transmission angle was determined by the intersection of the antenna measurements and the model predictions. Table VII-6 contains the resulting Q distributions for all three surfaces.

The Q distributions contained in Table VII-6 were used to generate the plots in Chapter IV relating to surface roughness. Figure IV-21 describes the predicted response of the brightness temperature of soil to soil moisture for the three surface preparations. The general trend of decreasing soil moisture response with increasing roughness that is evident in Figure VII-18 is predicted. This can be explained in physical terms by simply interpreting the surface roughness model. For a perfectly smooth surface only energy that is incident on the surface from below at a particular angle is transmitted across

Vertical Polarization
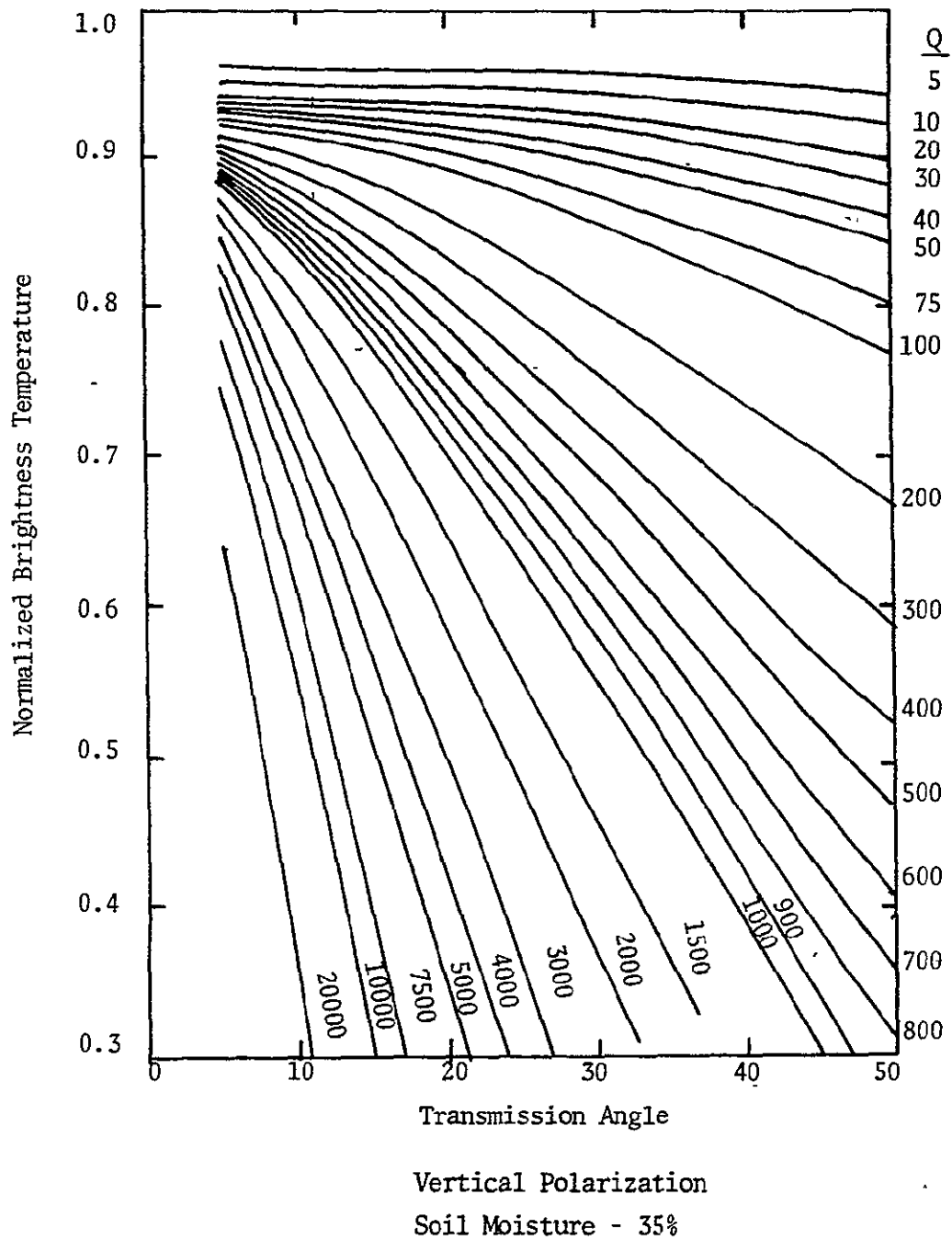
Soil Moisture - 35%

Figure VII-20.   Vertically polarized normalized brightness
temperature as a function of transmission
angle and Q, calculated for 35% soil
moisture.

Figure VII-21. Horizontally polarized normalized bright-
ness temperature as a function of trans-
mission angle and Q, calculated for 35%
soil moisture.

TABLE VII-6

Roughness Parameter, Q, for Each Surface

Preparation

Transmission Angle	Smooth (Field CS) Hor	Vert	Medium (Field CM) Hor	Vert	Rough (Field CR) Hor	Vert
5	–	–	19,524.0	19,000.0	13,774.0	13,923.0
10	9,375.0	9,375.0	5,642.0	5,486.0	3,680.0	3,900.0
20	1,942.0	2,166.0	1,166.0	1,313.0	738.0	980.0
30	638.0	820.0	380.0	494.0	265.0	381.0
35	386.0	529.0	224.0	336.0	164.0	266.0
40	239.0	355.0	143.0	222.0	97.0	188.0
50	84.0	166.0	54.2	108.0	34.0	100.0

the surface. This is due to Snell's law of refraction. However, as the surface is roughened, the allowable cone of angles from which energy can be transmitted across the surface boundary widens. This is illustrated in Figure VII-22. The larger the cone below the surface, the more energy is available to go across the surface. Thus, as the surface gets rougher, the brightness temperature increases.

This effect is more pronounced for wet soil than for dry soil due to the shape of the brightness temperature curve as a function of transmission angle. This can be explained in terms of the transmission across a smooth surface. Figure VII-23 depicts the vertical brightness temperature of a smooth surface for various soil moistures. Any point on Figure VII-23 describes the brightness temperature of a perfectly smooth surface. For a rough surface a weighted integration must be performed over transmission angle from nadir to the angle defining the cone described above. Note that performing such an integration over the curves in Figure VII-23 from nadir to θ_c will yield results that are proportionately larger than the smooth surface brightness temperature for very wet soil than for very dry soil. This is due to the compression of brightness temperature as a function of soil moisture at the higher transmission angles.
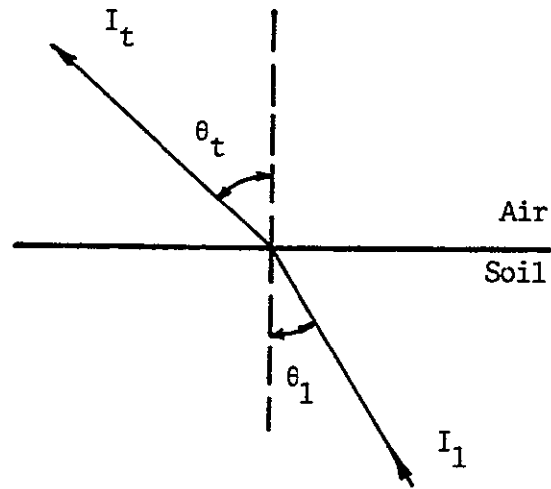
(a) Smooth
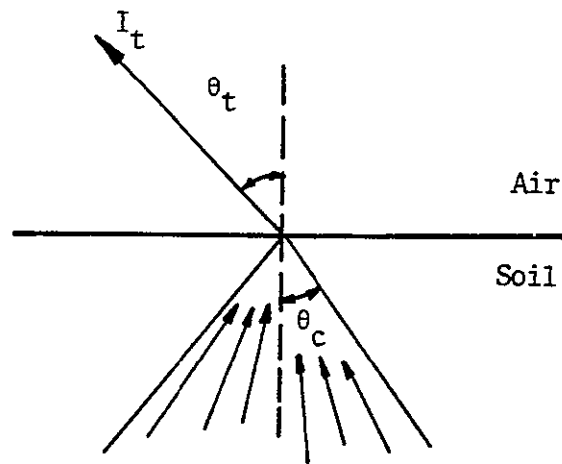
(b) Rough

Volume Radiation

Figure VII-22. Graphical illustration of a physical interpretation of the effect of roughness on the emission from a soil surface.
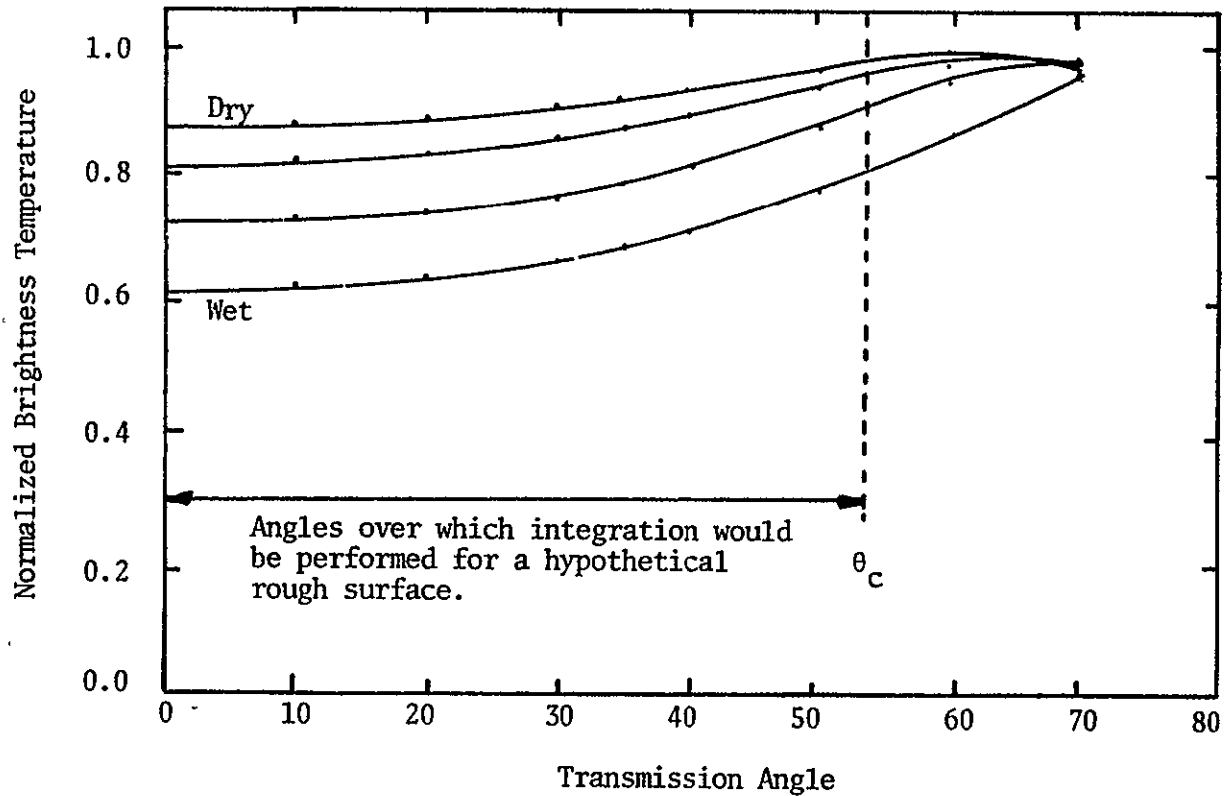
Figure VII-23. Illustration of the compression in the result of the integration effect (Figure VII-22) of a rough surface as the soil moisture changes from wet to dry.

At 10.6 GHz the "smooth" field (CS) appeared rough.
As a result there is no smooth surface measurement for
this frequency. This is demonstrated in Figure VII-24
for a transmission angle of 20°. The smooth and medium
rough measurements group together while the rough measure-
ments form a cluster with a slightly higher magnitude.

The scatter in the 10.6 GHz measurements in Figure
VII-24 is not due entirely to system noise. The nominal
standard deviation of the 10.6 GHz measurements was 1.7°K
while for 1.4 GHz it was 0.6°K. Much of the scatter is
due to inaccuracies in measuring the 0-1 cm soil moisture.
This problem is addressed in more detail in the last
section of this chapter where a soil moisture estimation
procedure is discussed.

In the above discussion measurements at only 20°
were presented. The soil moisture response for all three
surface preparations at nadir is very similar to the
response at 20°. However, as the transmission angle
is increased beyond 20° to 35° and 50°, the emission
tends to generally increase for all moistures and surfaces
at vertical polarization, and generally decrease for
horizontal polarization. However, the general effect
of surface roughness is maintained. Figures VII-25
through VII-27 are plots of the linear regressions in
Table VII-5. They demonstrate these effects at 20°, 35°
and 50°.
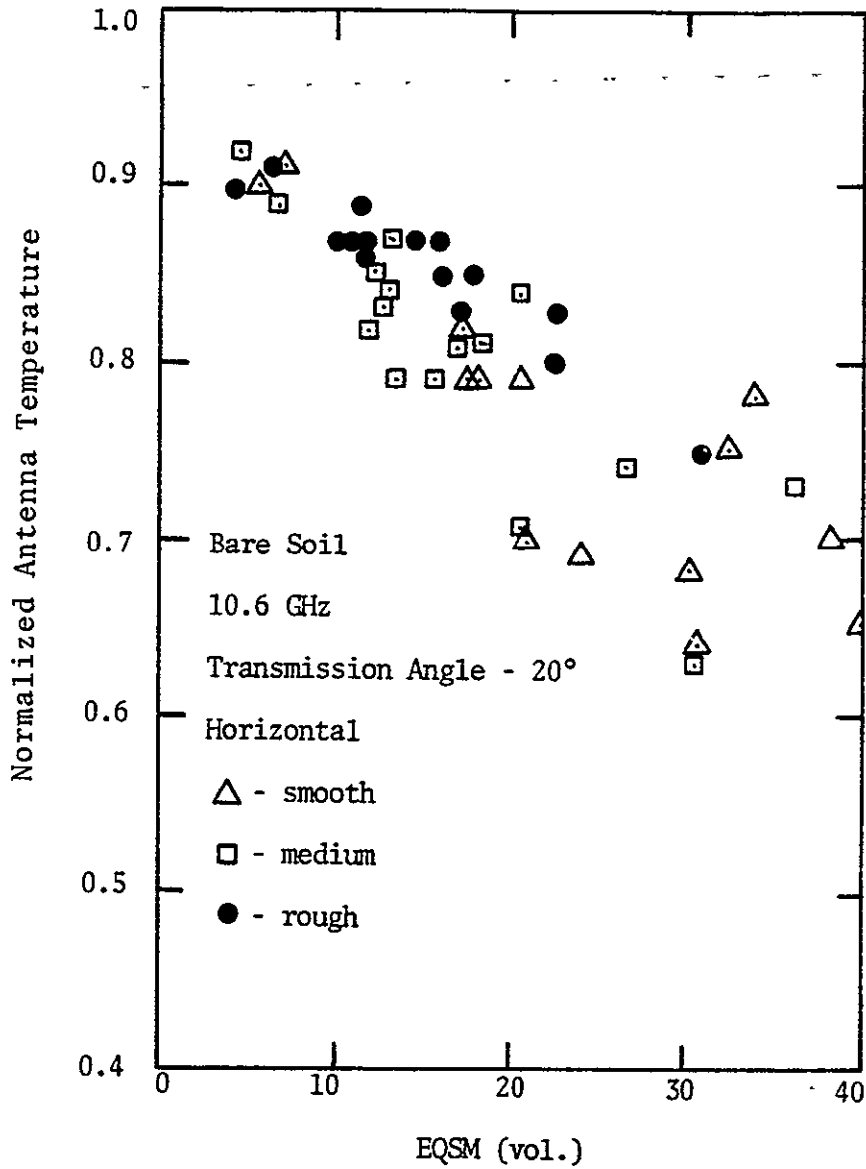
Figure VII-24. Horizontal 10.6 GHz antenna
temperature measurements as
a function of soil moisture
for three surface conditions.
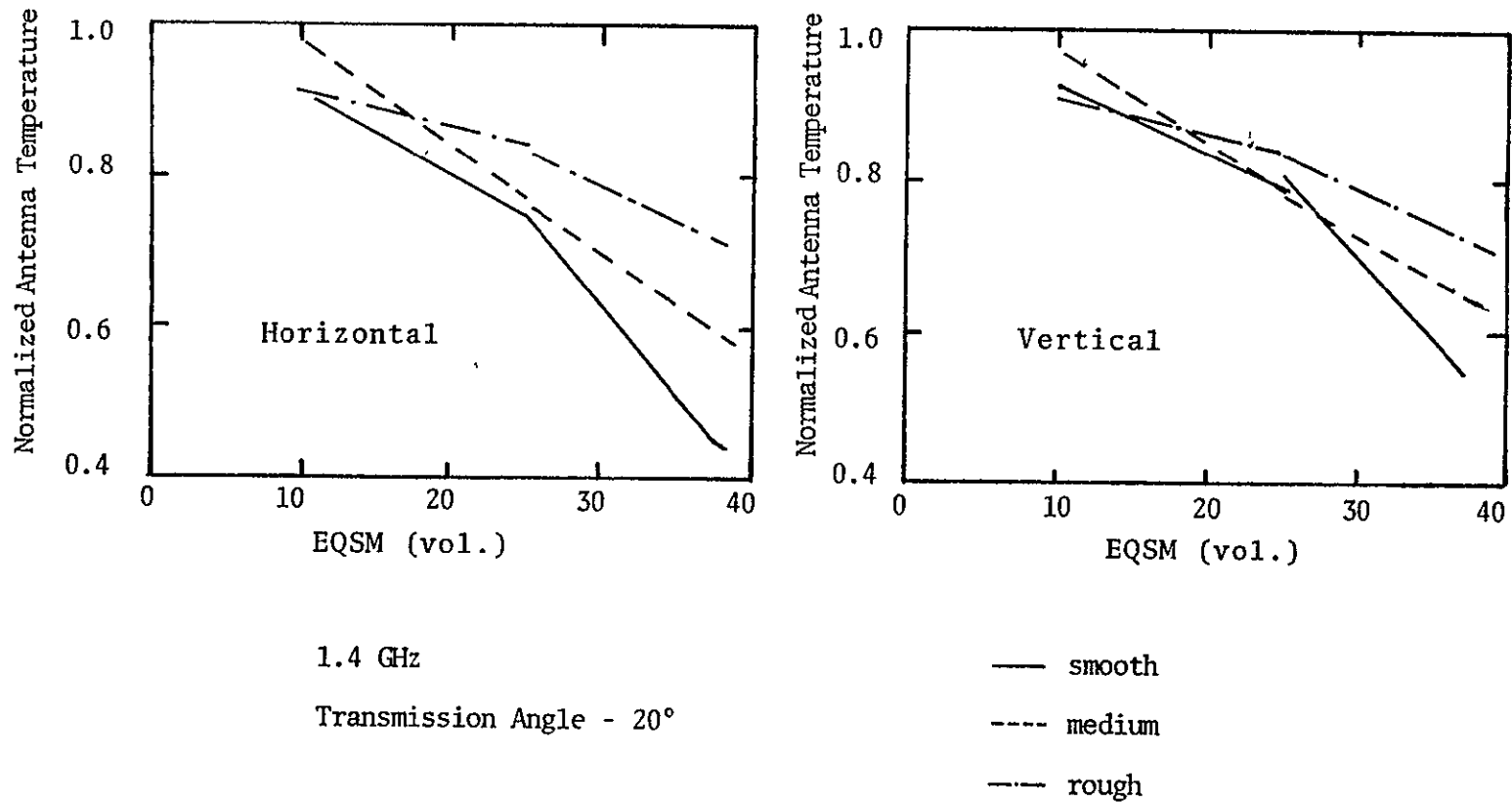
Figure VII-25. Linear regression fits to 1.4 GHz antenna temperature measurements of bare soil as a function of soil moisture for three surface preparations.

1.4 GHz

Transmission Angle - 35°

——— smooth

— — — medium

—·—·— rough

Figure VII-26. Linear regression fits to 1.4 GHz antenna temperature measurements of bare soil as a function of soil moisture for three surface preparations.

Figure VII-27. Linear regression fits to 1.4 GHz antenna temperature measurements of bare soil as a function of soil moisture for three surface preparations.

Effect of row direction - It was seen in the paragraphs
above that the effect of uniform roughness was to decrease
the sensitivity of the antenna temperature measurements
to soil moisture. The effects of row tillage on this
response will now be addressed. Only the bare field is
discussed at this time. The effects of vegetation are
discussed in the next section.

The 1975 experimental plots were prepared using
standard agricultural practices normally used in Phoenix,
Arizona. As a result, the surface was actually a composite
rough surface. The periodic row structure formed the large
scale surface roughness. The average height and width
of this row structure in field A, the bare field, was
20 cm and 95 cm, respectively.

The rms surface height deviations were not measured
for the overlying small scale roughness. However, another
parameter, the effective surface area per unit planar
surface area [107] was measured. This value is a unitless
quantity and was, on the average, 1.26 on the ridges and
1.15 in the furrows. This compares to an average of 1.85
for the bare medium rough 1974 field, CM, and an estimated
value of between 1.0 and 1.2 for the smooth 1974 field,
CS. The furrows were quite smooth in field A since the
field was flood irrigated and the water ran in the
furrows. As a result, one would expect the small scale

structure to have a rms surface height deviation that was somewhere in between the values for the 1974 smooth and medium rough fields.

A theoertical model for the emission from a composite surface is not discussed in this report. However, the results that were obtained with the uniform roughness model are very enlightening with respect to the 1975 row roughness measurements. The 1975 measurement set will not be analyzed in great detail, but the effect of the row structure on the change in emitted radiation due to changes in soil moisture will be pointed out. A general comparison will also be made between the 1974 and 1975 measurements sets. Measurements made at 1.4 GHz will be described first, then measurements made at 10.6 GHz will be briefly presented.

It was demonstrated for uniformly rough soil that the best response to soil moisture was obtained at low transmission angles. As a result, measurements at a transmission angle of 20° will be used to demonstrate the effects of row direction on the moisture dependence of antenna temperature measurements. Figures VII-28 through VII-32 demonstrate this effect at 1.4 GHz and a 20° transmission angle.

A moisture dependence is obviously retained for bare row tilled terrain, however, it is modified to a certain

Vertical

1.4 GHz

Field A - Bare

Horizontal
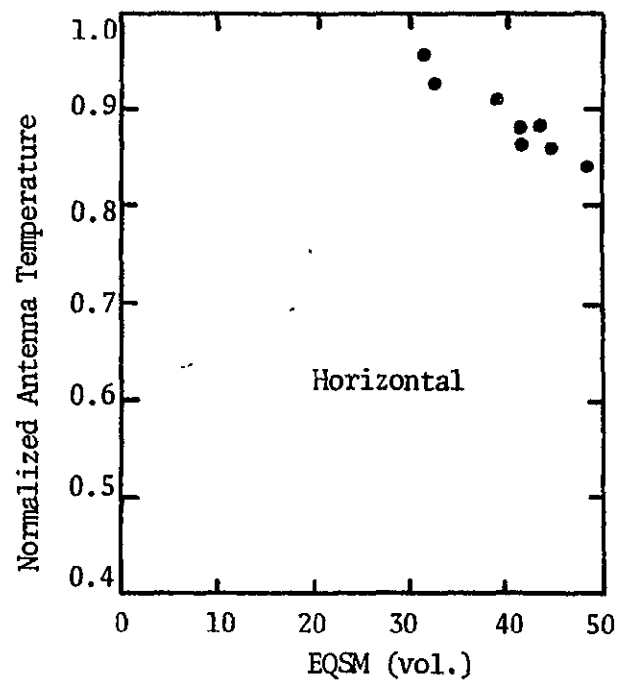
Transmission Angle - 20°

Azimuth Angle - 0°

Figure VII-28. 1.4 GHz antenna temperature measurements made at an azimuth angle of 0° with respect to the row direction, as a function of soil moisture.
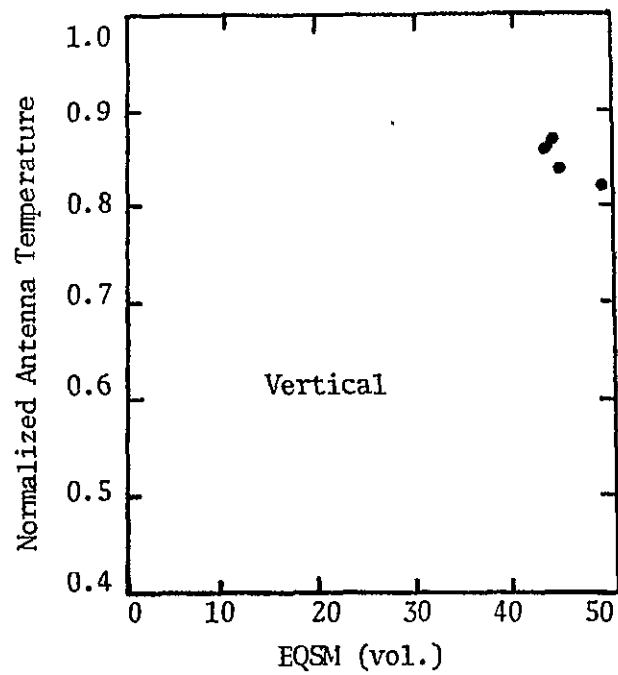
1.4 GHz

Field A - Bare

Transmission Angle - 20°

Azimuth Angle - 30°

Figure VII-29.   1.4 GHz antenna temperature measurements made at an azimuth
angle of 30° with respect to the row direction, as a function
of soil moisture.

Figure VII-30. 1.4 GHz antenna temperature measurements made at an azimuth angle of 45° with respect to the row direction, as a function of soil moisture.
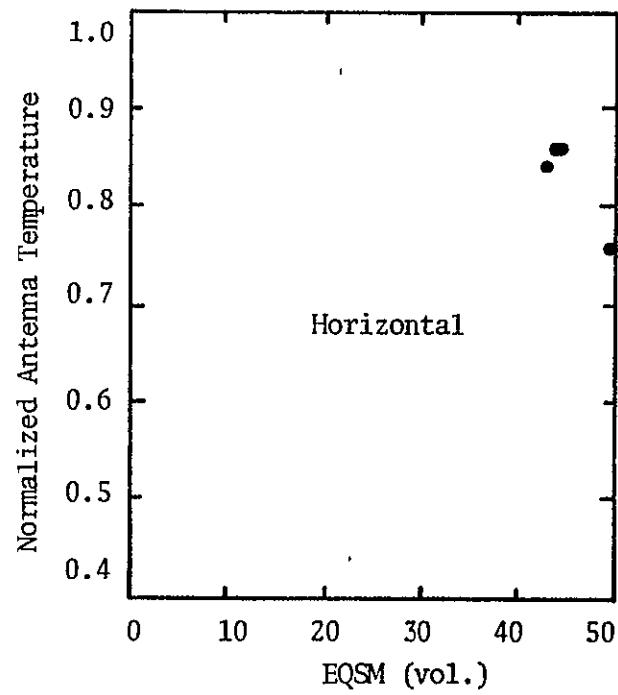
Figure VII-31. 1.4 GHz antenna temperature measurements made at an azimuth angle of 60° with respect to the row direction as a function of soil moisture.
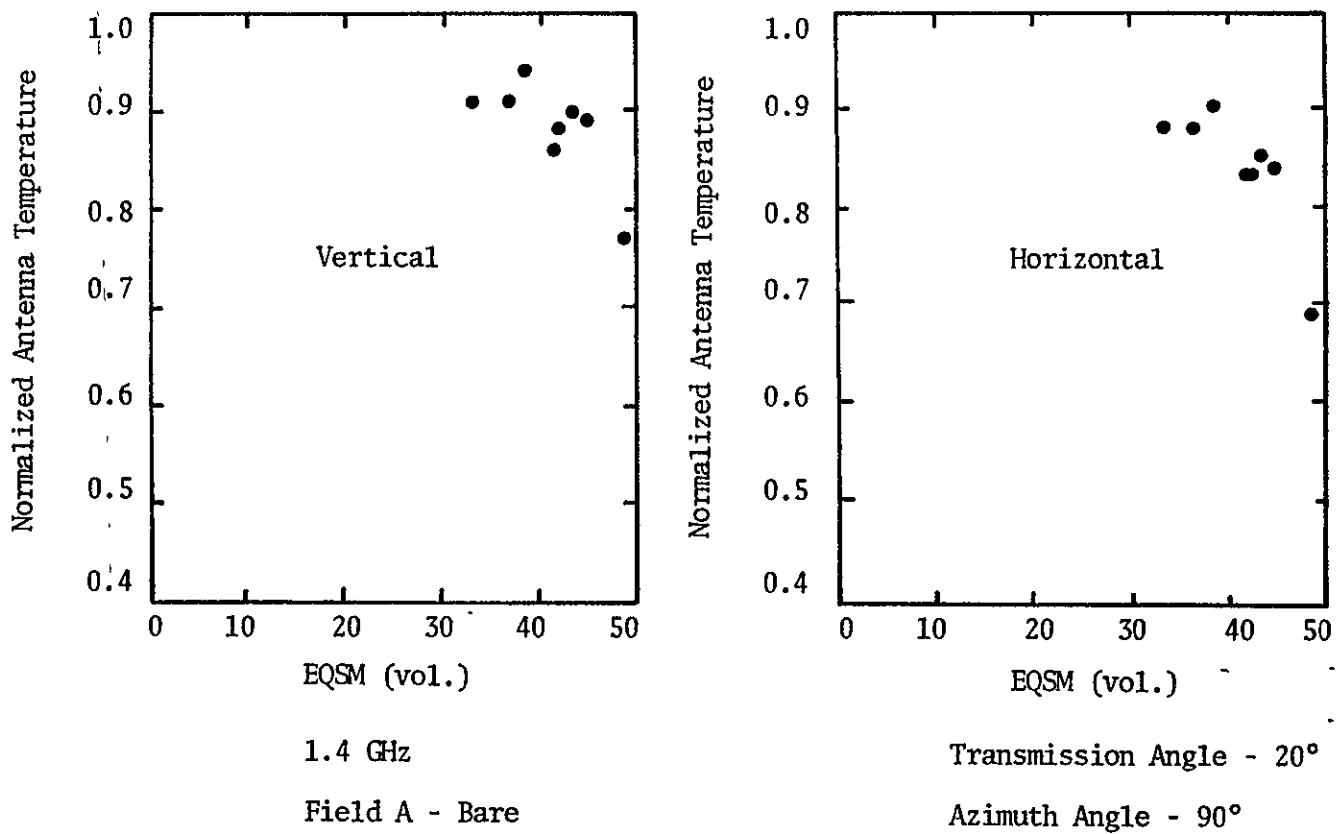
Figure VII-32. 1.4 GHz antenna temperature measurements made perpendicular to the row direction as a function of soil moisture.

degree from the response seen for a uniformly rough field.
Before discussing this modification, the difference in the
magnitude of the soil moisture parameter between the 1974
and 1975 measurements will be explained. It is obvious
from Figures VII-28 through VII-32 that the volumetric
equivalent soil moistures for the 1975 data set are much
larger than those of the 1974 data set. This was not
expected since both data sets are acquired over the same
soil type, Miller clay. The difference is a result of the
soil bulk density measurements. Table VII-7 demonstrates
that the bulk density measurements made in 1975 were
considerably larger than those made in 1974. The bulk
density measurements differ most likely as a result of
the difficulty in making the measurement and inconsist-
encies in the measurement techniques used in 1974 and 1975.

Soil moisture was initially measured on a weight
basis. It was converted to a volumetric basis using
(II-7) and the bulk density measurements contained in
Table VII-7. Since the bulk density measurements do not
compare from year to year, then the volumetric soil
moisture calculations do not compare. The gravimetric
soil moisture measurements, however, do compare between
the 1974 and 1975 measurements. This can be demonstrated
by comparing antenna temperature measured during each
of the two experiments on a soil moisture by weight basis.
This is reasonable since the experimental plots consisted

TABLE VII-7

Soil Bulk Density Measurements

| Depth (cm) | 1974 Experiment | | | | | | | 1975 Experiment |
| | Fields A and B | | | Field C | | | Field D | Fields A and B |
	Smooth	Medium	Rough	Smooth	Medium	Rough		
0-2	1.15	1.06	1.05	1.55	1.27	1.32	1.06	1.64
2-5	1.22	1.11	1.07	1.28	1.12	1.07	1.11	1.65
5-9	1.34	1.22	1.07	1.26	1.17	1.07	1.22	1.63
9-15	1.38	1.33	1.06	1.23	1.20	1.06	1.33	1.77

of the same soil type during both years. Figure VII-33
contains measurements from both 1974 and 1975. By removing
the inconsistency due to the bulk density measurements
the equivalent soil moisture axis becomes consistent
between measurement sets.

It can be seen in Figure VII-33 that the measurements
acquired in 1975 over the row tilled field are considerably
higher than those acquired over the uniformly rough field.
This magnitude increase cannot be explained at the present
time. However, since the 1975 data plotted in Figure
VII-33 were measured parallel to the rows, the soil moisture
response was expected to be comparable to the response
obtained for a uniformly rough field. This can be
confirmed by comparing the slope of a best fit straight
line drawn through the 1975 measurements to the slopes of
lines drawn through the 1974 bare field measurements.
Table VII-8 contains the results of linear least squares
regression fits to these data. Comparing slopes it can
be seen that the bare row tilled field does respond to
moisture in the same manner as would a uniformly rough
field with a rms surface height deviation somewhere between
the 1974 medium rough field (2.6 cm) and the 1975 rough
field (4.3 cm).

Neglecting the overall magnitude shift between the
1974 and 1975 measurements, the effects of row direction
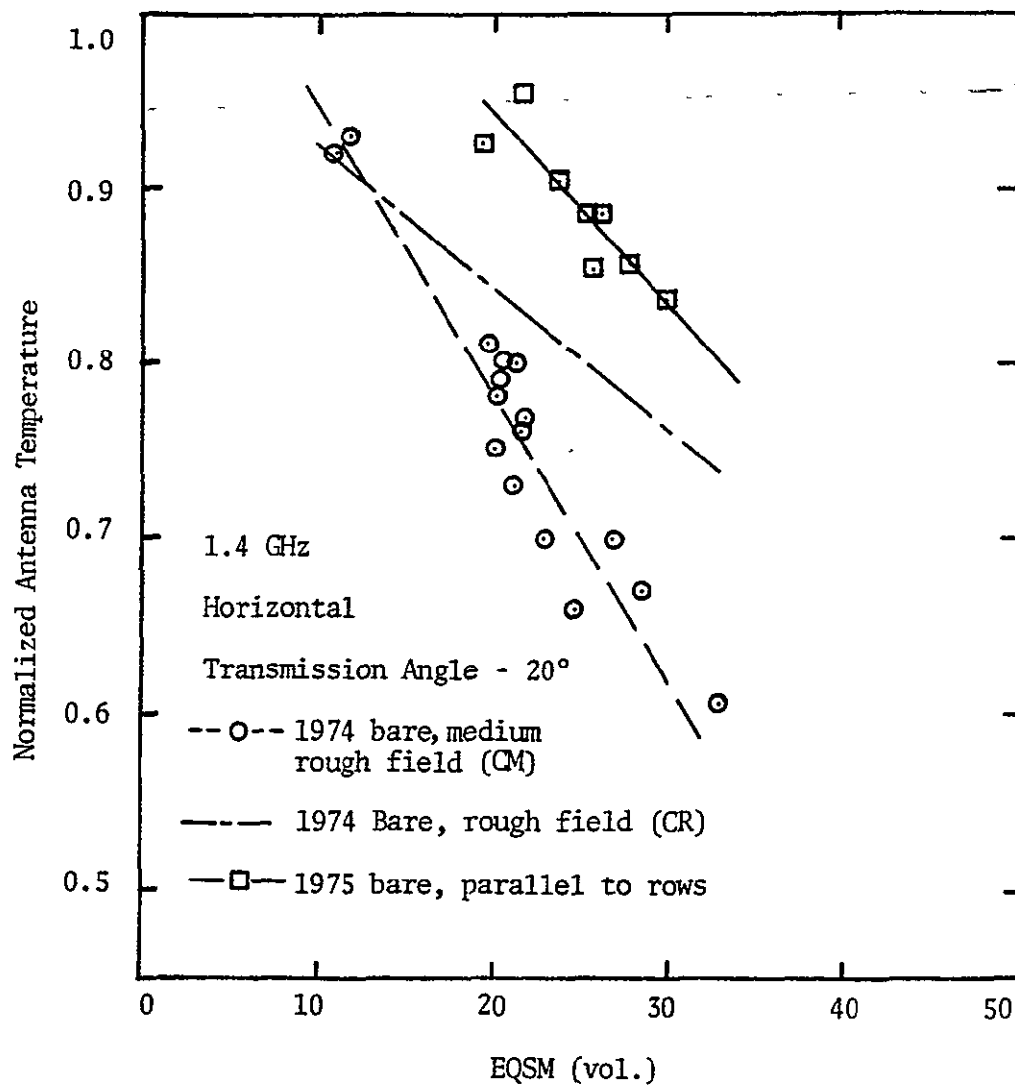
Figure VII-33. Comparison of linear regression fits to 1974 measurements of uniformly rough, bare surfaces to 1975 measurements of row tilled bare surfaces.

TABLE VII-8

Comparison Between 1974 and 1975 Measured Response to

Soil Moisture by Weight at a Transmission Angle of 20°

Field	Slope* m	Y Intercept* b	Regression Coefficient* r
(1975) A Parallel to rows	-0.0111	1.161	0.88
(1974) CS Smooth			
EQSM (WT) < 20	-0.0162	1.0527	0.89
EQSM (WT) > 20	-0.0174	0.9992	0.64
(1974) CM Medium Rough	-0.0168	1.116	0.93
(1974) CR Rough	-0.0084	1.0088	0.88

*Normalized Antenna Temperature (NAT) = m·EQSM(WT) + b

on the response to moisture changes will now be discussed.
By comparing Figures VII-28 through VII-32 it can be seen
that at 1.4 GHz a dependence on soil moisture is maintained
for all azimuth angles with respect to the row direction,
but that as the azimuth angle increases to 90° the scatter
in the measurements increases considerably. In addition,
the row tillage causes the effects of antenna beamwidth
to become much more severe.

In Chapter VI two effects of beamwidth were con-
sidered, polarization mixing and transmission angle averag-
ing. In the analysis in which the effects of transmission
angle averaging were discussed, the surface was assumed to
be such that the average mean surface height formed a
horizontal plane. In this case the range of transmission
angles over which the antenna collected energy was simply
defined by the antenna beamwidth. However, for a surface
containing large scale periodic undulations, the trans-
mission angles over which the antenna collects energy is
defined by the surface undulations and the direction from
which the antenna "views" these undulations. When measure-
ments are made parallel to the rows the transmission angles
over which the antenna averaging occurs are the same as
for a horizontally plane surface. However, as the
azimuth angle is increased, the range of transmission
angles over which averaging occurs increases. In addition,

beamwidth averaging is not uniform across these angles, but is weighted by the distribution of surface slopes that falls within the antenna beamwidth.

This can be visualized by intersecting the surface with a vertical plane and plotting the distrubition of surface slopes that would occur on this intersection. As the plane is rotated with respect to the surface row direction, the surface slope distribution changes from no slope, to distributions that become more heavily weighted at larger slopes. This is demonstrated in Figure VII-34. These slope distributions define the distribution of trans- mission angles over which the antenna averages. The effect of this phenomenon can be demonstrated using the measure- ments contained in Figures VII-28 through VII-32 by comparing the general characteristics of these plots to the characteristics of the measurements made over the uniform surfaces.

It was demonstrated in Figures VII-25 through VII-27 that for a uniformly rough field the vertical antenna temperature measurements generally increase as the trans- mission angle is increased and the horizontal measurements generally decrease. This same phenomena occurs for the row tilled surface as the azimuth angle, with respect to the row direction, is increased. Increasing the azimuth angle effectively increases the transmission angle at which the surface slope distribution peaks. In Figure
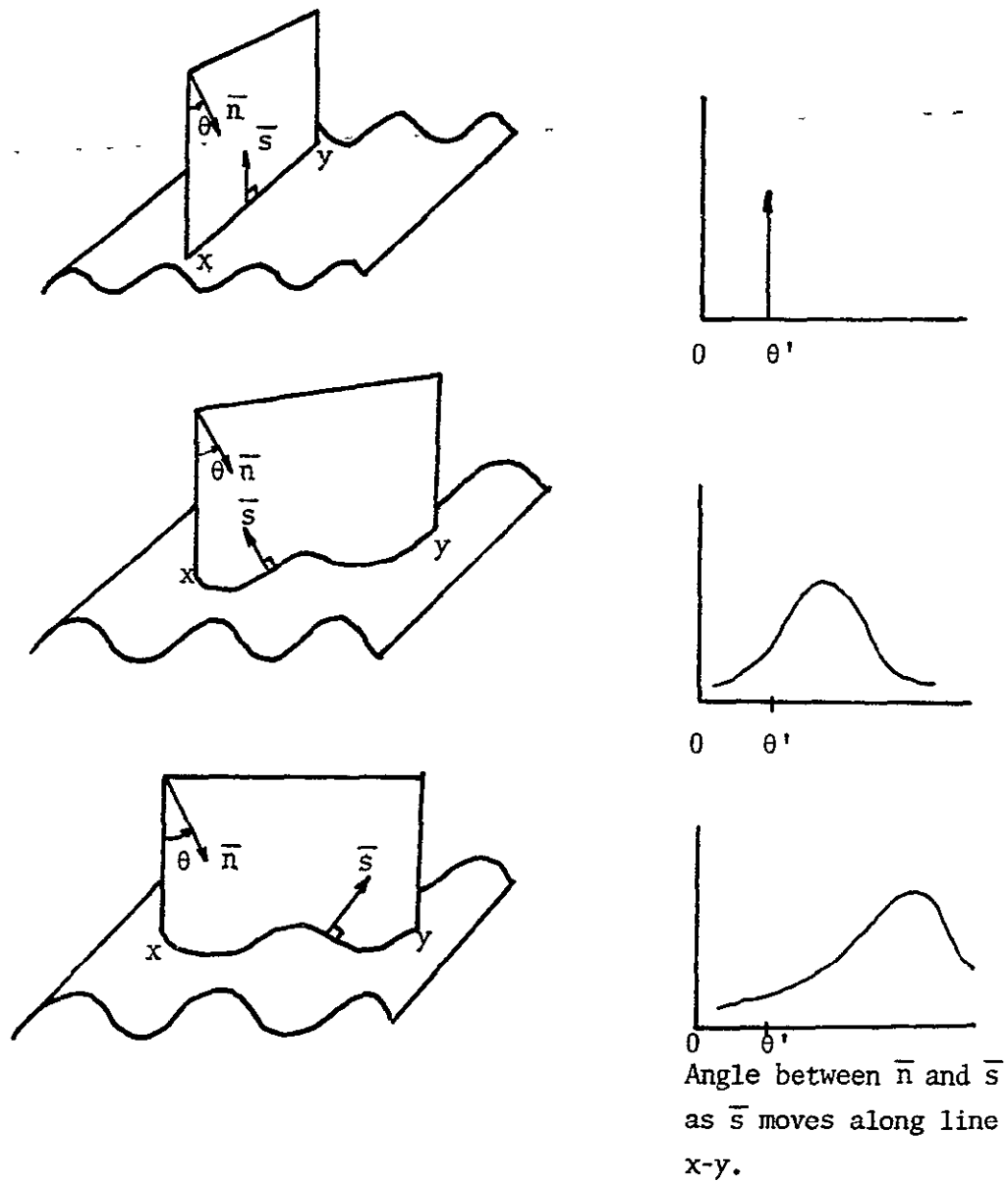
Figure VII-34. Illustration of how the distribution of transmission angles from which an antenna receives radiation changes as the azimuth angle between the plane of transmission and row direction is varied.

VII-28 the vertical and horizontal measurements are very
nearly the same magnitude. However, as the azimuth angle
increases, the vertically polarized measurements become
increasingly larger than the horizontally polarized
measurements (Figure VII-32).

The phenomenon described above can be used to demon-
strate that viewing a row tilled field parallel to the rows
is approximately the same as viewing a uniformly roughened
field with the same rms surface height deviations as is
superimposed on the row structure. Figures VII-35 through
VII-37 are plots of normalized antenna measurements of the
bare field made parallel to the rows at three different
transmission angles. They behave in the same manner as
the corresponding measurements of the uniformly roughened
fields (Figures VII-25 through VII-27). As the trans-
mission angle is increased, the vertical measurements
generally increase and the horizontal measurements generally
decrease. Also, the sensitivity to moisture decreases
with transmission angle for vertical polarization and
increases for horizontal polarizations as demonstrated
for uniform rough fields in Figure VII-15. This is
evidenced by the slope of linear least squares regression
lines.

In the discussion above the effects of transmission
angle averaging due to the antenna beamwidth were discussed,
but the effect of polarization mixing was not considered.
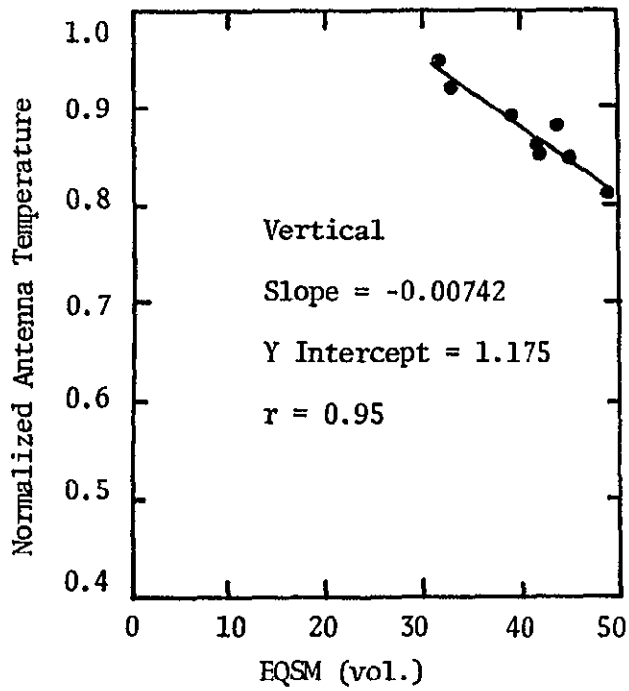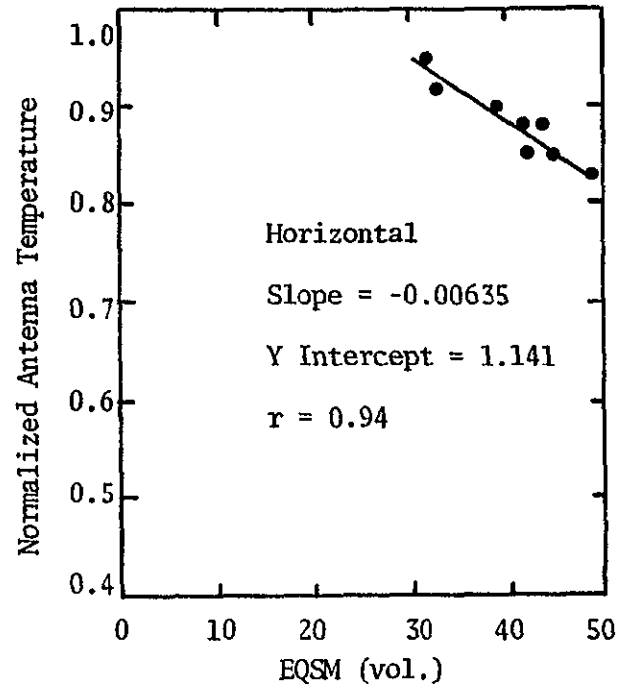
Figure VII-35.   1.4 GHz antenna temperature measurements made parallel to the
row direction at 20° as a function of soil moisture.
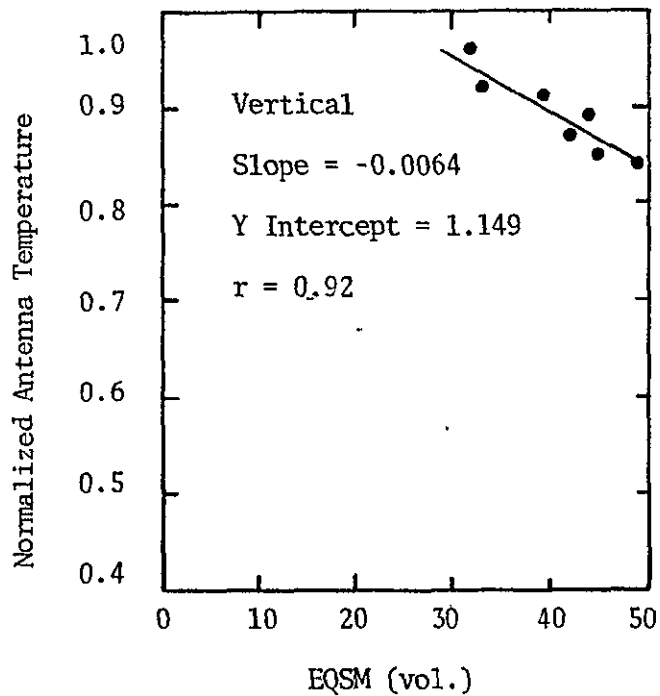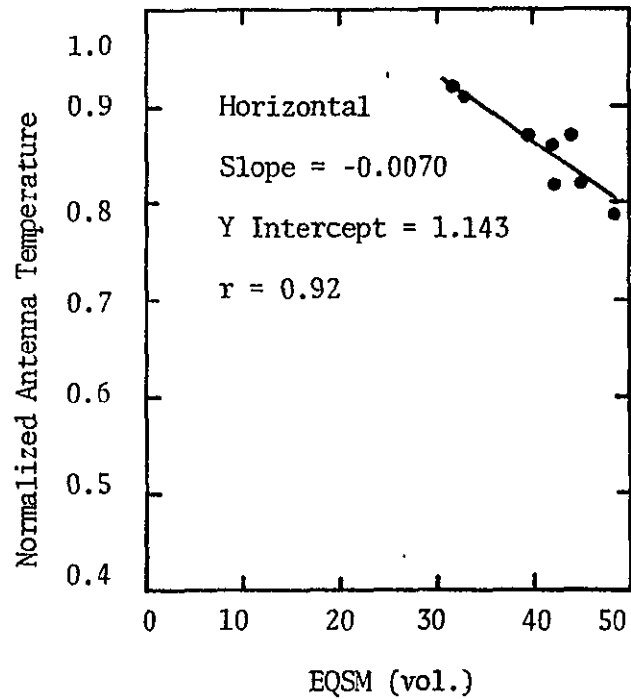
Figure VII-36. 1.4 GHz antenna temperature measurements made parallel to the row direction at 35° as a function of soil moisture.
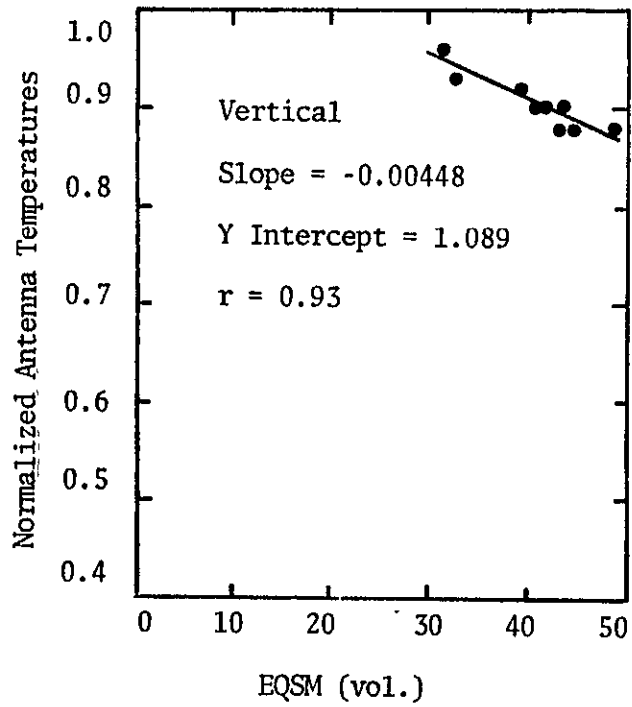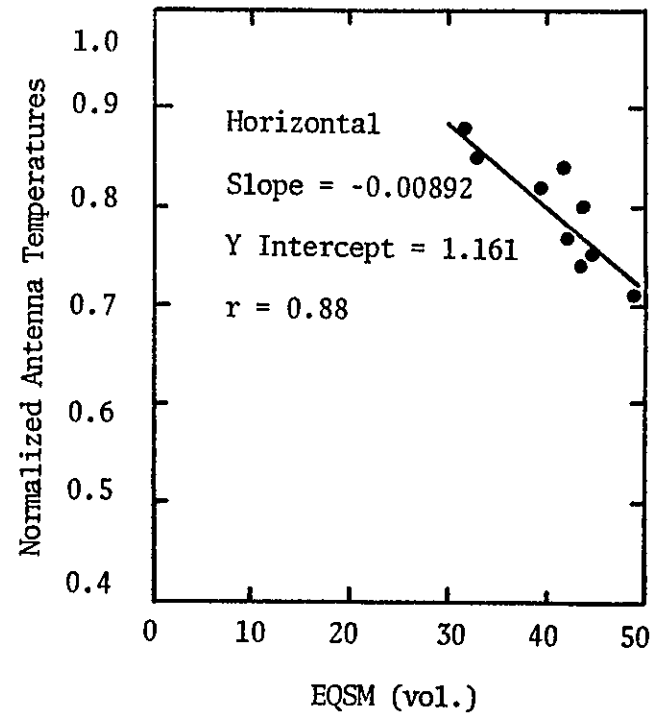
Figure VII-37. 1.4 GHz antenna temperature measurements made parallel to the row direction at 50° as a function of soil moisture.

For a row tilled field the effects of polarization mixing due to the antenna beamwidth can be much more severe than would occur for a generally flat surface.

In analyzing the effects of polarization mixing in Chapter VI, the emission from the surface was assumed to be constant across the surface area viewed by the antenna. For a surface with no large scale surface undulations this assumption is not too unreasonable since the emission across the area viewed by the antenna only changes as a result of the angular variations over the angle range defined by the antenna beamwidth. However, for a surface with large scale undulations, the radiation emitted from the area viewed by the antenna is modulated as a result of angular variations due to the surface slope distribution within the antenna footprint. Since this angular variation will generally be much greater than the angular variation that results from the antenna beamwidth, the effects of polarization mixing can be severe and will depend on the orientation of the antenna with respect to the row direction, even when the antenna is viewing the surface at nadir.

Measurements made at 10.6 GHz have not been discussed thus far. However, the comments made in the discussion above also apply to the 10.6 GHz measurements, except that the small scale surface height variations appear much rougher at the 10.6 GHz wavelength. Figures VII-38 and VII-39 are plots of 10.6 GHz measurements made in
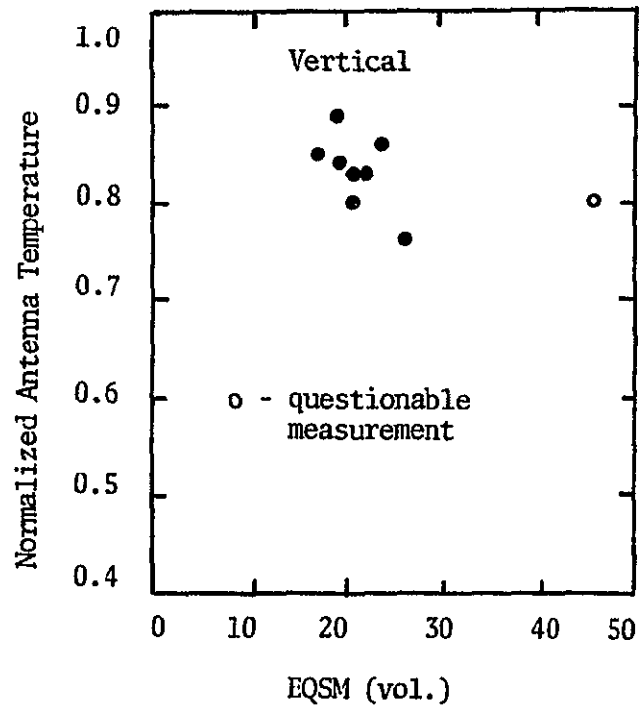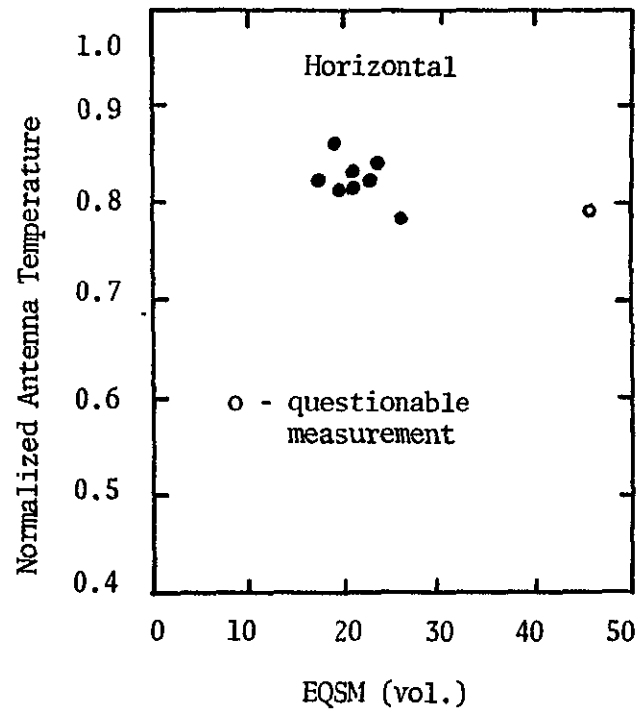
Figure VII-38.   10.6 GHz antenna temperature measurements made parallel to the row direction as a function of soil moisture.
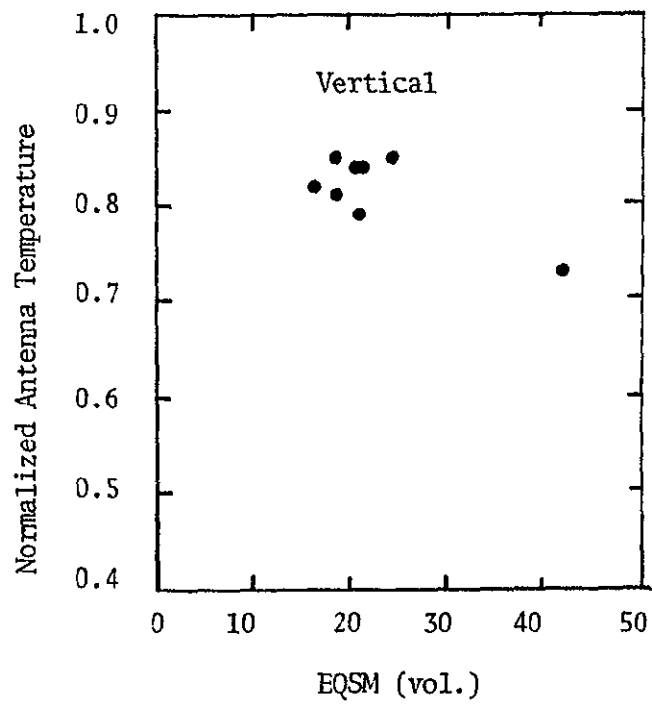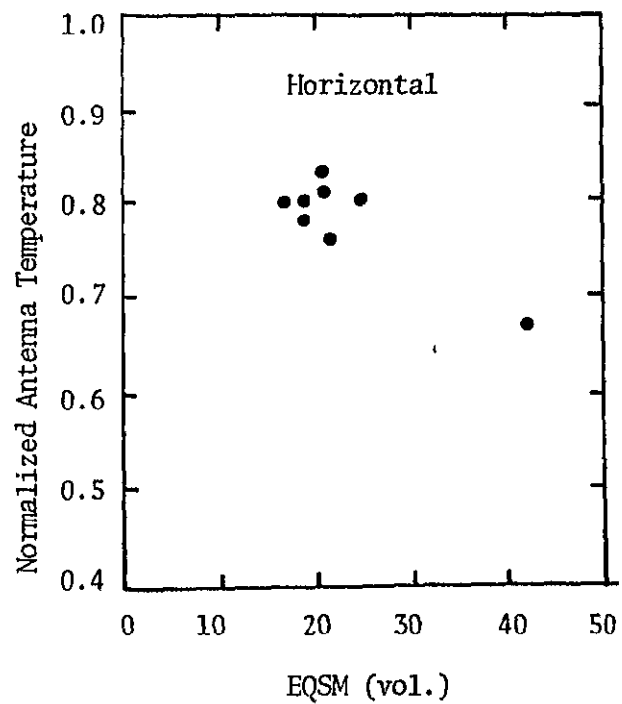
Figure VII-39.   10.6 GHz antenna temperature measurements made perpendicular
to the row direction as a function of soil moisture.

1975. As with the 1.4 GHz measurements, the moisture
sensitivity demonstrated in Figure VII-38 (measurements
parallel to the rows) is approximately the same as that
exhibited in Figure VII-24 for the smooth and medium
rough fields of 1974. Also the magnitude of the vertical
and horizontal measurements made parallel to the rows
at a 20° transmission angle are about the same (Figure
VII-38). In Figure VII-39 (measurements perpendicular to
the rows), the vertical measurements are higher than the
horizontal measurements. This was expected since the
antenna is averaging over predominately larger trans-
mission angles when viewing the rows at an azimuth angle
of 90°. In addition, the moisture sensitivity is reduced
as would be expected.

It should be noted that some of the scatter in the
1975 10.6 GHz measurements is due to a hardware problem.
The standard deviations of these measurements ranged from
1.7°K to 3.5°K. The lower value of 1.7°K is the standard
deviation that is normally observed when the system is
operating properly.

Effect of Vegetation

Measurements of vegetation canopies were made during
both the 1974 and 1975 measurements program. A uniform
cover of vegetation was planted in 1974, while a row

canopy was planted in 1975. The effect of uniform and row planted vegetation will be described below.

Uniform vegetation cover - In 1974 vegetation was uniformly planted in fields A and B. The average height of the vegetation in the smooth section of field A was 188 cm, and in the smooth section of field B it was 125 cm. The average plant moisture in both fields was approximately 63 percent. Since the average volumetric density [107] of the vegetation (a unitless quantity) in each of these fields was approximately one percent, the vegetation height-density products were 1.88 cm and 1.25 cm in fields A and B respectively. As expected from the results of the vegetation model presented in Figure IV-27, the vegetation effectively masks the soil emission at 10.6 GHz for these two fields. This is demonstrated in Figure VII-40.

Figures VII-41 and VII-42 demonstrate the effect of the vegetation in field B on the soil emission at 1.4 GHz for transmission angles of 20° and 35°. There is only a small effect. It appears that the emission is attenuated slightly for moistures below 20 percent EQSM and amplified slightly for moistures above 20 percent EQSM. This cannot be fully confirmed since there is only one measurement above 20 percent EQSM. However, at a transmission angle of 50° all of the 1.4 GHz measurements are increased. This is demonstrated in Figure VII-43.
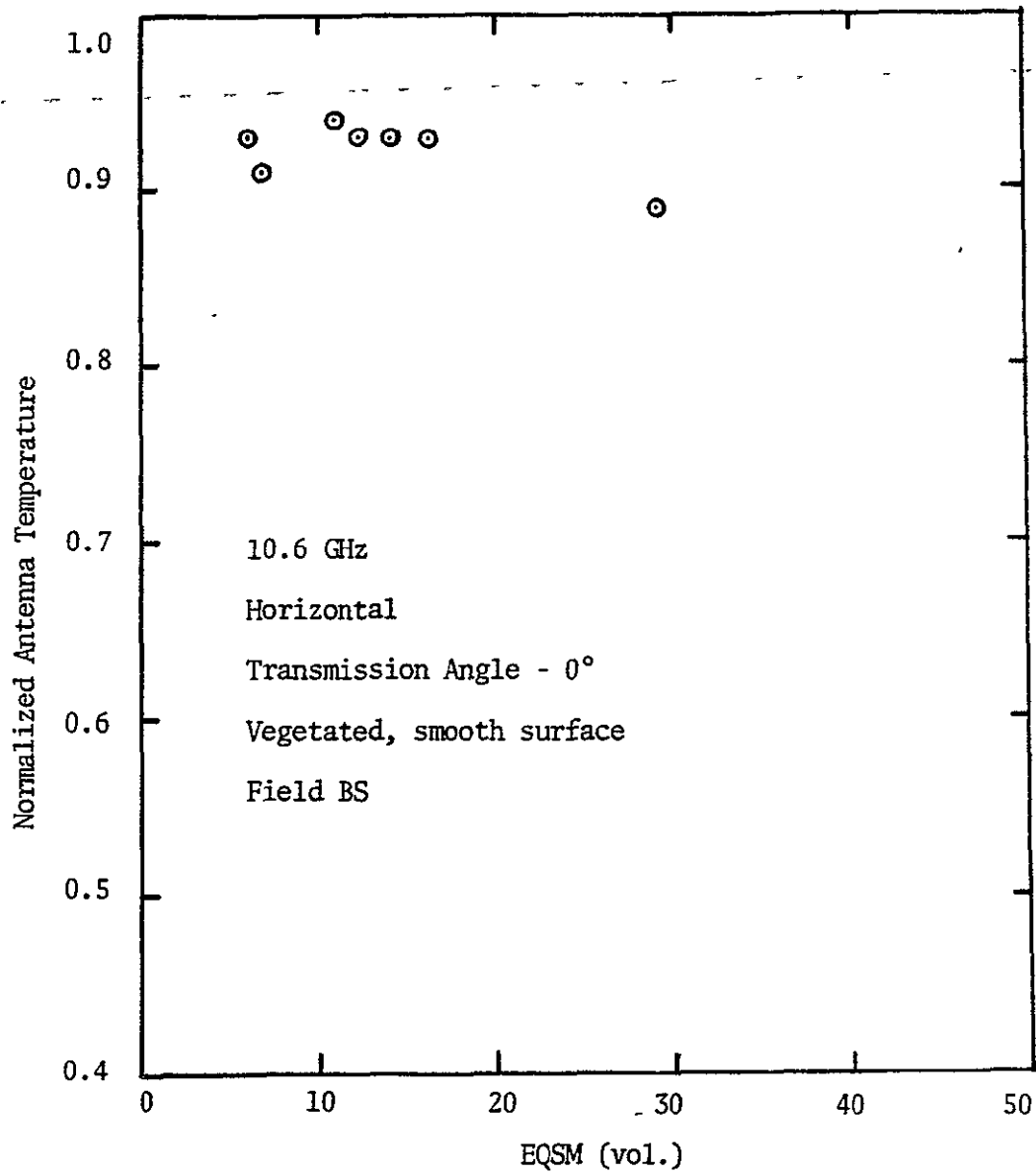
Figure VII-40. Horizontal 10.6 GHz antenna temperature
measurements of a vegetated smooth surface
as a function of soil moisture.
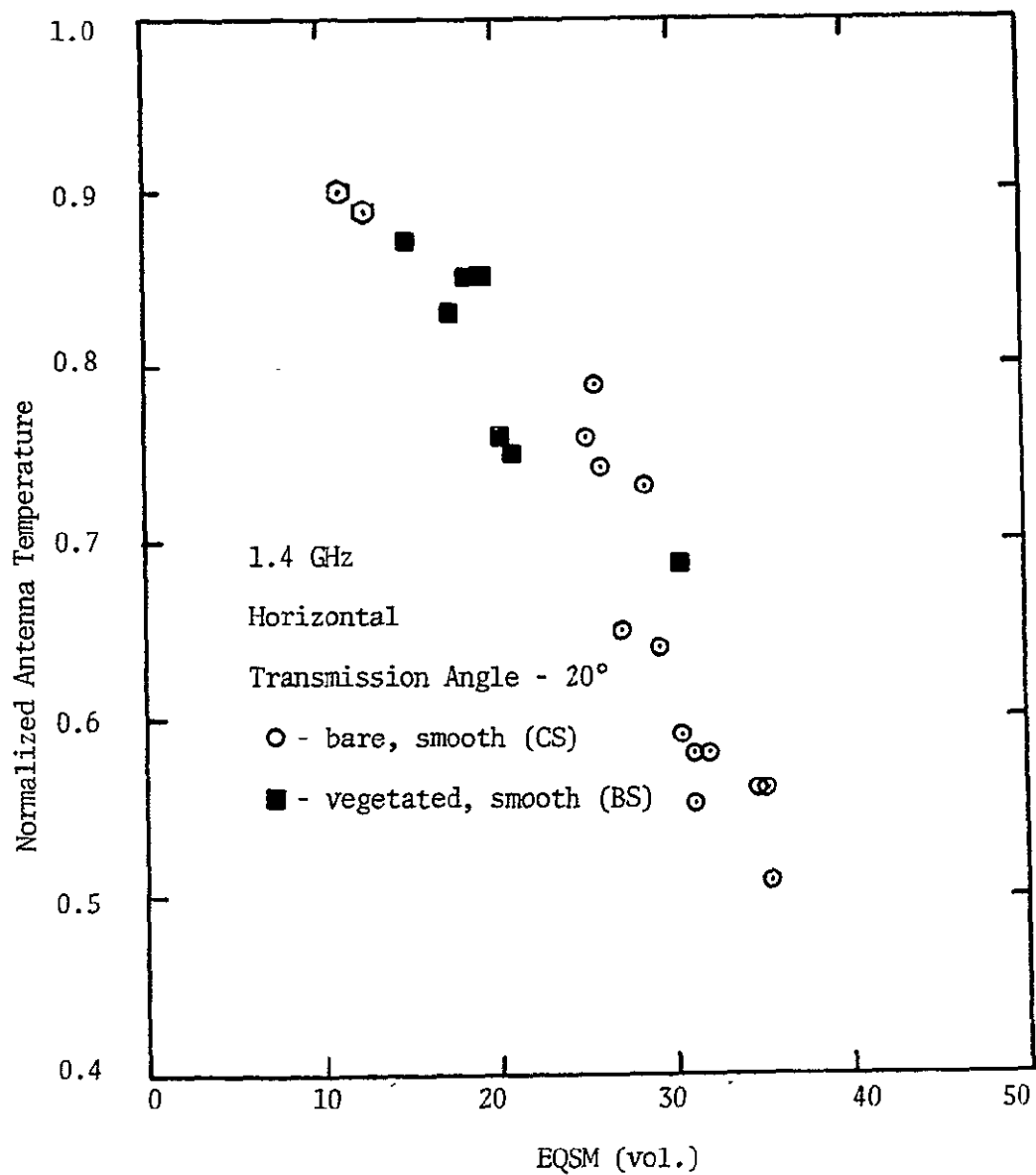
Figure VII-41.   Comparison of bare and vegetated
1.4 GHz measurements made as a
function of soil moisture at a
20° transmission angle.
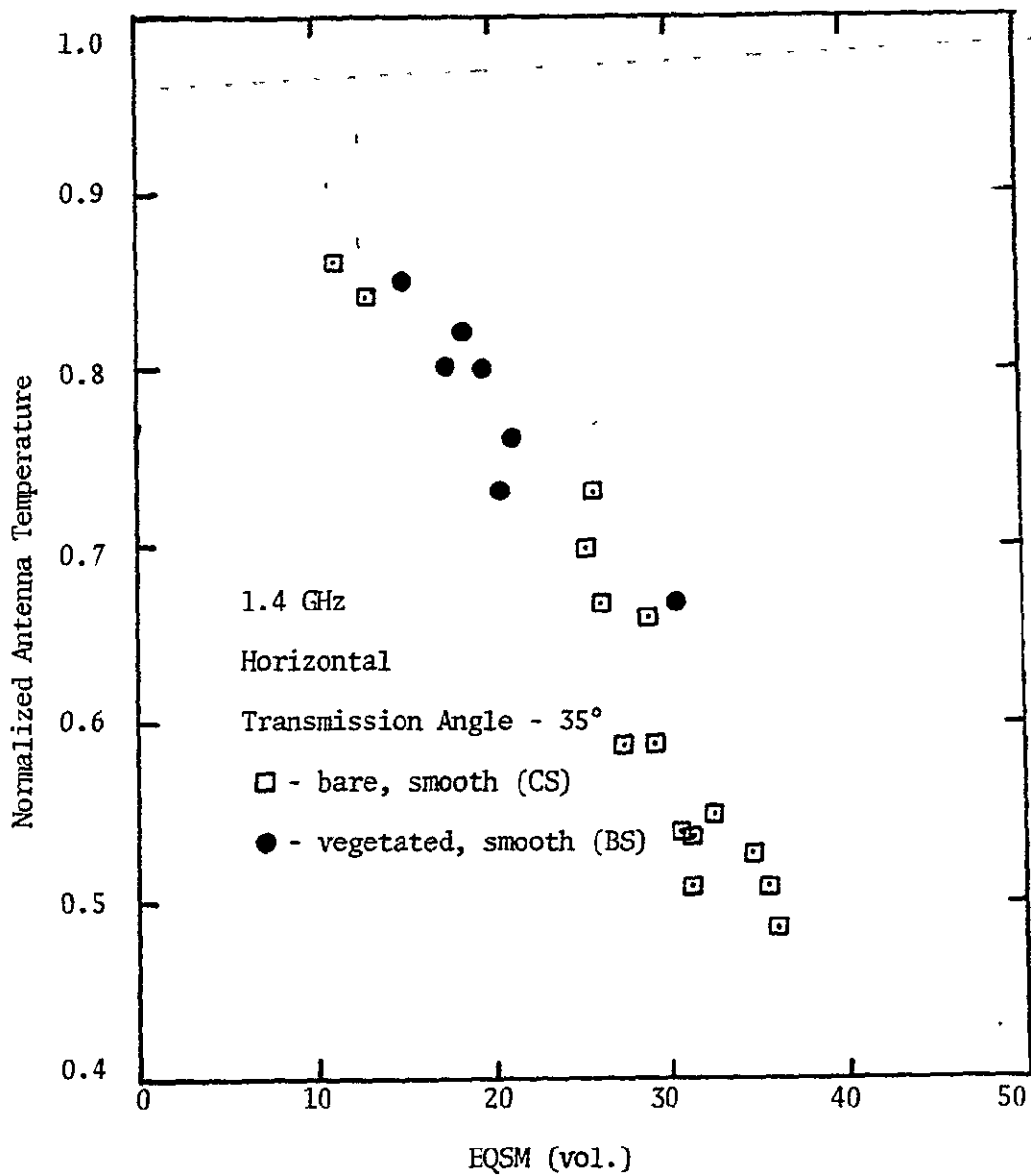
Figure VII-42. Comparison of bare and vegetated
1.4 GHz measurements made as a function
of soil moisture at a 35° transmission
angle.
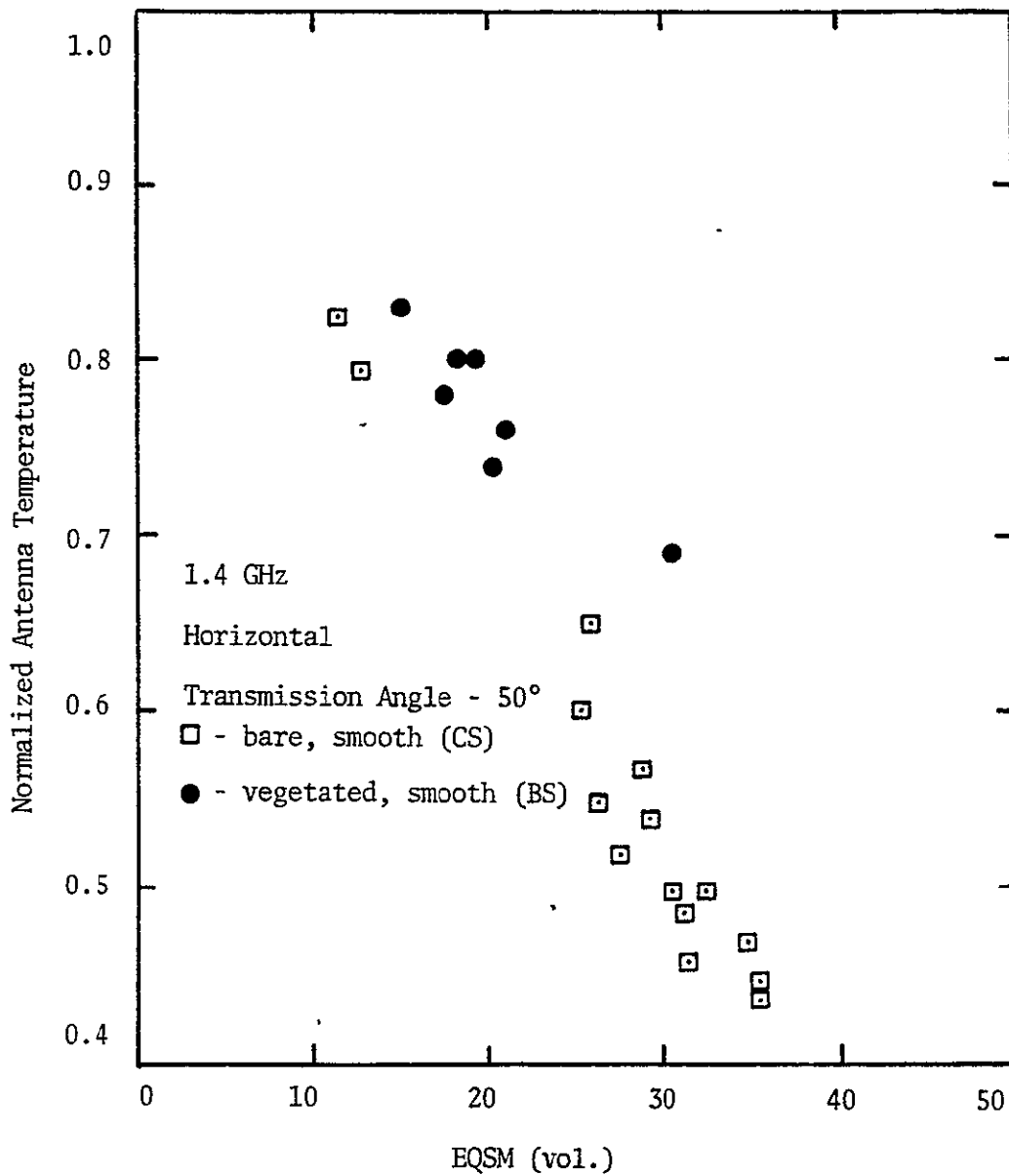
Figure VII-43. Comparison of bare and vegetated
1.4 GHz measurements made as a
function of soil moisture at a
50° transmission angle.

The above result indicates that as the vegetation
height-density product is increased, the emission from the
soil vegetation scene at 1.4 GHz increases. This is
confirmed by comparing 1.4 GHz measurements of the smooth
section of field A to the smooth section of field B.
Figure VII-44 and VII-45 demonstrate that even at a trans-
mission angle of 20°, a vegetation height-density product
increase from 1.25 cm to 1.88 cm increases the emission
at both vertical and horizontal polarizations.

Row vegetation cover - Field B of the 1975 experimental
plot was row planted in cotton that had an average height
of 61 cm, an average plant moisture content of 73 percent,
and an average volumetric density of 0.23 percent. As a
result, the vegetation height-density product was 0.14 cm.

Figures VII-46 and VII-47 demonstrate the effect of
this vegetation cover for measurements made parallel and
perpendicular to the rows at 10.6 GHz. These figures
demonstrate that the soil moisture dependence is greatly
reduced from the bare soil dependence. A comparison of
these figures demonstrate that the measurements made
parallel to the rows are larger than those made perpen-
dicular to the rows. The row vegetation model predicted
that the emission should be reduced in going from parallel
to the rows to perpendicular to the rows. However,
this model did not take into account the row structure
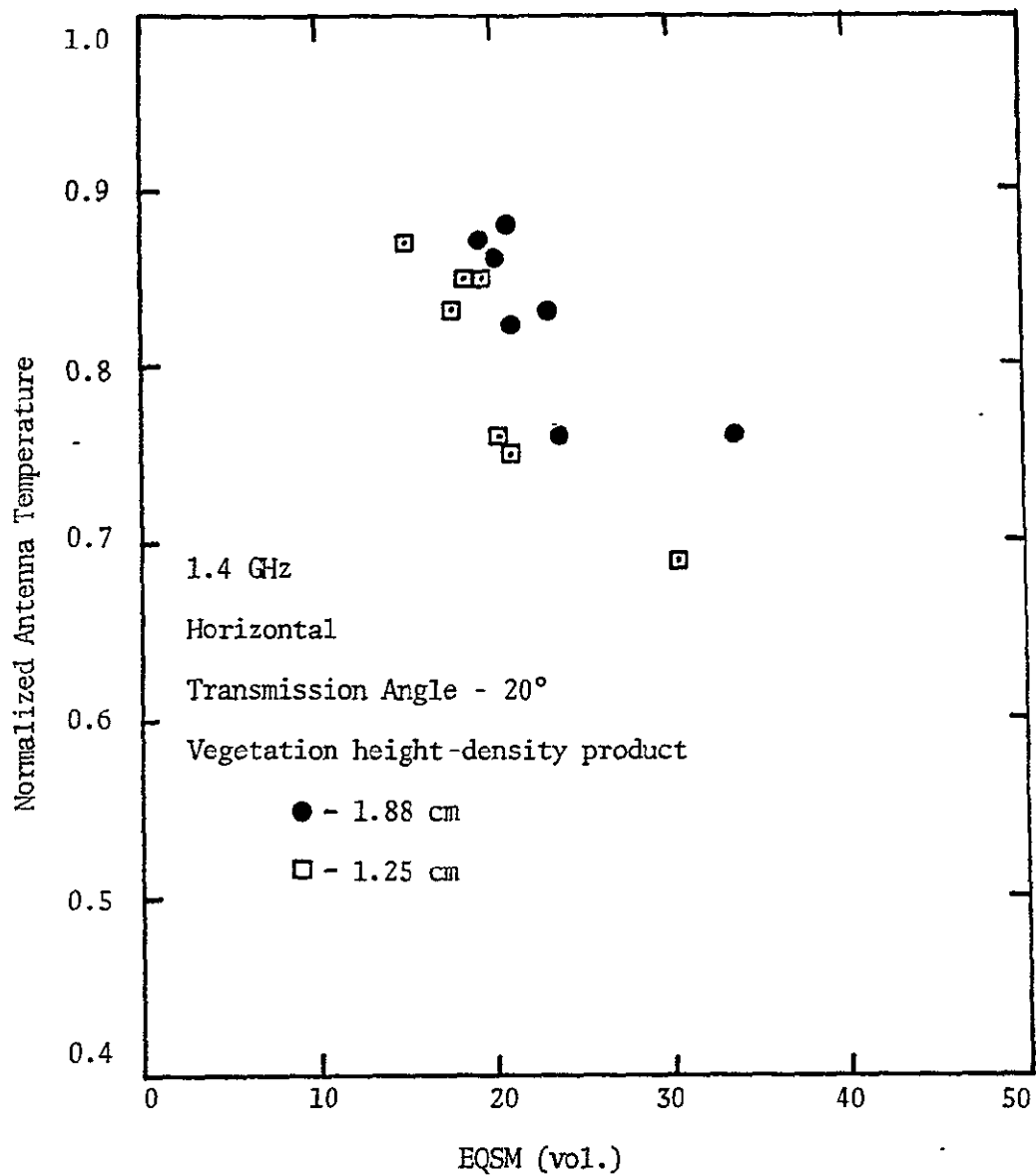
Figure VII-44. Comparison of horizontal 1.4 GHz
measurements of two uniform
vegetation densities.
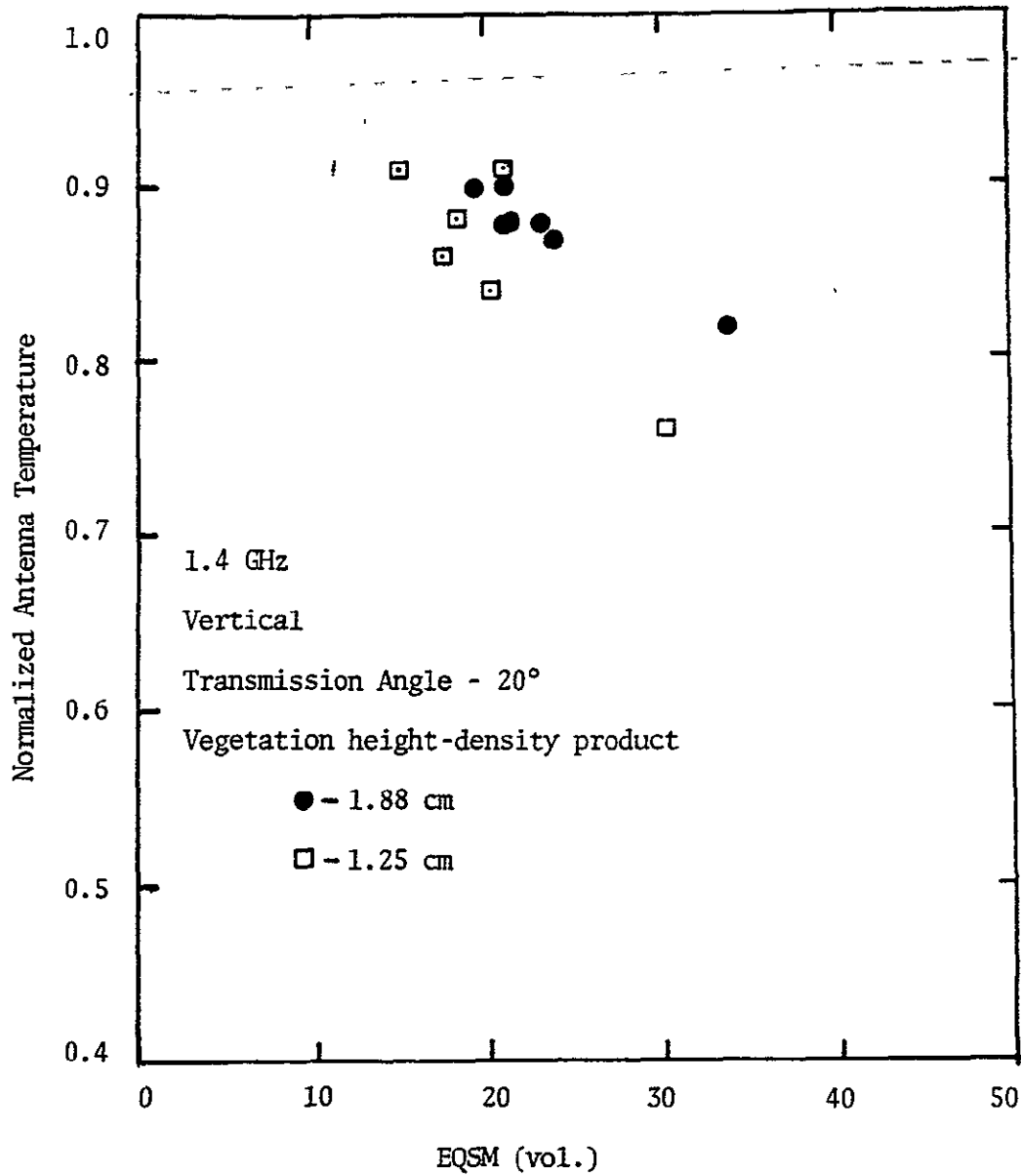
Figure VII-45. Comparison of vertical 1.4 GHz
measurements of two uniform
vegetation densities.
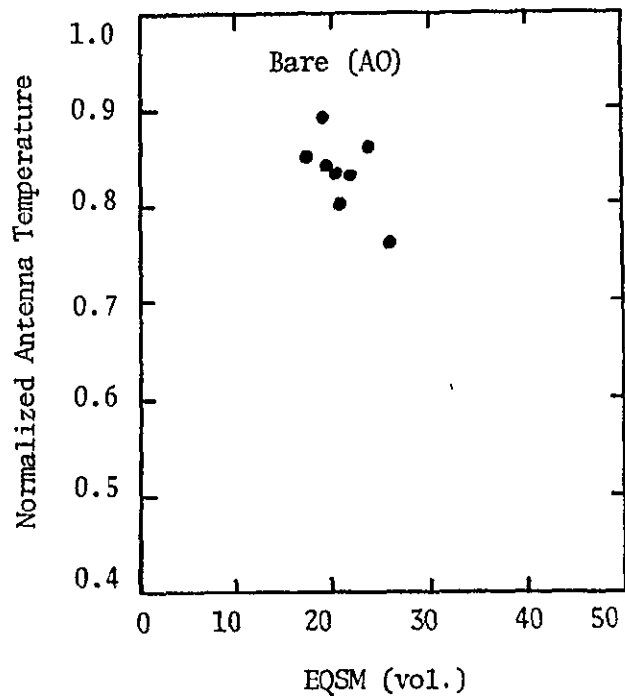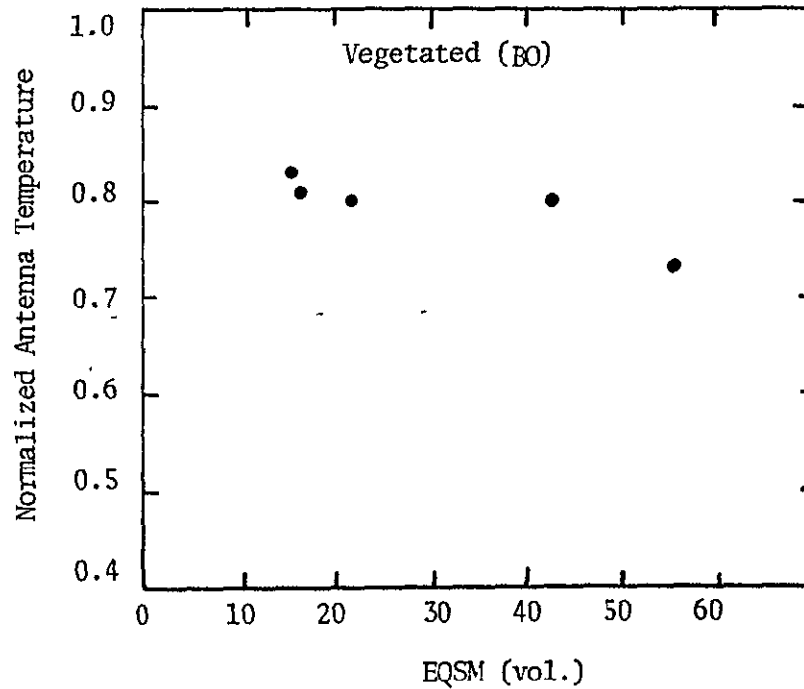
Figure VII-46. Comparison between bare and vegetated 10.6 GHz antenna temperature measurements made parallel to the row direction.
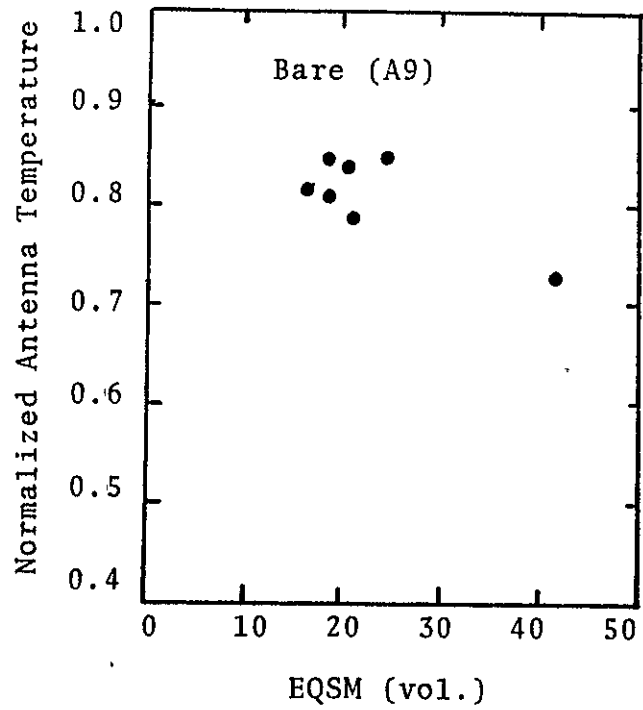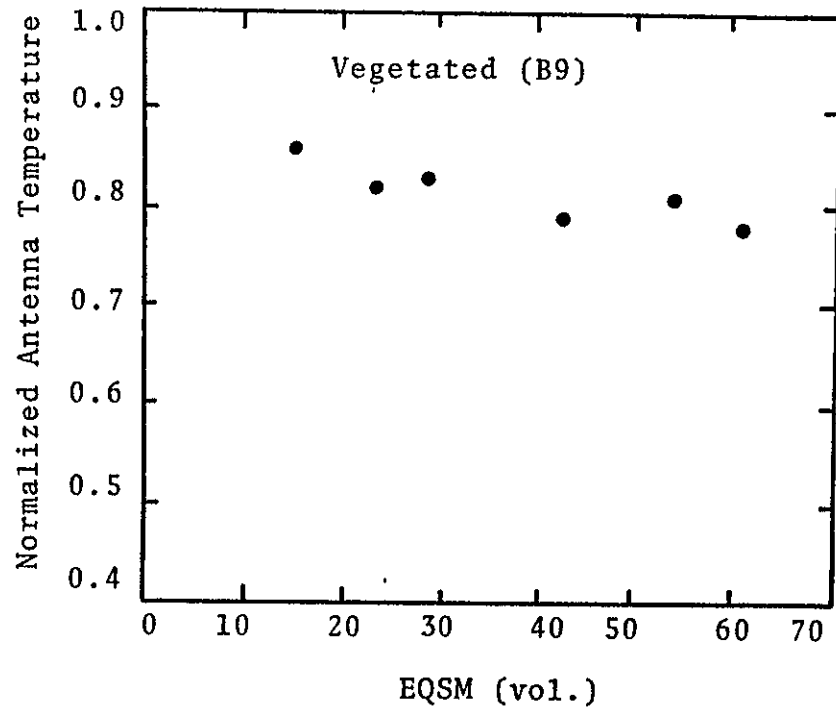
Figure VII-47. Comparison between bare and vegetated 10.6 GHz antenna temperature measurements made perpendicular to the row direction.

of the soil. It was previously shown in the bare soil measurements that the soil row structure will cause the vertically polarized antenna temperature measurements made perpendicular to the rows to be larger then those made parallel to the rows. This indicates that the soil row structure should be incorporated into the row vegetation model.

At 1.4 GHz Figure VII-48 demonstrates that the soil radiation effectively penetrates the vegetation cover when viewing the field parallel to the rows. The moisture response is retained without modification in measurements made parallel to the rows. Figure VII-49 shows evidence that the soil moisture dependence is affected when viewing the fields perpendicular to the rows. However, this statement is made as a result of the two points denoted by special symbols. If these two measurements are in error, then the soil moisture dependence is affected only by increased measurement scatter, as for the bare soil case.

Soil Moisture Estimation

Scope

The effect of soil moisture on the thermal microwave emission of bare and vegetated soil has been shown both theoretically and experimentally. Although the shape of
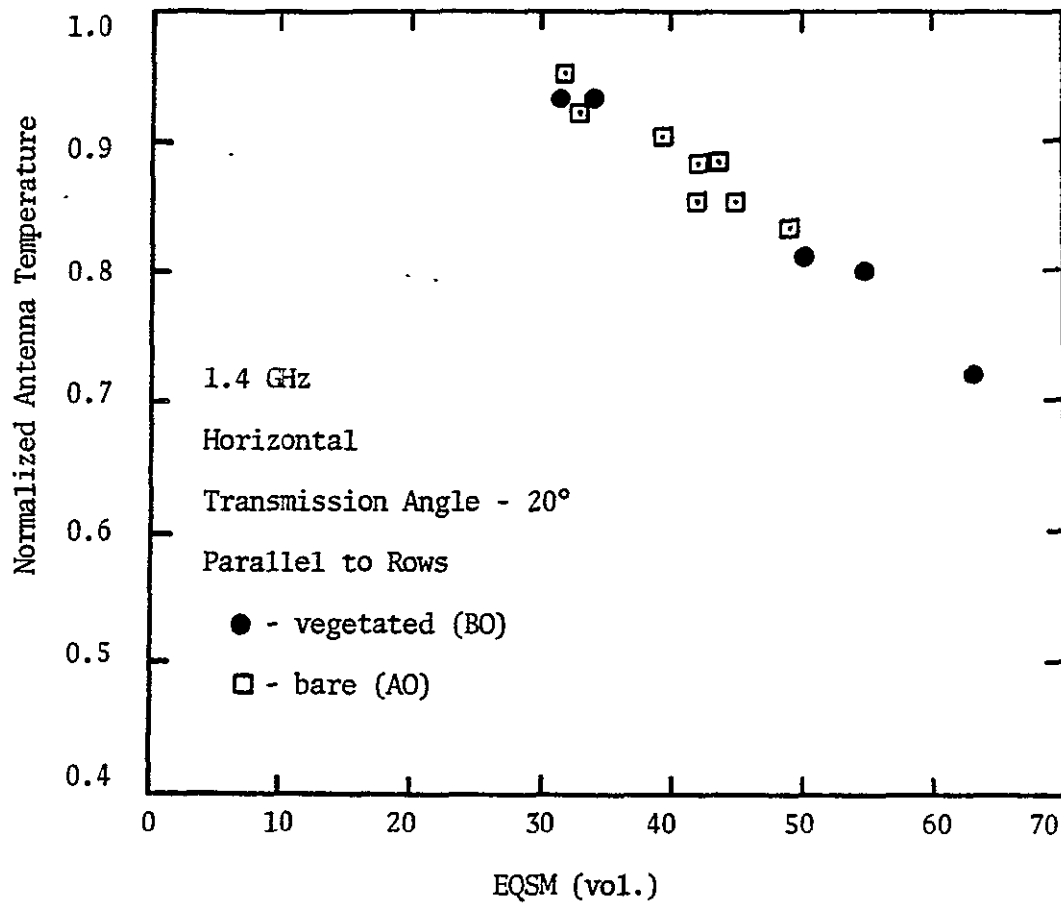
Figure VII-48. Comparison of bare and vegetated 1.4 GHz measurements of row tilled surfaces made parallel to the rows as a function of soil moisture.
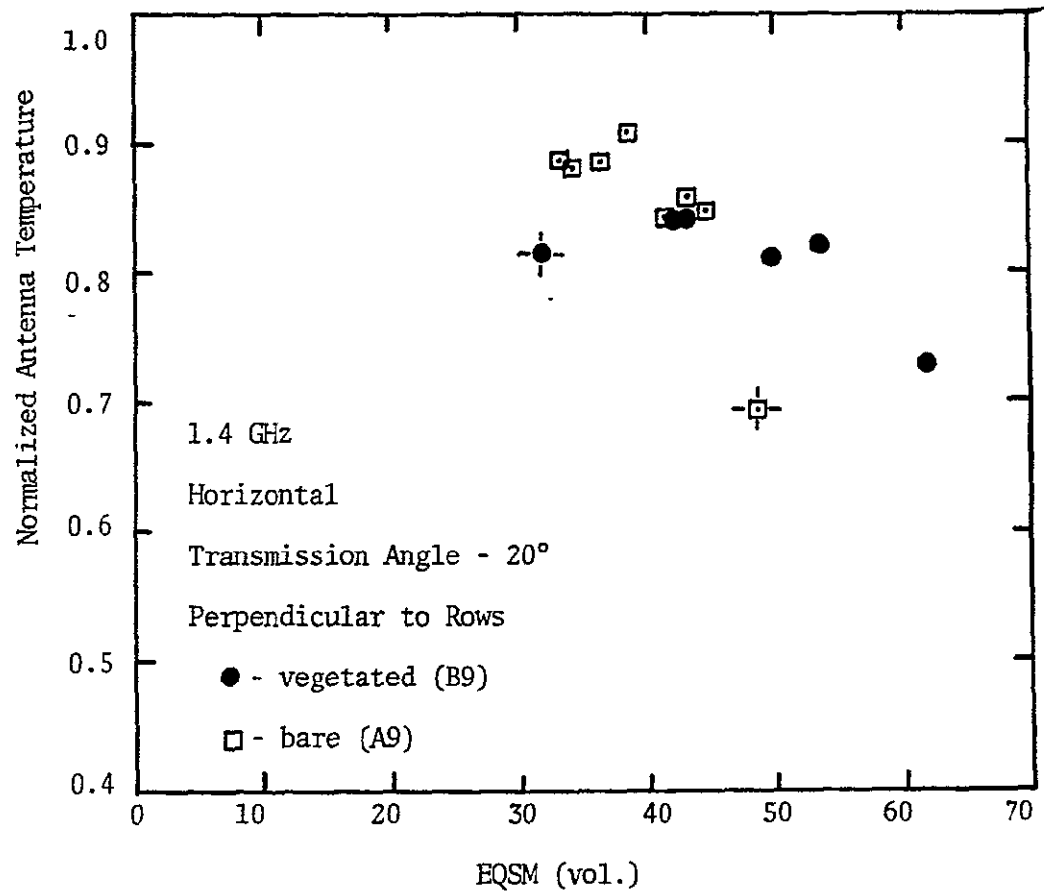
Figure VII-49. Comparison of bare and vegetated 1.4 GHz measurements of row tilled surfaces made perpendicular to the rows as a function of soil moisture.

the soil moisture profile affects the magnitude of the emission from the soil volume, it was shown that the soil moisture profile can be quantified by a parameter termed the equivalent incoherent soil moisture. This parameter is denoted by EQSM. It was further shown that the parameter can be interpreted as the average soil moisture in the soil moisture profile for some surface layer of soil. The depth of this layer is directly related to the magnitude of the EQSM, or average soil moisture, for 1.4 GHz measurements. At 10.6 GHz the layer is always between one and two centimeters thick.

The analysis summarized above and the antenna temperature measurements discussed earlier in this chapter demonstrate that soil moisture information and the depth with which that soil moisture corresponds can be measured remotely with passive microwave sensors. There are, however, scene parameters such as vegetation cover and surface roughness that modify the response of the soil emission to soil moisture. A technique of estimating the equivalent soil moisture parameter, EQSM, for uniformly smooth or rough soil will be illustrated below. The effect of a vegetation cover on this estimation technique will also be discussed.

The analysis presented below is structured around estimating the average volumetric soil moisture, EQSM. Soil moisture is estimated rather than matric potential

simply because the measurements reported in this document were acquired from experimental plots consisting of the same soil texture, and the matric potential versus soil moisture curves were not available for this soil. Due to the results presented in Chapter II, the analysis presented below should apply equally well to soil matric potential which could be converted to available plant water (depending on the plant of interest) for agricultural applications, or degree of soil saturation for hydrologic applications. Such an analysis would be independent of soil texture.

Uniform Roughness

It has been demonstrated that the emission from bare, smooth soil is sensitive to changes in the shape and overall magnitude of the soil moisture profile. However, as the soil surface is roughened the sensitivity to soil moisture decreases. Naturally, the effect of a given roughness is dependent on the wavelength of the radiation. For 1.4 GHz Figure VII-50 is a plot of 1.4 GHz antenna temperature measurements made at a 20° transmission angle. These data demonstrate the sensitivity reduction due to uniform roughness that is similar to flat tilled agricultural fields. At the 10.6 GHz wavelength the bare "smooth" field appeared rough. As a result there is no smooth surface measurements at 10.6 GHz. This was demonstrated in Figure VII-24.
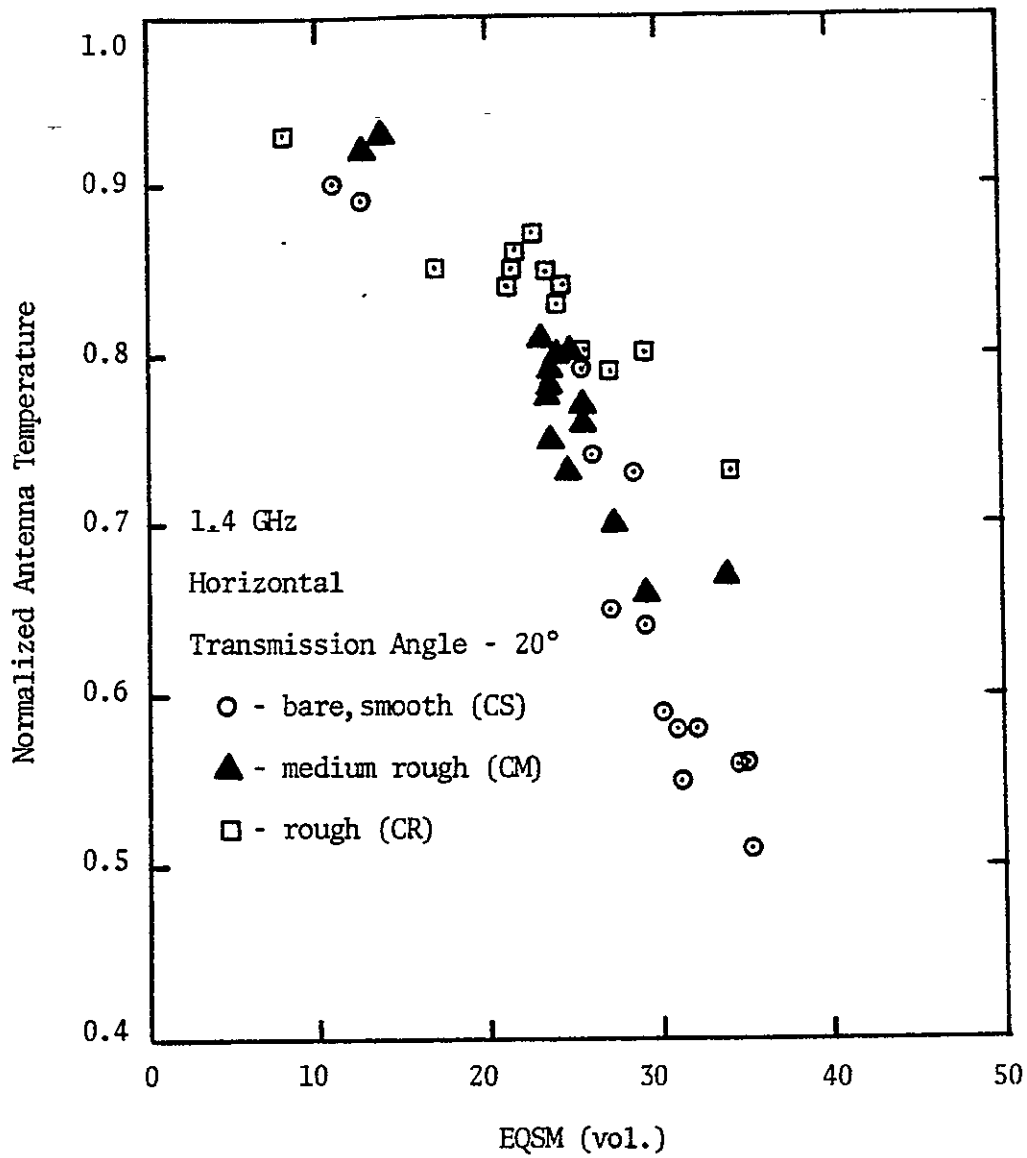
Figure VII-50. Horizontal 1.4 GHz antenna temperature measurements as a function of soil moisture for three surface conditions.

The individual antenna temperature measurements were plotted in Figures VII-24 and VII-50 to demonstrate the apparent scatter of the measurements. This scatter is not due entirely to the noise of the radiometer system. Much of the scatter is a result of the inaccuracies in measuring the soil moisture. This is especially true at 10.6 GHz since the EQSM plotted in Figure VII-24 is derived from surface (0-1 cm) soil moisture measurements. Figure VII-51 is a plot of the standard deviation versus the mean of the zero to one centimeter soil moisture measurements for the smooth and medium rough bare fields used in 1974. The magnitude of the standard deviation is seen to be quite large in comparison with the mean surface moisture, except for very dry conditions. These data indicate the uncertainity in measuring soil moisture.

Figure VII-51 demonstrates that although ground measurements are taken to be the standard to which the microwave measurements are compared, the error bars on the "ground truth" measurements can be extremely large. However, in the analysis below the ground soil moisture measurements to which the microwave measurements are compared are assumed to be exact quantities and not random variables. As a result, the estimates of the accuracy to which soil moisture can be remotely measured based on this analysis should be conservative estimates.
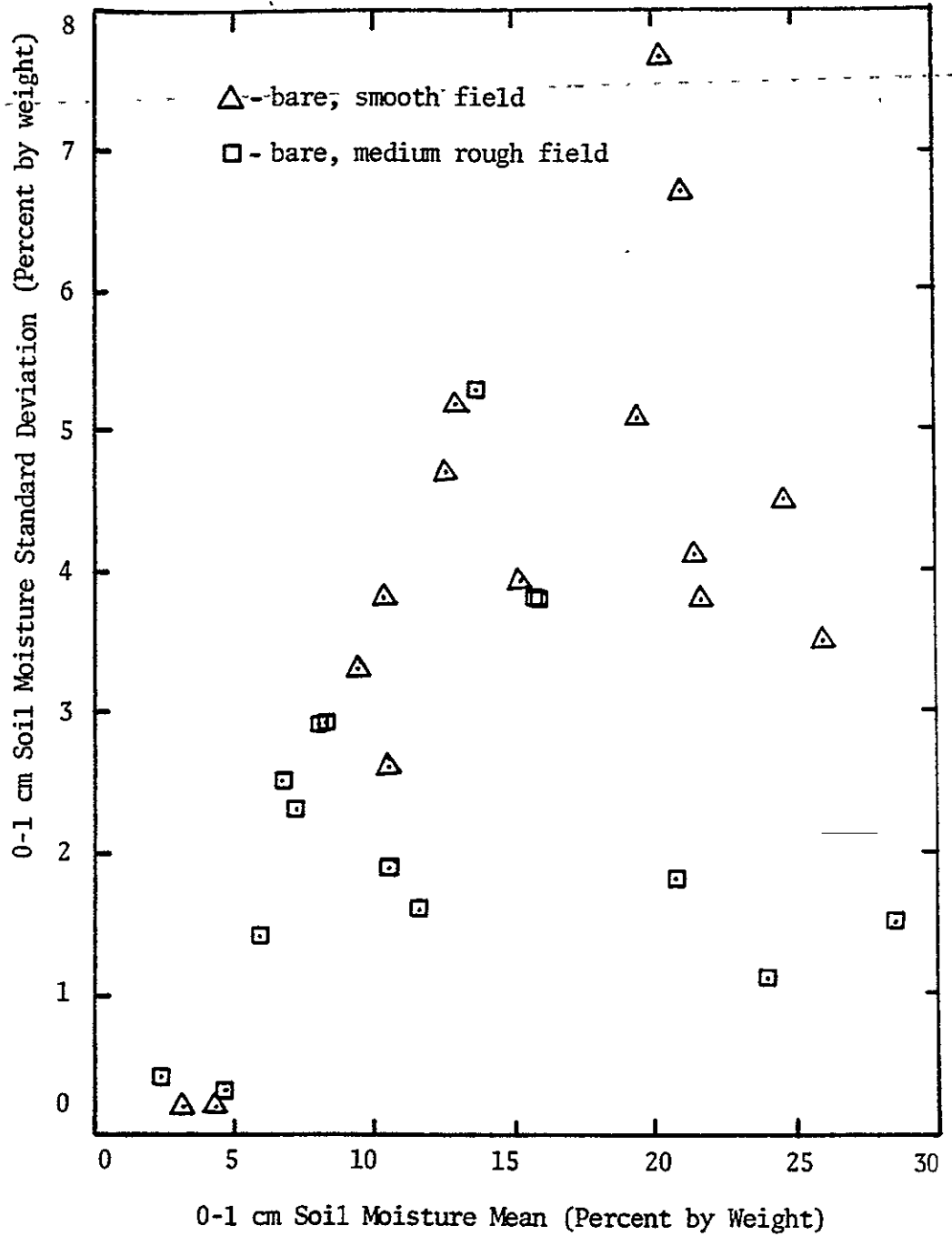
Figure VII-51. Comparison of the mean and standard deviation of the 0-1 cm soil moisture measured in fields CS and CM.

Surface roughness prediction - In order to utilize
passive microwave antenna temperature measurements for
estimating soil moisture for unknown terrain, it will be
necessary to remove the effects of surface roughness
from the measurements, or at least quantify the surface
roughness over which the measurements were made. If the
effects of roughness could be removed then a soil moisture
estimate could be made based on an effective smooth surface
soil moisture response. If the surface roughness was only
quantified, a soil moisture estimate could be made based
on the soil moisture response for that roughness. In
either case it is necessary to determine if surface
roughness can be quantified using only the antenna tem-
perature measurements.

A plot of 1.4 GHz normalized antenna temperature versus
transmission angle is shown in Figure VII-52 as a function
of surface roughness for a specific soil moisture condition.
Note that as the surface gets rougher the overall emission
increases. In addition, the vertical and horizontal
emission tends to get closer for off nadir angles as the
roughness increases. . As a result, the difference in the
vertical and horizontal antenna temperatures is a function
of surface roughness. It must now be determined if this
correlation can be used to estimate roughness with reason-
able accuracy, and for which transmission angle this
correlation is optimum.
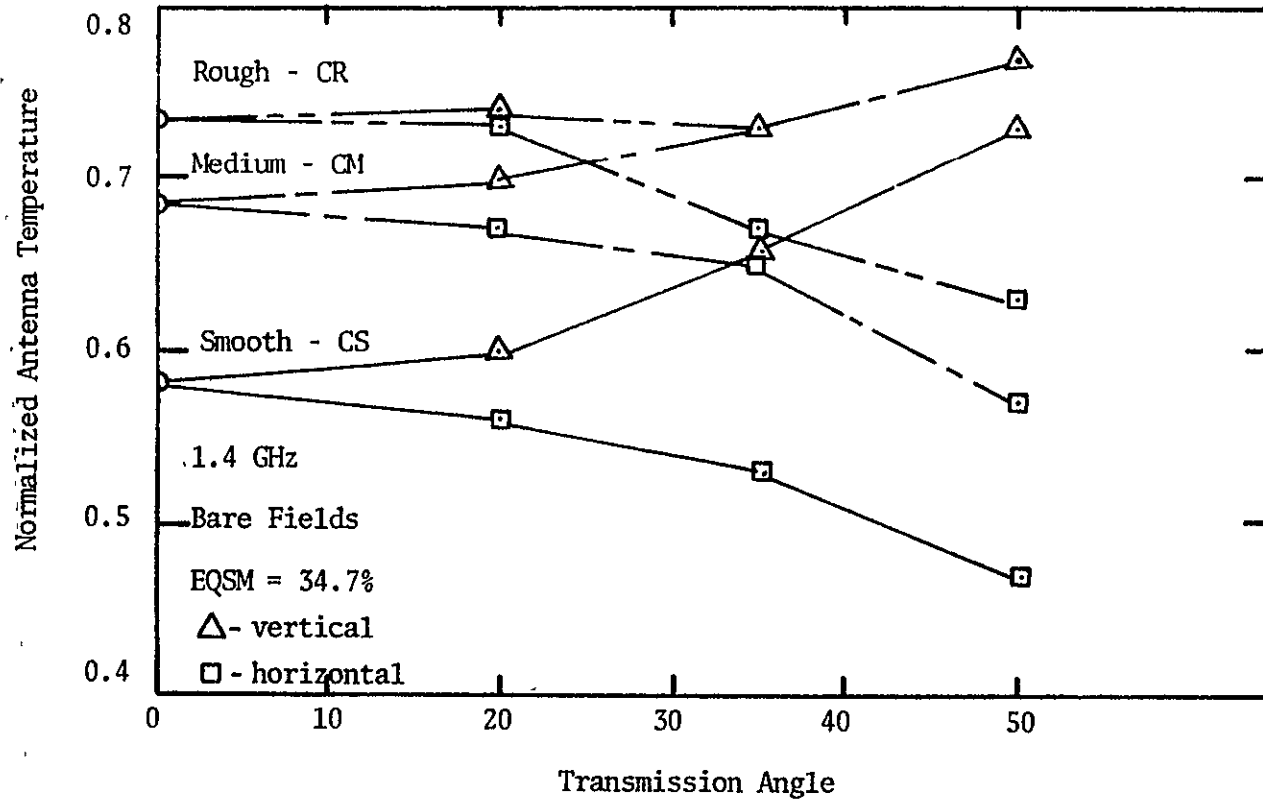
Figure VII-52. 1.4 GHz antenna temperature measurements made as a function of transmission angle for three surface preparations.

The relationship between the difference in the vertical and horizontal 1.4 GHz normalized antenna temperatures and surface roughness is shown in Figures VII-53 through VII-55. These plots are based on the linear . regression equations generated for the normalized antenna temperature versus EQSM (Table VII-5). Note that the difference between the vertical and horizontal normalized antenna temperatures not only changes with roughness, but that it also changes with moisture.

At a transmission angle of 20° the difference between the vertical and horizontal normalized antenna temperatures is very small. As a result, the relative sensitivity of this difference to changes in moisture is very large, at least for the smooth and medium rough fields. At the 50° transmission angle the difference between the vertical and horizontal measurements is large, but the relative . change in this difference with moisture is also large. However, the dependence of this difference on soil moisture is not consistent between rms surface height deviations. That is, the difference between the vertical and horizontal normalized antenna temperatures change 54% as the moisture changes from 15% to 35% for the smooth field (Field CS). For the same soil moisture change, this difference changes 66% for the medium rough field, and only 30% for the rough field. However, at a 35° transmission angle the difference
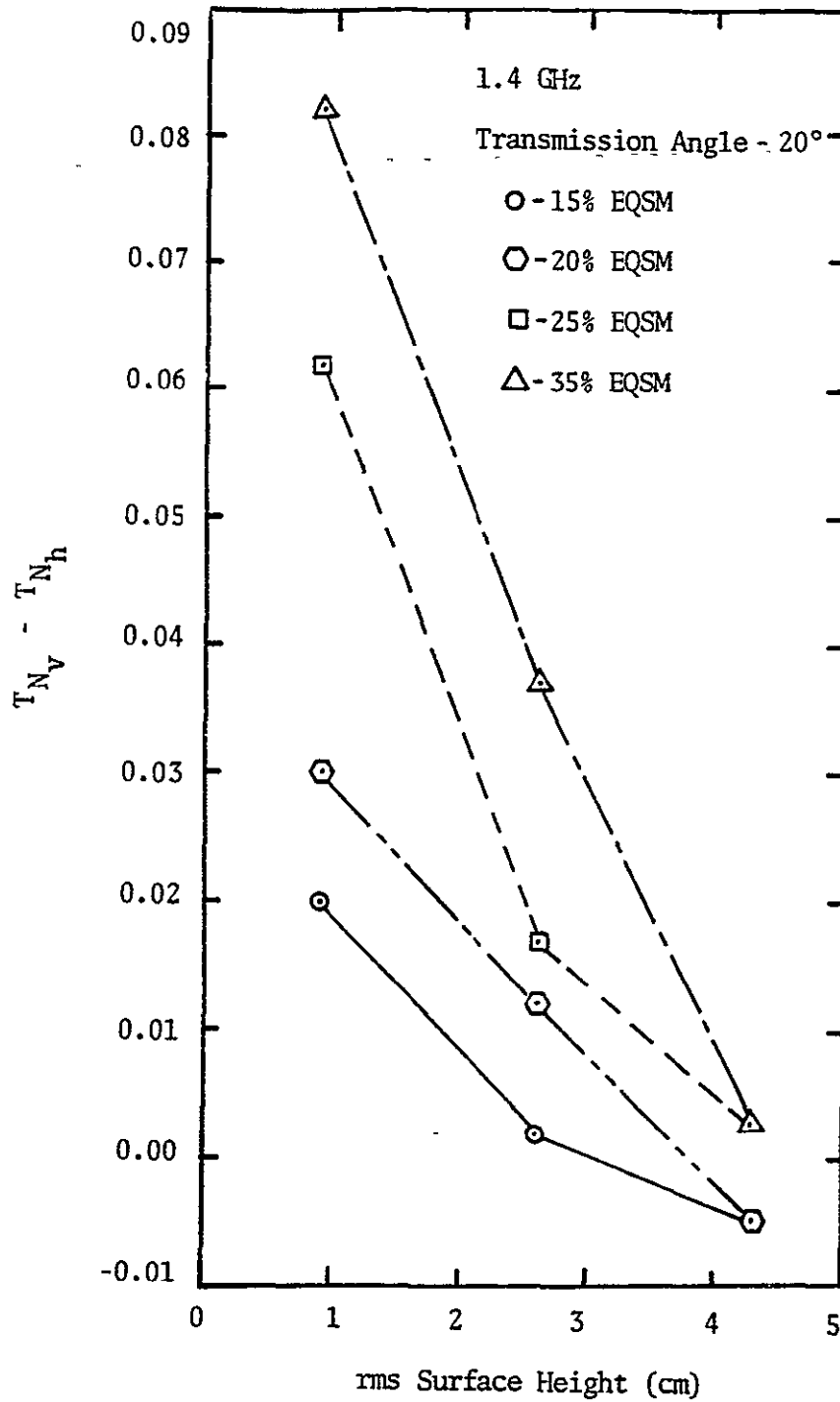
Figure VII-53. Comparison of the effect of soil mois-
ture on the difference between vertical
and horizontal normalized antenna
temperatures measured at 20° for three
rms surface heights.
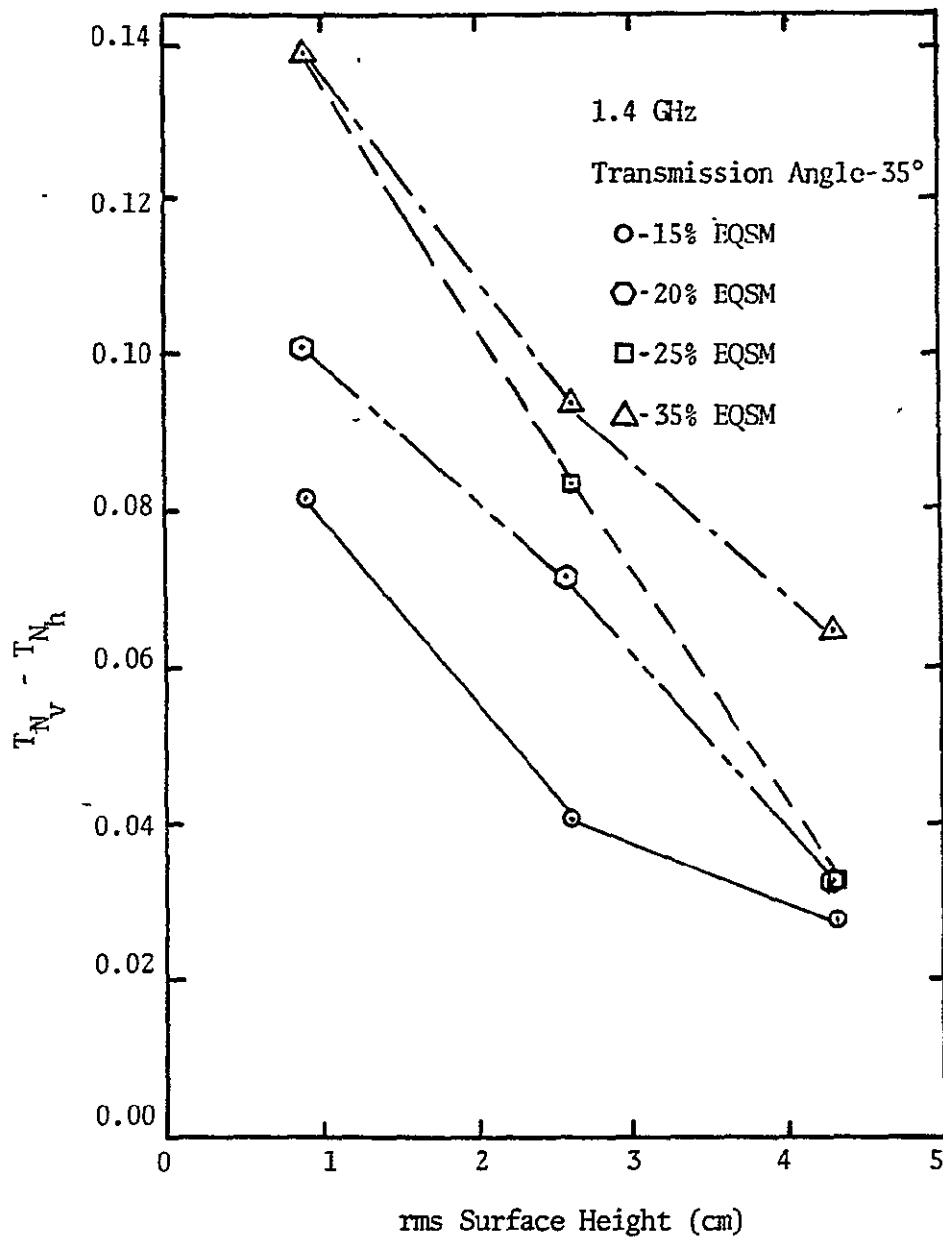
Figure VII-54. Comparison of the effect of soil
moisture on the difference between
vertical and horizontal normalized
antenna temperatures measured at
35° for three rms surface heights.
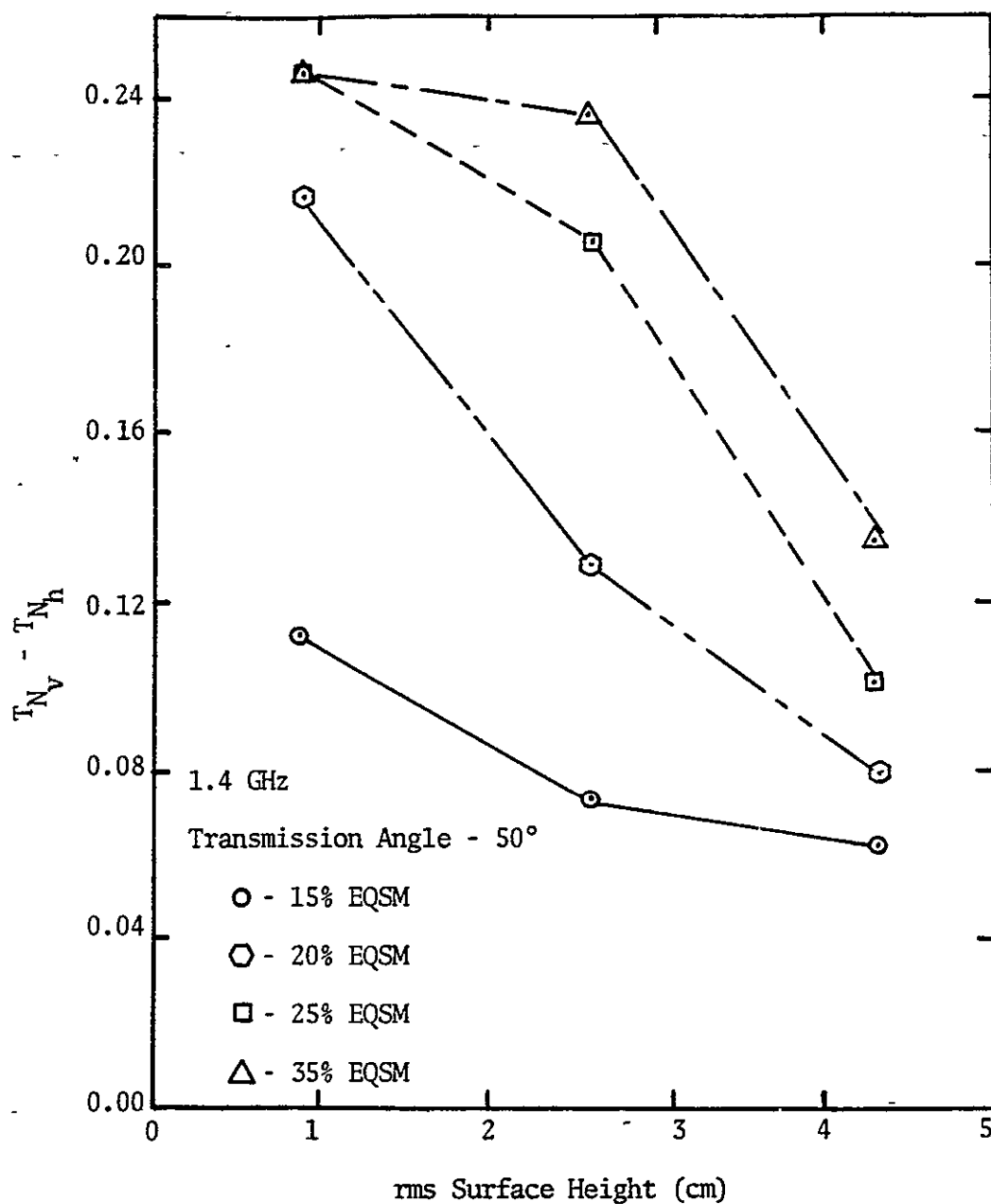
Figure VII-55. Comparison of the effect of soil moisture on the difference between vertical and horizontal normalized antenna temperatures measured at 50° for three rms surface heights.

between the vertical and horizontal normalized antenna temperatures change 41% for field CS, 38% for field CM and 27% for field CR as the moisture changes from 15% to 35%. In addition, the differences are large enough to be measurable. As a result, it appears from this crude analysis that the 35° transmission angle, of the three angles that were investigated, would yield the best results for estimating surface roughness for unknown moisture conditions.

It is possible that the effect of soil moisture on the difference between the vertical and horizontal normalized antenna temperature is not as large as is indicated by Figure VII-54. Plotting all of the points that are available at 35° (Figure VII-56), there are five points that are separated from the others. These points are denoted by the solid triangles. These particular points correspond to two measurement sets that were acquired before irrigation and while the soil was very dry. There is no way of knowing whether or not these points fall below the other points because of the low soil moisture condition, or whether or not all of the other points are higher than these points due to the surface smoothing effect of the irrigation.

Soil moisture measurement - Now that a parameter has been identified that is dependent on surface roughness,
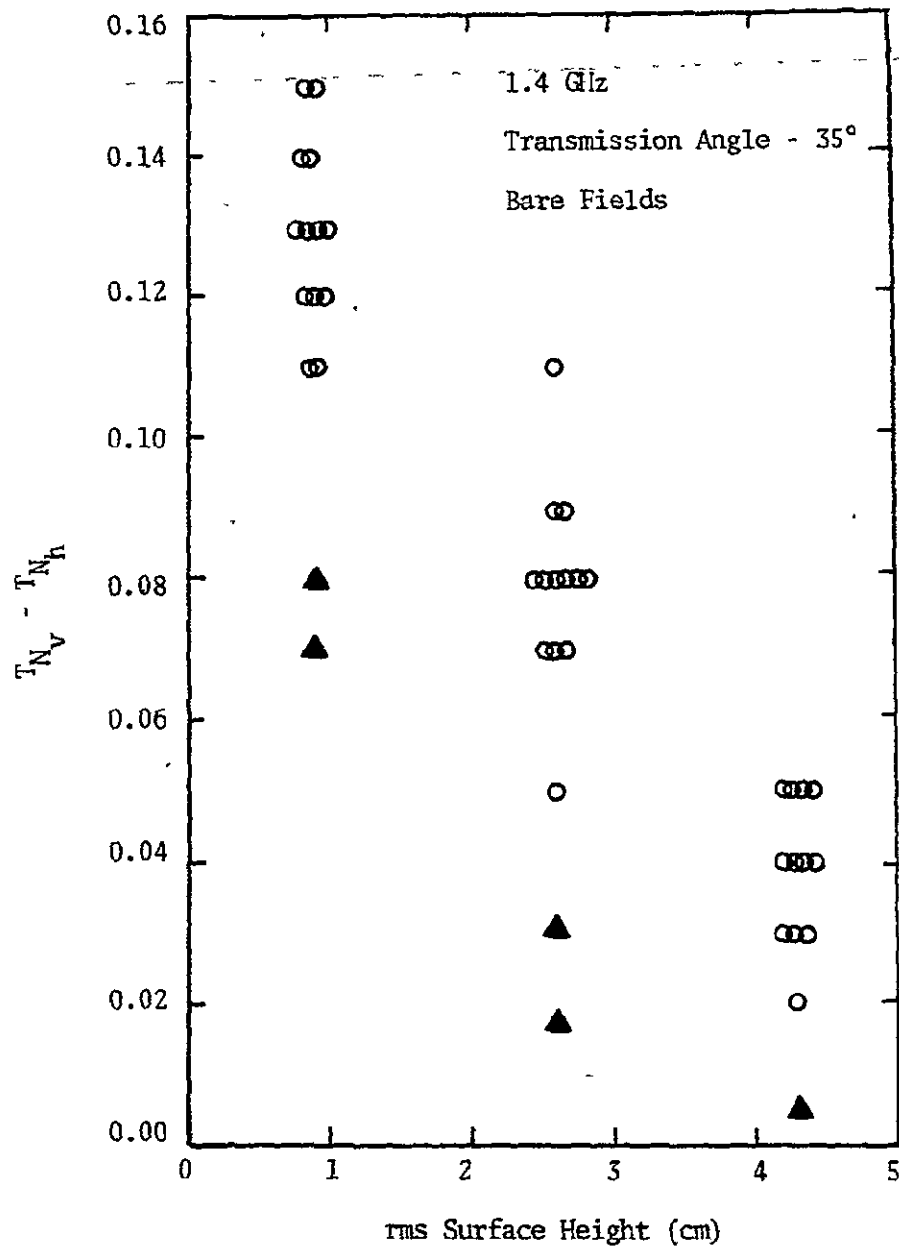
Figure VII-56. The difference between vertical and horizontal antenna temperatures measured at 35° for three rms surface heights.

this parameter can be used in conjunction with horizontal or vertical antenna temperature measurements to estimate soil moisture. It has been shown above that a transmission angle of 35° is probably the best transmission angle (of the three angles investigated) to use to estimate the roughness condition. A choice must now be made as to which polarization and which transmission angle will be used to estimate the soil moisture. It was demonstrated earlier that the highest sensitivity to soil moisture was obtained at a transmission angle of 20°, although measurements at the other angles also have a useable moisture sensitivity. At the 20° transmission angle horizontal and vertical antenna temperature measurements have about equal sensitivity to moisture. For purposes of illustration, horizontal antenna temperature measurements made at 20° will be used in conjunction with the difference between the vertical and horizontal antenna temperature measurements made at 35° to demonstrate a technique of estimating EQSM, the average soil moisture in a surface soil layer.

Using the difference between the vertical and horizontal antenna temperature measurements at 35° and the horizontal antenna temperature measurements at 20°, an algorithm can be devised that estimates both the surface roughness and average soil moisture (EQSM) simultaneously. A graphical representation of such an algorithm is

presented in Figure VII-57. The horizontal axis is the normalized horizontal antenna temperature measured at 20°, and the vertical axis is the difference between the vertical and horizontal normalized antenna temperatures measured at 35°. Note that both rms surface roughness and soil moisture information is displayed in this plot. The solid lines in the plot define the rms surface roughness. The dashed lines are EQSM contours. These contours are plotted in Figure VII-58 without the individual measurements.

Figure VII-58 can be utilized to estimate moisture and surface roughness by simply plotting the unknown measurements and determining which partition the measurements fall within. In order to get an estimate of the expected accuracy of an algorithm based on such an approach, 80% confidence intervals were calculated for the horizontal axis of Figure VII-58. It is obvious that these confidence intervals will depend on the surface roughness, with the estimation accuracy decreasing with roughness.

Table VII-9 contains the confidence intervals calculated at 35% EQSM for the normalized horizontal antenna temperature measurement at 20° for each surface roughness. These are confidence intervals on the mean of a population and not on individual measurements. By comparing these
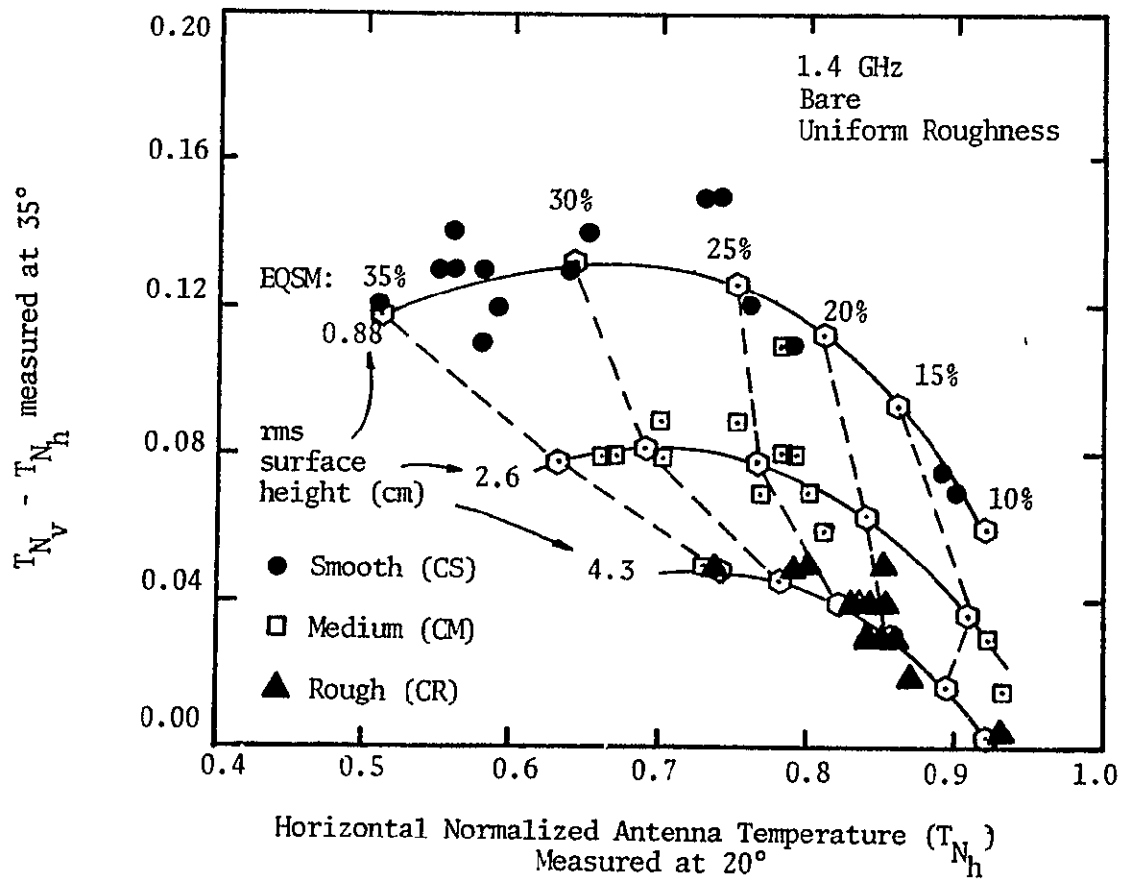
Figure VII-57. Demonstration of the separability of 1.4 GHz antenna temperature measurements into soil moisture and surface roughness classes.
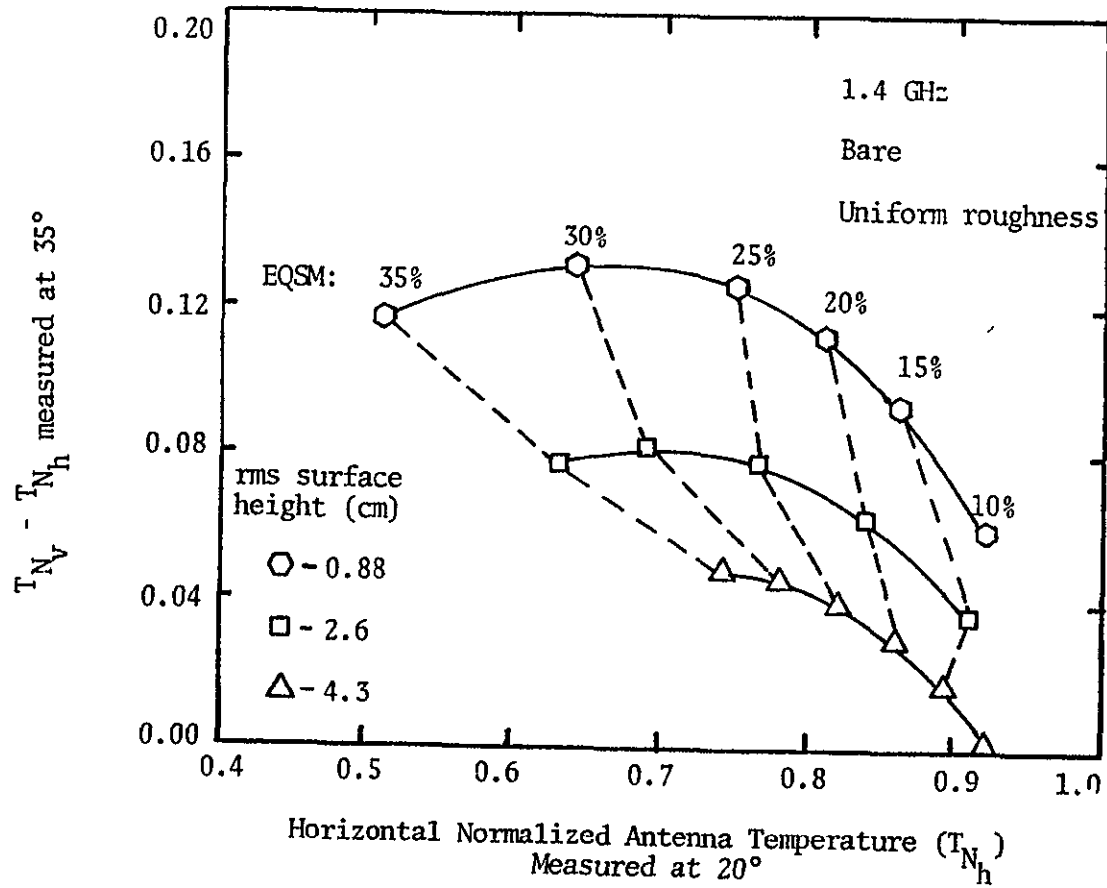
Figure VII-58. Soil moisture and surface roughness partitions obtained from Figure VII-57 for 1.4 GHz measurements.

TABLE VII-9

80% Confidence Intervals on the Population Mean at 25% EQSM

for T_{N_h} Measured at 1.4 GHz

Field	Surface Roughness	EQSM	T_{N_h}	Degree of Confidence
CS	0.88	25%	0.75 ± 0.064	80%
CM	2.6	25%	0.76 ± 0.058	80%
CR	4.3	25%	0.822 ± 0.043	80%

confidence intervals to the EQSM contours in Figure VII-58,

it can be seen that the soil moisture estimation accuracy

assuming the surface roughness is known is approximately

+3% and -6% EQSM for the smooth field, +4% and -5% EQSM

for the medium rough field, and +5.5% and -6% EQSM for

the rough field. These are only approximate estimates

obtained graphically from Figure VII-58 using the data

of Table VII-8. However, the estimates should be reason-

ably conservative since the ground data were taken to be

exact quantities when in reality the error in making

"ground truth" measurements is at least as large as the

error in the radiometer measurements. At any rate, these

approximations indicate that at 1.4 GHz for bare uniformly

rough soil, the average soil moisture in some surface

layer can be estimated with an 80% degree of confidence

to fall within a 9% EQSM window for smooth and medium

rough surfaces, and to within a 11% to 12% EQSM window

for a rough surface.

A technique capable of estimating EQSM using 1.4 GHz

measurements has been illustrated above. The depth for

which that average moisture corresponds can be estimated

from Figure VII-6. In Figure VII-6 a distinction was

made between inverted soil moisture gradients and non-

inverted soil moisture gradients. In order to make this

distinction, the EQSM measured at 1.4 GHz can be compared

with the EQSM measured at 10.6 GHz. Recall that at 10.6
GHz the EQSM estimate will always correspond to the 0-1 cm
to 0-2 cm surface layer. Thus, if the 10.0 GHz EQSM
estimate is greater than the 1.4 GHz EQSM estimate, then
the soil moisture profile can be assumed to be inverted.

It was earlier demonstrated that antenna temperature
measurements at 10.6 GHz are sensitive to smaller scales
of roughness than are 1.4 GHz measurements. As a result,
it is to be expected that the estimation accuracy of
EQSM using 10.6 GHz will not be as good as it is for 1.4
GHz. Figure VII-59 is the 10.6 GHz measurements plotted
in the same manner as the 1.4 GHz data are plotted in
Figure VII-57. Although the measurements from the three
surfaces generally cluster and do appear separable, the
clusters are much closer and less well defined than for the
1.4 GHz measurements. This was expected. No effort was
made to draw moisture and surface roughness contours on
Figure VII-59, however, the estimation accuracy calculated
for the measurements of the smooth and medium rough fields
were no better than ± 10% EQSM. For the rough field it
was approximately ± 6% EQSM. Although the moisture
sensitivity of the rough field was smaller, there was less
scatter in the antenna temperature measurements than there
was for the smooth and medium rough fields (Figure VII-24).
Again, these approximations are based on 80% confidence
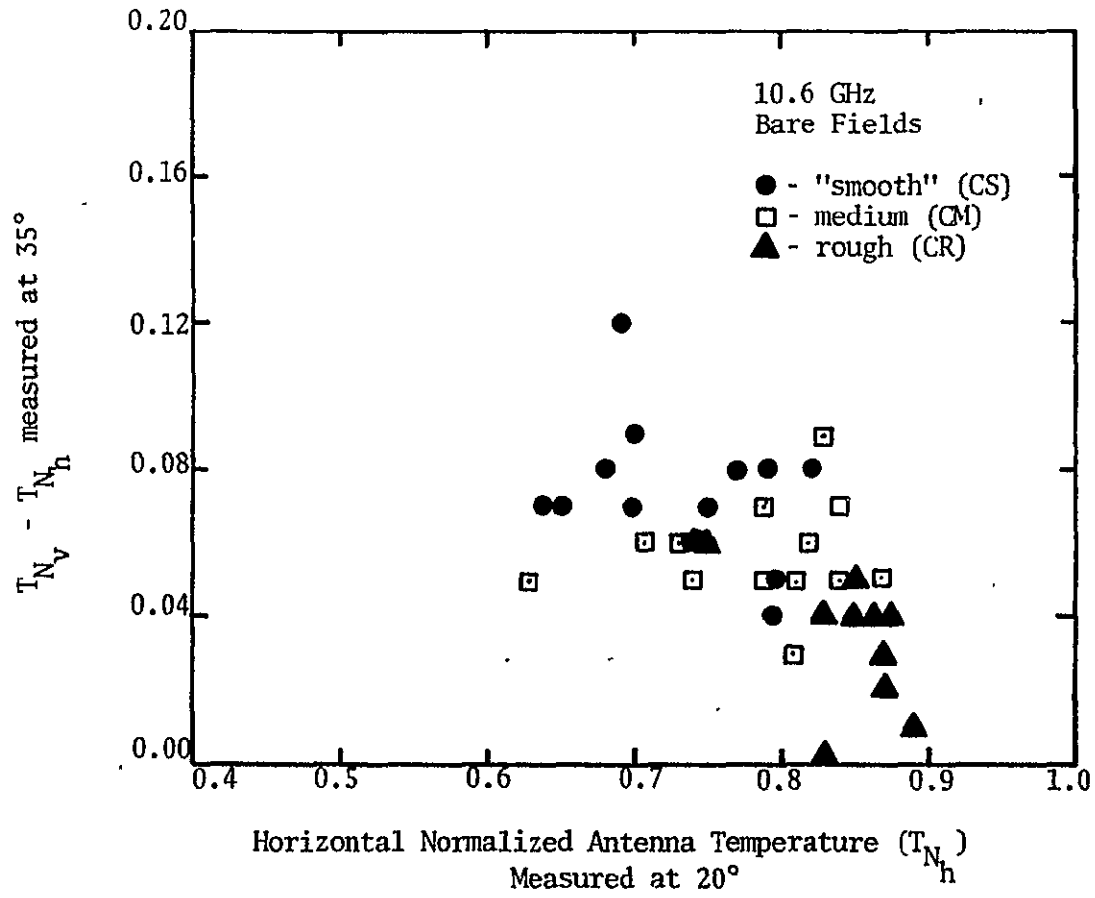
Figure VII-59. 10.6 GHz measurements plotted in a manner that demonstrates the separability of soil moisture and surface roughness (as in Figure VII-57).

limits of the population mean assuming the surface roughness is known. Although this accuracy seems poor, it is probably reasonable considering the scatter in the ground surface moisture measurements illustrated in Figure VII-51.

The two frequency approach described above for estimating the near surface soil moisture gradient can be implemented at 1.4 GHz and 10.6 GHz frequencies with promising results. However, the sensitivity to surface roughness at 10.6 GHz and resulting decrease in response to soil moisture indicate that for a two frequency system a slightly lower frequency than 10.6 GHz would increase the accuracy of the near surface estimate. In addition, the ability to estimate moisture at different depths by using different wavelengths indicate that the soil moisture profile could be estimated with increased accuracy simply by adding additional frequencies to the measurement system.

Row Structure

It was demonstrated in Figure VII-28 through VII-32 that 1.4 GHz measurements of bare row tilled terrain retain a reasonable moisture sensitivity. It was shown, however, that the moisture sensitivity was better when the measurements were made parallel to the rows. In fact, a soil moisture estimation accuracy similar to that obtained above for the medium rough field should be obtainable

from measurements made parallel to the rows. The measure-
ment accuracy will no doubt be reduced for measurements
made at larger azimuth angles with respect to the rows.

At 10.6 GHz, although there were very little data
available at high soil moistures, Figures VII-38 and
VII-39 indicate that there is a usable soil moisture sen-
sitivity in measurements made both parallel and per-
pendicular to the row direction. Burke and Paris [32]
demonstrated the potential of measuring the surface soil
moisture of row tilled fields at 10.6 GHz (Figure VII-60).
Although no ground samples were obtained from fields 313
and 296, irrigation had been partially completed on these
fields. In Figure VII-60 the measurements from fields
313 and 296 fall in higher moisture partitions indicating
that the 10.6 GHz measurements are sensitive to soil
moisture. The significance of Figure VII-60 lies in the
fact that the antenna temperature measurements were made
at a range of azimuth angles and not just parallel or
perpindicular to the rows.

Burke and Paris [32] used a smooth surface model to
generate Figure VII-60. Because of this they concluded
that the surface roughness effectively changed the look
direction from 50° to approximately 30°. This conclusion
was based on the fact that the difference in the vertical
and horizontal measurements was smaller than the smooth
surface model predicted (Figure VII-61). However, it was
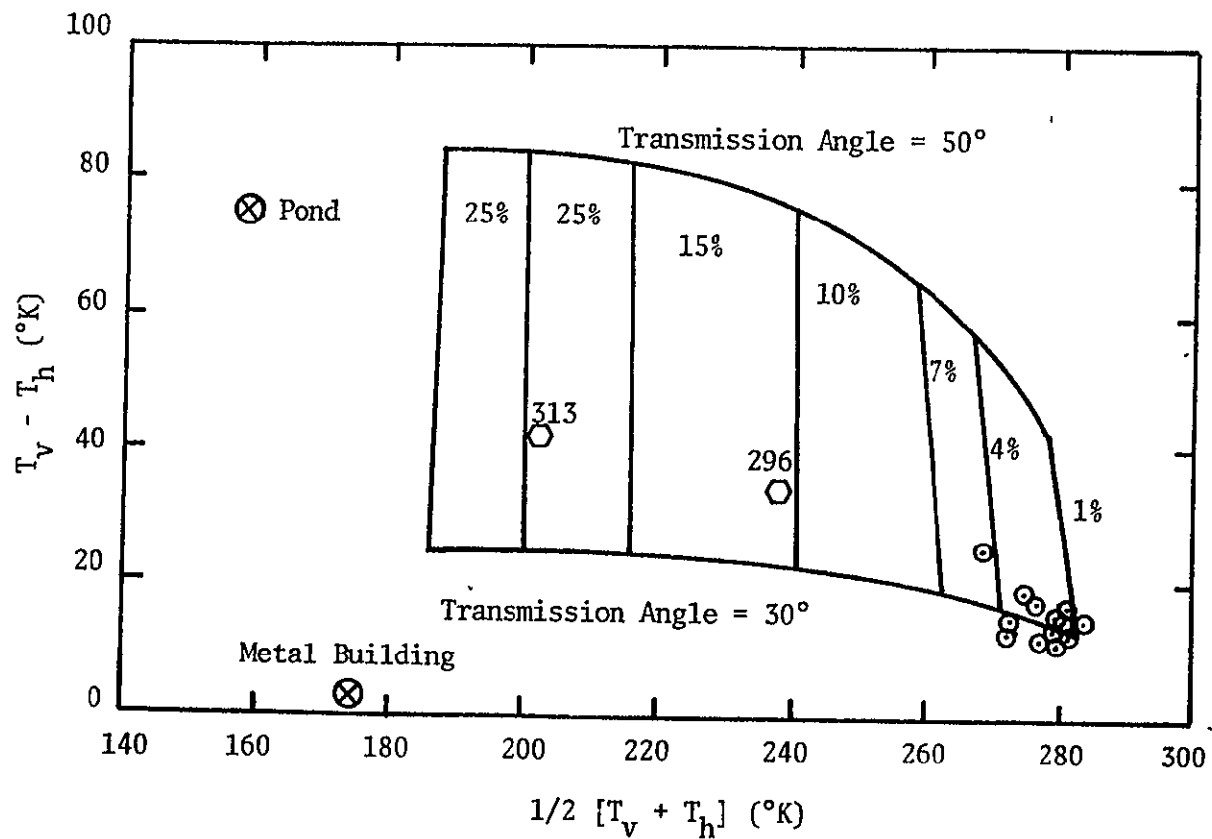
Figure VII-60. The difference between predicted brightness temperatures at vertical and horizontal polarization as a function of their average for transmission angles of 30° and 50°. The straight lines are lines of constant moisture in the top layer (after Burke and Paris [32]).
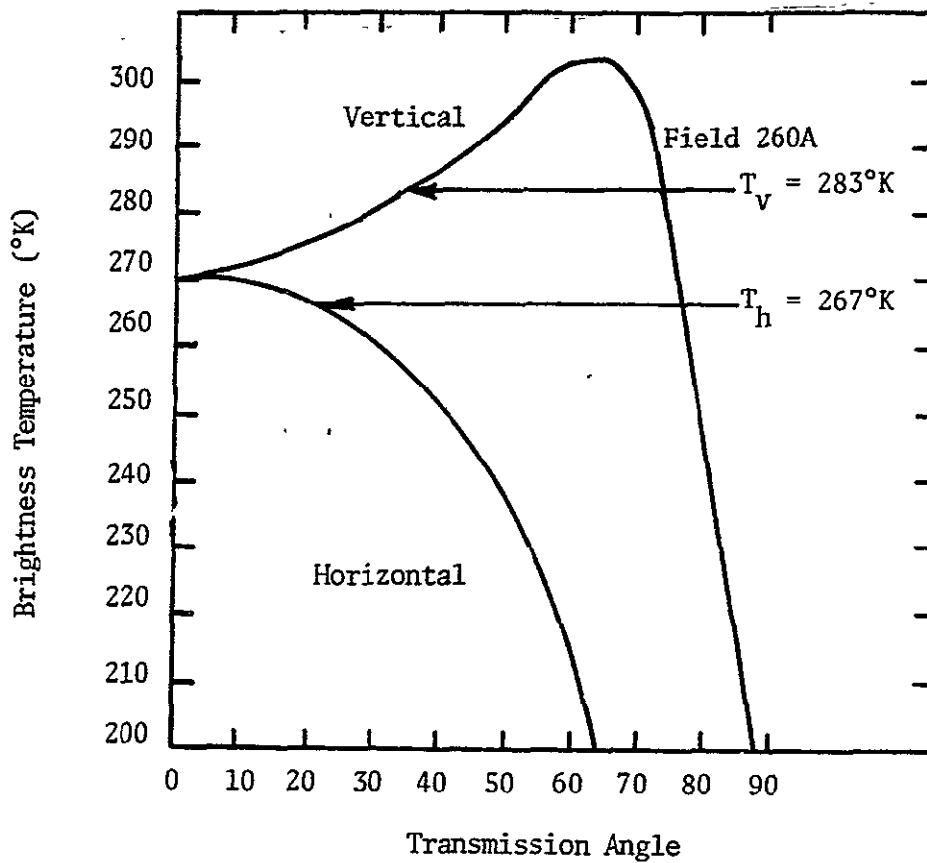
Figure VII-61.   Brightness temperature predictions for field 260A. Arrows mark the vertical and horizontal 10.6 GHz antenna temperature measurements (after Burke and Paris [32]).

demonstrated in this report that the small scale surface roughness superimposed on top of the row structure is responsible for the reduction in the difference between the vertical and horizontal antenna temperatures. Since the moisture partitions in Figure VII-60 are based on a smooth surface model and since it was shown earlier that surface roughness decreases the moisture response, then the moisture partitions drawn by Burke and Paris in Figure VII-60 are probably incorrect. They would tend to indicate a better moisture sensitivity than is actually observable.

Effect of Vegetation

Figures VII-40 through 42 demonstrate that a uniform cover of vegetation 125 cm tall has a minimal effect on the sensitivity of 1.4 GHz antenna temperature measurements to soil moisture. However, at 10.6 GHz such a vegetation cover completely masks the soil moisture dependence.

Figure VII-48 demonstrates that when viewing row planted vegetation 61 cm tall parallel to the rows at 1.4 GHz, the soil moisture dependence is unchanged from the bare soil situation. However, there is evidence that the same vegetation reduces the soil moisture dependence when the measurements are made perpendicular to the rows. Figures VII-46 and VII-47 show that the soil moisture sensitivity is greatly reduced at 10.6 GHz for measurements made both parallel and perpendicular to the rows.

It can be concluded that 1.4 GHz can be used to measure soil moisture through uniform vegetation up to 125 cm tall with approximately the same estimation accuracy that was demonstrated for the bare soil condition. No conclusions can be drawn about the amount of vegetation 10.6 GHz measurements can effectively "penetrate" except that it will be considerably less than the vegetation densities that were reported in this document.

CHAPTER VIII

CONCLUSION

Summary of Results

The work documented in this report consisted of a theoretical development of the physical phenomenon of thermal microwave emission from moist soil, and an experimental investigation to verify the phenomenon. The theoretical development was undertaken to provide a better understanding of: 1) the interaction of water with soil and its affect on soil permittivity, 2) the interaction of electromagnetic energy emitted from the soil volume with the surface boundary, and 3) the relationship between the thermal microwave energy emitted from the soil surface and the soil moisture. The purpose of the experimental investigation was to verify the theoretical predictions and to demonstrate the feasibility of estimating soil moisture remotely using passive microwave sensors.

The experimental measurements were utilized to demonstrate a procedure for estimating soil moisture using a passive microwave sensor. An understanding of the physical phenomenon of thermal microwave emission was provided by the theoretical development, and aided in the analysis of the microwave radiometer measurements. It was shown that the average moisture within a surface layer

can be estimated remotely. The depth to which the average
moisture corresponds can also be predicted. The depth of
measurement and the accuracy of the soil moisture prediction
is a function of the frequency of the emitted radiation.
The experimental measurements show that average moisture
can be measured to depths up to 20 cm at 1.4 GHz for rela-
tively dry soil, but that at 10.6 GHz only moisture in the
0-2 cm surface layer can be estimated regardless of soil
moisture.

The experimental investigation showed that 1.4 GHz
and 10.6 GHz can be used to estimate the average soil
moisture within two depths; however, it appears that a
frequency less than 10.6 GHz would be preferable for the
surface measurement. Average soil moisture within two
depths would provide information on the slope of the soil
moisture gradient near the surface. This information is of
considerable importance since it indicates the occurrence
of a recent water input event. Such information is vital
to soil water budget models used to predict the soil mois-
ture profile to depth. The ability to estimate average
moisture at different depths indicates that a multifrequen-
cy system could be used to estimate the near surface soil
moisture profile. For instance, measurements of 500 MHz
would provide average soil moisture estimates for a layer
from the surface to below 20 cm, and 5 GHz should provide
average soil moisture in a layer between 2 cm and 20 cm.

The theoretical development and the experimental measurements demonstrated that a uniform surface roughness similar to flat tilled fields reduces the sensitivity of the microwave emission to soil moisture changes. However, a technique of estimating surface roughness and soil moisture simultaneously was illustrated. Assuming that the surface roughness is known, the approximate soil moisture estimation accuracy at 1.4 GHz calculated for a 25% average soil moisture and a 80% degree of confidence, is +3% and -6% for a smooth bare surface, +4% and -5% for a medium rough surface, and +5.5% and -6% for a rough surface. At 10.6 GHz it was estimated that the surface soil moisture could be measured to within ± 10% for smooth and medium rough surfaces, and to within ± 6% for a rough surface. These approximate soil moisture estimation accuracies are considered to be conservative estimates since no error was assumed in the "ground truth" measurements.

The effect of row tillage on the ability to estimate soil moisture was also investigated experimentally. This investigation demonstrated that microwave emission measurements made parallel to the row direction have approximately the same response to soil moisture as would measurements made of a flat tilled field that had a surface roughness comparable to the small scale roughness superimposed on the

periodic row structure. Measurements made perpendicular to the row structure demonstrated that the moisture sensitivity is reduced. However, there were not enough experimental measurements to determine conclusively the degree of this reduction.

Measurements of vegetation canopies showed that the response to soil moisture at 1.4 GHz was not affected by uniformly planted sorghum 125 cm tall. An affect was evident on measurements of 188 cm tall sorghum, but a definite soil moisture response was still discernible. Row planted cotton 61 cm tall had no effecc on 1.4 GHz measurements made parallel to the rows. All of the vegetation canopies used during the experimental investigation greatly reduced the soil moisture sensitivity of the 10.6 GHz measurements. No conclusive statements can be made concerning the amount of vegetation 10.6 GHz radiation can effectively penetrate.

The theme of the analysis of the experimental measurements was to determine the ability to estimate soil moisture remotely. However, this was done simply because the necessary information was not available to convert the ground measurements of soil moisture to soil water matric potential. The investigation of the soil water interaction and its effect on soil permittivity showed that soil permittivity is dependent on soil water matric potential

and that soil water matric potential is independent of
soil texture. As a result, microwave sensors can be used
to estimate soil water matric potential and, in fact,
these estimates will be independent of soil texture.
This point is extremely significant since it is soil
matric potential that is the desired parameter in agri-
cultural or hydrological applications requiring soil water
information.

Recommendations

There are three recommendations that are considered
to be most important in terms of initiating activities
that will ultimately lead to the implementation of remote
microwave soil moisture estimation systems for agricultural
or hydrological applications. These recommendations call
for:

1. The development of a water budget model that uses
as its primary input the remote estimates of average soil
moisture for at least two depths. The purpose of such a
model would be to extend the near surface measurements of
soil moisture that are obtainable with passive microwave
sensors, to depths that are of concern to agriculturalists
and hydrologists. The primary input to this model should
be only remotely sensed information. No other soil mois-
ture information should be used; however, other parameters

that are readily available from geologic maps etc. could be incorporated. It is only through such a model that the ability to remotely sense soil moisture using micro-wave sensors can be utilized to its full advantage for applications that will exist in the foreseeable future.

2. A study to identify applications that could benefit by remote measurements of soil water parameters, and the accuracy, depth of measurement, and resolution requirements of these applications.

3. An evaluation of optimum sensor parameters and the engineering considerations involved in implementing such parameters to obtain the required accuracy and repeatability of soil moisture estimates. A study of the optimum sensor parameters should include an investigation of frequencies other than 1.4 GHz and 10.6 GHz to deter-mine other depths for which soil moisture can be measured. Such a study would also provide information to determine if surface moisture can be measured more accurately than at 10.6 GHz using a slightly lower frequency, perhaps 5 GHz, as a result of the decrease in the surface rough-ness effects. To decrease the complexity of implementing a system for estimating soil moisture, an estimation algorithm should be investigated using measurements at only one transmission angle (probably 35°) rather than from two as was done in the illustration of Chapter VII.

The primary engineering considerations that will have to be addressed in order to implement a usable system will be related to the antenna. This is primarily a result of the low frequency and relatively high resolution requirements that will most likely be specified for particular applications. The effect of beamwidth averaging and polarization mixing should be investigated further, especially for row tilled surfaces.

In addition to the recommendations made above, there are several investigations that should be initiated in order to provide a better understanding of the physical process of thermal microwave emission from soil and vegetation, and its interrelationship with soil moisture.

1. The model development presented in Appendix A should be pursued and the discrepancies indicated in that development resolved. The basic formulation and approach appear to be promising although the equations derived did not provide adequate results. It is believed that such a formulation will provide additional insight into the physical phenomenon of microwave emission from uniformly rough surfaces.

2. A model should be developed for the emission from a composite rough surface so that the effects of row direction on the soil moisture sensitivity of microwave emission can be better understood. Additional experimental

measurements should also be obtained to better demonstrate the effects and to validate the model.

3. A more rigorous vegetation model than was presented in Chapter IV should be developed. Specifically, this model should include effects of scattering in the vegetation canopy to determine the importance of this effect.

4. Additional vegetation measurements should be made to determine the effects of vegetation at 10.6 GHz and a frequency between 10.6 GHz and 1.4 GHz. No conclusions have yet been drawn concerning the amount of vegetation through which soil moisture estimates can be made at these frequencies.

REFERENCES

[1] Baver, L. D., W. H. Gardner, and W. R. Gardner, Soil Physics, John Wiley and Sons, Inc., New York, 1972.

[2] Kezdi, Arpad, Handbook of Soil Physics, Vol. I, Elsevier Scientific Publishing Company, New York, 1974.

[3] Spangler, M. G., Soil Engineering, International Textbook Company, 1963.

[4] Atterberg, A., "Die Mechanische Bodenanalyse und die Klassification der Mineralböden Schwedens," Intern Mitt. Bodenk, Vol. 2, 1912, pp. 312-342.

[5] Black, C. A. (editor in chief), Methods of Soil Analysis-Part 1, American Society of Agronomy, Inc., Madison, Wisconsin, 1965, p. 86.

[6] Kezdi, A., op. cit., pp. 47-48.

[7] Algee, B. B., J. C. Callaghan and A. E. Creelman, "Rapid Determination of Moisture Content in Soil Samples Using High Power Microwaves," IEEE Transactions On Geoscience Electronics, Vol. GE-7, No. 1, January 1969, pp. 41-43.

[8] Baver, L. D., W. H. Gardner, and W. R. Gardner, op. cit., p. 290.

[9] Miller, R. J., R. B. Smith and J. W. Biggar, "Soil Water Content: Microwave Oven Method," Soil Science Society of America Proceedings, Vol. 38, No. 3, May-June 1974, pp. 535-537.

[10] Taylor, S. A. and G. L. Ashcroft, Physical Edaphology, W. H. Freeman and Company, San Francisco, 1972.

[11] Baver, L. D., W. H. Gardner and W. R. Gardner, op. cit., pp. 381-383.

[12] Baver, L. D., W. H. Gardner and W. R. Gardner, op. cit., p. 400.

[13] Newton, R. W., and W. R. McClellan, "Permittivity Measurements of Soils at L-band," Technical Report RSC-58, Remote Sensing Center, Texas A&M University, College Station, Texas, June 1975.

[14] Cihlar, J. and F. T. Ulaby, "Dielectric Properties
      of Soils as a Function of Moisture Content," RSC
      Technical Report 177-97, Remote Sensing Laboratory,
      The University of Kansas Center for Research, Inc.,
      Lawrence, Kansas, November 1974.

[15] Wiebe, M. L., "Various Techniques of Dielectric
      Constant Measurements as Applied to the Relative
      Dielectric Constant of Sand as a Function of
      Moisture Content," Technical Memorandum RSC-22,
      Remote Sensing Center, Texas A&M University, College
      Station, Texas, May 1971.

[16] Lundien, J. R., "Terrain Analysis by Electromagnetic
      Means," Technical Report No. 3-693, Report 5, U.S.
      Army Engineer Waterways Experiment Station, Vicksburg,
      Mississippi, 1971.

[17] Idso, S. B., et al., "The Utility of Surface Tempera-
      ture Measurements for the Remote Sensing of Surface
      Soil Water Status," Journal of Geophysical Research,
      Vol. 80, No. 21, July 20, 1975, pp. 3044-3049.

[18] Hoekstra, P. and A. Delany, "Dielectric Properties of
      Soils at UHF and Microwave Frequencies," Journal of
      Geophysical Research, Volume 79, Number 11, April
      10, 1974.

[19] Haggis, G. H., J. B. Hasted, and T. J. Buchanan,
      "Dielectric Behavior of Water in Solutions," Journal
      of Chemical Physics, Volume 20, Number 9, September
      1952.

[20] Grant. E. H., T. J. Buchanan, and H. F. Cook,
      "Dielectric Behavior of Water at Microwave Frequen-
      cies," Journal of Chemical Physics, Volume 26,
      Number 1, January 1957.

[21] Lane, J. A. and J. A. Saxton, "Dielectric Dispersion
      in Pure Polar Liquids at Very High Radio Frequencies,
      (Part I)," Proc. Roy. Soc., Volume A, Number 213, 1952.

[22] Cole, K. S. and R. H. Cole, "Dispersion and Adsorption
      in Dielectrics; I. Alternating Current Characteris-
      tics," Journal of Chemical Physics, Volume 9, Number
      341, 1971.

[23] Geiger, F. E., and D. Williams, "Dielectric Constants
      of Soils at Microwave Frequencies," Goddard Space
      Flight Center, Greenbelt, Maryland, 1972.

[24] Hipp, J. E., "Soil Electromagnetic Parameters as a Function of Frequency, Soil Density, and Soil Moisture," *Proceedings of the IEEE*, Vol. 62, No. 1, 1974, pp. 98-103.

[25] Wiebe, M. L. "Laboratory Measurement of the Complex Dielectric Constant of Soils," Technical Report RSC-23, Remote Sensing Center, Texas A&M University, College Station, Texas, June 1971.

[26] Babai, P., "Measurement of Complex Dielectric Constant of Soil Types in X-band," Technical Memorandum RSC-95, Remote Sensing Center, Texas A&M University, College Station, Texas, June 1974.

[27] Poe, G. A., A. Stogryn, and A. T. Edgerton, "Determination of Soil Moisture Content Using Microwave Radiometry," Final Technical Report 1684-1, Aerojet General Corporation, El Monte, California, 1971.

[28] Carver, K. R., (Personal Communication).

[29] Peake, W. H., "Interaction of Electromagnetic Waves With Some Natural Surfaces," *IRE Transactions on Antennas and Propagation*, Vol. AP-7, December 1959, pp. 5324-5329.

[30] Stogryn, A., "The Brightness Temperature of a Vertically Structured Medium," *Radio Science*, Vol. 5, No. 12, December 1970, pp. 1397-1406.

[31] Tsang, L., E. Njoku, and J. A. Kong, "Microwave Thermal Emission From a Stratified Medium with Nonuniform Temperature Distribution," *Journal of Applied Physics*, Vol. 46, No. 2, December 1975, pp. 5127-5133.

[32] Burke, W. J. and J. F. Paris, "A Radiative Transfer Model for Microwave Emission from Bare Agricultural Soils," NASA Technical Memorandum TM X-58166, National Aeronautics and Space Administration, Lyndon B. Johnson Space Center, Houston, Texas, August 1975.

[33] Chen, S. N. L. and W. H. Peake, "Apparent Temperatures of Smooth and Rough Terrain," *IRE Transactions On Antennas and Propagation*, Vol. AP-9, December 1961, pp. 567-572.

[34] Richerson, J. A., "An Experimental Evaluation of A Theoretical Model of the Microwave Emission of a Natural Surface," Technical Report RSC-27, Remote Sensing Center, Texas A&M University, College Station, Texas, August 1971.

[35] Casey, K. F., "Application of Hill's Functions to Problems of Propagation in Stratified Media," IEEE Transactions on Antennas and Propagation, Vol. AP-20 No. 3, May 1972, pp. 368-374.

[36] Whittaker, E. T. and G. N. Watson, A Course of Modern Analysis, Cambridge University Press, New York, 1963, pp. 413-417.

[37] Landau, L., and E. Lifshitz, Electrodynamics of Continuous Media, Pergamon Press, London, 1960.

[38] Bekefi, G., Radiation Processes in Plasmas, John Wiley, New York, 1966.

[39] Tyrus, G., Radiation and Propagation of Electromagnetic Waves, Academic Press, New York, 1969.

[40] Paris, J. F., "Transfer of Thermal Microwaves in the Atmosphere," Ph.D. Dissertation, Department of Meterology, Texas A&M University, College Station, Texas, May 1971.

[41] Stogryn, A., "Electromagnetic Scattering by Random Dielectric Constant Fluctuations in a Bounded Medium," Radio Science, Vol. 9, No. 5, May 1974, pp. 509-518.

[42] Wilhelmi, G. J., J. W. Rouse, Jr., and A. J. Blanchard, "Depolarization of Light Backscattered from Rough Surfaces," Journal of the Optical Society of America, Vol. 65, No. 9, September 1975, pp. 1036-1042.

[43] England, A. W., "Thermal Microwave Emission From a Halfspace Containing Scatterers," Radio Science, Vol. 9, No. 4, April 1974, pp. 447-454.

[44] Stogryn, A., "The Apparent Temperature of the Sea at Microwave Frequencies," IEEE Transactions on Antennas and Propagation, Vol. AP-15, pp. 278-286, March 1967.

[45] Johnson, L. F., "On the Performance of Infrared Sensors in Earth Observations," Technical Report RSC-37, Remote Sensing Center, Texas A&M University, College Station, Texas, August 1972.

[46] Tyras, G., op. cit., p. 88.

[47] Beckmann, P., "Modeling of Rough Surfaces," AGARD,
      20th EWPP Meeting on Electromagnetic Wave Propagation
      Involving Irregular Surfaces and Inhomogeneous Media,
      The Hague, Netherlands, March 25-29, 1974.

[48] Kodis, R., "A Note On the Theory of Scattering From an
      Irregular Surface," IEEE Transactions on Antennas and
      Propagation, Vol. AP-14, No. 1, January 1966, pp.
      77-82.

[49] Barrick, D. E., "Rough Surface Scattering Based on
      the Specular Point Theory," IEEE Transactions on
      Antennas and Propagation, Vol. AP-16, No. 4, July
      1968, pp. 449-454.

[50] Fung, A. K., R. M. Axline, and H. L. Chan, "Exact
      Scattering From a Known Randomly Rough Surface,"
      Proceedings of the URSI, Commission II Microwave
      Scattering and Emission from the Earth, Berne,
      Switzerland, September 23-26, 1974.

[51] Spetner, L. and I. Katz, "Two Statistical Models
      for Radar Terrain Return," IRE Transactions on
      Antennas and Propagation, Vol. 8, May 1960, pp.
      242-246.

[52] Waite, W. P., "Broad-Spectrum Electromagnetic Back-
      scatter," CRES Technical Report 133-17, University
      of Kansas Center for Research, Inc., Lawrence,
      August 1970.

[53] Katzin, M., "On the Mechanisms of Radar Sea Clutter,"
      Proceedings of the IRE, Vol. 44, January 1957,
      pp. 44-54.

[54] Khamsi, H. R., A. K. Fung and F. T. Ulaby, "Rough
      Surface Scattering Based on Facet Model," RSL
      Technical Report 177-52, The University of Kansas
      Center for Research, Inc., Lawrence, Kansas,
      November 1974.

[55] Fung, A. K., "Scattering Theories and Radar Return,"
      CRES Report No. 48-3, University of Kansas Center
      for Research, Inc., 1966.

[56] Beckmann, P. and A. Spizzichino, The Scattering of
      Electromagnetic Waves From Rough Surfaces, The
      MacMillan Company, New York, 1963, p. 20.

[57] Brekkovskikh, L. M., "The Diffraction of Waves by a Rough Surface," Part I and Part II, Zh. Eksper. i Teur. Fiz., Vol. 23, 1952, pp. 275-304

[58] Beckmann, P. and A. Spizzichino, op. cit., p. 66.

[59] Fung, A. K., "On Depolarization of Electromagnetic Waves Backscattered From a Rough Surface," Planetary Space Sciences, Vol. 14, 1966, pp. 563-568.

[60] Stogryn, A., "Electromagnetic Scattering From Rough, Finitely Conducting Surfaces," Radio Science, Vol. 2 (New Series), No. 4, April 1967, pp. 415-428.

[61] Leader, J. C., "Bidirectional Scattering of Electromagnetic Waves From Rough Surfaces," Presented at the Spring meeting of the USNC/URSI of the IEEE, Washington, D.C., April 16, 1970.

[62] Rice, S. O., "Reflection of Electromagnetic Waves From Slightly Rough Surfaces," Communications of Pure and Applied Mathematics, Vol. 4, 1951, pp. 351-378.

[63] Lord Rayleigh, Theory of Sound, Vol. II, MacMillan Company, London, England, 1929, pp. 89-96.

[64] Valenzuela, G. R., "Depolarization of EM Waves By Slightly Rough Surfaces," IEEE Transactions on Antennas and Propagation, Vol. AP-15, No. 4, July 1967, pp. 552-557.

[65] Beckmann P., "Scattering by Composite Rough Surfaces," Proceedings of the IEEE, Vol. 53, August 1965, pp. 1012-1015.

[66] Wright, J. W., "A New Model for Sea Clutter," IEEE Transactions on Antennas and Propagation, Vol. AP-16, No. 2, March 1968, pp. 217-223.

[67] Chan, H. L. and A. K. Fung, "Backscattering From a Two-Scale Rough Surface with Application to Radar Sea Return," NASA Contract Report CR-2327, NASA Langley Research Center, November 1973.

[68] Wu, S. T. and A. K. Fung, "A Noncoherent Model for Microwave Emissions and Backscattering from the Sea Surface," Journal of Geophysical Research, Vol. 77, No. 30, October 20, 1972.

[69]   Rosenbaum, S. and L. W. Bowles, "Clutter Return
         From Vegetated Areas," IEEE Transactions on Antennas
         and Propagation, Vol. AP-22, No. 2, March 1974,
         pp. 227-236.

[70]   Sachs, D. L. and P. L. Wyatt, "A Conducting-Slab
         Model for Electromagnetic Propagation Within a
         Jungle Medium," Radio Science, Vol. 3 (New Series),
         No. 2, February 1968, pp. 125-134.

[71]   Tamir, T., "On Radio-Wave Propagation in Forest
         Environments," IEEE Transactions on Antennas and
         Propagation, Vol. AP-15, No. 6, November 1967,
         pp. 806-817.

[72]   Du, Li-Jen, "Scattering and Absorption by Large
         Leaves at Microwave Frequencies," Technical Report
         2440-6, Electro Science Laboratory, Ohio State
         University, Columbus, Ohio, January 1969.

[73]   Peake, W. H., "Theory of Radar Return from Terrain,"
         IRE International Convention Record, Vol. 7, Part 1:
         27, 1959.

[74]   Waite, W. P. and K. R. Cook, "Broad Spectrum Micro-
         wave Systems for Remotely Measuring Ecological
         Parameters," Final Report Project NSF 31515, Depart-
         ment of Electrical Engineering, University of
         Arkansas, Fayetteville, Arkansas, December 1974.

[75]   Sibley, R., "Microwave Emission and Scattering from
         Vegetated Terrain," Technical Report RSC-44, Remote
         Sensing Center, Texas A&M University, College Station,
         Texas, August 1973.

[76]   Evans, S., "Dielectric Properties of Ice and Snow,"
         Journal of Glaciology, Vol. 5, No. 42, October 1965,
         pp. 773-792.

[77]   Peake, W. H., and T. L. Oliver, "The Response of
         Terrestrial Surfaces at Microwave Frequencies,"
         Technical Report AFAL-TR-70-301, Electro Science
         Laboratory, Ohio State University, Columbus, Ohio,
         May 1971.

[78]   Basharinov, A. Ye, and A. M. Shutko, "Simulation
         Studies of SHF Radiation Characteristics of Soils
         Under Moist Conditions," Academy of Sciences USSR,
         Institute of Radio Engineering and Electronics
         (unpublished report), NASA Technical Translation,
         NASA TT F-16, 489, August 1975.

[79] Ulaby, F. T., J. Cihlar and R. K. Moore, "Active Microwave Measurements of Soil Water Content," Remote Sensing of Environment, Vol. 3, 1974, pp. 185-203.

[80] Ulaby, F. T. and P. P. Batlivala, "Optimum Parameters For Mapping Soil Moisture," IEEE Transactions on Geoscience Electronics, Vol. GE-14, No. 2, April 1976, pp. 81-93.

[81] Ulaby, F. T., "Radar Response to Vegetation," IEEE Transactions on Antennas and Propagation, Vol. AP-23, No. 1, January 1975.

[82] Ulaby, F. T. and P. P. Batlivala, "Diurnal Variations of Radar Backscatter From a Vegetation Canopy," IEEE Transactions on Antennas and Propagation, Vol. AP-24, No. 1, January 1976.

[83] Jean, B. R., "Selected Applications of Microwave Radiometer Techniques," Technical Report RSC-30, Remote Sensing Center, Texas A&M University, College Station, Texas, August 1971.

[84] Kroll, C. L., "Remote Monitoring of Soil Moisture Using Airborne Microwave Radiometers," Technical Report RSC-43, Remote Sensing Center, Texas A&M University, College Station, Texas, June 1973.

[85] Schmugge, T., T. Wilheit, W. Webster and P. Gloersen, "Remote Sensing of Soil Moisture with Microwave-Radiometers-II," Technical Note G-76114, Goddard Space Flight Center, Greenbelt, Maryland, June 1976.

[86] Schmugge, T., et al., "Results of Soil Moisture Flights During April 1974," NASA Technical Note TN D-8199, NASA Goddard Space Flight Center, Greenbelt, Maryland, May 1976.

[87] Jackson, R. D., "Diurnal Changes in Soil Water Content During Drying," Field Soil Water Regime, Soil Society of America, Madison, Wisconsin, 1973, pp. 37-51.

[88] Jean, B. R., J. A. Richerson and J. W. Rouse, Jr., "Experimental Microwave Measurements of Controlled Surfaces," Seventh International Symposium on Remote Sensing of Environment, University of Michigan, Ann Arbor, Michigan, May 17-21, 1971.

[89]   Blinn, J. C. and J. G. Quade, " Microwave Properties
        of Geologic Materials: Studies of Penetration
        Depth and Moisture Effects," 4th Annual Earth Re-
        sources Program Review, NASA Manned Spacecraft Center,
        Houston, Texas, January 17-21, 1972, pp. 53-1 to 53-12.

[90]   Blinn, J. C., J. E. Conel and J. G. Quade, "Micro-
        wave Emission From Geologic Materials: Observations
        of Interference Effects," Journal of Geophysical
        Research, Vol. 77, No. 23, August 10, 1972, pp.
        4366-4378.

[91]   Lee, S. L., "Dual Frequency Microwave Radiometer
      - Measurements of Soil Moisture for Bare and Vegetated
        Rough Surfaces, Technical Report RSC-56, Remote
        Sensing Center, Texas A&M University, August 1974.

[92]   Newton, R. W. et al., "On the Feasibility of Remote
        Monitoring of Soil Moisture with Microwave Sensors,"
        Ninth International Symposium on Remote Sensing of
        Environment, University of Michigan, Ann Arbor,
        Michigan, April 15-19, 1974.

[93]   Poe, G., A. Stogryn and A. T. Edgerton, "Determina-
        tion of Soil Moisture Content Using Microwave Radiom-
        etry," Summary Report 1684R-2, Aerojet General
        Corporation, El Monte, California, June 1971.

[94]   Riegler, R. L., "Radar and Microwave Radiometric
        Techniques for Geoscience Experiments," Report
        1903-2, The Ohio State University Research Foundation,
        Columbus, Ohio, June 1966.

[95]   Chandrasekhar, S., Radiative Transfer, Dover
        Publications, Inc., New York, 1960.

[96]   Goody, R. M., Atmospheric Radiation; I. Theoretical
        Basis, Clarendon Press, Oxford, 1964.

[97]   Stratton, J. A., Electromagnetic Theory, McGraw-
        Hill Book Company, Inc., New York, 1941.

[98]   Ramo, S., J. R. Whinnery, and T. V. Van Duzer,
        Fields and Waves in Communication Electronics, John
        Wiley and Sons, Inc., 1965.

[99]   Silver, S., Microwave Antenna Theory and Design,
        MIT Radiation Laboratory Series, Vol. 12, McGraw-
        Hill, New York, 1947.

[100] Hasted, J. B., "The Dielectric Properties of Water," _Progress in Dielectrics_, Vol. 3, John Wiley and Sons, Inc., New York, 1961, pp. 101-149.

[101] Cole, R. H., "Theories of Dielectric Polarization and Relaxation," _Progress in Dielectrics_, Vol. 3, John Wiley and Sons, Inc., New York, 1961, pp. 47-99.

[102] Hornbostel, D., "Hot and Cold Body Reference Noise Generators From 0 to 40 GHz," (work supported under NASA/MSC contracts NAS 9-11275 and NAS 9-12045), AIL, a division of Cutler Hammer, Commack, New York, December 1972.

[103] Newton, R. W., "Passive Microwave Data Report: Joint Soil Moisture Experiment at Texas A&M University; June 26-July 21, 1974", Technical Report RSC-65, Remote Sensing Center, Texas A&M University, College Station, Texas, January 1975.

[104] Newton, R. W. and E. A. Tesch, "Joint Soil Moisture Experiment: Ground Based Measurements at Texas A&M University; July 13-July 25, 1975," Technical Report RSC-71, Remote Sensing Center, Texas A&M University, College Station, Texas, January 1976.

[105] Clark, B. V. and R. W. Newton, "Revision to Operating System Software for Microwave Signature Acquisition System," Technical Report RSC-75, Remote Sensing Center, Texas A&M University, College Station, Texas, July 1976.

[106] Batlivala, P. P. and J. Cihlar, "Joint Soil Moisture Experiment (Texas): Documentation of Radar Backscatter and Ground Truth Data," RSL Technical Report 264-1, Remote Sensing Laboratory, University of Kansas, Lawrence, Kansas, April 1975.

[107] Newton, R. W. and S. L. Lee, "Ground Data Report: Joint Soil Moisture Experiment at Texas A&M University; June 26-July 21, 1974," Technical Report RSC-61, Remote Sensing Center, Texas A&M University, College Station, Texas, October 1974.

[108] Paris, J. F., "Data Processing Equations for the Microwave Signature Acquisition System (MSAS)," LEC/ASD 640-TR, A.D. 63-0497-3435-07, Lockheed Electronics Company, Inc., Aerospace Systems Division, Houston, Texas, December 1974.

[109]   Love, T. J., Radiative Heat Transfer, Charles E.
        Merrill Publishing Company, Columbus, Ohio, 1968.

[110]   Jordan, E. C., and K. G. Balmain, Electromagnetic
        Waves and Radiating Systems, Printice-Hall Inc.,
        Englewood Cliffs, New Jersey, 1968.

[111]   Peake, W. H., R. L. Riegler and C. H. Schultz, "The
        Mutual Interpretation of Active and Passive Microwave
        Sensor Outputs," Proceedings of the Fourth Symposium
        on Remote Sensing of Environment, Willow Run
        Laboratories, the University of Michigan, Ann
        Arbor, Michigan, December 1966, pp. 771-777.

[112]   Claassen, J. P. and A. K. Fung, "The Recovery of
        Polarized Apparent Temperature Distributions of
        Flat Scenes From Antenna Temperature Measurements,"
        IEEE Transactions on Antennas and Propagation, Vol.
        AP-22, No. 3, May 1974, pp. 433-442.

[113]   Grody, N. C., "Antenna Temperature for a Scanning
        Microwave Radiometer," IEEE Transactions on Antennas
        and Propagation (communication), Vol. AP-23, No. 1,
        January 1975, pp. 141-144.

[114]   Paris, J. F., "MAODAP - Microwave Atmospheric and
        Oceanic Data Analysis Program," LEC/HASD Document
        No. 640-TR-078, Lockheed Electronics Company, Inc.,
        Houston Aerospace Systems Division, Houston, Texas,
        December 1971.

[115]   Batlivala, P. P, and F. T. Ulaby, "Effects of Rough-
        ness on the Radar Response to Soil Moisture of Bare
        Ground," RSL Technical Report 264-5, Remote Sensing
        Laboratory, University of Kansas, Lawrence, Kansas,
        September 1975.

[116]   Ostle, B., and R. W. Mensing, Statistics in Research,
        The Iowa State University Press, Ames, Iowa, 1975.

APPENDIX A

DIFFERENTIAL TRANSMISSION COEFFICIENTS

An attempt was made to develop an expression for differential transmission coefficients using the Kirchhoff approximation in conjunction with the Stratton-Chu integral as modified by Silver [99]. In utilizing this approach the following assumptions were made:

1) The incident wave is plane and linearly polarized.

2) Multiple interaction and irregularities such as shadowing and multiple scattering may be neglected.

3) The observation point is in the far zone.

4) The integral is applied over a finite portion of a closed surface.

5) The surface can be approximated at any point as an infinite plane.

6) Only energy in the plane of incidence is considered.

The expression for the far field reradiation electric field, E_s, at a point P (Figure A-1) with the time variation understood is given by [99]:
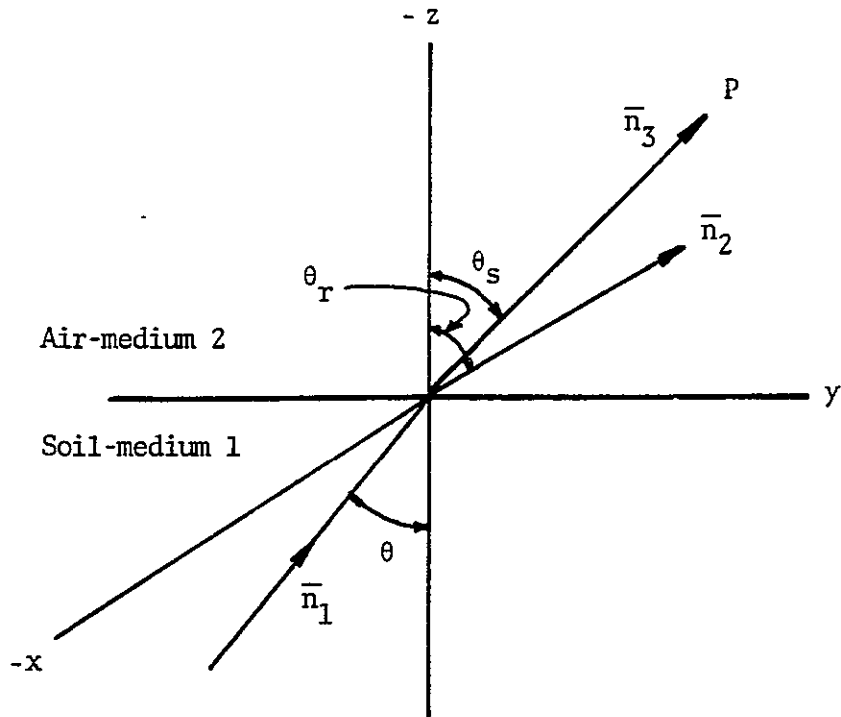
Figure A-1. Geometry used in describing the differential transmission coefficients.

$$E_s(P) = K \, \bar{m}_3 \times \iint\limits_{Area} \left[-\bar{m} \times E_s - \eta_1 \bar{m}_3 \times (-\bar{m} \times \bar{H}_s) \right] \cdot$$

(A-1)

$$\exp(j k_2 \bar{r} \cdot \bar{m}_3) dS$$

where

$$K = (-j k_2 \exp(-j k_2 R))(4\pi R)^{-1}$$

$\bar{r}$ - position vector from the origin of the coordinate system to the surface element dS

$\bar{n}_3$ - a unit vector in the direction of observation (to point P)

η_1 - intrinsic impedance of the soil

$\bar{n}$ - unit local surface normal

k_2 - wave number in air

R - distance from the origin to the point of observation (point P)

$\bar{E}_s$ - total transmitted electric field at the surface due to the radiation from the soil volume

$\bar{H}_s$ - total transmitted magnetic field at the surface due to the radiation from the soil volume

Propagation of the incident energy is along the vector $\bar{n}_1$. The transmitted energy is propagated along $\bar{n}_3$. The

unit vector $\bar{n}_2$ defines the smooth surface angle of refraction. Note that $-\bar{n} \times \bar{E}_s$ and $-\bar{n} \times \bar{H}_s$ are the currents on the surface that cause radiation into the upper hemisphere. These currents are due to the radiation impinging on the surface from the soil volume. Equation (A-1) therefore defines the electric field at point P due to the surface currents within the area of illumination that are a result of radiation from the soil volume.

Adapting the notation of Fung [55], two local ortho-normal coordinate systems are constructed, $\bar{n}_1$, $\bar{t}_1$ and $\bar{d}_1$ in the subsurface and $\bar{n}_2$, $\bar{t}_2$ and $\bar{d}_2$ above the surface.

$$\bar{t}_1 = (\bar{m}_1 \times \bar{m})(1 - \bar{m}_2 \cdot \bar{m})^{-\frac{1}{2}}$$

$$\bar{d}_1 = (\bar{m}_1 \times \bar{t}_1)$$

$$\bar{t}_2 = (\bar{m}_2 \times (-\bar{m}))(1 + \bar{m}_2 \cdot \bar{m})^{-\frac{1}{2}}$$

(A-2)

$$\bar{d}_2 = (\bar{m}_2 \times \bar{t}_2)$$

In order to determine the values of $(-\bar{n} \times \bar{E}_s)$ and $(-\bar{n} \times \bar{H}_s)$ at each point on the surface, the incident fields from the soil volume are resolved into local polarization components parallel and normal to the local plane of incidence, and multiplied by the corresponding transmission coefficient.

The incident electric and magnetic fields, with the time variations understood, can be defined as

$$\bar{E}_0 = \bar{a}_i \left[E_0 \exp(-j\,k_1\,\bar{m}_i \cdot \bar{r}) \right]$$

<div align="right">(A-3)</div>

$$\bar{H}_0 = (\bar{m}_i \times \bar{a}_i)\, E_0 / \eta_1$$

where

η_1 - intrinsic impedence of the soil

k_1 - wave number in the soil

Components of the transmitted fields normal to the plane of incidence (horizontal polarization) are given by:

$$E_s^h = \left[((\bar{a}_i \cdot \bar{t}_i)\,\bar{E}_0)\, t_h \right] \bar{t}_2$$

<div align="right">(A-4)</div>

$$H_s^h = \left[((\bar{a}_i \cdot \bar{t}_i)\, \bar{E}_0 / \eta_1\, t_h \right] \bar{d}_2$$

The components parallel to the plane of incidence (vertical polarization) are given by

$$\vec{E}_s^v = \left[((\vec{a}_1 \cdot \vec{d}_1) \, \vec{E}_0) \, t_v \right] \vec{d}_2$$

$$\tag{A-5}$$

$$\vec{H}_s^v = \left[(-(\vec{a}_1 \cdot \vec{d}_1) \, \vec{E}_0/\eta_1 \, t_v \right] \vec{t}_2$$

The local surface currents can now be expressed as

$$-\vec{m} \times \vec{E}_s = \left[t_h (\vec{a}_1 \cdot \vec{t}_1)(-\vec{m} \times \vec{t}_2) + t_v (\vec{a}_1 \cdot \vec{d}_1)(-\vec{m} \times \vec{d}_2) \right] E_0$$

$$-\vec{m} \times \vec{H}_s = \left[t_h (\vec{a}_1 \cdot \vec{t}_1)(-\vec{m} \times \vec{d}_2) + t_v (\vec{a}_1 \cdot \vec{d}_1)(-\vec{m} \times \vec{t}_2) \right] E_0/\eta_1$$

where

t_h - horizontal electric field transmission coefficient

t_v - vertical electric field transmission coefficient

The integral defining the electric field at point P and polarization i, (A-1), can now be written in the form

$$E_{s_x}(P) = K \iint \left[t_h(\bar{a}_1 \cdot \bar{t}_1) \bar{m}_3 \times (-\bar{m} \times \bar{t}_1) \right.$$

$$+ t_v(\bar{a}_1 \cdot \bar{d}_1) \bar{m}_3 \times (-\bar{m} \times \bar{d}_2) - \bar{m}_3 \times$$

$$\left[t_h(\bar{a}_1 \cdot \bar{t}_1) \bar{m}_3 \times (-\bar{m} \times \bar{d}_2) - t_v(\bar{a}_1 \cdot \bar{d}_1) \bar{m}_3 \times \right.$$ \hfill (A-6)

$$\left. \left. (-\bar{m} \times \bar{t}_2) \right] \right] E_0 \exp(j \bar{r} \cdot (k_2 \bar{m}_3 - k_1 \bar{m}_1) \, dS$$

where

$$\bar{n} = (-\bar{i} \, z_x - \bar{j} \, z_y + \bar{k})(z_x^2 + z_y^2 + 1)^{-1/2}$$

z_x - local surface slope in x direction

z_y - local surface slope in y direction

$\bar{n}_1 = \bar{j} \sin \theta_o - \bar{k} \cos \theta_o$

$\bar{n}_2 = \bar{a}_d \sin \theta_r - \bar{n} \cos \theta_r$

$\bar{a}_{d_2} = (-\bar{n} \times \bar{t}_2)$

$\bar{a}_1 = \bar{i}$, horizontal polarization

$\bar{a}_1 = \bar{j} \cos \theta_o + \bar{k} \sin \theta_o$; vertical polarization

Equation (A-6) is evaluated by converting the cross products to dot products using vector identities, then expanding the result in a Taylor series with respect to surface slopes z_x and z_y, and integrating. The expansion of (A-6) results in

$$E_{s_i}(P) = \bar{K} \bar{E_o} \iint [\bar{a_i} + \bar{z_y} a_{y_i}] \exp(j\bar{r}\cdot(k_2\bar{m_3} - k_1\bar{m_1})) \, dS \qquad \text{(A-7)}$$

For horizontal polarization

$$a_h = -\bar{\imath}\,(t_h \cos\theta_s + t_h \cos\theta_r)\Big|_{z_x=z_y=0}$$

$$a_{y_h} = -\bar{\imath}\,\Big(\cos\theta_s \frac{\partial t_h}{\partial z_y} + t_h + \cos\theta_r \frac{\partial t_h}{\partial z_y} \qquad \text{(A-8)}$$

$$+ t_h \frac{\sin^2\theta_r \cos\theta_o}{\sin\theta_o \cos\theta_r}\Big)\Big|_{z_x=z_y=0}$$

and for vertical polarization

$$a_v = \bar{\jmath}\,\big(-t_v + t_v \sin^2\theta_s - t_v \cos\theta_r \cos\theta_s\big)\Big|_{z_x=z_y=0}$$

$$+ \bar{k}\,\big(-t_v \sin\theta_s \cos\theta_r - t_v \cos\theta_s \sin\theta_s\big)\Big|_{z_x=z_y=0} \qquad \text{(A-9)}$$

$$a_{y_v} = \bar{j} \left(-t_v \frac{\cos \theta_s \cos \theta_o \sin^2 \theta_r}{\cos \theta_r \sin \theta_o} - t_v \cos \theta_s \sin \theta_s \right.$$

$$\left. + \frac{\partial t_v}{\partial z_y} \sin^2 \theta_s - \frac{\partial t_v}{\partial z_y} \cos \theta_s \cos \theta_r - \frac{\partial t_v}{\partial z_y} \right) \bigg|_{z_x = z_y = 0}$$

$$+ \bar{k} \left(\cos \theta_s \cos \theta_o \sin \theta_r - \cos \theta_s \cos \theta_r \right.$$

$$- t_v \frac{\sin \theta_s \sin^2 \theta_r \cos \theta_o}{\sin \theta_o \cos \theta_r} + t_v \cos \theta_s \cos \theta_o$$

$$\left. - t_v \cos \theta_s \cos \theta_r - \frac{\partial t_v}{\partial z_y} \sin \theta_s \cos \theta_r \right) \bigg|_{z_x = z_y = 0}$$

Note that there are no "edge effect" terms (i.e., there is no dependence on $\partial t_i / \partial z_x$). This is a result of the fact that the radiation incident on the surface from below is not depolarized by the surface. There are no terms involving t_v for horizontal polarization and no terms involving t_h for vertical polarization.

Leader [61] has evaluated the corresponding integral to (A-7) for the bistatic scattering case. An analogous integration of (A-7) results in

$$I_{s_{ii}} = \frac{\langle E_{s_i}(P) E_{s_i}^*(P) \rangle}{Real(\eta_{air})}$$

$$= \frac{2\pi A}{(4\pi R)^2} \left| E_{o_i}\left(a - \frac{m_y}{m_z} a_y\right) \right|^2 \frac{Q m_z^2}{\left(m_z^4 + m_y^2 Q\right)^{3/2}} \quad (A-10)$$

where

$$\bar{n}_y = \sin \theta_s - \sin \theta_r$$

$$\bar{n}_z = -\cos \theta_s + \frac{\beta_1}{\beta_2} \cos \theta_r$$

β_1 - phase constant in the soil

β_2 - phase constant in the air (1.0)

Q - parameter related to surface roughness

Again, the first subscript on I_s indicates the polarization of the incident radiation and the second indicates the polarization of the transmitted radiation.

Note that the surface roughness is defined by the parameter Q. Leader [61] relates Q to the autocorrelation of the surface. For the case under consideration,

$$Q = \left[k_1 \, C'(\tau_0) \, \sigma_z^2 \right]^{-2} \tag{A-11}$$

where

k_1 - wave number in the soil

$C'(\tau_0)$- derivative of the autocorrelation function of the surface evaluated at a point

τ_0 - point of expansion of $C(\tau)$ in the evaluation of the integral (A-7)

σ_z^2 - surface height variance

The point of expansion increases with angle θ_0. Since $C'(\tau)$ increases with τ, Q decreases with increasing angle θ_0 [61].

The differential transmission coefficients are defined by

$$\mathcal{T}_i(\theta_o, \phi_o; \theta_s \phi_s) = \mathcal{T}_i(o, s) = \frac{4\pi R^2 I_{s_{ii}}}{(I_{o_i} \cos \theta_o) A} + \frac{4\pi R^2 I_{s_{ji}}}{(I_{o_i} \cos \theta_o) A}$$

<div align="right">(A-12)</div>

$$= \mathcal{T}_{ii}(o, s) + \mathcal{T}_{ji}(o, s)$$

It was shown above that

$$I_{s_{ji}} = 0$$

so

$$\mathcal{T}_{ij}(o, s) = \mathcal{T}_{ji}(o, s) = 0$$

Noting that

$$I_{o_i} = \frac{|E_{o_i}|^2}{Real(m_i)}$$

then the differential scattering coefficient is

$$\tau_{\lambda}(0,s) = \tau_{\lambda\lambda}(0,s) = \frac{4\pi R^2}{\cos\theta_0 A} \frac{2\pi A}{(4\pi R)^2} \frac{Real(m_1)}{Real(m_2)} \cdot$$

$$\left| a - \frac{m_y}{m_z} a_y \right|^2 \frac{Q m_z^2}{(m_z^4 + Q m_y^2)^{3/2}}$$

(A-13)

$$\tau_{\lambda}(0,s) = \frac{1}{2\cos\theta\sqrt{\varepsilon_{r_1}'}} \left| a - \frac{m_y}{m_z} a_y \right|^2 \frac{Q m_z^2}{(m_z^4 + Q m_y^2)^{3/2}}$$

where

ε'_{r_1} - real part of the relative soil permittivity

Equation (A-10) is only a function of angle θ_0 in the plane of incidence, $\phi = 0°$. It was assumed at the beginning of the derivation that the contribution to the electric field at point P due to radiation incident on the surface outside the plane of incidence would be neglected. Equation (A-13) can therefore be written

$$\tau_{\lambda}(\theta_0,\theta_s) = \frac{1}{2\cos\theta_0\sqrt{\varepsilon_{r_1}'}} \left| a - \frac{m_y}{m_z} a_y \right|^2 \cdot$$

(A-14)

$$\frac{Q m_z^2}{(m_z^4 + Q m_y^2)^{3/2}} \delta(\phi_0 = 0°)$$

where $\delta(\phi_0 = 0°)$ is the direct delta function evaluated at $\phi_0 = 0°$. This allows (A-14) to be integrated over ϕ_0 to yield

$$BT_{SOIL_i}(\theta_s) = \frac{1}{4\pi} \int_{\theta_0} \tau_{ii}(\theta_0, \theta_s) \, BT_{Volume_i}(\theta_0) \, SIN \, \theta_0 \, d\theta_0 \qquad (A-15)$$

since $\tau_{ji}(\theta_0, \theta_s)$ is zero.

Although the derivation of (A-14) is based on sound physical principles, calculations based on (A-15) did not adequately match antenna measurements. Currently, it is uncertain as to whether or not the poor results were due to improper implementation of (A-14) and A-15), or an error in the derivation. The calculations demonstrated that the change in magnitude of the term

$$\frac{Q \, m_z^2}{\left(m_z^4 + Q \, m_y^2\right)^{3/2}}$$

with soil moisture was too large. It caused an unrealistic dependence of soil brightness temperature (as defined by (A-15)) on soil moisture.

APPENDIX B

CORRECTION OF DATA FOR SELF EMISSION

The Self Emission Contribution

Inspection of data acquired over Easterwood Pond (Figures B-1 and B-2) reveals anomalously high radiometric antenna temperatures for angles near nadir. This effect will be demonstrated to be a result of noise emission from the MSAS being reflected off of the water surface back into the MSAS receiving aperture. As expected this effect is also apparent in the bare soil measurements, but to a lesser degree because of the smaller soil permittivity. This effect is a function of the backscattering coefficient of the scene which depends on permittivity and surface roughness. As a result, the noise contribution to the measured antenna temperature resulting from self emission will vary with moisture content, surface roughness, and incident angle. The 1974 measurement set will be used below to demonstrate the magnitude of the self emission component.

The theoretical variation of the brightness temperature of a smooth surface as a function of transmission angle and polarization is given in Figure B-3. Note that the brightness temperature varies little between nadir and 20°. Also, the brightness temperature at nadir is
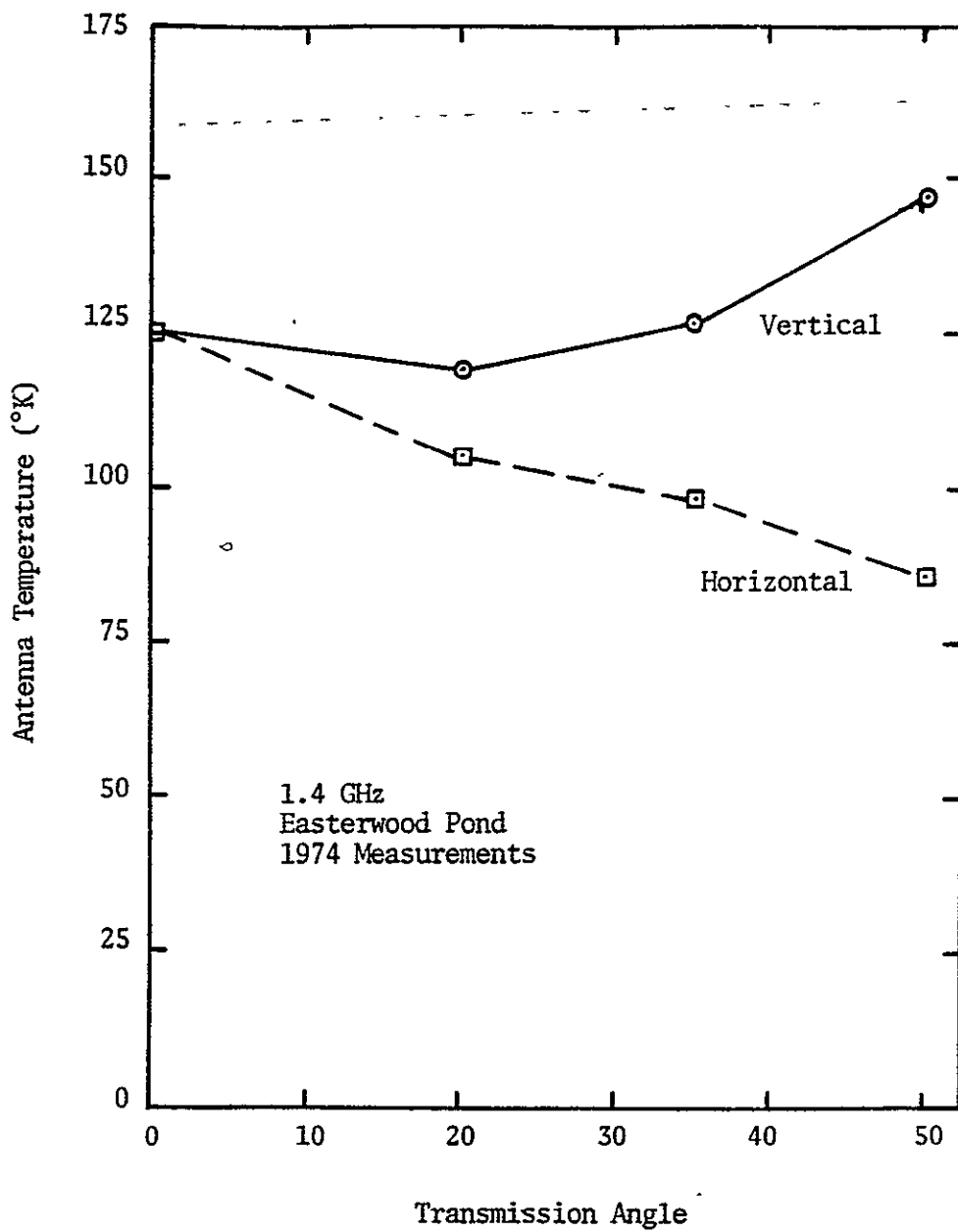
Figure B-1. 1.4 GHz fresh water measurements that demonstrate the effect of self emission near nadir.
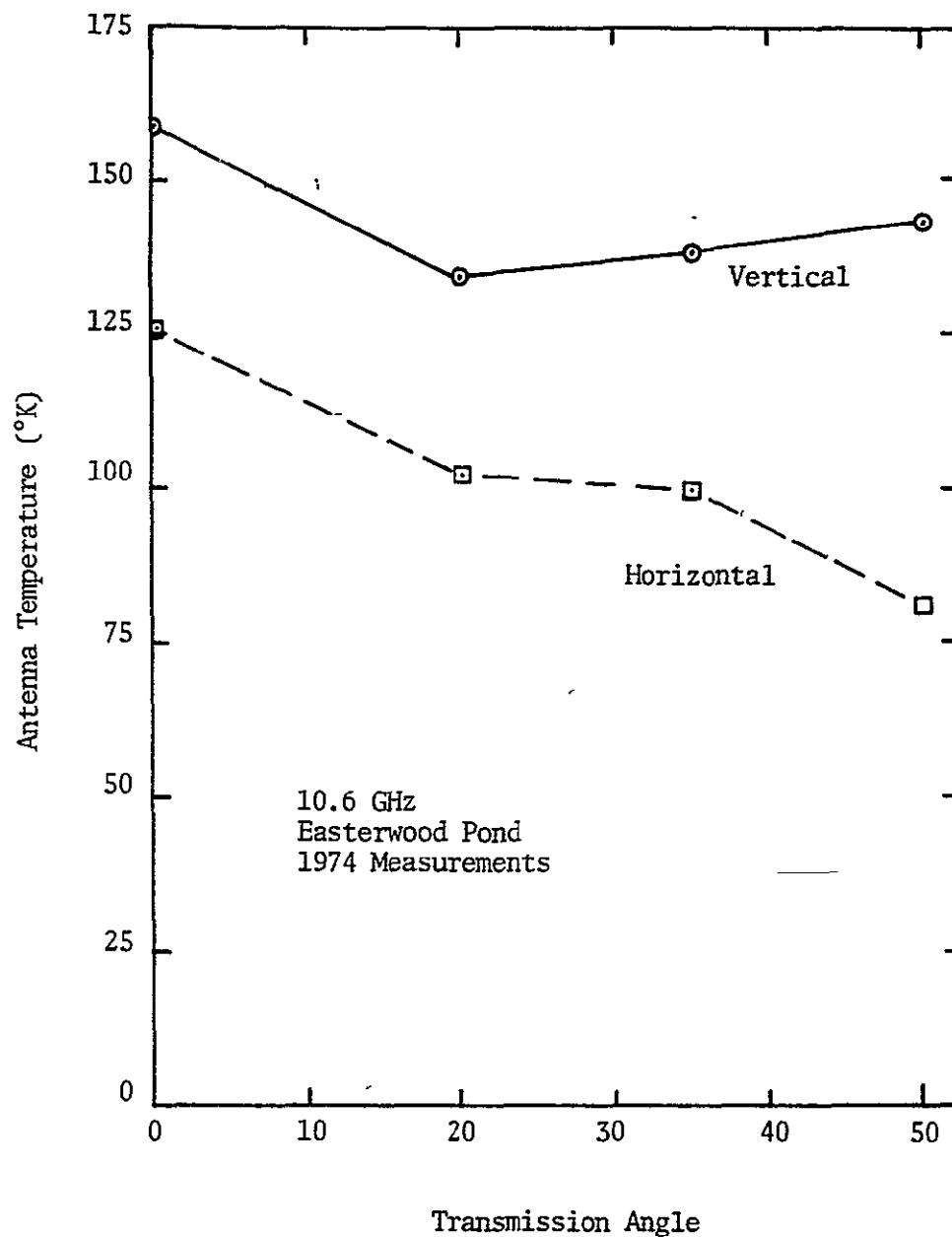
Figure B-2.   10.6 GHz fresh water measurements
that demonstrate the effect of self
emission near nadir.
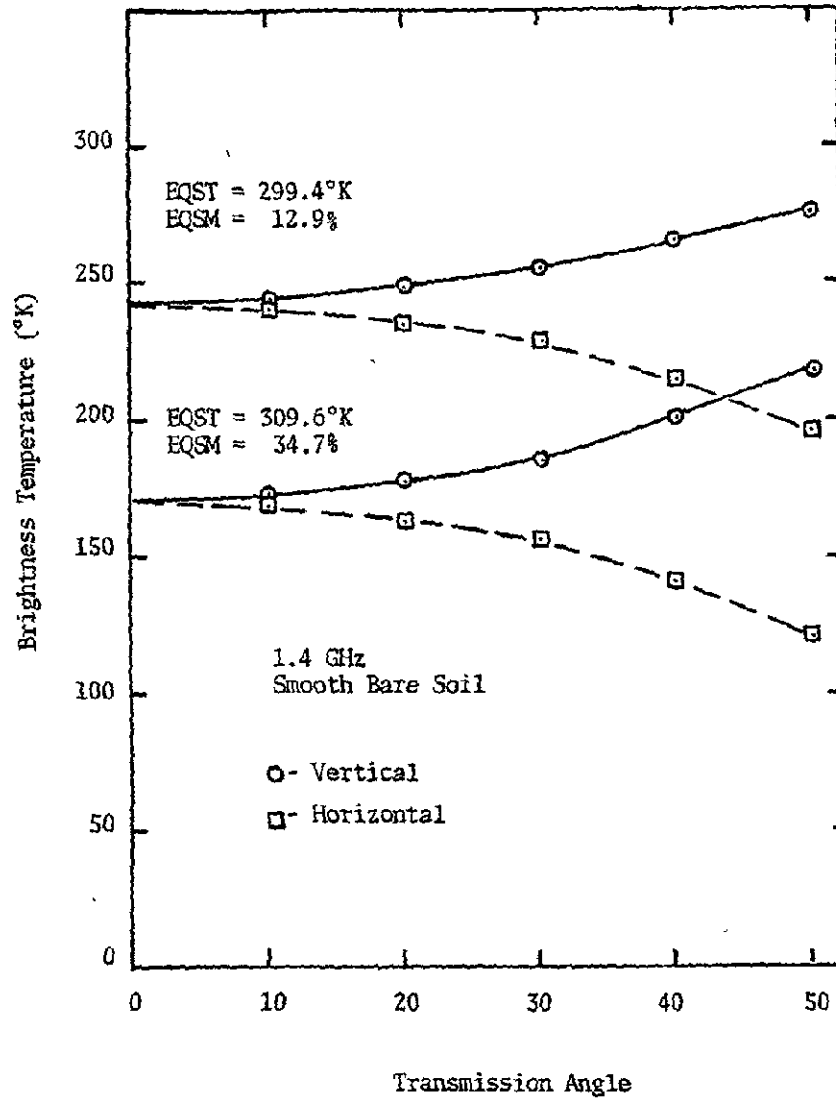
Figure B-3. Calculations of the brightness
temperature of smooth bare soil
for two extreme moisture conditions.

approximately equal to the horizontal brightness temperature at 20° plus one half of the difference between vertical and horizontal brightness temperatures at 20°. A similar relationship can also be expected for the brightness temperatures of rough surfaces between nadir and 20°. With this in mind, the effect of self emission is apparent in the data of Figures B-4 through B-6. The dotted lines in these figures show the expected normalized antenna temperatures approximated as described above. Note that the self emission at nadir decreases as the surface roughness increases and as the soil moisture decreases.

Correction Scheme Using Radar Data

The self emission component to the measured antenna temperature does not only occur at nadir, but—is present for all transmission angles. However, the magnitude of this component is a direct function of the backscattering coefficient at each transmission angle (note that transmission angle and incident angle are equivalent). For most surfaces, except perhaps the very rough surface, the magnitude of the backscattering coefficient decreases rapidly with transmission angle. As a result, the self emitted noise energy reflected back to the receiving aperture is a very small component of the total apparent radiation received by the antenna at angles greater than about 20°.
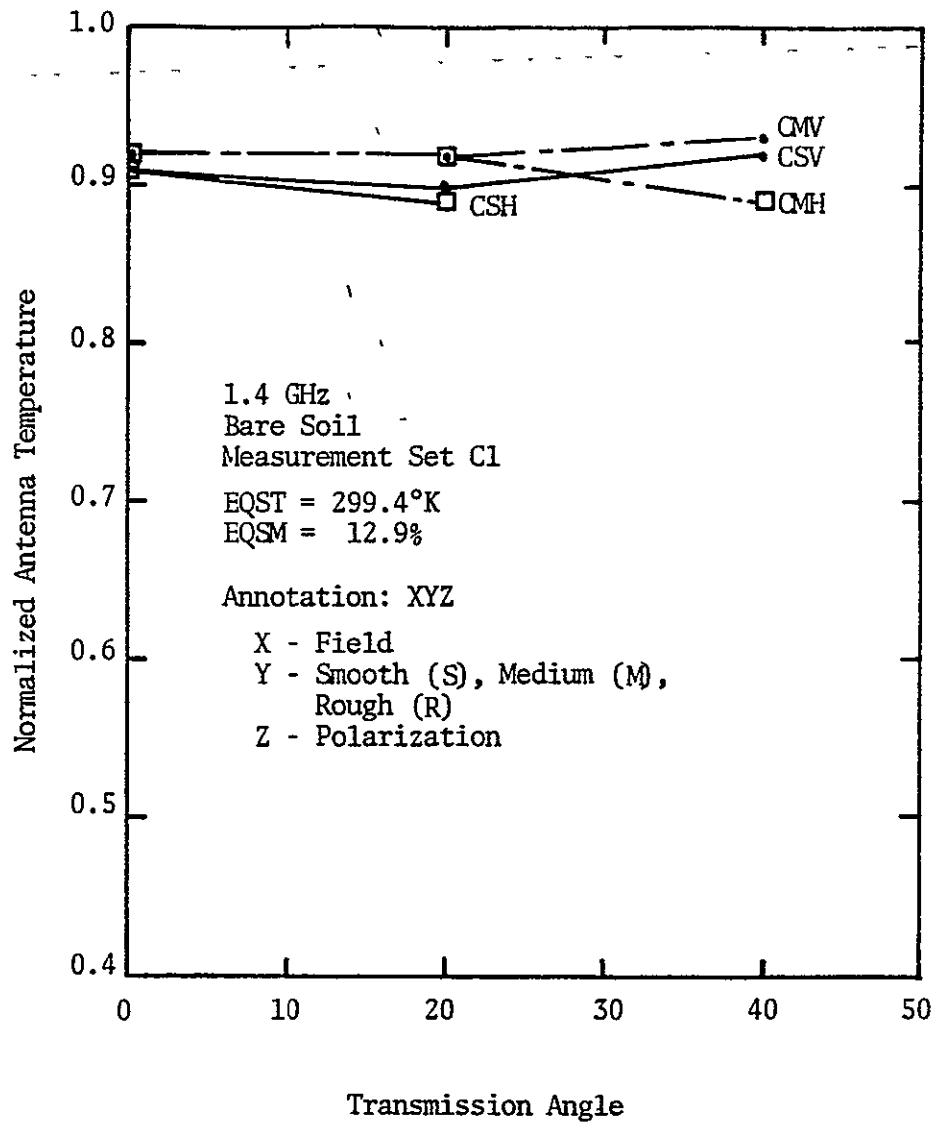
Figure B-4. Measurements of emission from dry bare soil at 1.4 GHz.
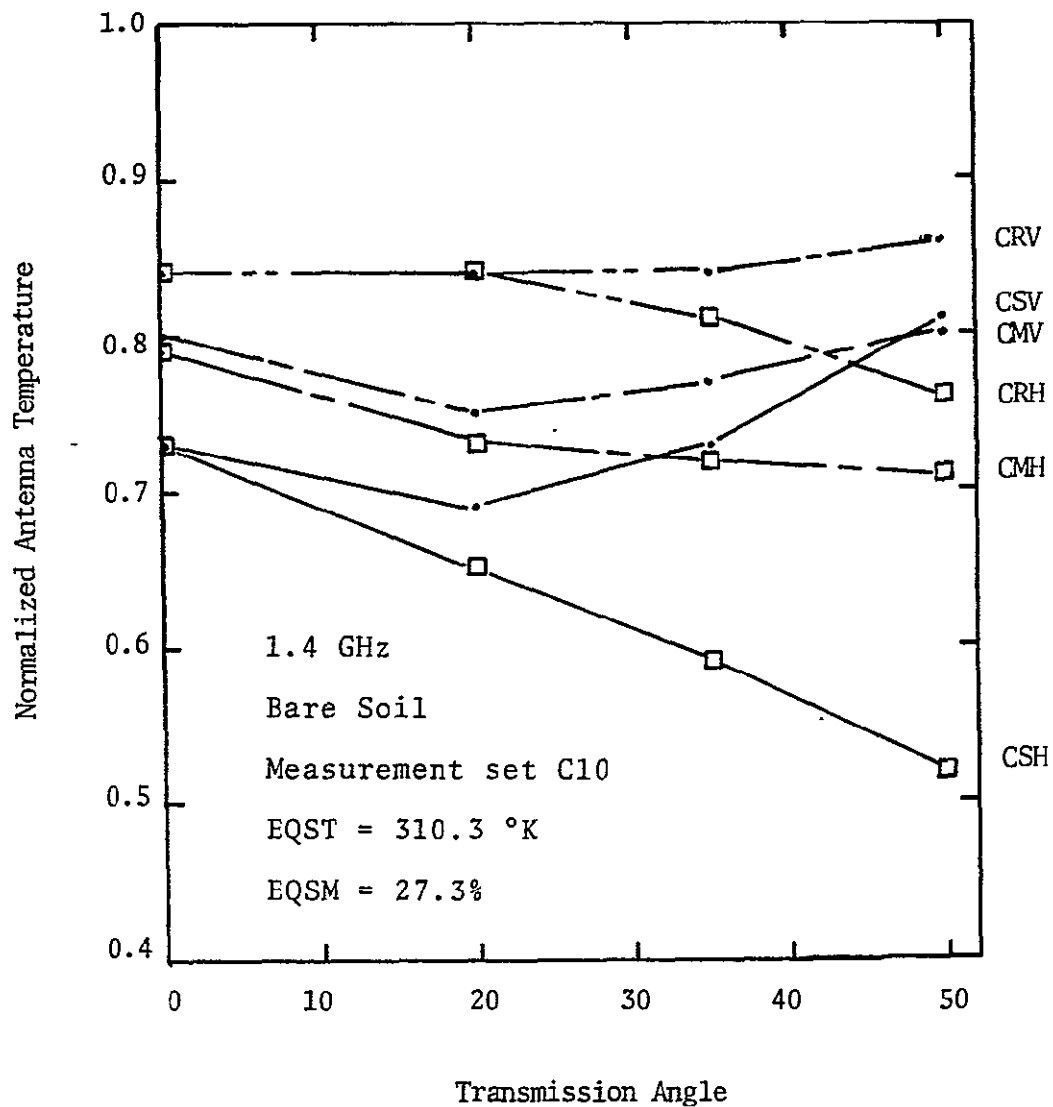
Figure B-5.   Measurements of emission from moist bare soil at 1.4 GHz.
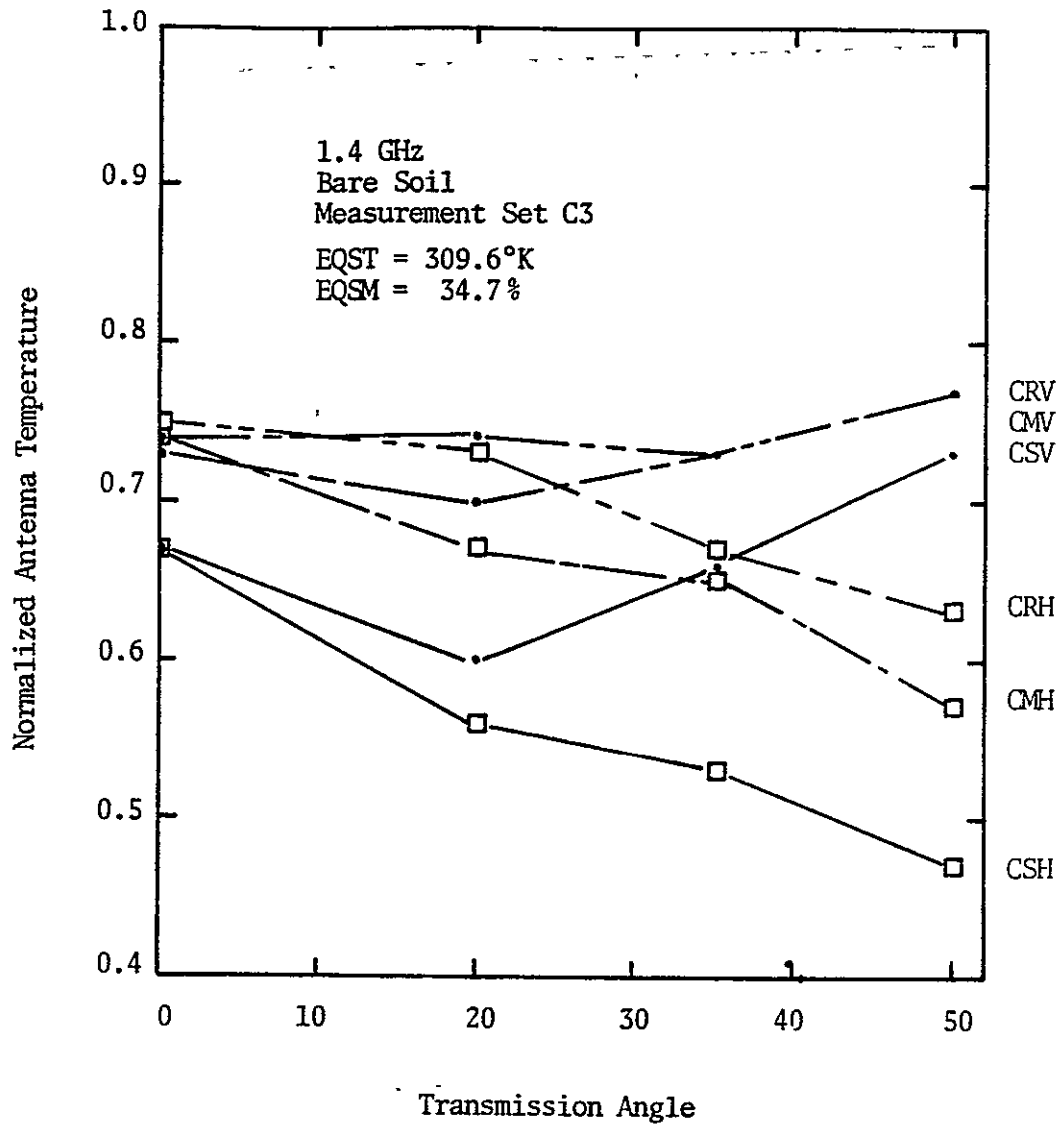
Figure B-6. Measurements of emission from wet
bare soil at 1.4 GHz.

Since the self emitted component of the measured
antenna temperature is a function of the backscattering
coefficient, it is possible to calculate the self emitted
component using the radar backscatter measurements reported
by Batlivala and Cihlar [106]. The bare fields were ir-
rigated just prior to measurement set number three. As
a result, measurement set three has the highest self emis-
sion component of all of the 1974 measurements. For this
reason this measurement set will be used to demonstrate
the magnitude of the self emission component.

, Neglecting atmospheric effects and antenna beamwidth
effects, the measured antenna temperature can be decomposed
into two components.

$$T_m = T_s + T_{se} \qquad \text{(B-1)}$$

T_m is the measured apparent antenna temperature, T_s is the
contribution of the soil and T_{se} is the component of the
noise power emitted by system that is reflected from the
surface back into the antenna aperture. T_{se} is related to
the noise power emitted by the system through the back-
scatter radar cross section of the surface. Measurements
of normalized radar cross section were reported by Batlivala

and Cihlar [106]. Since these measurements were obtained
simultaneously with the passive measurements, they can be
used in conjunction with the radar equation to calculate
the noise emission of the system. Batlivala and Cihlar
only reported measurements between 2 GHz and 8 GHz, so
their data had to be extrapolated to 1.0 GHz and 10 GHz.
Table B-1 contains the results of this extrapolation as a
function of incident angle.

Self Emission at 1.4 GHz

In order to use the radar equation to calculate the
power emitted by the system, one must first determine T_{se},
the backscattered component of the self emitted power. T_{se}
can be determined by comparing theoretical calculations of
the brightness temperature of the soil to the measured
antenna temperature. Figure V-7 is a comparison of the
measured antenna temperature of the smooth surface to the
calculated brightness temperature of smooth soil at 1.4 GHz.
In Figure V-7 the theoretical calculations were purposely
shifted so that they matched the measurements at 20°. This
was done to again demonstrate that the measurements at nadir
should fall approximately halfway between the measurements
at 20°. Using this criterion, the brightness temperature of
the smooth surface at nadir will be assumed to be 173.5°K.
The measurement was 201.5°K. Using (B-1), the backscattered
self emitted component is 28°K.

TABLE B-1

Values of σ° Extrapolated from Measurements

Reported by Batlivala and Cihlar [106]

Field*	Angle	Normalized Radar Cross Section			
		1.0 GHz	(VV&HH)	10.0 GHz	(VV&HH)
CS-2	0	19.5 dB	89.13	13.0 dB	19.95
	20	- 4.5 dB	0.35	- 2.0 dB	0.63
	35	-10.0 dB	0.10	- 6.0 dB	0.25
	50	-12.5 dB	0.06	- 8.0 dB	0.16
CM-2	0	13.0 dB	19.95	0.0 dB	1.00
	20	5.5 dB	3.55	- 0.5 dB	0.89
	35	2.0 dB	1.58	- 0.5 dB	0.89
	50	- 1.5 dB	0.71	- 1.0 dB	0.79
CR-2	0	6.6 dB	4.57	- 1.0 dB	0.79
	20	5.2 dB	3.31	- 2.0 dB	0.63
	35	3.7 dB	2.34	- 3.0 dB	0.50
	50	2.2 dB	1.66	- 3.7 dB	0.43

*Measurement set two reported by Batlivala and Cihlar [106]
correspond to measurement set three reported by Newton [103]
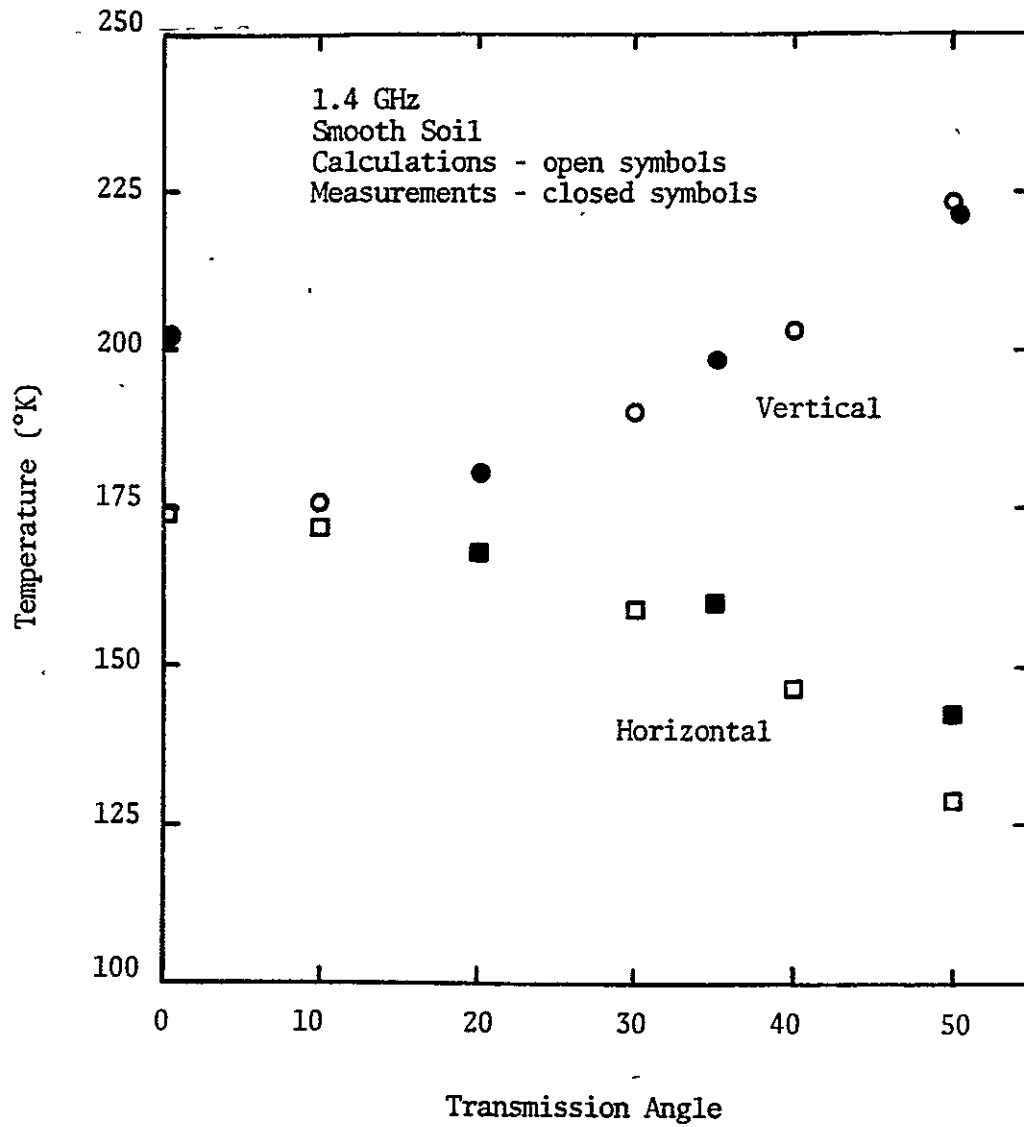
Figure B-7. Comparison of measurements to calculations of emission from smooth soil.

The radar equation can now be used to calculate the self emitted noise power of the 1.4 GHz system using a T_{se} of 28°K and the radar cross section measured at nadir in Table B-2. The radar equation is

$$P_r = \frac{G_t P_t}{4\pi r^2} \frac{\sigma}{4\pi r^2} \frac{G_r \lambda^2}{4\pi}$$

(B-2)

where:

P_r - power received (watts)

P_t - power transmitted (watts)

G_t - maximum gain of the transmitting antenna

G_r - maximum gain of the receiving antenna

λ - wavelength (m)

σ - radar cross section (m^2)

r - distance from the scene to the antennas (m)

Batlivala and Cihlar [106] report normalized radar cross section, $\sigma°$, which is related to σ by

$$\sigma° = \frac{\sigma}{A} = \sigma \frac{\cos \theta}{r^2 \Delta\Omega}$$

(B-3)

TABLE B-2

Parameters used to Calculate the Self Emitted

Noise Power of the L-band System

Parameter	Value Used
P_r @ nadir	9.299×10^{-15} watts
G_r*	183.35
G_t*	183.35
$\Delta\theta$; $\Delta\phi$	15°
λ	0.212 meter
r	12.3 meter
$\sigma°$ @ nadir	89.13
P_t @ nadir	8.13×10^{-14} watts

*Based on the approximate equation

$$G = \frac{41,253}{\Delta\theta\Delta\phi}$$

where $\Delta\theta$ and $\Delta\phi$ are beamwidths in degrees

where A is the area of the scene subtended by the beam width, ΔΩ, of the transmitting and receiving antennas (Figure B-8). T_{se} can be converted to watts using

$$P = kTB \tag{B-4}$$

where:

k - Boltzman's constant $(1.23 \times 10^{-23} \frac{watts}{sec^\circ K})$

B - bandwidth (27 MHz @ 1.4 GHz)

T - temperature (°K)

Table B-2 contains a list of the parameters used in (B-2) through (B-4) to calculate the self emitted power of the 1.4 GHz system. The self emitted power is approximately 8.12×10^{-14} watts. This converts to a noise temperature of 244.8°K.

This system noise emission can be related back to system parameters using the relationship describing the noise emission of passive components.

$$T_{emitted} = t_0(1 - L) \tag{B-5}$$

Antenna

$\Delta\Omega$

r

$r^2\Delta\Omega$

A
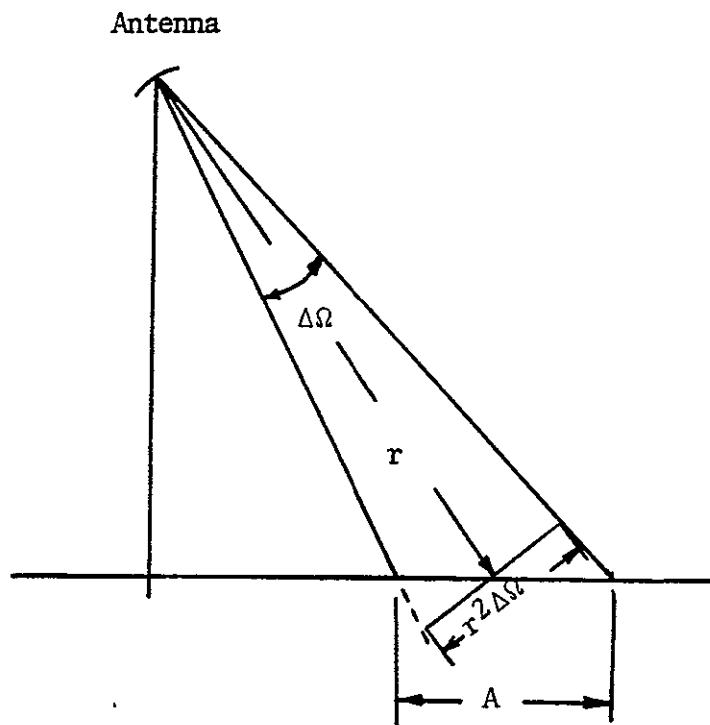
Figure B-8. Relationship between the area "viewed"
by an antenna and its beamwidth.

where t_o is the physical temperature of the component and L is the transmittance of the component. Since the emission of a passive component is dependent upon its temperature, the self emission of the 1.4 GHz system can be viewed as consisting of two components. The receiver section which is temperature controlled at 55°C, and the antenna and cable connecting the receiver and antenna which is at ambient temperature. Thus

$$T_{se} = T_{receiver \atop emission} + t_{antenna}(1 - L_{antenna})$$
$$+ t_{cable}(1 - L_{cable})$$

(B-6)

Newton [103] gives L_{cable} as 0.934 and $L_{antenna}$ as 0.86. Assuming that the antenna and cable temperatures are 300°K, then $L_{receiver}$ can be calculated using (B-7).

$$L_{receiver} = 1 - \frac{T_{se} - T_{antenna}(1 - L_{antenna}) - T_{cable}(1 - L_{cable})}{T_{receiver \atop emission}}$$

(B-7)

The effective receiver transmittance calculated in this fashion is 0.442. The reciprocal of $L_{receiver}$ converts to 3.55 dB. This can be interpreted to mean that the 1.4 GHz receiver section has a lumped "insertion loss" of 3.55 dB.

It is now of interest to determine how large a contribution this self emitted power makes to the measured antenna temperature as a function of angle and surface roughness. This can be done using the radar equation and the normalized radar cross sections contained in Table B-1. Table B-3 contains the results of such calculations for 1.4 GHz. Measurement set three is considered to be the worst case condition since the measured radar cross sections were the largest for this set due to the very wet soil conditions. It is clear from Table B-3 that the self emission component is only significant at angles near nadir.

Self Emission at 10.6 GHz

The effect of self emission on the 10.6 GHz measurements has not been discussed. This is a result of the fact that the "smooth" field actually appears as a relatively rough field at 10.6 GHz. This is demonstrated by Figure B-9 which is a plot of 10.6 GHz measurements for the "smooth" bare field. These data do not have the characteristics of the emission of a smooth field. Also, the vertical measurement at 20° appears to be invalid. As a result, it was not possible to assume a value at nadir based on the 20° measurements. However, an

TABLE B-3

Calculations of the L-band Self Emitted Component;

Measurement Set Three

| Field | Angle | Self Emitted Component | |
		Power (watts)	Noise Temperature (°K)
CS	0	9.30×10^{-15}	28.00
	20	3.90×10^{-17}	0.12
	35	1.28×10^{-17}	0.04
	50	9.79×10^{-18}	0.03
CM	0	2.09×10^{-15}	6.29
	20	3.96×10^{-16}	1.19
	35	2.02×10^{-16}	0.61
	50	1.16×10^{-16}	0.35
CR	0	4.79×10^{-16}	1.44
	20	3.69×10^{-16}	1.11
	35	2.99×10^{-16}	0.90
	50	2.71×10^{-16}	0.82
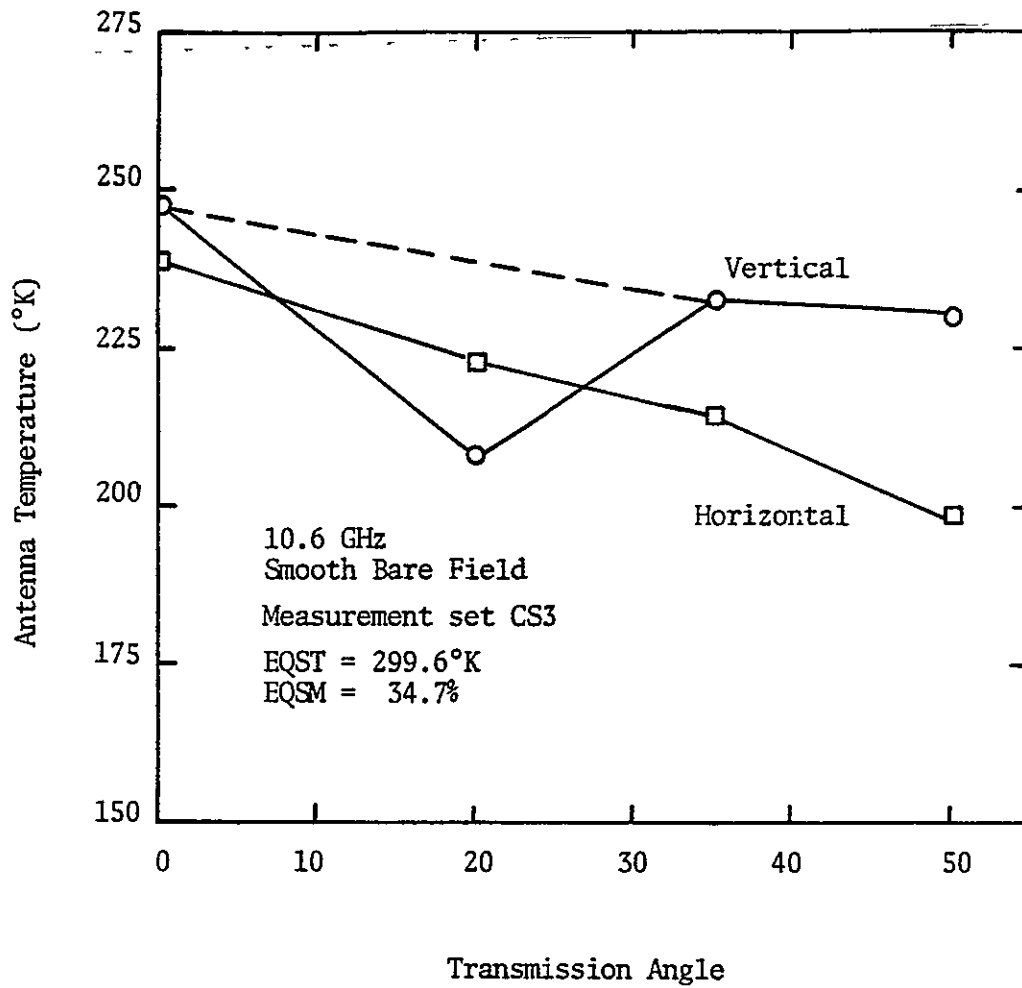
Figure B-9. 10.6 GHz measurements of a wet smooth
bare field.

estimate of the X-band self emission for the 10.6 GHz
system can be made by considering the design of the 10.6 GHz
front end.

Figure B-10 is a block diagram representation of the
10.6 GHz front end. During normal operation, circulator
two is in a position to pass energy from the hot reference
load to circulator one. Circulator one switches with a
duty cycle of one-half, alternately passing energy to the
receiver from the hot reference load and the antenna. When
circulator one is in a position to pass energy from the
antenna to the receiver, it inherently allows energy to
pass from the hot reference load out the antenna. Likewise,
when it is in a position to pass energy from the hot
reference load toward the receiver, it also passes noise
energy from the receiver out the antenna.

Neglecting circulator losses, the average noise energy
transmitted out of the 10.6 GHz antenna is

$$T_{se} = \left[\tfrac{1}{2} T_{generator} + \tfrac{1}{2} T_{receiver} \right] L_{cA} L_{A}$$

$$+ L_{A} \left(t_{cA} (1 - L_{cA}) \right) + t_{A} (1 - L_{A})$$

(B-8)

L_A - transmittance of the antenna

L_{CA} - transmittance of the cable
connecting the antenna to the
receiver enclosure at point B

L_C - transmittance of the cable
connecting the circulators

L_H - transmittance of the cable
connecting the hot reference
load to circulator 2
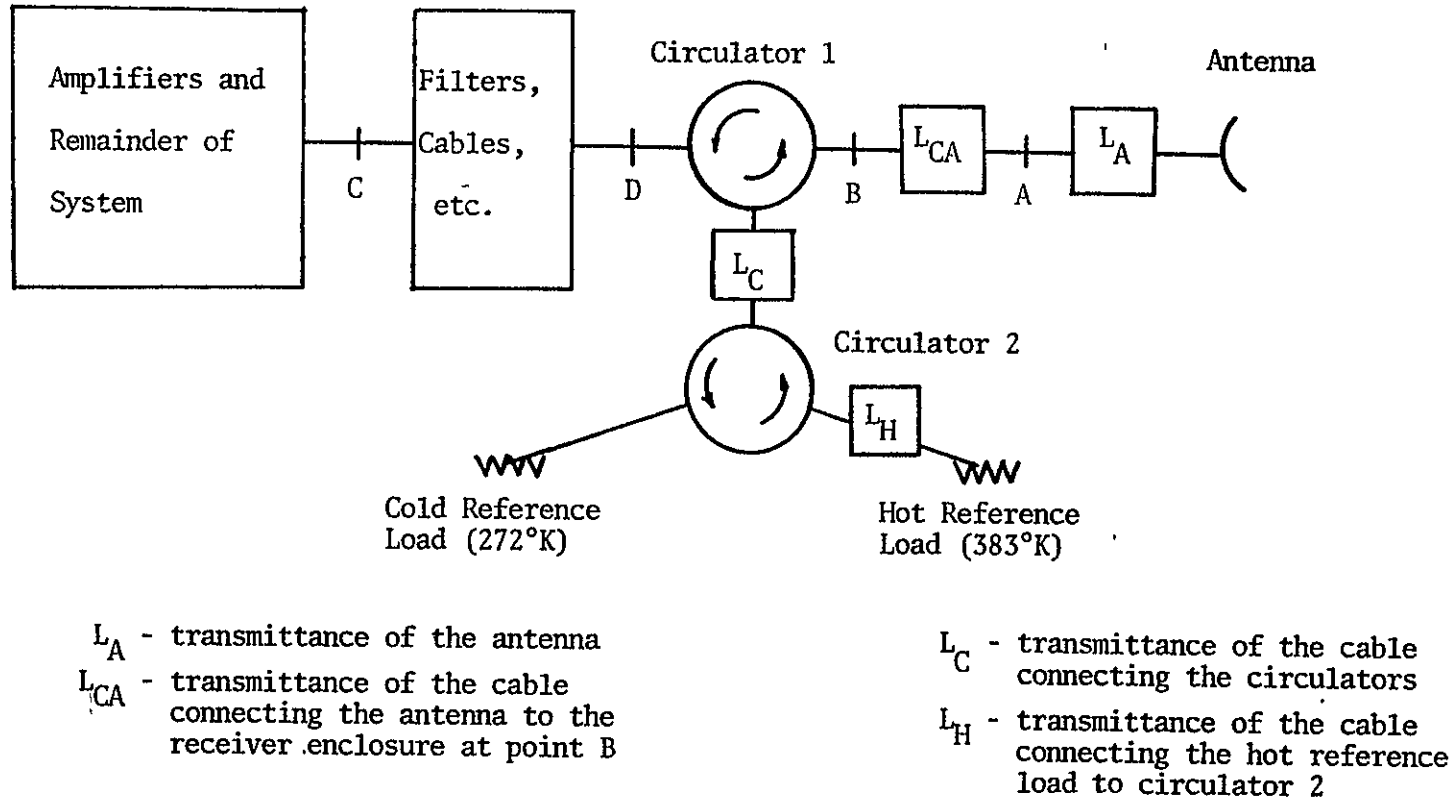
Figure B-10. Simplified block diagram of the 10.6 GHz front end.

$$T_{generator} = 383(L_H L_c) + L_c(t_H(1-L_H)) + t_c(1-L_c) \qquad \text{(B-9)}$$

$$T_{receiver} = t_{receiver}(1 - L_{receiver}) \qquad \text{(B-10)}$$

The transmittances are defined in Figure B-10. The lower case t's stand for physical temperatures of the respective components. As mentioned before, the receiver is temperature controlled at 55°C, so $t_{receiver}$, t_H, and t_c are 328°K. The "lumped" insertion loss of the receiver is given by the sum of the losses of circulator one, the isolator, the filter, the mixer and the cables. Assuming each of these are 0.5 dB, the lumped insertion loss of the X-band receiver is 2.5 dB. This corresponds to an $L_{receiver}$ of 0.56 and a $T_{receiver}$ of 143.6°K. Assuming L_H and L_C are both 0.97, then $T_{generator}$ is 379.75°K. Newton [103] gives L_{CA} as 0.97 and L_A as 0.86. Assuming that t_{CA} and t_A were 300°K, the self emission of the 10.6 GHz system is calculated to be 268°K using (B-8).

The worst case self emitted contribution to the 10.6
GHz measurements can be estimated as a function of angle
and roughness using the computed value of 268°K as the self
emission of the X-band system, and the normalized radar
cross section measurements of data set three. The radar
measurements are tabulated in Table B-1, and Table B-4
contains the values of the 10.6 GHz parameters used in the
radar equation. Table B-5 contains the results of the
calculations. These calculations follow the trend that would
be expected based on the 1.4 GHz results. Only the
measurements of the "smooth" field near nadir have a sig-
nificant self emission component. It is also obvious from
these calculations that, at 10.6 GHz, the "smooth" field
appears to be a relatively rough field.

TABLE B-4

Parameters Used to Calculate the Self Emitted

Component of the X-band System

Parameter	Value Used
P_t	6.59×10^{-13} watts
$G_r{}^*$	1145.92
$G_t{}^*$	1145.92
λ	0.028 meters
r	12.3 meters
$\Delta\theta$; $\Delta\phi$	6°

*approximated by

$$G = \frac{41,253}{\Delta\theta\Delta\phi}$$

where $\Delta\theta$ and $\Delta\phi$ are beamwidths in degrees

TABLE B-5

Calculations of the X-band Self Emitted Component

for Measurement Set Three

| Field | Angle | Self Emitted Component | |
		Power (watts)	Noise Temperature (°K)
CS	0	5.19×10^{-15}	2.11
	20	1.72×10^{-16}	0.07
	35	7.62×10^{-17}	0.03
	50	5.89×10^{-17}	0.02
CM	0	2.60×10^{-16}	0.11
	20	2.44×10^{-16}	0.10
	35	2.72×10^{-16}	0.11
	50	2.91×10^{-16}	0.12
CR	0	2.06×10^{-16}	0.08
	20	1.72×10^{-16}	0.07
	35	1.53×10^{-16}	0.06
	50	1.58×10^{-16}	0.06

APPENDIX C

EQUIVALENT SOIL MOISTURE AND SOIL
TEMPERATURE TABULATIONS

This appendix contains tabulations of equivalent
incoherent soil moisture and soil temperature calculated
using the soil moisture and soil temperature profiles
from the 1974 and 1975 experiments. Equation (VII-3)
was used to calculate the equivalent incoherent soil mois-
ture. An analogous equation was used to calculate the
equivalent incoherent soil temperature.

Table C-1 contains equivalent soil moistures and soil
temperatures for the 1974 experiment. In 1974 ground
data were normally acquired simultaneously with the micro-
wave measurements at four locations along each side of the
experimental plots. The entries in Table C-1 were cal-
culated using the average of these eight soil moisture
and soil temperature profiles.

Table C-2 contains equivalent soil moistures and soil
temperatures for the 1975 experiment. In 1975 ground
data were acquired at 12 locations within each field as
shown in Figure V-11. Only those profiles that fell within
the antenna footprint during each transmission angle
scan were used to calculate average soil moisture and
soil temperature profiles used in developing Table C-2.

Table C-3 lists those ground measurement locations from which ground data were averaged for each scan direction. Soil temperature profiles obtained from the row ridges and row furrows were averaged with equal weighting.

TABLE C-1

Equivalent Soil Moisture and Soil Temperature

Calculations for the 1974 Experiment

| Measurement Set | 1.4 GHz | | | 10.6 GHz | | |
| | EQST (°K) | EQSM (Percent) | | EQST (°K) | EQSM (Percent) | |
		Weight	Volume		Weight	Volume
AS 1	293.1	27.6	33.9	292.6	29.0	33.4
AS 2	297.2	18.2	23.2	294.3	14.8	17.0
AS 3	300.3	18.8	23.9	302.3	13.1	15.1
AS 4	302.7	16.3	21.0	302.3	9.9	11.5
AS 5	300.3	16.3	21.1	298.3	8.8	10.2
AS 6	302.8	15.5	20.1	302.6	8.6	9.9
AS 7	305.2	14.8	19.4	308.2	7.3	8.5
AM 1	295.8	31.6	35.4	294.9	36.2	38.3
AM 2	299.1	28.6	32.3	302.3	29.2	30.9
AM 3	296.2	21.7	25.2	294.9	21.2	22.5
AM 4	300.2	21.2	24.9	302.0	15.0	15.9
AM 5	299.4	20.3	23.9	298.1	15.1	16.0
AM 6	298.6	18.1	21.6	296.7	11.3	12.0
AM 7	302.9	16.7	20.0	303.6	9.7	10.4
AM 8	308.0	15.6	18.9	312.5	9.2	9.8
AR 2	294.5	26.5	28.1	291.4	27.2	28.5
AR 3	294.3	28.1	29.9	291.3	29.1	30.5

Table C-1 (Continued)

| Measurement Set | 1.4 GHz | | | 10.6 GHz | | |
| | EQST (°K) | EQSM (Percent) | | EQST (°K) | EQSM (Percent) | |
		Weight	Volume		Weight	Volume
AR 4	300.8	21.0	22.3	301.6	24.1	25.3
AR 5	298.8	22.0	23.4	299.3	22.3	23.4
AR 6	299.0	19.9	21.1	299.5	17.1	17.9
BS 1	292.7	24.6	30.5	292.1	25.3	29.1
BS 2	295.1	16.6	21.1	291.4	14.2	16.3
BS 3	301.9	16.0	20.5	303.7	12.3	14.2
BS 4	300.7	15.1	19.5	300.1	10.9	12.5
BS 5	301.7	13.7	17.7	301.5	9.5	11.0
BS 6	306.2	14.0	18.5	309.1	5.9	6.9
BS 7	303.0	11.3	15.1	301.7	5.3	6.2
BM 1	300.7	25.9	26.6	303.0	26.3	27.9
BM 2	291.8	24.7	28.4	291.3	26.1	27.6
BM 3	293.0	19.2	22.5	290.2	18.3	19.4
BM 4	300.8	18.0	21.3	301.4	13.2	14.0
BM 5	301.4	16.4	19.6	301.5	12.7	13.5
BM 6	300.9	16.3	19.4	302.3	11.4	12.1
BM 7	300.9	16.2	19.3	302.3	13.1	13.9
BM 8	304.3	13.2	16.2	304.5	8.0	8.5
BM 9	304.8	12.5	15.4	307.9	6.7	7.2

Table C-1 (Continued)

Measurement Set	1.4 GHz			10.6 GHz		
	EQST (°K)	EQSM (Percent)		EQST (°K)	EQSM (Percent)	
		Weight	Volume		Weight	Volume
BR 1	302.6	22.2	23.6	305.3	17.2	18.0
BR 2	292.8	18.6	19.8	290.9	14.2	14.9
BR 3	294.1	15.8	16.8	291.7	8.6	9.1
CS 1	309.6	10.3	12.9	312.5	3.8	5.5
CS 2	295.7	8.9	11.3	289.5	4.7	7.0
CS 3	299.4	28.2	40.2	300.5	27.2	42.2
CS 4	301.4	22.0	30.4	304.5	21.8	33.8
CS 5	296.1	22.7	31.0	296.0	19.4	30.1
CS 6	299.3	23.5	32.2	300.5	20.8	32.3
CS 7	302.0	25.1	35.4	304.9	25.9	40.1
CS 8	299.8	25.2	35.2	298.9	24.5	38.0
CS 9	303.2	22.7	31.2	305.8	20.3	31.5
CS 10	301.3	20.4	27.3	299.9	13.5	20.8
CS 11	300.6	21.6	29.2	302.1	15.5	24.0
CS 12	300.6	21.5	28.6	299.5	13.2	20.4
CS 13	301.0	19.1	25.3	302.3	10.9	16.9
CS 14	301.3	19.7	26.2	302.3	11.6	18.0
CS 15	300.8	19.5	25.7	300.5	11.3	17.5
CM 1	305.5	10.8	12.8	308.0	3.6	4.3
CM 2	293.8	11.8	14.0	290.1	5.2	6.4

Table C-1 (Continued)

| Measurement Set | 1.4 GHz | | | 10.6 GHz | | |
| | EQST (°K) | EQSM (Percent) | | EQST (°K) | EQSM (Percent) | |
		Weight	Volume		Weight	Volume
CM 3	296.1	28.4	34.1	296.0	28.4	36.1
CM 4	299.1	22.5	26.9	302.8	20.8	26.4
CM 5	299.6	20.0	23.7	299.0	14.2	18.0
CM 6	296.3	21.6	25.5	295.9	16.0	20.4
CM 7	302.6	21.8	25.7	305.8	13.1	16.6
CM 8	304.0	24.5	29.3	307.1	24.0	30.5
CM 9	297.8	23.0	27.3	296.6	16.2	20.6
CM 10	305.7	21.1	24.8	308.6	12.1	15.4
CM 11	300.9	20.1	23.7	299.6	10.6	13.4
CM 12	303.8	20.3	23.8	307.3	9.8	12.3
CM 13	301.7	21.3	25.0	300.5	10.2	12.9
CM 14	304.1	20.6	24.2	306.8	10.2	12.9
CM 15	302.3	20.2	23.7	304.4	9.9	12.5
CM 16	303.5	19.9	23.3	305.0	9.5	11.9
CR 1	304.5	7.3	7.9	308.8	3.5	4.3
CR 2	294.8	7.7	8.4	290.6	5.0	6.3
CR 3	311.3	29.0	34.4	315.8	28.8	30.8
CR 4	298.6	26.0	29.5	303.1	12.8	16.8
CR 5	298.9	15.7	17.3	301.8	8.6	11.2
CR 6	300.0	21.9	24.3	299.2	12.0	15.7

Table C-1 (Continued)

| Measurement Set | 1.4 GHz | | | 10.6 GHz | | |
| | EQST (°K) | EQSM (Percent) | | EQST (°K) | EQSM (Percent) | |
		Weight	Volume		Weight	Volume
CR 7	300.8	21.8	24.3	304.1	11.8	15.5
CR 8	305.3	23.7	27.1	307.1	16.9	22.3
CR 9	297.0	22.8	25.7	296.0	17.6	22.2
CR 10	306.8	19.6	21.4	310.8	8.9	11.5
CR 11	299.1	21.9	24.6	298.0	13.4	17.6
CR 12	309.0	20.2	21.9	313.9	7.8	10.0
CR 13	301.7	21.3	23.6	300.6	10.8	14.2
CR 14	306.7	19.9	21.7	311.7	8.2	10.6
CR 15	305.4	20.8	22.8	308.5	8.9	11.5
DO 1	302.3	15.8	18.7	305.2	12.9	13.7
DO 2	301.0	33.8	37.7	301.9	36.3	38.5
DO 3	304.2	31.6	35.6	304.6	33.3	35.3
DO 4	304.3	29.4	33.3	305.1	28.0	29.7
D9 1	303.1	16.2	19.2	304.0	11.3	12.0
D9 2	298.7	34.4	38.4	298.7	35.9	38.0
D9 3	303.6	29.7	33.6	304.9	30.4	32.2
D9 4	303.6	26.4	30.3	304.2	22.2	23.5

TABLE C-2

Equivalent Soil Moisture and Soil Temperature

Calculations for the 1975 Experiment

| Measurement Set | 1.4 GHz | | | 10.6 GHz | | |
| | EQST (°K) | EQSM (Percent) | | EQST (°K) | EQSM (Percent) | |
		Weight	Volume		Weight	Volume
AO 1	307.6	26.4	43.5	308.7	12.7	20.9
AO 2	300.2	29.8	48.9	301.3	27.9	45.8
AO 3	298.0	27.3	44.9	298.8	15.9	26.0
AO 4	304.9	26.6	43.8	302.5	13.9	22.9
AO 5	300.9	25.5	42.0	302.2	11.9	19.5
AO 6	300.6	25.4	41.9	302.3	14.5	23.8
AO 7	299.4	23.8	39.3	299.1	12.8	21.0
AO 8	300.9	21.9	36.1	301.3	11.7	19.2
AO 9	305.1	19.8	32.8	309.6	10.5	17.2
A3 1	309.7	26.5	43.7	312.3	12.4	20.3
A3 2	300.7	30.0	49.3	302.0	27.1	44.5
A3 3	300.8	27.2	44.8	301.8	15.4	25.2
A3 4	305.2	26.7	44.0	303.5	12.5	20.5
A3 5	300.1	26.4	43.5	300.2	11.6	19.0
A3 6	303.4	25.7	42.4	306.2	13.8	22.6
A3 7	300.5	23.9	39.4	301.2	12.7	20.8
A3 8	299.8	21.6	35.7	301.2	11.6	19.1
A3 9	305.2	20.6	34.0	308.2	10.2	16.6

Table C-2 (Continued)

| Measurement Set | 1.4 GHz | | | 10.6 GHz | | |
| | | EQSM (Percent) | | | EQSM (Percent) | |
	EQST (°K)	Weight	Volume	EQST (°K)	Weight	Volume
A4 1	309.7	26.4	43.5	312.4	13.5	22.2
A4 2	300.7	29.8	49.0	302.0	26.5	43.5
A4 3	300.8	27.1	44.5	301.8	15.2	24.9
A4 4	305.2	26.8	44.1	303.5	14.5	20.5
A4 5	300.1	26.4	43.4	300.2	11.5	18.8
A4 6	303.4	25.7	42.3	306.1	13.3	21.8
A4 7	300.5	23.8	39.3	301.2	12.6	20.7
A4 8	299.8	21.6	35.7	301.2	11.5	18.8
A4 9	305.3	20.4	33.8	308.1	10.1	16.5
A6 1	309.8	26.9	44.3	312.4	14.1	23.1
A6 2	300.8	30.3	49.8	302.0	27.7	45.5
A6 3	300.6	27.1	44.6	301.9	15.9	26.1
A6 4	305.1	26.9	44.3	303.5	13.7	22.5
A6 5	300.1	26.1	43.0	300.2	11.5	18.9
A6 6	303.4	25.9	42.8	306.2	14.2	23.2
A6 7	300.5	23.7	39.0	301.2	12.8	21.0
A6 8	299.8	22.2	36.7	301.2	11.7	19.3
A6 9	305.2	20.3	33.6	308.2	10.2	16.8
A9 1	308.0	26.9	44.2	309.6	13.9	22.7
A9 2	299.8	29.5	48.5	300.9	25.5	41.9

Table C-2 (Continued)

| Measurement Set | 1.4 GHz | | | 10.6 GHz | | |
| | EQST (°K) | EQSM (Percent) | | EQST (°K) | EQSM (Percent) | |
		Weight	Volume		Weight	Volume
A9 3	301.1	27.1	44.6	302.2	15.0	24.5
A9 4	305.6	26.2	43.1	303.9	12.4	20.4
A9 5	303.3	25.4	41.9	302.9	11.4	18.8
A9 6	301.7	25.1	41.3	304.0	12.9	21.1
A9 7	300.9	23.4	38.5	301.4	12.6	20.6
A9 8	302.9	21.6	35.6	304.6	11.3	18.6
A9 9	306.1	20.1	33.2	309.2	10.0	16.5
BO 1	305.8	38.5	63.2	306.7	38.8	63.6
BO 2	302.8	30.6	50.3	303.2	26.1	42.9
BO 3	306.3	27.5	45.3	308.0	19.2	31.6
BO 4	305.0	33.3	54.7	306.1	34.0	55.8
BO 5	307.5	25.6	42.1	309.6	13.5	22.1
BO 6	302.9	20.4	33.7	302.1	9.5	15.5
BO 7	310.1	18.8	31.1	310.6	10.1	16.6
B3 1	305.3	40.1	65.8	306.3	40.2	65.9
B3 2	301.3	31.8	52.3	301.4	29.4	48.3
B3 3	306.7	27.6	45.4	308.2	18.9	31.0
B3 4	302.4	31.9	52.4	303.6	28.9	47.4
B3 5	307.8	26.0	42.8	310.1	14.3	23.5

Table C-2 (Continued)

Measurement Set	1.4 GHz			10.6 GHz		
	EQST (°K)	EQSM (Percent)		EQST (°K)	EQSM (Percent)	
		Weight	Volume		Weight	Volume
B3 6	304.1	20.0	33.2	304.2	9.3	15.3
B3 7	309.3	18.7	31.0	312.1	9.8	16.1
B4 1	305.3	40.0	65.7	306.3	40.0	65.6
B4 2	301.3	31.6	51.9	301.4	28.1	46.1
B4 3	306.7	27.4	45.1	308.2	19.0	31.1
B4 4	302.4	31.4	51.6	303.6	28.2	46.3
B4 5	307.7	25.5	42.1	310.1	13.0	21.4
B4 6	303.9	19.9	33.0	304.2	9.3	15.2
B4 7	309.3	18.8	31.3	312.1	10.0	16.4
B6 1	305.3	39.9	65.5	306.3	40.3	66.1
B6 2	301.3	31.6	51.9	301.4	29.0	47.6
B6 3	306.7	27.7	45.5	308.2	19.5	32.0
B6 4	302.5	31.8	52.3	303.6	30.4	49.9
B6 5	307.8	25.8	42.5	310.1	41.1	23.2
B6 6	304.0	20.6	34.1	304.2	9.25	15.2
B6 7	309.3	18.6	30.9	312.1	9.7	15.9
B9 1	305.2	37.7	62.0	306.2	37.2	61.0
B9 2	302.2	30.4	50.0	302.5	25.9	42.5

Table C-2 (Continued)

Measurement Set	1.4 GHz			10.6 GHz		
	EQST (°K)	EQSM (Percent)		EQST (°K)	EQSM (Percent)	
		Weight	Volume		Weight	Volume
B9 3	306.7	26.3	43.3	308.1	14.5	23.8
B9 4	301.9	32.3	53.6	302.6	32.9	54.0
B9 5	307.1	26.0	42.7	308.9	17.4	28.6
B9 6	304.5	19.4	32.1	305.1	9.2	15.1
B9 7	309.6	18.0	29.9	311.7	10.0	16.4

TABLE C-3

Ground Sampling Locations that Correspond to the Antenna

Temperature Measurement Sets Made at Each Azimuth Angle

Field	Azimuth Angle with Respect to Row Direction	Ground Sampling Location
A	0°	1, 2, 3, 4, 9, 10
	30°	1, 4, 5, 6, 9, 10, 11
	45°	1, 5, 6, 9, 10, 11
	60°	1, 2, 5, 6, 10, 11
	90°	1, 2, 7, 8, 9, 10, 11, 12
B	0°	1, 2, 9, 10, 11, 12
	30°	1, 2, 3, 5, 6, 7, 8, 11
	45°	1, 2, 5, 6, 7, 11
	60°	1, 2, 5, 7, 8, 10, 11
	90°	1, 2, 3, 4